

NORTHWESTERN UNIVERSITY

The $(e, e'p)$ Reaction Mechanism in
the Quasi-Elastic Region

A DISSERTATION

SUBMITTED TO THE GRADUATE SCHOOL
IN PARTIAL FULFILLMENT OF THE REQUIREMENTS

for the degree
DOCTOR OF PHILOSOPHY

Field of Physics

By
Dipankar Dutta
EVANSTON, ILLINOIS

June 1999

© Copyright by Dipangkar Dutta 1999
All Rights Reserved

ABSTRACT

The $(e, e'p)$ Reaction Mechanism in the Quasi-Elastic Region

Dipangkar Dutta

Coincidence $(e, e'p)$ yield for the quasi-elastic scattering of electrons from hydrogen, carbon, iron and gold nuclei were measured at squared four momentum transfer of 0.64, 1.28, 1.79 and 3.25 (GeV^2). The experimental yield divided by the yield from a Plane Wave Impulse Approximation simulation of the experiment was used to calculate the transparency of the nuclear medium to the recoiling proton. Transparency is studied as a function of momentum transfer and nuclear size. The experimental yield was also used to extract deradiated spectral function for carbon, iron and gold. These spectral functions were used to separate the longitudinal and transverse components of the spectral function for carbon, iron and gold at squared four momentum transfer of 0.64 (GeV^2) and carbon and iron at squared four momentum transfer of 1.79 (GeV^2).

The goal of this experiment was to study the reaction mechanism of the quasi-elastic scattering process and the propagation of protons through atomic nuclei. The results of this experiment identify important aspects of the final state interactions between the recoiling proton and the residual nucleus. The results also provide insight into the single-nucleon knockout picture of the quasi-elastic reaction mechanism and verify the validity of approximations such as the Impulse Approximation and other reaction mechanisms used to describe $(e, e'p)$ scattering.

Acknowledgments

It is truly a monumental task to acknowledge all who have contributed to the successful completion of this thesis. Firstly I would like to acknowledge the steady support, encouragement and mentoring I received from my advisors Ralph Segel and Don Geesaman. Their vast knowledge and passion for learning has been truly inspiring. This work would not have been possible without their constant support, dedication and patience. I consider myself very fortunate to have worked and learned under the supervision of these two great teachers and scientists.

Reflecting back on the time I spend at CEBAF (JLab), I can safely claim that my training as an experimental physicist was in the ancient Indian “Gurukula” tradition. I was “exiled” for two years to the “wilderness” called CEBAF, where I learned under the able tutelage of Guru Rolf Ent. His enthusiasm and dedication is infectious and his love and knowledge of physics is inspiring. He has the right mix of - carrying the weight of the world and throwing his weight around to get all the tough jobs done with consummate ease.

The whole academic experience at CEBAF was greatly enhanced by the excellent group of fellow “sishtyas” (listed here in roughly chronological order): John Arrington, Dave Meekins, Gabriel Niculescu, Ioana Niculescu, Bart Terburg, Derek van Westrum, Chris Bochna, Chris Armstrong, Valera Frolov, Chris Cothran, Jin-seok Cha, Rick Mohring, Doug Koltenuk and Kenneth Gustafson. Their hard work

and comraderie is greatly appreciated. I am especially grateful to John Arrington for taking me under his wings when I arrived at CEBAF as a novice to electron scattering. He was always available to answer the numerous and frequent questions I had and went out of his way in helping me throughout my stay.

I would also like to acknowledge the rest of the Hall C staff and postdocs: Joe Mitchell, Cynthia Keppel, Dave Mack, Steve Wood, Bill Vulcan, Keith Baker, Dave Abbott, Kevin Bailey, Hamlet Mkrtchyan, Ketevi Assamagan, Jim Dunne, Paul Gueye and Roger Carlini, without their help the experiment would never be finished. I am thankful to the technicians who build and maintained Hall C; Steve Lassiter, Mike Fowler, Paul Hood, Steve Knight, Mark Hogerl, Joe Beaufait and numerous others whom I never met.

Many have called Newport News (the home of JLab) 'The Swamp'. Despite all its similarities to a wilderness, I must say that I had thoroughly enjoyed my stay there. This was mostly because of the spirit and friendship of many of my colleagues, notably; John Arrington, Rolf Ent, Derek van Westrum, Bart Turburg, Dave Meekins, the Niculescus and Thierry Auger. I thank them for all the fun we had together both working and playing.

It has been a great pleasure to work with Derek van Westrum as my thesis partner. Ours was easily the most frictionless, co-operative and fruitful partnership among all the data sharing students at CEBAF. He is responsible for neutralizing all my disdain for "team work" and his friendship is certainly an invaluable gain.

The Analysis for this thesis was done at Argonne National Lab. The physics division at ANL is by far the best working environment I have come across so far. I am grateful to all the members of the group at ANL for making it such a fun place to work in. Many thanks to Dave Potterveld for being an excellent systems administrator and for all his work on the calibration of the SOS.

Back at Northwestern I am grateful to the HEP group for letting me use their computers and for the use of their office space. My friends and colleagues at Northwestern were in good measure responsible for making the stressful graduate student life not just bare-able but rather enjoyable. I thank them all for helping me maintain my sanity and achieve balance in my life. Finally I thank my family for all the support and the encouragement which they tirelessly provided. I am very grateful to my parents for giving me the freedom to choose my own way when it was most unusual among their contemporaries to do so.

ॐ पूर्णमदः पूर्णमिदं पूर्णात् पूर्णमुदच्यते ।
पूर्णस्य पूर्णमादाय पूर्णमेवावशिष्यते ॥

Om. That is infinite and this is infinite. The infinite proceeds from the infinite.
Realizing the infinitude of the infinite , it remains as the infinite alone.

Bṛhadaraṇyaka Upaniṣad 5.1.1

Contents

Abstract	iii
Acknowledgments	iv
1 Introduction	1
2 Quasi-Elastic Scattering	5
2.1 Introduction	5
2.2 Plane Wave Born Approximation	9
2.3 Plane Wave Impulse Approximation	10
2.3.1 The Nucleon Response Functions	16
2.4 Distorted Wave Impulse Approximation	18
2.5 Additional Corrections to The DWIA	22
2.5.1 Nuclear Density Dependent Coupling	22
2.5.2 Coulomb Corrections	24
2.5.3 Meson Exchange Currents and Isobar Currents	25
2.5.4 Relativistic Distorted Wave Models	27

2.6	Glauber and Other High-Energy Approximations	28
2.6.1	Glauber Approximation	28
2.6.2	High Energy Approximation for Final State Interactions . . .	31
2.6.3	Correlated Glauber Approximation	33
2.7	Interpretation of Existing $(e, e'p)$ Data	34
2.7.1	Spectral Functions from $(e, e'p)$ Data	35
2.7.2	Excitation Energies and Occupation Probabilities	39
2.7.3	The Koltun Sum Rule	42
2.7.4	The L and T Response Functions	43
2.7.5	Multi-nucleon Knockout	46
2.7.6	Nuclear Transmission	49
2.8	Summary	52
3	The Experimental Apparatus	54
3.1	Introduction	54
3.2	Accelerator	55
3.2.1	Beam	57
3.2.2	Current Monitors	59
3.3	Target	61
3.3.1	Solid targets	62
3.3.2	Cryotarget	64
3.4	Spectrometers	66

3.4.1	High Momentum Spectrometer	66
3.4.2	The HMS Detector Package	72
3.4.3	Short Orbit Spectrometer	78
3.4.4	The SOS Detector Package	80
3.5	Detector Electronics	85
3.5.1	Introduction	85
3.5.2	Hodoscope	85
3.5.3	Shower Counter	86
3.5.4	Čerenkov Counter	88
3.5.5	Trigger	88
3.5.6	Trigger Supervisor	90
3.5.7	Other Diagnostic Signals	92
3.6	Data Acquisition	93
3.7	Kinematics	93
4	Data Analysis	96
4.1	Introduction	96
4.2	Analysis Engine	96
4.2.1	Event Reconstruction	99
4.2.2	Cebaf Test Package	101
4.3	Tracking	102
4.3.1	Multiple Tracks	104

4.3.2	Tracking Efficiency	104
4.4	Event Reconstruction	105
4.4.1	Experimental Procedure	108
4.4.2	Optimization Procedure	110
4.5	Spectrometer and Beam Energy Calibrations	112
4.5.1	Beam Energy	112
4.5.2	Spectrometer Momentum	120
4.5.3	Spectrometer Angles	123
4.5.4	Spectrometer Resolutions	127
4.6	Detector Calibrations	127
4.6.1	Hodoscope Timing Corrections	128
4.6.2	Lead Glass Calorimeter Calibrations	130
4.7	Coincidence Timing	131
4.7.1	Coincidence Blocking and Synchronization Corrections . . .	133
4.8	Electronic Dead Time and Computer Dead time Corrections	137
4.9	Detector Efficiencies	139
4.10	Proton Absorption	140
4.11	The $(e, e'p)$ Monte Carlo Simulation - SIMC	144
4.11.1	The Philosophy	144
4.11.2	Spectrometer Models	145
4.11.3	Off-Shell σ_{ep} Cross-section	148
4.11.4	Model Spectral Functions	148

4.11.5	Generation Weight	151
4.11.6	Radiative Corrections	152
4.11.7	Coulomb Corrections	159
4.12	Extracting Transparency	163
4.13	Extraction of Spectral Functions	165
4.13.1	Derivation	165
4.13.2	Procedure	170
4.14	Deradiating the Spectral Functions	173
4.15	Longitudinal and Transverse Separation of the Spectral Function .	178
4.16	Error Analysis	182
5	Results	185
5.1	Absolute Normalization	185
5.2	Systematics of The Experiment	189
5.2.1	Systematic Variations in The Data	189
5.2.2	Constraint Dependency	193
5.2.3	Summary	195
5.3	Transparency	196
5.3.1	Model Dependence	205
5.3.2	Comparison to Theoretical Models	211
5.3.3	Summary	217
5.4	Spectral Functions	217

5.4.1	Systematic Variations	219
5.4.2	p_m and E_m Distributions	221
5.4.3	Comparison to Theoretical Models	237
5.5	Separated Response Functions	244
5.5.1	Systematic Uncertainties	247
5.5.2	The $Q^2 = 0.6$ (GeV ²) Results	247
5.5.3	The $Q^2 = 1.8$ (GeV ²) Results	256
5.5.4	R_G for Carbon, Iron and Gold	262
5.5.5	Summary	268
6	Summary and Conclusion	273
	References	277
	Appendix	283
A	Parameters of The Model Spectral Functions	283

List of Tables

1	Occupation Numbers N_α and Separation Energies E_α from DWIA analysis of $(e, e'p)$ experiments.	40
2	Solid Targets used in E91013	63
3	Measured HMS Performance	70
4	SOS Performance	81
5	8LM Trigger Logic	91
6	Table of Kinematics for Experiment E91-013	95
7	Parameters used in the tracking algorithm	103
8	Beam energy uncertainties for the differential recoil method.	117
9	Uncertainties in the beam energy determination using the diffractive minima method	119
10	Uncertainties in beam energy determination using $H(e, e'p)$	120
11	Beam energy measurements	121
12	Uncertainty in the Scattering Angle of HMS and SOS	127
13	Calorimeter and Čerenkov Efficiencies	140
14	Materials in SOS.	142

15	Materials in HMS.	143
16	Fermi Energy for the Three Targets.	150
17	Correlation tail correction to the transparency	151
18	Coulomb radius and the Coulomb factor for the three targets. . . .	161
19	Change in the missing momentum ΔP_m and the correction to the cross-section.	162
20	Change in counts between 0-80 MeV in E_m with and without Coulomb corrections.	162
21	Change in counts between 0-80 MeV in E_m with cuts on Coulomb shifted and non-shifted missing momentum	163
22	Standard Data Constraints	164
23	Nominal Data Constraints	186
24	Data/Monte Carlo for $H(e, e'p)$ and $H(e, e')$ scattering	188
25	Singles Yield Stability	191
26	Coincidence Yield Stability	192
27	Constraint dependence of the Transparency	193
28	Offsets between data and simulated spectra	194
29	Systematic Uncertainties in the Data	195
30	Nuclear Transparency	204
31	Model-Dependent Uncertainties	210
32	Variation with Constraints	220
33	Systematic Uncertainties for spectral functions	221

34	Number of Protons	232
35	Spectroscopic Factors	233
36	Nuclear Transparency from Measured Spectral Functions	234
37	Koltun sum rule	236
38	Systematic Variations	248
39	All systematic uncertainties	249
40	Systematic uncertainties in separated spectral functions	249
41	R_G for Carbon, Iron and Gold	263
42	Nuclear Transparency from Separated Spectral Function	270
43	Model Parameters for ^{12}C	283
44	Model Parameters for ^{56}Fe	284
45	Model Parameters for ^{197}Au	285

List of Figures

1	A schematic of the $(e, e'p)$ scattering process	6
2	$(e, e'p)$ scattering diagram under complete distorted wave Born approximation	7
3	The electric and magnetic form factors of the proton	12
4	$(e, e'p)$ scattering diagram under plane wave impulse approximation	14
5	$(e, e'p)$ scattering diagram under distorted wave impulse approximation	19
6	Calculated momentum distribution for 1p knockout from $^{12}C(e, e'p)$ at $T_p = 70$ MeV in parallel kinematics.	23
7	Feynman diagram for MEC and IC contributions to the two-body current.	26
8	The recoil momentum distribution for $^{12}C(e, e'p)$ measured at Saclay, Tokyo and Frascati	36
9	The recoil momentum distribution for $^{12}C(e, e'p)$ measured in parallel and perpendicular kinematics	38
10	The experimental occupations probability for ^{208}Pb	41
11	Separated transverse and longitudinal response functions	45

12	The transverse enhancement factor η as a function of missing energy	46
13	The missing energy spectrum for $^{12}\text{C}(e, e'p)$ in the dip region. . . .	47
14	The missing energy spectrum for $^{12}\text{C}(e, e'p)$ in the quasi-elastic region.	48
15	Measurement of nuclear transmission at $Q^2 = 0.34 \text{ GeV}^2$	50
16	Measurement of nuclear transmission at Q^2 ranging from 1 to 6 GeV^2 .	51
17	Complete layout of the CEBAF Accelerator	56
18	Hall C Arc	57
19	Hall C Beamline	58
20	Schematic of the Unser Monitor	60
21	The target rotation angle	63
22	Schematic of the Cryotarget Cells	65
23	Side view of the spectrometer co-ordinate system	67
24	Side view of the HMS	68
25	Extreme beam envelope of the HMS for a point-to-point tune . . .	71
26	HMS Detector Hut	73
27	Schematic of the wire arrangement in the HMS Drift Chambers . .	74
28	The HMS hodoscope	76
29	Side view of the SOS	79
30	Front and Top Views of the SOS Drift Chambers.	82
31	Hodoscope electronics	86
32	Calorimeter electronics	87
33	Gas Čerenkov Electronics	88

34	HMS/SOS single arm trigger electronics	89
35	Trigger Supervisor Electronics	92
36	Schematic of the Data Acquisition System in Hall C	94
37	Software Flow Chart for the Hall C Analysis Engine.	98
38	Software Flow Chart for the HMS Event Reconstruction.	100
39	The Focal Plane	106
40	The Hms and the SOS sieve slits	108
41	The Slanted Target	109
42	Optimized reconstruction of the angles x'_{tar} and y'_{tar} for the SOS . .	113
43	Optimized y_{tar} reconstruction for the SOS.	114
44	The dispersive minima in ^{12}C	118
45	Difference in the reconstructed and expected invariant mass as a function of central momentum, for the HMS	121
46	Difference between expected and the measured central momentum of the SOS.	122
47	HMS focal point variation with momentum	123
48	HMS and SOS Scattering Plane	124
49	HMS and SOS mispointing	125
50	HMS and SOS magnet motion	126
51	HMS and SOS resolution	128
52	A typical corrected coincidence time spectrum	132
53	Self timed events in the HMS in log scale	134

54	In sync and out of sync events	136
55	The computer deadtime vs pretrigger rate.	138
56	The reconstruction of $H(e, e'p)$ scattering	147
57	The reconstruction of $^{12}\text{C}(e, e'p)$ scattering	149
58	Plot of E_m vs p_m for hydrogen with and without radiation	157
59	Missing energy spectrum of hydrogen	157
60	Spectral Function Extracted from Monte Carlo Data	175
61	Schematic of the iterative procedure used to handle the model de- pendence	177
62	The model dependence of the deradiation process	177
63	ω vs q for the forward and back angle data	180
64	Forward and backward angle q	181
65	Data/Monte Carlo for $H(e, e'p)$ and $H(e, e')$ scattering	187
66	The reconstruction of $H(e, e'p)$ scattering	190
67	Carbon Missing Energy Spectra	198
68	Iron Missing Energy Spectra	199
69	Gold Missing Energy Spectra	200
70	Transparency as a function of proton angle for C	201
71	Transparency as a function of proton angle for Fe	202
72	Transparency as a function of proton angle for Au	203
73	Transparency vs. Q^2	206
74	Transparency vs Nucleon Number	207

75	Transparency vs Q^2	212
76	Transparency vs Q^2	214
77	Transparency vs Q^2	216
78	Transparency vs Q^2	218
79	p shell and s shell momentum distribution of carbon	223
80	p shell and s shell momentum distribution of carbon	224
81	p shell and s shell momentum distribution of carbon	225
82	momentum distribution of carbon	226
83	momentum distribution of iron	227
84	momentum distribution of iron and gold	228
85	momentum distribution of gold	229
86	Missing Energy Distributions	230
87	momentum distribution of carbon compared to DWIA calculation .	238
88	momentum distribution of iron compared to DWIA calculation . . .	240
89	momentum distribution of iron compared to calculations	241
90	Missing energy distribution for iron compared to the calculations of Benhar et al.	242
91	momentum distribution of gold compared to calculations	243
92	momentum distribution for iron compared to the Timora calculation	245
93	Missing energy distribution for iron compared to the Timora calcu- lation	246
94	Forward and Backward momentum distribution of Carbon	250

95	Separated spectral functions for carbon	252
96	Forward and Backward momentum distribution of Iron and Gold .	253
97	Separated spectral functions for iron	254
98	Separated spectral functions for gold	255
99	Forward and Backward momentum distribution of carbon	257
100	Separated spectral functions for carbon	258
101	Separated spectral functions for iron	259
102	Separated spectral functions	260
103	Separated spectral functions compared with previous data.	261
104	The R_G vs momentum transfer squared for ^{12}C p shell	264
105	The R_G vs momentum transfer squared for ^{12}C s shell	265
106	The R_G vs momentum transfer squared	266
107	Transparency from Longitudinal Spectral Function	269

Chapter 1

Introduction

In 1962 Jacob and Maris [1] pointed out that quasi-elastic $(e, e'p)$ scattering had the potential to be a powerful experimental technique to probe the energy levels and structures of the shells of light and medium nuclei. In the same year M. Croissiaux [2] was able to detect electron-proton coincidences in inelastic electron-Deuteron scattering, using the Stanford Mark III linear accelerator and a pair of spectrometers at R. Hofstadter's laboratory. This was followed by measurements of the coincidence cross-section of quasifree electron-proton scattering from ^3H and ^3He in 1964 [3]. The shell structure of ^{12}C and ^{27}Al and the shell binding energies were first measured with quasi-elastic $(e, e'p)$ scattering in 1964 by U. Amaldi et al. [4] at the Frascati synchrotron. These results convinced experimenters that quasi-elastic $(e, e'p)$ scattering was a very versatile tool indeed. Ever since it has lent itself dutifully as an excellent tool for studying nuclear structure. The advantages of $(e, e'p)$ scattering are the relative weakness of electro-magnetic interaction which enables the electron to probe the entire nuclear volume and the thorough knowledge of the electron-photon vertex, which helps isolate the strong interaction in the nucleus. Over the last three decades the results of quasi-elastic $(e, e'p)$ scattering from a host of nuclei have provided very convincing evidence of the nuclear

shell structure and precise information about the properties of these shells. Many results of the quasi-elastic scattering can be explained in terms of Plane Wave Impulse Approximation (PWIA) and an Independent Particle Shell Model (ISPM). However, these models cannot reproduce some of the observations, such as the 20-30% reduction in the occupancy of orbitals deduced from the data [4, 5, 6, 7, 9] and the indications of contributions from multi-nucleon currents [10, 12, 11]. In order to understand these observations one needs to study the mechanism of the $(e, e'p)$ scattering carefully and systematically.

The $(e, e'p)$ reaction has three basic components:

- (i) the electron-proton coupling, ie. the interaction of the incident electron with a proton embedded in the nuclear medium.
- (ii) the single particle structure of the target nucleus.
- (iii) the final state interaction, ie. the interaction of the knocked out proton with the residual nucleus.

The careful investigation of the primary electron-proton coupling can tell us if there are any media modifications of this coupling or if there are signatures of non-nucleonic effects in the nuclei. It is common practice to describe the e-p coupling as a interaction between an electron and a free proton with some corrections for the binding of the proton (for example the prescription due to T. de Forest [13]). The nuclear medium may modify this coupling, as suggested by inclusive electron scattering experiments [14] which have shown that the ratio of the transverse to the longitudinal response functions in the quasi-elastic region deviates significantly from what is expected if the coupling is same as that for a free proton. There are several theories which can be used to account for these effects in terms of modification of the electromagnetic properties of the nucleon in the nuclear environment.

Some of these theories propose partial de-confinement of the quarks [15, 16], while others predict similar effects with meson models [17]. The correct descriptions can only be picked out with further experimentation.

The final state interactions (FSI) provide information about the proton propagation through the nuclei and about the coupling between the various reaction channels. An elegant method to study proton propagation is to measure the nuclear transparency via $(e, e'p)$ reactions. Transparency is the fraction of the protons which escape from the nucleus without interaction. The $(e, e'p)$ reaction is especially suited for studying proton propagation since the electron can probe the entire nuclear volume, unlike proton-nucleus scattering which primarily probe the surface.

In theoretical models FSI are usually (in distorted wave impulse approximation, DWIA) incorporated in terms of proton optical potentials, the parameters of which are obtained from proton-Nucleus elastic scattering experiments. There are indications that FSI need more detailed investigation [18], of effects such as the role of channel coupling in the final state of $(e, e'p)$ scattering.

Thus both the electron-proton coupling and the FSI need to be studied in order to decipher the momentum distribution of the nucleons, the occupation numbers of nuclear shells and the ground-state correlations in nuclei. Part of the work described in this thesis is intended for this very purpose. The aim of the study described here is to understand FSI by comparing measured cross-sections with various model calculations and to provide momentum distributions of the nucleons to help understand the nuclear structure and the reaction mechanism.

With the advent of CW (continuous wave) electron accelerators and high resolution and large acceptance spectrometers it has become possible to probe the nuclear structure very accurately. The experiment to study proton propagation

and the reaction mechanism of quasi-elastic $(e, e'p)$ scattering was carried out at the Thomas Jefferson National Accelerator Facility (TJNAF, a CW accelerator) in experimental Hall C, using the High Momentum Spectrometer (HMS) and the Short Orbit Spectrometer (SOS) in coincidence. Data were collected on three nuclear targets Carbon, Iron and Gold, at four momentum transfer squared Q^2 , ranging from 0.6 to 3.2 GeV^2 (in this thesis we use the convention; speed of light, $c = 1$ and Planck's constant divided by 2π , $\hbar = 1$), and over a range of final proton angles to span the typical initial momentum of the nucleons in the nucleus.

This thesis presents the analysis of the aforementioned data to better understand the quasi-elastic $(e, e'p)$ reaction mechanism. Chapter 2 contains a survey of the formalism of the $(e, e'p)$ reaction, the physics picture that can be derived from existing data and also some results from previous experiments which help motivate this experiment. Chapter 3 and chapter 4 describe the experiment and the data analysis. Chapter 5 contains the final results which include extraction of nuclear transparency and momentum distributions of the protons in the nucleus and the separated longitudinal and transverse response functions. Finally Chapter 6 has the conclusions and the summary.

Chapter 2

Quasi-Elastic Scattering

2.1 Introduction

This chapter presents a brief survey of the quasi-elastic $(e, e'p)$ reaction. A simple schematic (Figure 1) is used to introduce the scattering process followed by a discussion of a general formalism of the process under the Born approximation. Next the plane wave impulse approximation (PWIA) is described followed by a discussion of an improvement to this approximation, the distorted wave impulse approximation (DWIA). Finally some alternative approximation schemes called high energy or Glauber approximations are described. The approximation schemes discussed in this chapter are the ones used in the different theoretical calculations which will be compared to the experimental data presented in this thesis. A more general discussion and detailed derivation of the cross-sections for this process can be found in any of the several review articles on the subject. The most notable among them are the extensive review by Frullani and Mougey [19] and the recent review by J. Kelly [20]. Only aspects of the theory needed to interpret the present data are reviewed. The final section of this chapter reviews some of the existing $(e, e'p)$ scattering data and their physical interpretation.

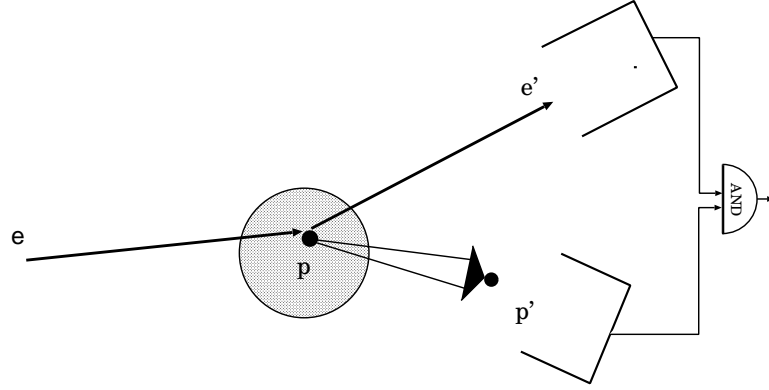


Figure 1: A schematic of the $(e, e'p)$ scattering process

The $(e, e'p)$ scattering process involves an incoming electron scattering off a proton in the target nucleus knocking it out of the target, the scattered electron and the knocked out proton being detected in coincidence. The schematic is shown in Figure 1 and the process can be written as:

$$e + A \rightarrow e' + p + B \quad (1)$$

One would like to describe this process as generally as possible. However, due to incomplete knowledge of the nuclear interactions, one is forced to make some approximations. The first approximation is that the interaction responsible for the electron-nucleus scattering (denoted by H_I) can be separated from the other interactions which are treated as distortions to the particle waves. Denoting the various electron-nucleus interactions as h_i and h_f (Figure 2), and the distorting potential between p and B as \bar{V} , the process can be described in the complete distorted wave Born approximation. The diagram for the process under this approximation is shown in Figure 2. The total Hamiltonian for the initial state is,

$$H = H_i + h_i + H_I, \quad (2)$$

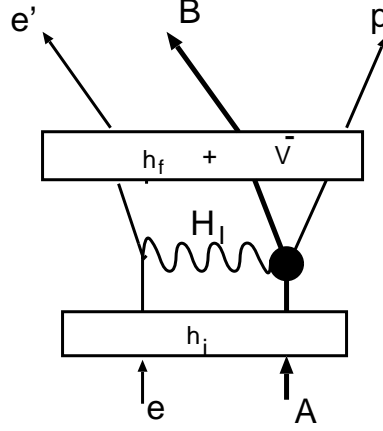


Figure 2: $(e, e'p)$ scattering diagram under complete distorted wave Born approximation

where H_i is the free Hamiltonian describing the initial asymptotic state where the different particles (the electron and the nucleus) are free from interaction. Similarly the total Hamiltonian for the final state is,

$$H = H_f + h_f + \bar{V} + H_I, \quad (3)$$

here H_f is the free Hamiltonian describing the final asymptotic state where the particles (the scattered electron, proton and B) are free from interaction. Under the Born approximation (the interaction H_I acts only once or a single photon is exchanged) and considering the distorting electron-nucleus interaction h and the the distorting potential \bar{V} to all orders one gets the transition matrix between the initial and final state as:

$$T_{fi} = \langle \bar{\phi}_f^{(-)} | H_I | \bar{\phi}_i^{(+)} \rangle. \quad (4)$$

Here $|\bar{\phi}_f^{(-)}\rangle$ and $|\bar{\phi}_i^{(+)}\rangle$ are the distorted state-vectors, which are the solutions of $H_f + h_f + \bar{V}$ and $H_i + h_i$ respectively. Here the approximation about the separation

of the interactions ensures that transition amplitude arising due to the distorting potentials (h and \bar{V}) vanish, because these interactions cannot connect the initial and final channels. These set of approximations are called the complete distorted wave Born approximation (CDWBA).

The most general expression for electron-nucleus interaction is ,

$$\hat{H}_I(x_\lambda) = -eA^\mu(x_\lambda)\hat{J}_\mu(x_\lambda), \quad (5)$$

where $A^\mu(x_\lambda)$ is the Moller potential at 4-space point x_λ representing the electromagnetic field associated with the electron and $\hat{J}_\mu(x_\lambda)$ is the nuclear current density operator at the same 4-space point. The Moller potential is related to the electron current density operator according to the Maxwell equation:

$$\square A_\mu(x_\lambda) = < j_\mu(x_\lambda) > . \quad (6)$$

where,

$$< j_\mu(x_\lambda) > = e\Psi(\bar{x}_\lambda)\gamma_\mu\Psi(x_\lambda), \quad (7)$$

here Ψ and $\bar{\Psi}$ are the positive energy solutions to the Dirac equation for free particles.

One can substitute Equation 5 as the expression for the electron-nucleus interaction in the expression for the transition amplitude (Equation 4), to derive the general expression for the coincidence cross-section by evaluating the square of the transition amplitude over all initial and final states $\sum_{ss',h_i} |T_{fi}|^2$. The distorted state-vectors are calculated in terms of the expansions -

$$|\bar{\phi}_i^{(+)} > = |\phi_i > + \frac{1}{E - (H_i + h_i) + i\epsilon}(h_i)|\phi_i >, \quad (8)$$

and

$$|\bar{\phi}_f^{(-)}\rangle = |\phi_f\rangle + \frac{1}{E - (H_f + h_f + \bar{V}) + i\epsilon} (h_f + \bar{V}) |\phi_f\rangle. \quad (9)$$

Here $|\phi_i\rangle$ and $|\phi_f\rangle$ are the stationary solutions of H_i and H_f respectively and are products of electron state vectors and nuclear state vectors. Using this formulation one can derive the most general expression for the coincidence cross-section for the $(e, e'p)$ scattering process. However, these calculations can be done only be done by employing further approximations, as the exact nature of all the interactions are not known. Various approximation schemes were developed which help calculate the coincidence cross-section much more easily and elegantly. Some of these approximations are explained in the following sections.

2.2 Plane Wave Born Approximation

The simplest method to make the above problem tractable is called Plane Wave Born Approximation. In this scheme the distorted state vectors shown in Equation 8 and 9 are approximated by the plane waves which form the first terms of those expansions. This reduces the transition amplitude (Equation 4) to:

$$T_{fi} = \langle \phi_f | H_I | \phi_i \rangle \quad (10)$$

and the square of the transition amplitude over all initial and final states $\sum_{ss', h_i} |T_{fi}|^2$ can be obtained as the contraction of the electron tensor $\sum_{ss'} A^\mu A^{\nu*} = \eta^{\mu\nu}$ and the nuclear tensor $W_{\mu\nu} = \sum h_i \langle \hat{J}_\mu \rangle \langle \hat{J}_\nu^* \rangle$,

$$\sum_{ss', h_i} |T_{fi}|^2 = K \eta^{\mu\nu} W_{\mu\nu} \quad (11)$$

Under this assumption one gets the coincidence cross-section to be of the form

$$\frac{d^6\sigma}{dk_{0'}d\Omega_{k'}d\Omega_{p'}} = K(\rho_{00}f_{00} + \rho_{++}f_{++} + \rho_{0+}f_{0+} + \rho_{+-}f_{+-}), \quad (12)$$

where K is a kinematic factor and $\rho_{\mu\nu}$ are the nonzero components of the electron current density tensor, while the form factors $f_{\mu\nu}$ are components of the nuclear current density tensor and their physical significance is listed below.

- f_{00} describes the nuclear response function for a purely longitudinal virtual photon coupling to an electron.
- f_{++} corresponds to the response to coupling between a purely transverse virtual photon with an electron.
- f_{0+} is a longitudinal-transverse interference term.
- f_{+-} is a transverse-transverse interference term.

2.3 Plane Wave Impulse Approximation

The elastic electron-proton scattering is the simplest $(e, e'p)$ reaction where plane wave initial and final states are an excellent approximation. The scattering cross-section calculated for one photon exchange is called the Rosenbluth cross-section. It has the form:

$$\frac{d\sigma}{d\Omega} = \left(\frac{d\sigma}{d\Omega} \right)_{Mott} \frac{Q^2}{|\vec{q}|^2} [G_E^2(Q^2) + \tau \epsilon^{-1} G_M^2(Q^2)], \quad (13)$$

where $\tau = \frac{|\vec{q}|^2}{Q^2} - 1$, ϵ is the virtual photon polarization parameter, $\epsilon = \frac{1}{1 + 2(1 + \tau)\tan^2 \frac{\theta}{2}}$ and Q^2 is the momentum transfer squared given by $Q^2 = -q_\mu q^\mu$, here q^μ is the 4-momentum transfer given by $q^\mu = (\omega, \vec{q})$, where ω is the energy loss given by

the difference between the incident and the final electron energies while \vec{q} is the vector difference between the initial and final electron momenta. The differential cross-section for elastic scattering off a point charge $(\frac{d\sigma}{d\Omega})_{Mott}$, called the Mott cross-section, is given by,

$$(\frac{d\sigma}{d\Omega})_{Mott} = \frac{\alpha^2 \cos^2(\theta/2)}{4E^2 \sin^4(\theta/2)}. \quad (14)$$

Here α is the fine structure constant. In this picture the structure of the proton is accounted for in terms of the electric and the magnetic form factors G_E and G_M respectively. These form factors can be approximated in terms of the dipole form [22], shown below:

$$\begin{aligned} G_E(Q^2) &\approx (1 + \frac{Q^2}{0.71})^{-2}, \\ G_M(Q^2) &\approx \mu_p G_E(Q^2), \end{aligned} \quad (15)$$

where μ_p is the magnetic moment of the proton. These forms were determined by parameterizing elastic electron-proton scattering data over a wide range of momentum transfer Q (Figure 3).

When we study $(e, e'p)$ scattering from nuclear targets, this simple picture is no longer valid. The bound nucleon is off shell and the electro-magnetic current which couples to the virtual photon is now dependent on the interaction of the nucleon with the surrounding nuclear matter. Also the initial and the final energy and momentum of the particles involved can be modified by initial state and final state interactions. Initial state interactions include Coulomb distortions of the incoming electron and the correlations between the primary nucleon involved in the scattering with the other nucleons in the target. Final state interactions include rescattering of the knocked out proton and other interactions of the outgoing proton with the rest of the nucleons. These processes are described by adopting a

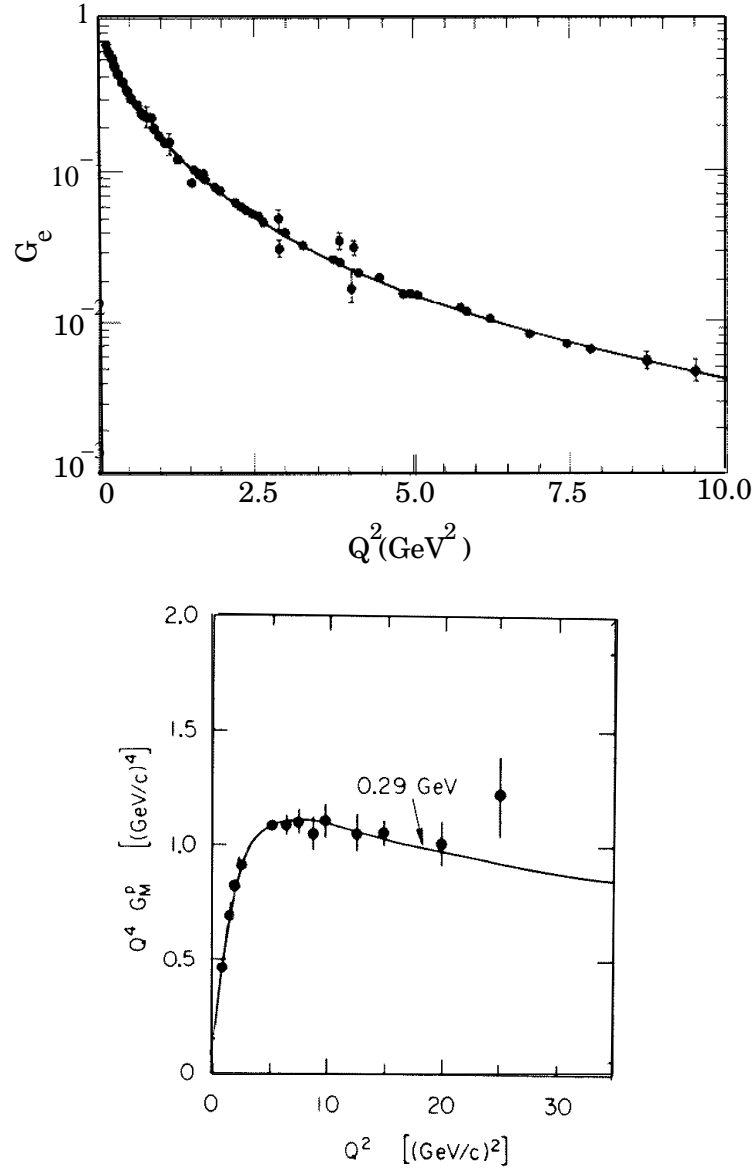


Figure 3: The top panel is the proton electric form factor as a function of Q^2 , the solid line is the dipole proton form factor [21], the bottom panel is the proton magnetic form factor, the solid line is the parameterizations by Gary and Krumplemann [22]

set of approximations known as the plane wave impulse approximation (PWIA). The kinematics of the $(e, e'p)$ reaction under PWIA is shown in the Figure 4. The incoming electron with momentum \vec{k} emits a virtual photon with energy ω and momentum \vec{q} , the scattered electron has momentum \vec{k}' . The photon is assumed to couple to a single proton in the target nucleus which is knocked out of the nucleus with momentum \vec{p} . The scattered electron and the scattered proton are detected in coincidence. The PWIA includes a set of approximations known as Impulse Approximation (IA) whereby the nucleons are treated as independent current/charge distributions interacting in the mean field of the rest of the nucleons, neglecting all exchange currents between the nucleons. The other assumptions used are; undistorted plane waves can be used to describe the incident and the final electron and nucleon wave functions, single photon exchange is sufficient to describe the scattering process, free nucleon form factors can be used to describe the bound nucleons and the kinematics of the reaction is not changed by the final state interactions. Several of these approximations improve with increasing energy and momentum transfer, as the strength of the higher order terms and the effect due to the final state interactions of the knocked out nucleon with the residual nucleons decreases (although FSI increases) at higher energies.

Important kinematic quantities which can be measured under these assumptions (PWIA) are the missing energy, E_m and missing momentum, \mathbf{p}_m . These can be interpreted as measures of the separation energy and initial momentum of the proton in the nucleus. The definitions of these quantities in the lab frame, where $E_A = M_A$ and separation energy $E_s = M_{A-1} + M_p - M_A$ are given below;

$$E_m = \omega - T_{p'} - T_{A-1} = \omega - E_{p'} + M_p - T_{A-1}, \quad (16)$$

$$\vec{p}_m = \vec{p}' - \vec{q}. \quad (17)$$

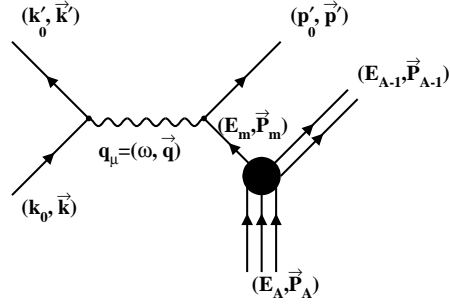


Figure 4: $(e, e'p)$ scattering diagram under plane wave impulse approximation

Here ω is the energy transfer, \vec{q} is the 3 momentum transfer from the electron to the nuclear system, \vec{p}' is the momentum of the outgoing proton, M_p is the proton mass, $T_{p'}$ and T_{A-1} is the kinetic energy of the outgoing proton and the recoiling A-1 nucleons respectively. There are two kinematic configuration which are commonly used in $(e, e'p)$ experiments, parallel kinematics where \vec{p}' is parallel to \vec{q} and perpendicular kinematics where \vec{q} and ω are kept constant and the p_m is varied by changing the angle between \vec{q} and \vec{p}' .

Under the PWIA the coincidence $(e, e'p)$ cross-section is expressed in terms of four form factors [23],

$$\frac{d^6\sigma}{dE_{e'}d\Omega_{e'}dE_{p'}d\Omega_{p'}} = p'E_{p'}\sigma_{Mott} [\lambda^2 W_L(q, \omega) + (\frac{\lambda}{2} + \tan^2(\frac{\theta}{2}))W_T(q, \omega) + \lambda(\lambda + \tan^2(\frac{\theta}{2}))^{1/2}W_{LT}(q, \omega) \cos(\phi) + \frac{\lambda}{2}W_{TT}(q, \omega) \cos(2\phi)]. \quad (18)$$

Where $\lambda = \frac{Q^2}{|\vec{q}|^2}$, θ is the scattering angle and ϕ is the azimuthal angle between the scattering plane and the plane containing \vec{q} and \vec{p}' . The response functions $W_{L,T,LT,TT}$ contain the information about the nuclear structure and the electron-photon coupling which we aim to learn from $(e, e'p)$ experiments. These response functions can be expressed in terms of the product of matrix elements M_μ of the nucleon current between the initial and final nuclear states [24]:

$$M_\mu = \int d\mathbf{p}_i ds \delta(\mathbf{p}_m - \mathbf{p}_i) J_\mu(q, \mathbf{p}_i, \sigma) \Phi_{if}(\mathbf{p}_i, s). \quad (19)$$

Here we have used the plane wave approximation to represent the wave function of the outgoing proton, μ corresponds to a particular component of the nucleon current operator, \mathbf{p}_i is the initial momentum of the proton in the nucleus, s is the nuclear spin, σ is the spin operator, J_μ is the nucleon current operator and Φ_{if} is the overlap integral between the initial and the final nuclear states. A detailed description of the nucleon current J_μ and its connection to the response function is discussed at the end of this section.

When summed over all spins Equation 19 becomes:

$$M_\mu = J_\mu(q, \mathbf{p}_m) \Phi_{if}(\mathbf{p}_m). \quad (20)$$

The overlap integral $\Phi_{if}(\mathbf{p}_m)$ can also be written as:

$$\Phi_{if}(\mathbf{p}_m) = \frac{1}{(2\pi)^{3/2}} \int \Phi_{if}(\mathbf{r}) \exp(-i\mathbf{p}_m \cdot \mathbf{r}) d\mathbf{r}. \quad (21)$$

In the independent particle shell model (IPSM) [24]:

$$\Phi_{if}(\mathbf{r}) = S_i(E_i)^{1/2} R_{nlj}(r) Y_{lm}(\Theta, \phi), \quad (22)$$

here $S_i(E_i)$ is the probability of finding a proton with binding energy E_i and quantum number i while R_{nlj} and Y_{lm} are the radial and angular part of the

wave function. This is valid only in IPSM. If one were to consider the final state interaction and the ground state correlations in the wave function of the target nucleus then the overlap integral would have a much more complicated form.

If one substitutes the expression for the matrix element Equation (19) into the cross-section expression Equation (18), then the cross-section factorizes as [19]:

$$\frac{d^6\sigma}{dE_{e'}d\Omega_{e'}dE_{p'}d\Omega_{p'}} = p'E_{p'}\sigma_{ep}S(E_s, \mathbf{p}_m) \quad (23)$$

where σ_{ep} is the off-shell electron-proton cross section, which is calculated in terms of the on-shell nucleon form factors with corrections for the binding of the nucleon. For σ_{ep} a prescription based on current conservation developed by de Forest [13] is most commonly used. $S(E_s, \mathbf{p}_m)$ is called the spectral function which is the probability of finding a proton, with momentum \mathbf{p}_m and separation energy E_s , inside the nucleus. It is given by:

$$S(E_s, \mathbf{p}_m) = \sum_f N_f |\Phi_{if}(\mathbf{p}_m)|^2 \delta(E_s - E_f - E_i). \quad (24)$$

N_f is the occupation number of the orbital f with $\sum_f N_f = Z$. The normalization of the spectral function $S(E_s, \mathbf{p}_m)$ is given in terms of the spectroscopic sum rule:

$$Z = \int S(E_s, \mathbf{p}_m) d^3\mathbf{p}_m dE_s. \quad (25)$$

2.3.1 The Nucleon Response Functions

We have seen from Equation (19) above that the nucleon response functions arise from the products of different components of the nuclear current. Here we take a closer look at each of these components. The matrix element of the nuclear current density between the initial and the final states is $J_{fi}^\mu = (\rho_{fi}, \mathbf{J}_{fi})$. Choosing the z

direction to be along \vec{q} we see that there are three independent components of the nuclear current [24, 20].

$$\begin{aligned} J_{fi}^z(\vec{q}) &= \frac{\omega}{|\vec{q}|} J_{fi}^0(\vec{q}), \\ J_{fi}^\pm(\vec{q}) &= \mp \frac{1}{\sqrt{2}} (J_{fi}^x(\vec{q}) \pm i J_{fi}^y(\vec{q})). \end{aligned} \quad (26)$$

Using this one can write down the four response function as [24, 20]:

$$\begin{aligned} W_L &= |J_{fi}^0(\vec{q})|^2 = |\rho_{fi}(\vec{q})|^2, \\ W_T &= |J_{fi}^{+1}(\vec{q})|^2 + |J_{fi}^{-1}(\vec{q})|^2 = \langle J_\parallel J_\parallel^\dagger + J_\perp J_\perp^\dagger \rangle, \\ W_{TT} &= 2Re J_{fi}^{+1}(\vec{q})^* J_{fi}^{-1}(\vec{q}) = \frac{-1}{\cos 2\phi} \langle J_\parallel J_\parallel^\dagger - J_\perp J_\perp^\dagger \rangle, \\ W_{LT} &= -2Re \rho_{fi}(\vec{q})^* (J_{fi}^{+1}(\vec{q}) - J_{fi}^{-1}(\vec{q})) = -\frac{1}{\cos \phi} \langle \rho J_\parallel^\dagger + J_\parallel \rho^\dagger \rangle. \end{aligned} \quad (27)$$

Here J_\parallel is nuclear current in the scattering plane, and J_\perp is the current orthogonal to the scattering plane. ϕ is the angle between the scattering plane and the plane containing the incident electron and the scattered proton. The longitudinal response function W_L is due to the charge only (longitudinal component of the current), while the transverse response function W_T is the incoherent sum of contributions from the components transverse to the direction of the virtual photon \vec{q} . The other two terms are interference terms. From these expressions one also notices the advantages of parallel kinematics (which was introduced in the previous section). In parallel kinematics the scattered proton is detected parallel to the direction of \vec{q} thus the two interference terms drop out since they are averaged over all out of plane angles ϕ and also because they are functions of $\sin \theta^c$ and $\sin^2 \theta^c$.

respectively with θ^c being the angle between the \vec{q} and the outgoing proton ($\theta^c = 0$ for parallel kinematics). This implies one can separate the longitudinal and the transverse response functions by keeping the momentum transfer constant while varying the scattering angle. This technique is known as the Rosenbluth separation. The interference response functions W_{TT} can be extracted by measuring the proton out of plane with respect to the scattering plane, while the W_{LT} response function can be extracted in plane by making measurements away from parallel kinematics.

2.4 Distorted Wave Impulse Approximation

In the previous section we made an assumption that there is no interaction between the knocked out proton and the residual nucleons, that is, no final state interactions (FSI). However, to calculate the coincidence cross-section accurately one has to relax this approximation. In this section we will examine one such model, the distorted wave impulse approximation (DWIA) where this assumption is discarded. We still retain the assumption that a single photon is exchanged in these reactions. The Feynman diagram for the process is shown in Figure 5.

In the previous section the matrix element of the nucleon current (Equation 19) was simplified by using a plane wave for the outgoing proton. In this section these matrix elements have to be evaluated in terms of the distorted wave function, $\xi_{p'}^*$, of the outgoing proton. So the equation for the matrix element now becomes:

$$M_\mu = \int d\mathbf{p}_i ds \xi_{p'}^*(q + p_i, s) J_\mu(q, \mathbf{p}_i, \sigma) \Phi_{if}(\mathbf{p}_i, s). \quad (28)$$

The distorted wave functions, $\xi_{p'}^*$ are usually single particle wave functions in an average optical potential and are calculated by doing a partial wave expansion

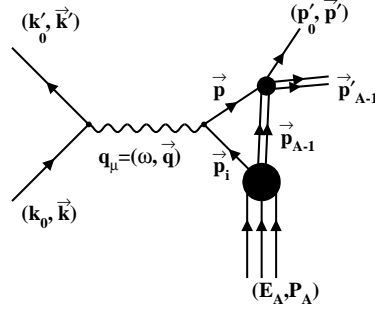


Figure 5: $(e, e'p)$ scattering diagram under distorted wave impulse approximation (Equation 29). The partial waves are computed by solving the radial Schroedinger equation (Equation 30):

$$\xi_{\mathbf{p}'}^*(\mathbf{r}) = \frac{4\pi}{p'} \sum_l i^l \frac{f_l^*(r)}{r} \sum_m Y_{lm}(\theta_e, \phi_e) Y_{lm}^*(\theta_{p'}, \phi_{p'}), \quad (29)$$

$$\frac{d^2 f_l^*(k'r)}{d(kr)^2} + \left(1 - \frac{l(l+1)}{(kr)^2} - \frac{U^*(r)}{E_k}\right) f_l^*(kr) = 0. \quad (30)$$

Here $E_k = (\hbar k)^2/2\mu$, where μ is the reduced mass $\frac{A-1}{A}M_{proton}$ and $U(r)$ is the optical potential which usually has a real and an imaginary part. The central potential of a typical optical potential is shown below,

$$U(r) = V_C(r) - |V| \frac{1}{1 + \exp(r - R)/a} - i|W| \frac{1}{1 + \exp(r - R')/a'} + i|W'| \frac{\exp(r - R')/a'}{(1 + \exp(r - R')/a')^2}. \quad (31)$$

where V_C is the standard Coulomb potential and the next two terms of the potential have the Wood-Saxon shape, while the last term is a differential of the Wood-Saxon shape. The different parameters of the optical potential are determined from proton-scattering data. A realistic optical potential must also have a spin-orbit term. Calculations which include the spin-orbit term (Equation 32) in the optical potential are called a generalized DWIA.

$$U_{so}(r) = [V_{so} \frac{\exp(r - R_s)/a_s}{r(1 + \exp(r - R_s)/a_s)^2} + iW_{so} \frac{\exp(r - R'_s)/a'_s}{r(1 + \exp(r - R'_s)/a'_s)^2}] \mathbf{l} \cdot \boldsymbol{\sigma}. \quad (32)$$

In the DWIA approach the $(e, e'p)$ cross-section can be factorized in terms of the e-p cross-section σ_{ep} and a distorted spectral function $S^D(E_m, \mathbf{p}_m, \mathbf{p}')$ as shown below,

$$\frac{d^6\sigma}{dE_{e'} d\Omega_{e'} dE_{p'} d\Omega_{p'}} = p' E_{p'} \sigma_{ep} S^D(E_m, \mathbf{p}_m, \mathbf{p}'), \quad (33)$$

where the distorted spectral function is given by

$$S^D(E, \mathbf{p}_m, \mathbf{p}') = \frac{1}{2j+1} |\phi^D(\mathbf{p}_m, \mathbf{p}')|^2 \delta(E - \epsilon_b + \epsilon_a), \quad (34)$$

where ϵ_b and ϵ_a are the energy eigenvalues of the residual and initial nucleus and $\phi^D(\mathbf{p}_m, \mathbf{p}')$ is the overlap function given by:

$$\phi^D(\mathbf{p}_m, \mathbf{p}') = \int d\mathbf{p}_i \xi_p^*(\mathbf{q} + \mathbf{p}_i) \Phi_{if}(\mathbf{p}_i). \quad (35)$$

These are calculated by doing a Fourier expansion in r-space which gives

$$\phi^D(\mathbf{p}_m, \mathbf{p}') = \frac{1}{2\pi^3} \int \xi_p^*(\mathbf{r}) \exp(i \frac{A-1}{A} \mathbf{q} \cdot \mathbf{r}) \Phi_{if}(\mathbf{r}) d\mathbf{r}. \quad (36)$$

where the wave function, $\xi_p^*(\mathbf{r})$ are calculated using an optical potential as described earlier.

In the generalized DWIA calculations however, factorization is not possible and one has to calculate the one-photon exchange amplitude of the process, using the distorted wave function for the outgoing protons. The difference between these two approaches are shown in the Figure 6. Various improvements which can be included in the generalized calculation are examined below.

Some of the important improvements involve including effects due to the energy dependence of the optical potentials. The energy dependence in general arises partly because the effective interaction is non-local and partly because of an intrinsic energy dependence. The intrinsic energy dependence is included by varying the parameters of the potential with proton energy, using proton-scattering data to constrain the variations. The non-locality of the optical potential is included by using an ansatz, first suggested by Perey [25], called the Perey factor :

$$\begin{aligned}\Psi_{\text{non-local}} &= C_{\text{Perey}} \Psi_{\text{local}}, \\ C_{\text{Perey}} &= [1 - \frac{m_p \beta^2}{2\hbar^2} V(r)]^{-1/2}.\end{aligned}\tag{37}$$

Here β is the range of the non-locality and is usually taken to be 0.85 fm. This ansatz is based on an assumption that well inside the nuclear surface the non-local potential function is constant. In addition it is based on the empirically observed fact that the predictions of a given non-local model can be fitted almost perfectly with a purely local calculation. This implies that the wave functions produced by local and non-local calculations are closely similar. The ansatz follows from a comparison of the non-local wave equation with the local wave equation under the afore mentioned assumptions. Alternatively it can be seen to arise from the

dispersion relation of the nucleons :

$$E(k, \mathbf{r}) = \frac{\hbar^2}{2m} k^2 + V(k, \mathbf{r}) \quad (38)$$

here k is the momentum of the nucleon. Although this is used as a general relationship, it has been shown [26] that the Perey factor can be different depending on the source of the non-locality.

The calculations can also be further improved by including distortions of the electron waves (Coulomb distortions). This can be done by expanding the electron wave, which satisfy Dirac equation, in inverse powers of the electron energy, retaining terms up to order $Z\alpha$, an alternative approach to treating Coulomb distortions is discussed in Section 2.5.2. These distorted electron waves are then used to evaluate the nucleon-current matrix elements in r space. It has been shown by Giusti and Pacati [24] that for heavier nuclei one needs to include the second order term in $Z\alpha$. Figure 6 compares momentum distributions for $^{12}\text{C}(e, e'p)$ based on DWIA and with different corrections added on.

2.5 Additional Corrections to The DWIA

2.5.1 Nuclear Density Dependent Coupling

One of the improvements involves including the nuclear density dependence of the electron-proton coupling. This effect is more important for heavier nuclei. If the coupling term is density dependent then we can no longer factorize the cross-section into the coupling term (σ_{ep}) times the spectral function, as shown in Equation 33. In the density independent case the spectral function involves the square of the radial integral over the initial and the final wave functions Equation 36. However, in the density dependent case since the form factors (coupling constants) are density

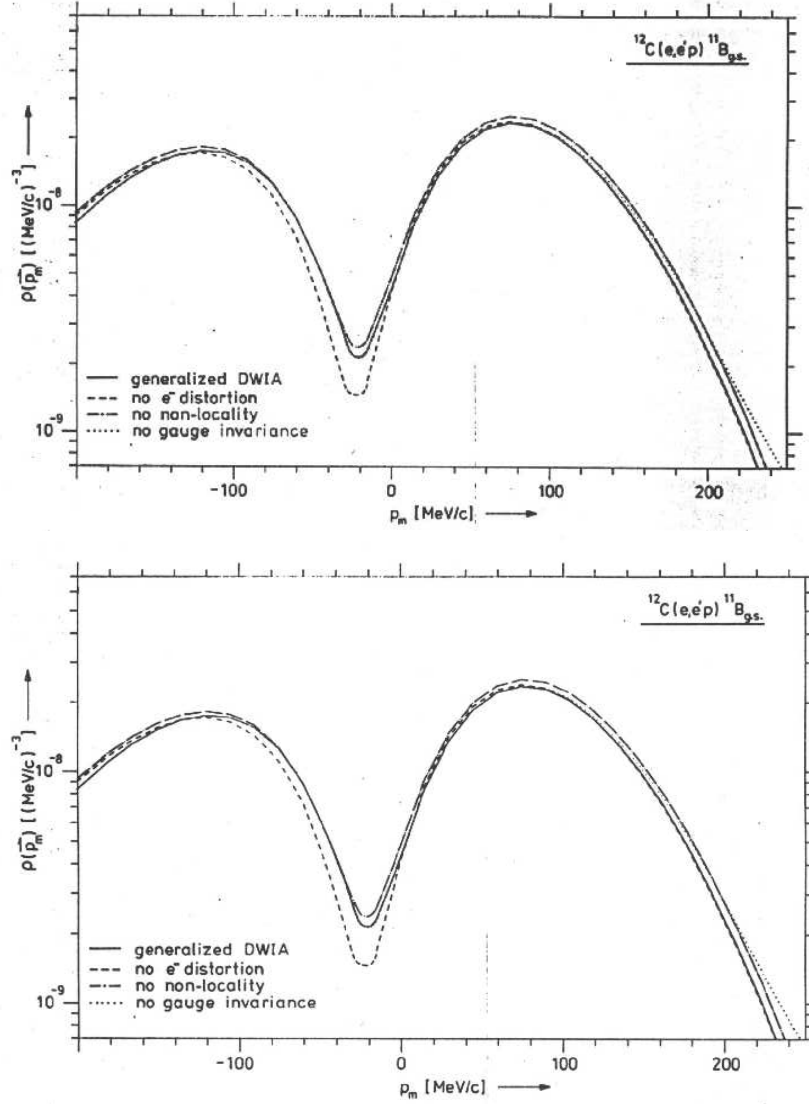


Figure 6: Calculated momentum distribution for 1p knockout from $^{12}\text{C}(e, e'p)$ at $T_p = 70$ MeV in parallel kinematics.

The top panel shows the momentum distribution under PWIA (solid), the conventional DWIA calculation (dashed) and the generalized DWIA calculation (dot dash). The Lower panel shows the generalized DWIA calculation (solid) and the momentum distributions correspond to DWIA calculations without e^- distortions (dashed), without non-locality corrections (dot dash) and without gauge-invariance (dotted).

dependent, they must be included in the radial integral. Thus we have to redefine the radial integral Equation (36) by a pair of density ($\rho(r)$) dependent radial integrals $\phi_L(E_m, \mathbf{p}_m, \mathbf{p}', \rho)$ and $\phi_T(E_m, \mathbf{p}_m, \mathbf{p}', \rho)$, corresponding to the longitudinal and the transverse form factors [24]

$$\phi_i(E_m, \mathbf{p}_m, \mathbf{p}', \rho) = \frac{1}{2\pi^3} \int \xi_p^*(\mathbf{r}) \exp(i \frac{A-1}{A} \mathbf{q} \cdot \mathbf{r}) \psi_\alpha(\mathbf{r}) F_i(Q^2, \rho(r)) d\mathbf{r}. \quad (39)$$

Where $\xi_p^*(\mathbf{r})$ is the outgoing proton wave function, $\psi_\alpha(\mathbf{r})$ is the proton bound state wave function and $F_i(Q^2, \rho(r))$ is the density dependent form factor. Using these integrals we get the density dependent spectral function as:

$$S^{dd}(E_m, \mathbf{p}_m, \mathbf{p}', \rho) = \frac{\epsilon \phi_L^2(E_m, \mathbf{p}_m, \mathbf{p}', \rho) + \phi_T^2(E_m, \mathbf{p}_m, \mathbf{p}', \rho)}{\epsilon F_L^2(Q^2, \rho = 0) + F_T^2(Q^2, \rho = 0)} \quad (40)$$

Where $F_L(Q^2, \rho = 0) = G_E(Q^2)$ and $F_T(Q^2, \rho = 0) = (\frac{Q^2}{4m^2})^{1/2} G_E(Q^2)$ are the free nucleon form factors. This formalism is valid only for parallel kinematics since the interference terms are neglected. There are various approximations to the density dependence of the form factors which can be used to look at the effect of density dependent coupling utilizing the spectral function Equation (40). One such approximation is the local density approximation where m is replaced by an effective mass m^* which is defined as $m^* = m + S[\rho(r)/\rho(r = 0)]$, where S is a scalar potential.

2.5.2 Coulomb Corrections

The calculations are further improved by considering distortions of the electron waves. These distortions are primarily Coulomb distortions of the electron waves and are due to the fact that the incoming and outgoing electron interacts with the long range Coulomb field of the target nucleus. The effect of the Coulomb potential is to increase the momentum transfer q and also to cause an increase

in the electron flux in the vicinity of the target nucleus. These effects can be accounted for by appropriately changing the electron wave used to calculate the coincidence cross-section of the $(e, e'p)$ reaction. This approach is also equivalent to summing the contributions from Feynman diagrams in which the electron and the nucleus exchange one, two, ... photons while the nucleus still remains in its initial state. It can be shown that this kind of distortion of the electron wave can be approximated by attaching a phase factor to the plane wave expansion [27], which scales with the nuclear dimension and the strength of the Coulomb field. In addition the effective momentum of the electron is changed to $\bar{\mathbf{k}} = \mathbf{k} - \Delta k$, where Δk is the average electro static field around the electron, given by,

$$\Delta k = \frac{\int V_c(\mathbf{r})\psi^2(\mathbf{r})d\mathbf{r}}{\int \psi^2(\mathbf{r})d\mathbf{r}} = f \frac{Z\alpha}{R_c} \quad (41)$$

here the R_C is the Coulomb radius and the factor f varies between 1.1 and 1.5 depending on the size of the nucleus. Such calculations have been done by Knoll et al. [27], and they provide an useful formula to estimate the effect of the Coulomb distortion on the quasi-elastic cross-section:

$$\frac{\Delta\sigma}{\sigma_{max}}(\%) \approx 0.3 \frac{q}{k'_o} Z \quad (42)$$

Where σ_{max} is the cross-section at the maximum of the distribution and k'_o is the momentum of the incident electron. This equation suggests that the Coulomb corrections becomes smaller with increasing energy of the incident electron.

2.5.3 Meson Exchange Currents and Isobar Currents

Up to this point we have looked at the nucleus in terms of the A nucleons and the binding forces have been considered through an effective potential and nucleon wave functions. However, if this binding is considered in-terms of virtual mesons

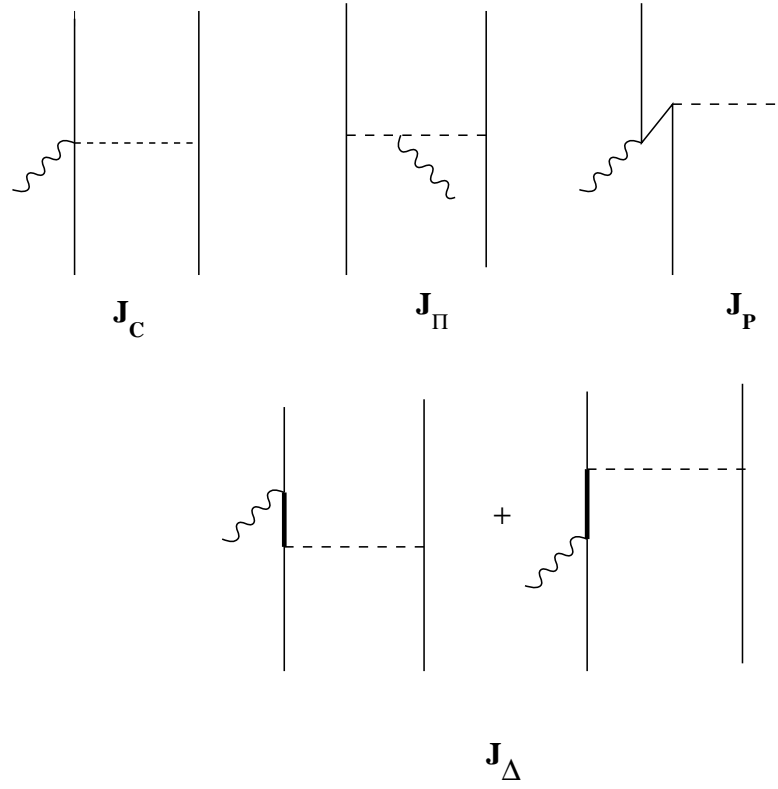


Figure 7: Feynman diagram for MEC and IC contributions to the two-body current. J_C is the contact, J_π the pion in flight, J_P the pair contribution to MEC and J_Δ is the isobar current term.

then in the effective potential picture we are neglecting the direct interactions of the virtual photon with the virtual mesons. In addition the interaction of the virtual photon with the nucleon pairs which modify the nucleon wave function are also neglected. We have also overlooked possible coupling of the virtual photon with the virtual excitation of the nucleon resonances like the Delta(Δ) resonance. The first two kinds of interaction are computed by evaluating Feynman graphs shown in Figure 7 as the contact, pair and pion exchange diagrams. The later is calculated by evaluating the diagrams in Figure 7 showing the coupling of the photon to the delta resonance. These diagrams are usually evaluated by using a phenomenological effective Lagrangian. It is found that in the nonrelativistic limit these two-body currents just have transverse components, thus only the transverse component of the current operator are affected by these two-body currents. Most recently two groups Boffi *et al.* [28] and Ryckebusch *et al.* [29], have calculated the contributions of MEC and IC to the coincidence $(e, e'p)$ cross-section. This has been reviewed extensively in Reference [20]. Although the two groups predict very different effects both calculations agree that two-body currents play very important role in single-nucleon knockout. The differences between the two groups can only be resolved through systematic experimentation. Since MEC contributions are primarily transverse in nature, experiments measuring the transverse and the interference response functions in $(e, e'p)$ scattering are the best candidates to investigate the role of MEC.

2.5.4 Relativistic Distorted Wave Models

Relativistic DWIA models use the Dirac equation instead of the Schroedinger equation to calculate the electron and nucleon wave function. Such treatment implies an exact calculation of the Coulomb distortion of the electron wave and

of the final proton wave. In addition Dirac Phenomenology is used to arrive at the effective optical potential from the proton scattering data. These effective potentials usually still use the Wood-Saxon (some authors also use other forms like the wine bottle shape, etc.) as in conventional optical potentials, however, the strength of the potential is usually higher by a factor of 3 - 4. Although a relativistic approach would seem preferable because the spin and the spin-orbit term occurs more naturally, it should be remembered that the Dirac equation applies to point particles only. It would be of considerable interest to compare $(e, e'p)$ data at high proton energies with relativistic and non-relativistic DWIA calculations.

2.6 Glauber and Other High-Energy Approximations

Final state interactions and other deviations of realistic nuclear systems from the PWIA can also be evaluated in terms of some high energy approximations reviewed in this section.

2.6.1 Glauber Approximation

The high energy approximation (also called Glauber approximation) to scattering theory was developed by R. J. Glauber [30], and involves two basic assumptions:

- 1. The incident energy is much larger than the magnitude of the interaction potential and
- 2. The particle wavelength is much smaller than the potential width 'a', and the linear term in the potential dominates.

$$\frac{V}{E} \ll 1, \quad ka \gg 1. \quad (43)$$

Here V is the magnitude of the potential while E and k are the energy and momentum of the incident particle, respectively. Under these conditions we can assume that back-scattering will be very weak and the wave function of the particle can be separated as [30]:

$$\psi(\vec{r}) = e^{i\vec{k} \cdot \vec{r}} \phi(\vec{r}) \quad (44)$$

Substituting this wave function in a Schroedinger equation gives us an integral equation of the form:

$$\psi_k(\vec{r}) = e^{i\vec{k} \cdot \vec{r}} - \frac{2m}{4\pi\hbar^2} \int \frac{e^{ik|\mathbf{r}-\mathbf{r}'|}}{|\mathbf{r}-\mathbf{r}'|} V(\mathbf{r}') \psi_k(\mathbf{r}') d\vec{r}'. \quad (45)$$

An important point to note is that this wave function does not have a spherically outgoing wave this is because it is necessary to know the wave function only within the volume of the potential in order to find the scattering amplitude; therefore it need not represent the wave function elsewhere. Another important consequence of this approximation is that this formalism describes small angle scattering only, limits of which are given in terms of $\theta^2 \ll \frac{1}{ka}$.

From this one obtains the function $\phi(\vec{r})$ as:

$$\phi(\vec{r}) = 1 - \frac{2m}{4\pi\hbar^2} \int \frac{e^{ik|\vec{r}-\vec{r}''|} - i\vec{k} \cdot \vec{r}''}{|\vec{r}''|} V(\vec{r} - \vec{r}'') \phi(\vec{r} - \vec{r}'') d\vec{r}'', \quad (46)$$

where $\vec{r}'' = \vec{r} - \vec{r}'$. Now we have to use the small angle approximation to neglect terms of the order $1/ka$. Another approximation is that the product $V\phi$ varies very slowly within a particle wavelength, ensuring that the largest contributions to the integral (Equation 46) comes from points \vec{r}'' which lie close to the direction of \vec{k} .

This is one of the most important and reoccurring approximation in this formalism.

Carrying out the angular integration using these approximations gives,

$$\phi(\vec{r}) = 1 - \frac{i}{\hbar v} \int_0^\infty V(r - r'') \phi(r - r'')|_{r'' \parallel \vec{k}} dr'', \quad (47)$$

which is approximately,

$$\phi(\vec{r}) = e^{-\frac{i}{\hbar v} \int_0^r V(r'') dr''}. \quad (48)$$

This implies the wave function can be written as

$$\psi(\vec{r}) = e^{i\vec{k} \cdot \vec{r} - \frac{i}{\hbar v} \int_0^r V(r'') dr''}. \quad (49)$$

Now one is interested in evaluating the scattering amplitude and it is useful to redefine the problem in terms of some alternative coordinate vectors. We take \hat{k} as the unit vector in the direction of \vec{k} and define $\vec{r} = \vec{b} + \hat{k}z$, where \vec{b} is perpendicular to the incident propagation direction \vec{k} , hence $|\vec{b}|$ can be thought of as the impact parameter. Using this notation the wave function can be rewritten as :

$$\psi(\vec{r}) = e^{i\vec{k} \cdot \vec{r} - \frac{i}{\hbar v} \int_0^z V(\vec{b} - \hat{k}z') dz'} \quad (50)$$

Substituting this wave function into the standard expression for scattering amplitude we get,

$$f(\vec{k}', \vec{k}) = -\frac{2m}{4\pi\hbar^2} \int e^{-i\vec{k}' \cdot \vec{r}} V(\vec{r}) e^{i\vec{k} \cdot \vec{r} - \frac{i}{\hbar v} \int_0^z V(\vec{b} - \hat{k}z') dz'} dz d^2b. \quad (51)$$

Once again we use the small angle approximation such that $\exp[i(\vec{k} - \vec{k}') \cdot \hat{k}z] \sim 1 + \theta^2 ka \approx 1$. This simplifies the integration over z to a exact differential, carrying out the integration over gives,

$$f(\vec{k}', \vec{k}) = \frac{k}{2\pi i} \int e^{i(\vec{k} - \vec{k}') \cdot \vec{b}} [e^{-\frac{i}{\hbar v} \int_0^z V(\vec{b} - \hat{k}z') dz'} - 1] d^2b. \quad (52)$$

From this one gets the expression for total scattering cross-section as

$$\sigma_{tot} = \frac{4\pi}{k} \text{Im} f(\vec{k}, \vec{k}') = 2 \int (1 - \text{Re}(e^{i\xi(\vec{b})})) d^{(2)}b, \quad (53)$$

where

$$\xi(\vec{b}) = -\frac{1}{\hbar v} \int_{-\infty}^{\infty} V(\vec{b} + \hat{k}z) dz. \quad (54)$$

2.6.2 High Energy Approximation for Final State Interactions

An alternative formalism for a realistic many body calculation which includes the final state interactions (FSI) between the knocked out nucleon and the recoiling spectator system, is shown here. [31]

The nuclear matrix element, for $(e, e'p)$ process in which the recoiling system is left in a bound state is,

$$M_{\alpha}(\mathbf{p}, \mathbf{q}) = \langle \Psi_{\alpha p}^{(-)} | \sum_k a_{k+q}^{\dagger} a_k | \Psi_0 \rangle. \quad (55)$$

where $a_{k+q}^{\dagger}(a_k)$ is the creation (annihilation) operator and the $|\Psi_0\rangle$ is the target ground state. To isolate the effects of FSI the nuclear Hamiltonian is split up as :

$$H_A = \sum_{i=1}^A t_i + \sum_{j>i=1}^A v_{ij} = H_0 + H_1, \quad (56)$$

where t_i is the kinetic energy of the i -th nucleon and v_{ij} is the interaction potential between i -th and j -th nucleon. The final scattering state $|\Psi_{\alpha p}^{(-)}\rangle$ is decomposed as:

$$|\Psi_{\alpha p}^{(-)}\rangle = \Omega_p^{(-)} |\Phi_{\alpha p}^{(-)}\rangle, \quad (57)$$

where $|\Phi_{\alpha p}^{(-)}\rangle$ denotes the eigenstate of H_0 with no interaction between the particles and the spectator, while the operator $\Omega_p^{(-)}$ describes the distortion to the wave function by the rescattering of the knocked out nucleon. It is written as:

$$\Omega_p^{(-)} = \lim_{t \rightarrow \infty} T e^{-i \int_0^t dt' \hat{H}_1(t')}, \quad (58)$$

where T is the time ordering operator.

The so called high-energy approximation is used in evaluating $\Omega_p^{(-)}$. The basic assumption is that the kinetic energy of the knocked out nucleon is much larger than that of the spectator system, so after rescattering of the knocked out nucleon off the spectator, we get $\mathbf{p}_f = \mathbf{p}_i + \Delta$, with $\Delta \ll p_i$, which means the kinetic energy can be written as $\frac{p_f^2}{2m} \approx \frac{p_i^2}{2m} + \frac{\mathbf{p}_i \cdot \Delta}{m}$. This implies that after the rescattering process, the struck nucleon moves undeflected along a straight trajectory parallel to its original direction. When extended to the case of many spectators it also means the spectators can be regarded as a collection of fixed scattering centers. These two approximations are called the eikonal and the frozen approximations. These approximations imply that the distortion operator $\Omega_p^{(-)}$ can be written as :

$$\Omega_p^{(-)} = e^{-\sum_{j=2}^A \int_0^\infty dt' W_p(|\mathbf{r}_1 + \mathbf{v}t' - \mathbf{r}_j|)}, \quad (59)$$

where \mathbf{v} is the velocity of the struck nucleon and W_p is the complex effective two body interaction. Now putting together all these components one can evaluate the nuclear matrix element and arrive at observables like the scattering cross-section. [31]

2.6.3 Correlated Glauber Approximation

We have seen in the section 2.6.1 that the wave function of the struck proton with momentum \vec{k} can be written as:

$$\psi(\mathbf{r}) = e^{i\vec{k} \cdot \vec{r}} \exp\left[-\frac{1}{2} \int_{z'}^z dz'' W(k, \rho(r''))\right]. \quad (60)$$

The imaginary part of the optical potential $W(k, \rho)$ is related to the partial lifetimes of the proton due to n-p and p-p collisions by,

$$W(k, \rho) = \frac{m^*(k, \rho)}{m} \frac{\hbar}{2\tau(k)}, \quad (61)$$

where $\frac{1}{\tau(k)} = \frac{1}{\tau_n(k)} + \frac{1}{\tau_p(k)}$, and τ_a are the partial lifetimes due to p-a collisions. Here m^* is the effective mass which is related to the dispersion relation of nucleons in the nuclear matter. The dispersion relation is:

$$E(k, \rho) = \frac{\hbar^2}{2m} k^2 + U(k, \rho), \quad (62)$$

and the effective mass is defined as :

$$\frac{\hbar k}{m^*(k, \rho)} = \frac{1}{\hbar} \frac{dE(k, \rho)}{dk}. \quad (63)$$

The effective cross-section for scattering off a proton with momentum k by neutrons or protons in nuclear matter of density ρ is defined as:

$$\begin{aligned} \sigma_{pp}^* &= \frac{m^*(k, \rho)}{\hbar k \rho_p \tau_p(k)}, \\ \sigma_{np}^* &= \frac{m^*(k, \rho)}{\hbar k \rho_n \tau_n(k)}, \end{aligned} \quad (64)$$

This implies that the imaginary part of the optical potential $W(k, \rho)$ can be written as:

$$W(k, \rho) = \frac{\hbar^2}{2} \frac{k}{m} [\rho_p \sigma_{pp}^* + \rho_n \sigma_{np}^*]. \quad (65)$$

The effective cross-sections σ^* is the medium corrected (including Pauli-blocking) cross-sections. Now we can put this back into the the wave function of the struck proton to get:

$$\psi(\mathbf{r}) = e^{i\vec{k}\cdot\vec{r}} \exp[-1/2 \int_{z'}^z dz'' (\rho_p(\mathbf{r}'')\sigma_{pp}^*(k, \rho) + \rho_n(\mathbf{r}'')\sigma_{np}^*(k, \rho))]. \quad (66)$$

However, the absorption of the struck proton is due to the A-1 remaining nucleons, so it is wrong to use just the density $\rho(\mathbf{r}'')$; instead one must also include the distribution of other nucleons. These distributions are given by pair distribution functions $g_{pa}(\mathbf{r}', \mathbf{r}'')$ defined as

$$g_{pa}(\mathbf{r}', \mathbf{r}'') = \frac{\rho_{pa}(\mathbf{r}', \mathbf{r}'')}{\rho_p(\mathbf{r}')\rho_a(\mathbf{r}'')}. \quad (67)$$

Here $\rho_{pa}(\mathbf{r}', \mathbf{r}'')$ is the two-body density which gives the joint probability of finding a proton at \mathbf{r}' and another nucleon at \mathbf{r}'' . The pair distribution function is usually < 1 at small distances, because $\rho_p(\mathbf{r}')\rho_a(\mathbf{r}'') - \rho_{pa}(\mathbf{r}', \mathbf{r}'')$ (also called the correlation hole) is positive.

Now the wave function of the struck proton becomes:

$$\begin{aligned} \psi(\mathbf{r}) = e^{i\vec{k}\cdot\vec{r}} \exp[-1/2 \int_{z'}^z dz'' (&g_{pp}(\mathbf{r}', \mathbf{r}'')\rho_p(\mathbf{r}'')\sigma_{pp}^*(k, \rho) \\ &+ g_{np}(\mathbf{r}', \mathbf{r}'')\rho_n(\mathbf{r}'')\sigma_{np}^*(k, \rho))]. \end{aligned} \quad (68)$$

This modification of the standard Glauber approximation is known as the correlated Glauber approximation.

2.7 Interpretation of Existing $(e, e'p)$ Data

The reaction mechanism of quasi-elastic $(e, e'p)$ scattering had been explored by several experiments performed at Saclay, MIT-Bates, NIKHEF-K, Mainz and other

laboratories around the world, on a host of nuclear targets. A brief survey of some key experiments and their interpretation is provided in this section.

2.7.1 Spectral Functions from $(e, e'p)$ Data

In Section 2.3 it was mentioned that under the PWIA one can factorize the $(e, e'p)$ cross-section as a product of an elementary cross-section σ_{ep} and a probability $S(E_s, \mathbf{p}_m)$:

$$\frac{d^6\sigma}{dE_{e'}d\Omega_{e'}dE_{p'}d\Omega_{p'}} = p' E_{p'} \sigma_{ep} S(E_s, \mathbf{p}_m). \quad (69)$$

Here the spectral function $S(E_s, \mathbf{p}_m)$ is the probability that the knocked out proton will have a missing momentum \mathbf{p}_m and have a separation energy of E_s .

Over the last two decades numerous $(e, e'p)$ experiments have been performed at electron accelerators around the world. Data have been collected on various complex nuclei ranging from ^2H to ^{208}Pb . Spectral functions were extracted from many of these data. Some of the experimental measurements of the spectral function and their comparison with various theoretical calculations is examined in this sub-section. The spectral functions from $^{12}\text{C}(e, e'p)^{11}\text{B}$ experiments will be used to get an overview of experimental spectral functions. The next subsection will discuss other important properties like occupation probability, mean and peak energies, which can be extracted from these spectral functions.

The recoil momentum distributions from the first generation of experiments at Saclay [7], Tokyo [32] and Frascati [5] are shown in Figure (8). The characteristic shape of the $1p$ and $1s$ momentum distributions is seen in these distributions. They have been compared with DWIA calculations in the same figure, showing that the experimental spectral functions can be described reasonably well by DWIA spectral functions.

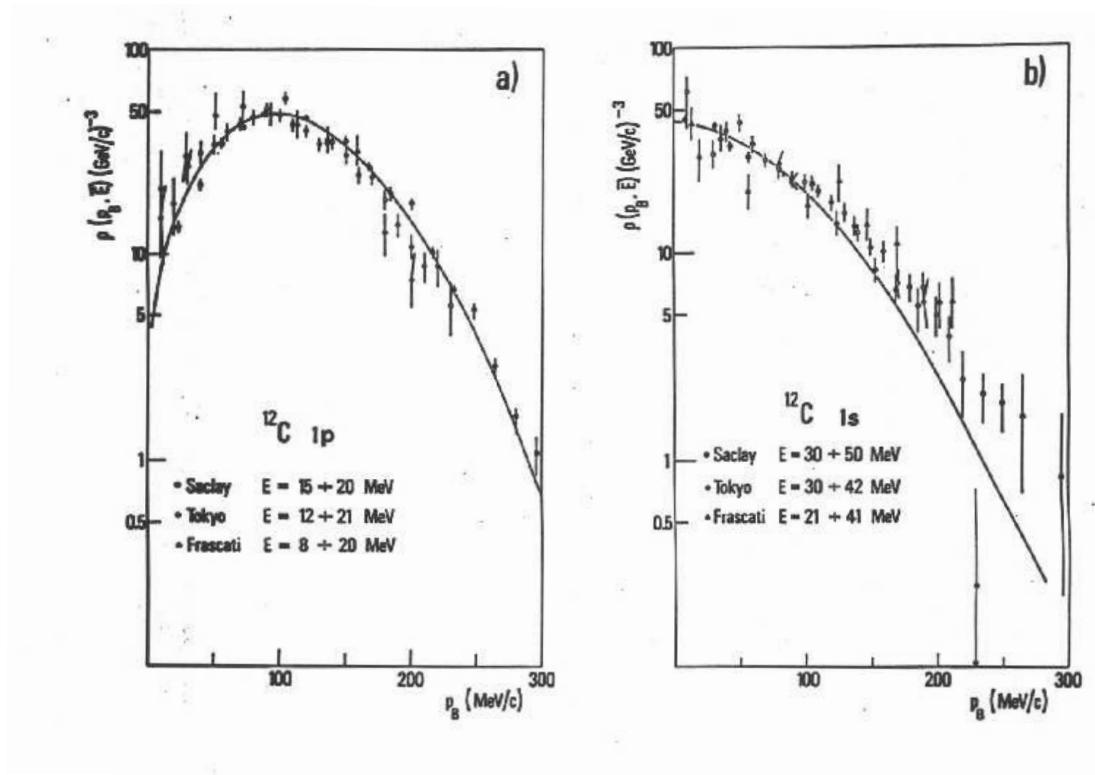


Figure 8: The recoil momentum distribution for $^{12}\text{C}(e, e'p)$ measured at Saclay, Tokyo and Frascati

However, these comparisons between data and DWIA calculations are sensitive to various parameters of the optical potential used in the calculations. The influence of variation in these parameters were studied by Royer *et al.* [33]. They found a strong influence of the RMS radius on the momentum distribution and also found that the imaginary part of the optical potential effects the higher momentum components of the distribution. Since one uses the factorization assumption of DWIA (introduced in Section. 2.4) one can test this assumption by comparing with data at different angles Θ_p (the angle between recoil momentum direction and the scattered proton direction).

Other checks of the adequacy of DWIA calculations involve comparing with data at parallel and perpendicular kinematics (Section. 2.3). In perpendicular kinematics the spectral function was expected mainly to be symmetric around the momentum transfer q direction, while in parallel kinematics a slight asymmetry is expected due to the fact that value of q is different for recoil momentum parallel or anti-parallel to the scattered proton direction for fixed proton momentum. Results from a measurement done at Saclay in parallel and perpendicular kinematics is shown in Figure 9 [18].

The asymmetry in the parallel kinematics can be explained by DWIA however the asymmetry in perpendicular kinematics is unexplained. It can be accounted for by introducing a symmetry breaking spin-orbit term in the optical potential (eg. in a GDWIA calculation), which also destroys the factorization assumption. Thus more complete and systematic experimental and theoretical studies are needed to establish the magnitude and the causes of this asymmetry.

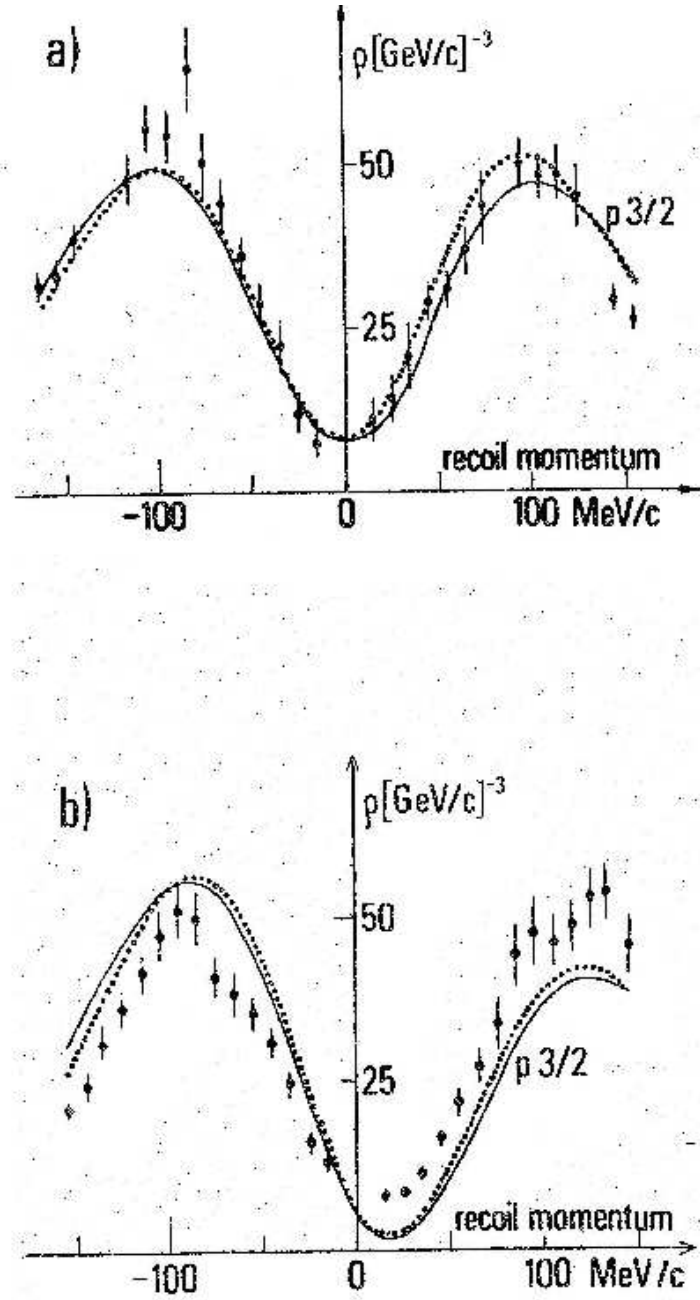


Figure 9: The recoil momentum distribution for $^{12}\text{C}(e, e'p)$ measured in parallel (top) and perpendicular (bottom) kinematics

2.7.2 Excitation Energies and Occupation Probabilities

The proton occupation number for a given orbital α is obtained by integrating the energy distribution $\omega_\alpha(E)$, so $N_\alpha = \int \omega_\alpha(E) dE$. This is same as zeroth-order moment of the spectral function,

$$\rho^{(0)} = \langle \psi_\alpha | a_\alpha^\dagger a_\alpha | \psi_\alpha \rangle. \quad (70)$$

The occupation number N_α is also related to the spectroscopic factors S_{α, f_α} , where f_α is the subset of states of the orbital α which contribute to the sum. $N_\alpha = \sum_{f_\alpha} S_{\alpha, f_\alpha}$.

Similarly, the mean removal energy is the energy weighted integral of the energy distribution $P_\alpha(E)$,

$$E_\alpha^{mean} = \frac{1}{N_\alpha} \int E P_\alpha(E) dE. \quad (71)$$

This is also the first-order moment of the spectral function,

$$\rho_\alpha^{(1)} = \frac{1}{\rho_\alpha^{(0)}} \langle \psi_\alpha | a_\alpha^\dagger [a_\alpha, H] | \psi_\alpha \rangle, \quad (72)$$

and is also the energy weighted sum over the spectroscopic factors S_{α, f_α} ,

$$E_\alpha^{mean} = \frac{1}{N_\alpha} \sum_{f_\alpha} S_{\alpha, f_\alpha} (\epsilon^{f_\alpha} - \epsilon^0). \quad (73)$$

Another quantity which can be measured experimentally is the peak energy E_α^p of the distribution.

The experimentally measured occupation number and mean removal energies are listed in Table 1. The occupation number is found to be typically 20-30% less than shell-model predictions, but the relative occupation numbers agree very well with shell-model predictions. The absolute value of occupation numbers are

Table 1: Occupation Numbers N_α and Separation Energies E_α from DWIA analysis of $(e, e'p)$ experiments.

Nucleus	State	N_α^{IPSM}	N_α Tokyo	N_α Saclay	E_α Tokyo	E_α Saclay
${}^6\text{Li}$	1s	2	1.46 ± 0.04		22.6 ± 0.2	
	1p	1	0.72 ± 0.03		4.5 ± 0.2	
${}^7\text{Li}$	1s	2	1.88 ± 0.04		26.0 ± 0.2	
	1p	1	0.79 ± 0.03		10.1 ± 0.2	
${}^9\text{Be}$	1s	2	0.74 ± 0.04	1.4	27.1 ± 0.4	32 ± 1
	1p	2	1.40 ± 0.05	1.4	18.1 ± 0.2	18.0 ± 0.3
${}^{12}\text{C}$	1s	2	1.34	1.0	36.9 ± 0.3	38.1 ± 1.0
	1p	4	2.6	2.5	15.5 ± 0.1	17.5 ± 0.4
${}^{16}\text{O}$	1s	2		1.6		44 ± 2
	1p	6		3.6		17.7 ± 0.8
${}^{27}\text{Al}$	1s	2	-		57 ± 3	
	1p	6	2.4 ± 0.2		32 ± 3	
	1d	5	1.6 ± 0.1		14.0 ± 0.6	
	2s	-	0.12 ± 0.01		14.3 ± 0.2	
${}^{28}\text{Si}$	1s	2		0.9		51
	1p	6		2.9		32
	1d	6		3.6		16.1 ± 0.6
	2s	-		0.4		13.8 ± 0.5
${}^{40}\text{Ca}$	1s	2	3.7 ± 0.2	1.5	58.7 ± 1.2	56
	1p	6	10.2 ± 0.9	5.7	35.3 ± 0.5	41
	1d	10	4.7 ± 1.6	7.7	18.4 ± 1.6	14.9 ± 0.8
	2s	2	2.0 ± 0.2	1.3	13.6 ± 0.4	11.2 ± 0.3
${}^{52}\text{V}$	1s	2	-		60 ± 3	
	1p	6	1.1 ± 0.1		40 ± 1	
	1d	10	1.7 ± 0.3		19.5 ± 0.5	
	2s	2	0.3 ± 0.1		15.1 ± 0.2	
	1f	3	0.4 ± 0.1		10.3 ± 1.1	
${}^{58}\text{Ni}$	1s	2		1.0		62
	1p	6		6.8		45
	1d	10		8.9		21
	2s	2		1.9		14.7 ± 0.5
	1f	8		7.5		9.3 ± 0.3

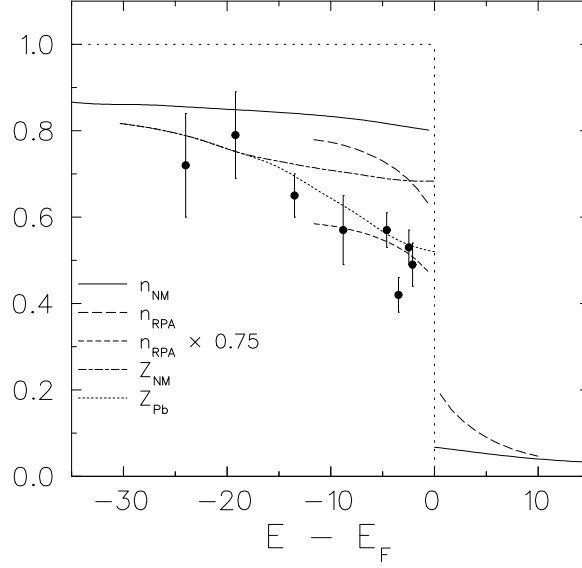


Figure 10: The occupation number for ^{208}Pb from $(e, e'p)$ data is shown along with various theoretical calculation. The solid curve represents the nuclear matter occupation probability [34], the long dashes include an RPA correction [35], the medium dashes is $n \approx 0.75(n_{nm} + \delta n_{RPA})$ fitted to the data [20], the dot dash is the quasi-particle strengths for nuclear matter and the short dash is the quasi-particle strengths for lead.

very difficult to determine, because of the uncertainties in the various approximations used (such as the truncation of high energy strength etc.), so the occupation number is usually determined to about $\approx 20\%$. Within these uncertainties the occupation number agrees with various theoretical calculations as shown in Figure 10. In this figure (Figure 10), the occupation numbers for ^{208}Pb were determined by Quint *et al.* [36] from $(e, e'p)$ data. They integrated the experimental spectral function for excitation energies up to 25 MeV, and for deeply bound orbitals the spectral function was extrapolated beyond the measured range using a Gaussian parameterization. However more recent analysis of the same data give different results, making it fair to say that the occupation number is known to about \approx

20 %. These results are compared with theoretical calculations of Pandharipande *et al.* [35] and Benhar *et al.* [37]. Pandharipande *et al.* calculate the occupation probabilities of nuclear matter using correlated basis function (CBF) [34] and the Urbana v_{14} + TNI interaction [38]. However, ^{208}Pb being a finite nucleus, there is additional depletion of states near the Fermi surface due to long range correlations and collective mode interactions at the surface of the nuclei. These effects are accounted for by using the RPA theory of Gogny [39]. Benhar *et al.* on the other hand argue that integrating the $(e, e'p)$ data with respect to missing energy does not include a significant part of the background contributions of the spectral function, which is spread thinly over a wide range of energy. Hence they should be compared to quasi-particle strength rather than occupation probability. Their calculation of the quasi-particle strength using the CBF theory for the nuclear matter is also shown in Figure 10. They account for the finite nuclei by modifying the imaginary part of the CBF mean field to reproduce the experimental spreading of widths.

2.7.3 The Koltun Sum Rule

A general property of the spectral function, known as the energy weighted sum rule or the Koltun sum rule [40], relates the total binding energy per nucleon to the average removal and kinetic energy. The average kinetic energy $\langle T \rangle$ and $\langle E \rangle$ is the average removal energy is given by:

$$\begin{aligned}\langle T \rangle &= \frac{1}{A} \int \frac{\mathbf{p}^2}{2M} S(E, \mathbf{p}) dE d^3\mathbf{p} \\ \langle E \rangle &= \frac{1}{A} \int E S(E, \mathbf{p}) dE d^3\mathbf{p}\end{aligned}\tag{74}$$

The spectral function can be written in the form,

$$S(E, \mathbf{p}) = \langle \psi_a | a^\dagger(\mathbf{p}) \delta(E - H) a(\mathbf{p}) | \psi_a \rangle \quad (75)$$

where a^\dagger and a are the creation and annihilation operators and the Hamiltonian H is given by $H = T + V$ (contains just one body and two body terms), and the total binding energy E_A is given by $E_A = A \langle T \rangle + \langle \psi_a | V | \psi_a \rangle$. Using these relations one can show that [19],

$$\frac{E_A}{A} = \frac{1}{2}(\langle T \rangle - \langle E \rangle) \quad (76)$$

This is known as the Koltun sum rule. The $(e, e'p)$ data from Saclay, Tokyo and Frascati shown in the last two subsections were used to test the Koltun sum rule [19], but because the experimental spectral functions are not the true but distorted spectral functions it is necessary to correct for this fact. These corrections are of the order of 10%. It was found that except for the ^{40}Ca case there is significant deviation from the predictions of the sum rule (ranging from 1.4 MeV for ^9Be to 3.9 MeV for ^{58}Ni). Some of the explanations for this divergence from the Koltun sum rule include; the limited energy-momentum range covered in an experiment and breakdown of the assumption that the three body and other many body interactions can be neglected. Thus the measurement of the spectral functions over a wide range of E and \mathbf{p} is very desirable in order to have a better understanding of this problem.

2.7.4 The L and T Response Functions

The longitudinal and the transverse response functions for $^{12}\text{C}(e, e'p)$ in the quasi-elastic region were separated by Ulmer *et al.* [10], at MIT-Bates using the Rosenbluth method outlined earlier in Section. (2.3.1). The momentum transfer for

the experiment was $Q^2 \approx 0.16 \text{ GeV}^2$. The separated response function and their difference is shown in Figure 11. The MIT data demonstrates that the transverse/longitudinal coupling for the 1p-shell of Carbon is same as that of a free proton. The broad peak for 1s-shell is difficult to separate from the underlying continuum that begins beyond the two nucleon knockout threshold. However, the transverse response function is significantly enhanced in the continuum region.

Similar experiments were also performed at NIKHEF with higher momentum resolution but at lower momentum transfer on C [12], Li [11] and Ca [41] targets. They have plotted their data in terms of a ratio η which is defined as $\eta = \frac{R_G(expt)}{R_G(DWIA)}$, where R_G is the ratio of the transverse to the longitudinal response function integrated over the quasi-free peak. The results are shown in Figure 12. This data shows that the ratio below the 2-nucleon threshold is unity but at higher missing energy there is enhancement of the ratio.

The available data shows that the response functions are similar to free nucleon response functions at small missing energy but there is excess transverse strength above the 2-nucleon knockout threshold. This suggests additional transverse currents are involved in the process. Since multi-nucleon currents like the meson exchange currents are primarily transverse in nature (Section 2.5.3) it has been suggested that these and other multi-nucleon processes give rise to the observed enhancement in the transverse response function. Although some fraction of the effect might be due to the modification of the single nucleon currents in the nuclear medium, the large excess in the transverse strength points towards multi-nucleon currents. However at the low proton energies and for light targets, there is considerable uncertainty due to final state interactions, in the available data. There is a clear need for more systematic data on the separated response functions at higher proton energies and heavier targets.

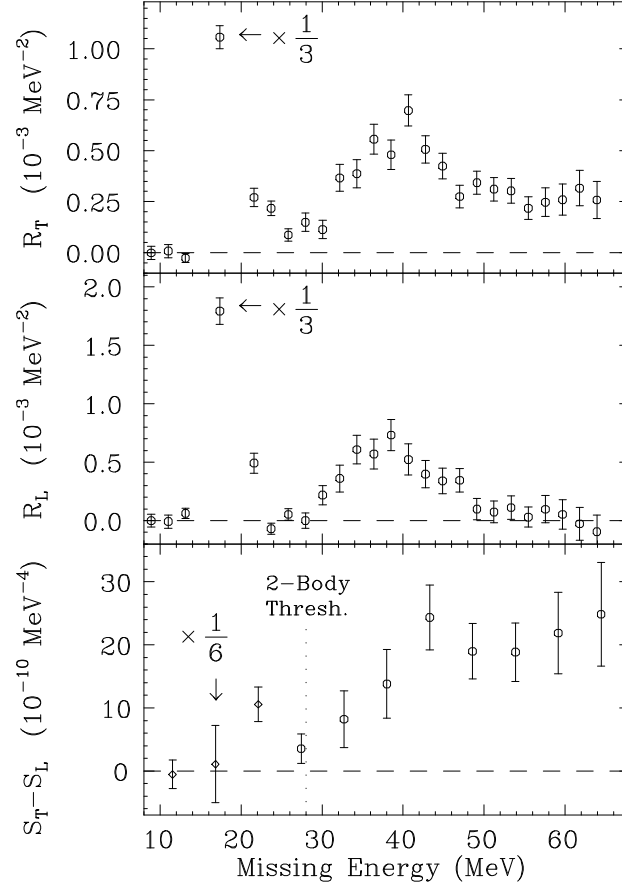


Figure 11: Separated transverse and longitudinal response functions R_T and R_L and the difference $S_T - S_L$, for $^{12}\text{C}(e, e'p)$ as a function of missing energy. Data taken in parallel kinematics near the quasi-free peak with $Q^2=0.16 \text{ GeV}^2$ [10].

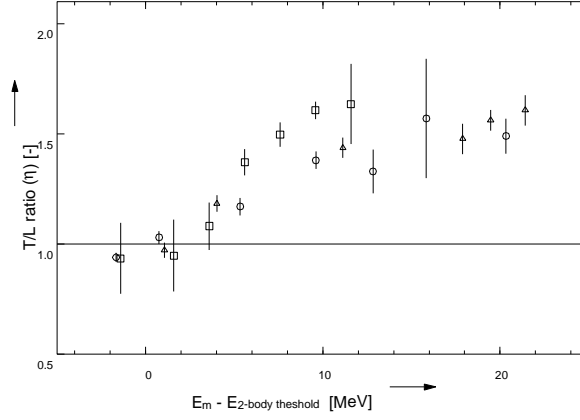


Figure 12: The transverse enhancement factor η as a function of missing energy above the two-nucleon knockout threshold. ^{12}C (squares), ^6Li (triangles) and ^{10}B (circles) [20]

2.7.5 Multi-nucleon Knockout

There is a host of experimental evidence suggesting contributions from multi-nucleon currents. Some of the experimental evidence are discussed here. Figure 13 [43] shows the missing energy spectrum for $^{12}\text{C}(e, e'p)$ in the dip region ($\omega = 0.2 \text{ GeV}$ for $Q^2 = 0.16 \text{ GeV}^2/c$) between the quasi-free region and the delta resonance region. This region is known to be predominantly transverse in nature. The figure also shows that the continuum extends to large missing energies. The area above the dotted line shows the expected strength from $1s$ knockout, while the solid curve is from a quasi-deuteron calculation by Laget [44]. The dotted line suggests that the multi-nucleon contributions start close to the two-nucleon knockout threshold and are nearly uniform over a large range of missing energy. The quasi-deuteron calculation can account for some of the excess strength at low missing energy but cannot explain the large excess beyond 80 MeV in missing

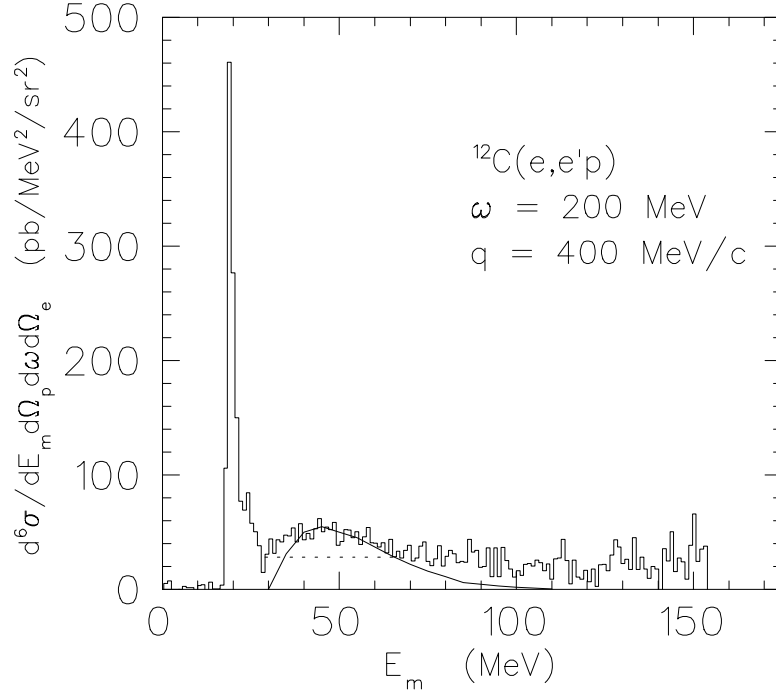


Figure 13: The missing energy spectrum for $^{12}\text{C}(e, e'p)$ in the dip region, with $\omega = 0.2$ GeV and $q = 0.4$ GeV [20]. The area under the dotted line is attributed to the $1s_{1/2}$ shell and the solid line is the quasi-deuteron calculation [44].

energy.

There are similar data from Weinstein et al. [45] of missing energy spectra for $^{12}\text{C}(e, e'p)$ at $0.58 < q < 0.82$ GeV in the quasi-free region (Figure 14). These spectra show that the strength at large missing energies (> 80 MeV) increases with momentum transfer q and is a significant fraction of the total yield. However, the ratio of the continuum yield to the quasi-free yield is relatively constant in this range of q .

Various authors [46, 45] have estimated the contribution to the excess continuum strength in terms of proton re-scattering. These estimates indicate that a very small fraction of the continuum yield arises from proton re-scattering. These

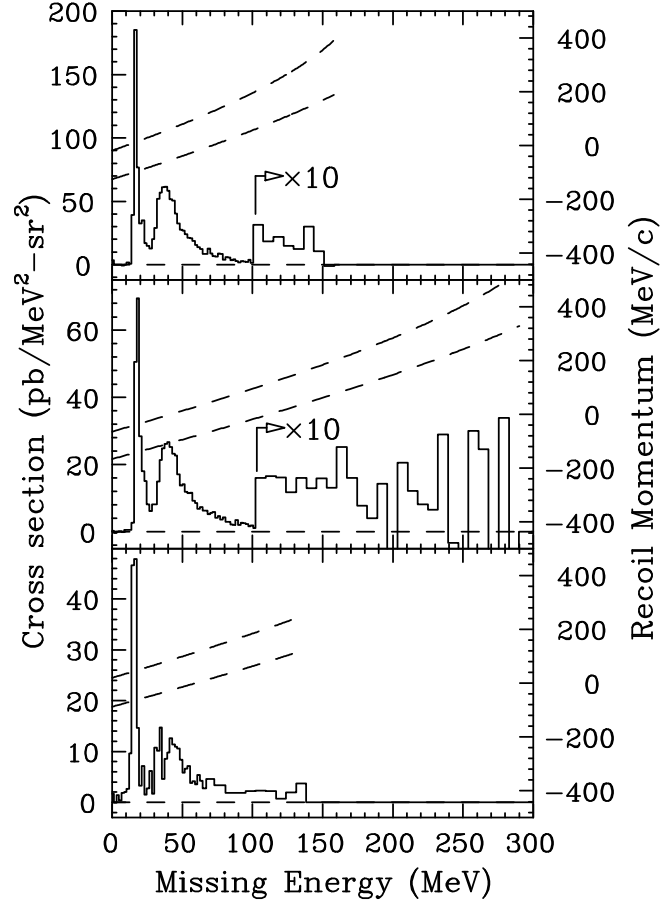


Figure 14: The missing energy spectrum for $^{12}\text{C}(e, e'p)$ in the quasi-elastic region, at $0.58 < q < 0.82 \text{ GeV}$ [45]. (a) $q = 585 \text{ MeV}/c$, $\omega = 210 \text{ MeV}$; (b) $q = 775 \text{ MeV}/c$, $\omega = 355 \text{ MeV}$; and (c) $q = 827 \text{ MeV}/c$, $\omega = 325 \text{ MeV}$. The recoil momentum range at each missing energy is indicated by the dashed curve.

observations indicate that multi nucleon absorption must have a big role in the continuum yield. Multi nucleon mechanisms involving meson-exchange currents, pion production and reabsorption are dominantly transverse in nature and are thus expected to play a major role in explaining the continuum yield. And once again to study these effects it is necessary to obtain separated response functions at large missing energies.

2.7.6 Nuclear Transmission

Final state interactions and proton propagation can be studied in terms of nuclear transmission, which is defined as the probability of escape of a knocked out proton in a quasi-elastic scattering process. The knocked out proton can be deflected or absorbed in the spectator nuclei and hence the nuclear transmission is expected to be governed by the total NN cross-section, which should increase with energy till the inelastic NN cross-section reaches its asymptotic value. Transmission/transparency measurements are expected to be simpler to interpret at higher energies because of the relative independence of the NN cross-section with energy at high energies. In addition $(e, e'p)$ scattering is an ideal tool to study proton propagation since the electron can probe the entire nuclear volume, unlike proton-nucleus scattering experiments which can primarily probe just the surface of the nucleus and have the additional problem of requiring separation the incident protons from the knocked out protons.

At low energies the nuclear transmission was measured experimentally in terms of the ratio of the coincident $(e, e'p)$ cross-section to the inclusive quasi-free electron scattering cross-section. Transmission data from an experiment at Bates using 780 MeV electrons at $Q^2 = 0.34 \text{ GeV}^2$ on ^{12}C , ^{27}Al , ^{58}Ni and ^{181}Ta targets is shown in Figure 15 [47]. The curves in the figure show the contributions of different effects

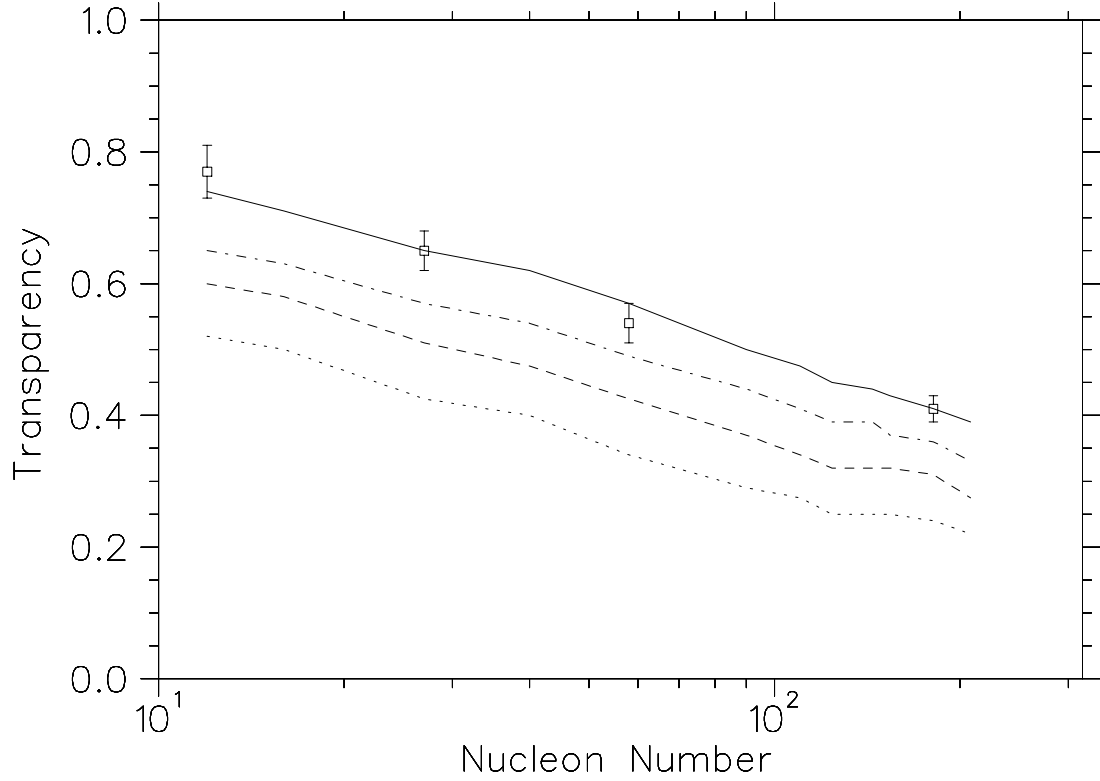


Figure 15: The dotted line is a calculation using free N-p cross-section, dashed line is when Pauli blocking is included, dot-dashed includes density dependent effects too and solid has the correlation hole effect as well.

like Pauli blocking, density dependent effects and correlation hole effects added to a semi-classical proton multiple scattering calculation using free p-n scattering cross-sections [48]. The solid curve which includes all the effects mentioned above seems to agree very well with the data.

At higher energies this technique cannot be used to measure the nuclear transmission because there are significantly large contribution from inelastic processes to the inclusive quasi-elastic cross-section. Thus at higher energies the nuclear transmission is usually measured in terms of the ratio of the experimentally measured coincidence cross-section to the cross-section calculated under the plane wave

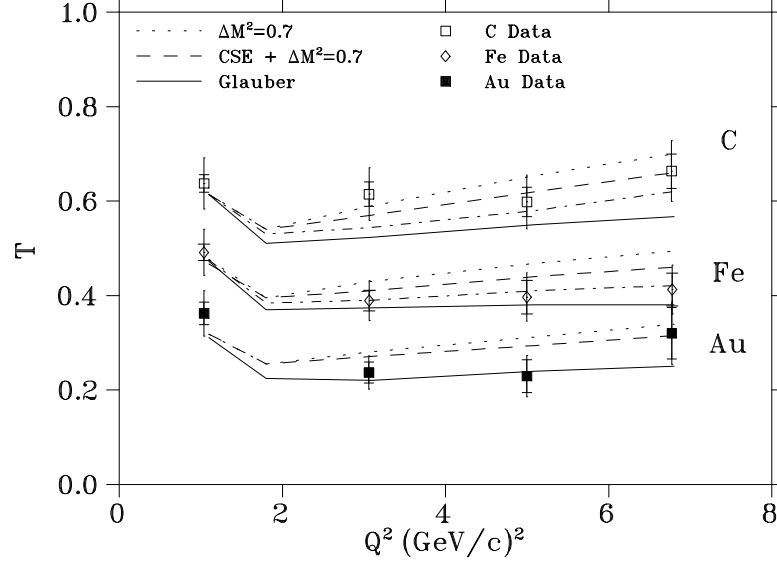


Figure 16: Measurement of nuclear transmission at Q^2 ranging from 1 to 6 GeV^2 .

impulse approximation (PWIA). Since in the PWIA it is assumed that there is no final state interactions, the ratio of the experimental cross-section to the PWIA cross-section gives the fraction of the knocked out protons which make it out of the target nucleus without further interactions on their way out. The measured nuclear transmission from experiment NE18 at SLAC [49], at Q^2 ranging from 1.0 to 6.8 GeV^2 on ^{12}C , ^{56}Fe and ^{197}Au targets are shown in Figure 16. Various Glauber type calculations are shown along with the data. It's clear that one needs more accurate measurements in order to discriminate between the various theoretical calculations. One should note that there is a continuous ambiguity between transparency and spectroscopic factor, since the measured cross-section is actually a product of the transparency and the spectroscopic factor.

2.8 Summary

A general formalism to calculate the $(e, e'p)$ cross-section was introduced in this section, however, it was shown that to make the calculations more tractable certain approximations are essential. Many approximation schemes were discussed, starting with the PWIA which does not include any final state interactions. Then two different schemes for doing a more complete calculations including final state interactions and other distortions not included in the simplistic PWIA, were described. These schemes are the DWIA and the Glauber approximations. Calculations based on these approximation schemes were compared the experimental data and will be presented in Chapter 5. Finally the existing data from a host of experiments were examined. The sum total of existing data answer many questions about the validity of the different approximations, but they also raise many new questions and point to a great need for more precise data over a wide range of proton energies and momentum transfer. The unresolved issues can be summarized as :

- Validity of the factorization assumption of DWIA. This can be tested by comparing data at different proton angles.
- The asymmetry in perpendicular kinematics.
- The mechanism which gives rise to the 20-30% depletion of the experimentally measured occupation numbers compared to shell model predictions.
- The breakdown of the energy weighted sum rule (Koltun sum rule).
- The mechanism which gives rise to the excess transverse strength observed in separated response functions.
- The importance of and contributions from final state interactions and nucleon-nucleon correlations in knockout reactions.

- Extent of the modification of the electron-proton coupling in the nuclear medium.

Experiment E91-013 which is described in the remaining chapters of this thesis was designed to address this need for more data. It was also tailored to investigate some of these aforementioned questions about the reaction mechanism.

Chapter 3

The Experimental Apparatus

3.1 Introduction

The experiment titled “Energy Dependence and A Dependence of Proton Propagation in Nuclei Studied with Quasi-Elastic ($e, e'p$) Scattering” (experiment E91-013), was carried out using the 100% duty factor beam at the Continuous Electron Beam Accelerator Facility, (CEBAF, now called Jefferson Lab). Data were collected in two time periods, the first period was in November-December 1995 and the experiment was completed in April-May 1996. The experiment involved impinging the electron beam onto a nuclear target and knocking out a proton from within the target nucleus. This knocked out proton was then detected in coincidence with the inelastically scattered electron, using the two Hall C spectrometers, the High Momentum spectrometer (HMS) and the Short Orbit Spectrometer (SOS). Data were taken on three nuclear targets, C, Fe and Au, and a liquid Hydrogen target was used for calibration. In this chapter the experimental equipment and setup is described.

3.2 Accelerator

The experiment was conducted at CEBAF which is a continuous wave (CW) machine, accelerating electrons to energies up to 4.0 GeV. The machine has a racetrack-shaped layout with two super-conducting linacs (north and south) connected by super-conducting magnetic arcs on either end (Figure 17). Each of the two linacs consists of 160 niobium super-conducting rf (SRF) cavities. These cavities are grouped in pairs and four pairs of cavities are put in thermally insulated tanks which are called cryo-modules. The cavities have an active length of 0.5 m and are operated at a temperature of 2 K. Each cavity is separately powered by a 5 kW klystron which produces an accelerating gradient of about 5 MV/m which can be increased to about 8 MV/m. The two arcs house the super-conducting bending magnets; there is one layer of magnets for each pass the beam makes through these arcs and the magnets are stacked on top of each other.

The injector to the accelerator is situated at the start of the north linac; it consists of a thermionic electron gun and 18 SRF cavities. Here the beam is accelerated to 45 MeV and injected into the machine. The beam is then accelerated by 800 MeV on each pass through the entire circuit. A maximum of five passes is possible, hence a maximum beam energy of 4.045 GeV. The beam switch-yard situated at the west end of the south linac houses the extraction and recombination magnets. The switch-yard can extract the beam at any pass to any of the three experimental halls. This experiment was carried out in Hall C which was the only hall operational during the experiment.

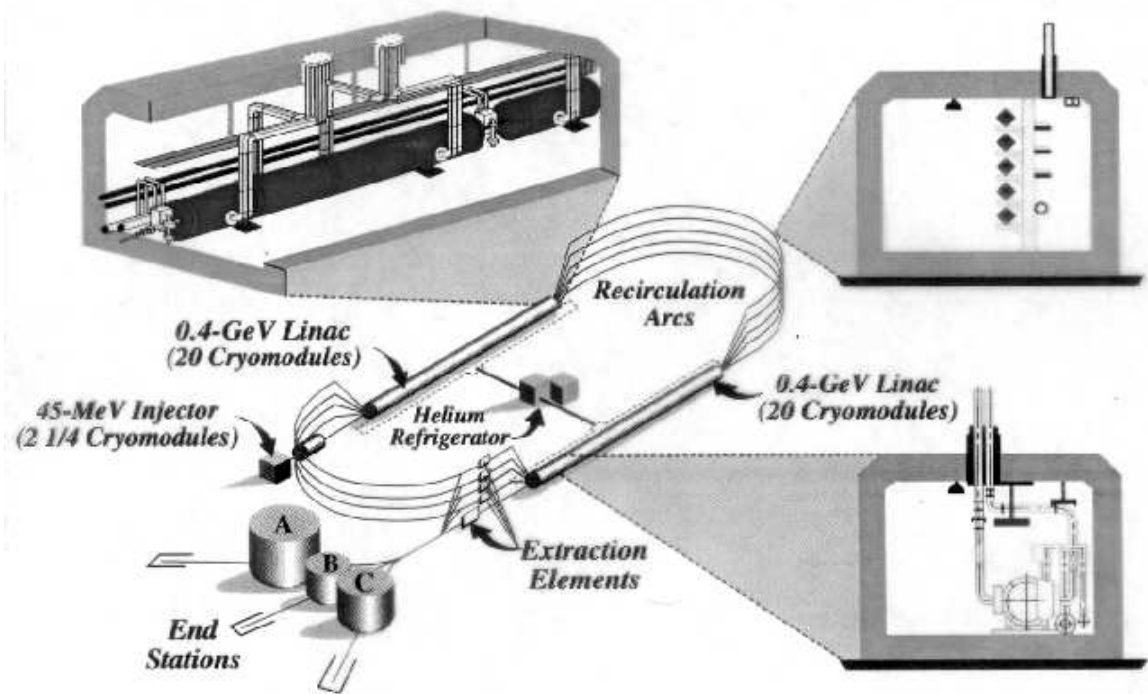


Figure 17: Complete layout of the CEBAF Accelerator

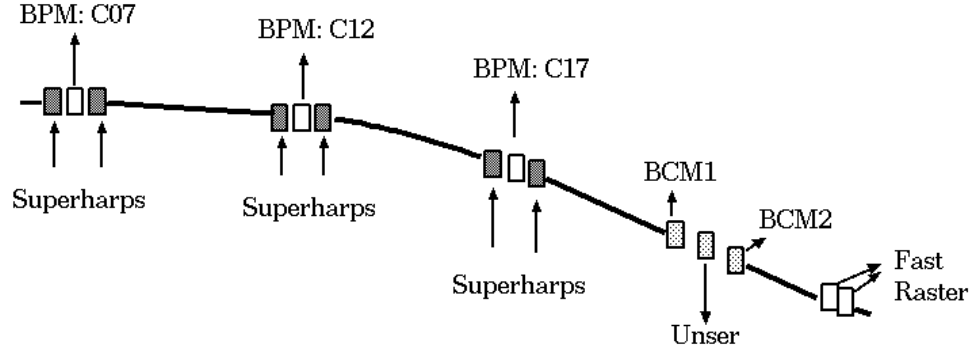


Figure 18: Top view of the components and the layout of the arc which transports the beam from the switch-yard to the hall.

3.2.1 Beam

An unpolarized CW electron beam of energy ranging from 0.8 - 3.2 GeV and of beam currents ranging from 10-50 μA was used in the experiment. The beam consists of 1.67 ps bursts coming at 1497 MHz. Each hall receives a third of these bursts, which results in a frequency of 499 MHz per hall. The beam had a fractional energy spread of 2.5×10^{-4} . The relative beam energy can be measured in principle to 10^{-4} using the bending magnets in the Hall C arc (used to transport beam from the switch-yard to Hall C, Figure 18) while measuring the beam position with super-harps. The beam energy was determined absolutely to 10^{-3} (for one pass only) using kinematic methods which are described in Section 4.5.1. The CW nature of the beam is very important to coincidence experiments. Since the yield of real events is proportional to the current while the yield of random events is proportional to the square of the current, the CW beam ensured orders of magnitude improvement in the real-to-randoms ratio compared to previous ($e, e'p$) experiments, conducted at MIT/Bates (beam duty factor $\approx 1.0\%$) and SLAC (beam duty factor $\approx 0.03\%$) and enabled collection of much higher statistics data.

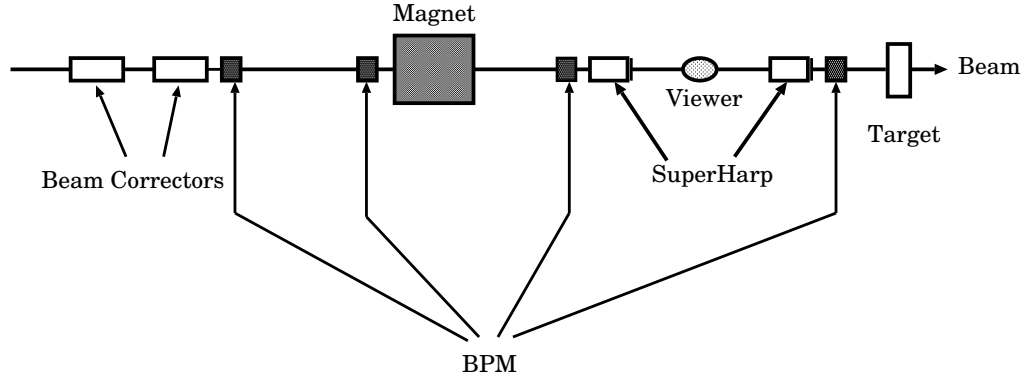


Figure 19: The components and the layout of the Hall C beamline

The beam profile was recorded by several harps located throughout the accelerator and by super-harps located in the Hall C arc. A harp consists of a frame with three wires, two vertical wires and one horizontal wire. Analog to Digital converters (ADCs) connected to each wire read the signal on the wires as the frame is moved in and out of the beam, while an encoder determines the position where the wire intercepts the beam. Thus the two vertical wires measure the horizontal beam profile while the horizontal wire measures the vertical beam profile. The super-harps are essentially the same as the harps, but more accurately surveyed to enable absolute position measurements. Three pairs of super-harps are located on aligned granite tables at the beginning, middle, and end of the Hall C beamline (Figure 19). They are used along with the field maps of the bending magnets in the arc to determine beam energy and emittance.

The beam position in the Hall C arc was measured using four beam position monitors (BPMs). These are cavities with four antennae that pick up the harmonics of the fundamental frequency of the beam passing through the cavities. The signals are proportional to the distance between the beam and the antennae. The

relative position of the beam is determined by using the amplitude of the signals from the antennas and the absolute position is determined by calibrating the BPMs with the super-harps. The beam position was monitored with an accuracy of $\approx \pm 0.5$ mm. Accurate knowledge of the beam position is very important since the experimental goal is to measure cross-sections with an accuracy of a few percent.

3.2.2 Current Monitors

A precise measurement of the charge is needed to convert measured counts to cross sections. To this end the Hall C experimental setup includes three beam current monitoring microwave cavities (BCMs) and an Unser cavity (a parametric DC current transformer). The beam current being delivered to the hall is measured with the three microwave cavities. The beam excites resonant modes in the cylindrical cavities/wave guides and the wire loop antennas in the cavities couple to these resonant modes. The signal in the antenna is proportional to the beam current for all resonant modes. In addition, for certain modes like the TM_{010} mode, the signal is insensitive to the beam position. By varying the size of the cavity, one can choose the frequency of the TM_{010} mode to be identical to the accelerator RF frequency, making the cavity selectively sensitive to this mode. The quality factor of the cavity, defined as the ratio of stored energy to dissipated power, weighted by the resonant frequency, $Q = \omega_0 W / P_d$, can be changed by varying the material and the length of the cavity. The Q of the cavity affects the temperature dependence of the current measurement, hence the Q is optimized to lower the temperature variation of the measurement. The signal from the antenna is amplified and converted to a DC level which is then converted to a rate by a V-F converter and counted in a scaler. However, these cavities cannot measure the current absolutely as the power output is dependent on factors like surface finish which cannot be

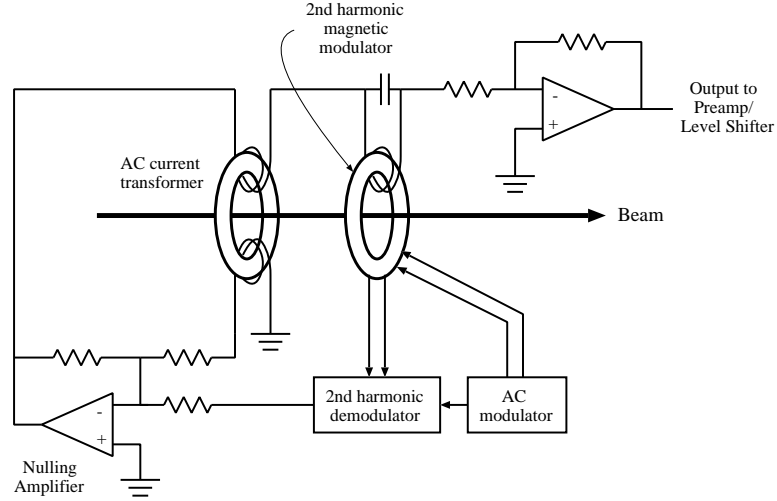


Figure 20: Schematic of the Unser Monitor

quantified easily. Hence the current monitors were calibrated using a parametric DC current transformer (Unser monitor). This transformer measures the total charge passing through the device. A simplified schematic of the Unser monitor is shown in Figure 20 [50]. One of the toroids measures the AC fluctuations while the other picks up the DC fluctuations. An AC modulator is used to drive the toroid along its hysteresis curve, which is symmetric for zero DC fluctuations. In the presence of DC fluctuations however, the hysteresis curve is biased and loses its symmetry. A feedback loop is used to restore the symmetry of the hysteresis curve and the amount of current needed to restore symmetry is the output of the device. This output is also converted in a V-F converted and counted by a scaler.

The Unser monitor is known for its linearity over a wide range of currents and its very stable gain. The absolute gain of the Unser can be measured to 10^{-4} . The gain of the Hall C Unser was measured to $\pm 2.0 \times 10^{-4}$ using a precision voltage source and resistor. However, the baseline of the Unser monitor tends to drift

with time ($\sim 1\mu\text{A}$ per day) making it inaccurate for direct current measurements. On the other hand the BCMs have negligible baseline drifts but their gains can drift slowly with time and they are not linear over the whole range of currents to be measured. The calibration scheme used the gain stability of the Unser to periodically re-calibrate the other three BCMs. The calibration procedure involves changing the beam current in a series of steps, each two minutes long, going from zero to the maximum. Each step was inter-spaced by 2 minutes of zero current. The zero current intervals were used to determine the baseline for all four monitors. Once the baseline is determined, one uses the known and stable gain of the Unser to determine the gains of the three BCMs. The beam current was measured with an accuracy of 1.0%. The current can be measured more accurately ($\sim 0.5\%$) at higher currents. This is because the BCMs have better linearity at higher currents and the measurement is less sensitive to the drifts in the offsets.

3.3 Target

This experiment used three solid targets suspended on a steel ladder and a liquid hydrogen cryogenic target hung on a separate ladder. During the first part of the experiment (Dec. 1995) the cryo-target was not operational, hence only the solid target ladder was used. During the later part of the experiment (Apr. 1996) both the cryogenic target and the solid targets ladders were used. Both ladders were housed in a scattering chamber and either one of them could be rotated into the beam. The scattering chamber is a large Al cylinder, with 2.5 inch thick walls and an inner diameter of 48.5 inches. The cylinder has cutouts for the two spectrometers and entrance and exit snouts for the beam. There are also pumping and viewing ports. The HMS cutout is eight inches tall and covered with an aluminum window 0.016 inches thick. The SOS port is five inches tall and covered

with a 0.008 inch Al window. The top cover plate contains openings for the cryo-target plumbing and lifting mechanisms and the solid target ladder mechanism.

3.3.1 Solid targets

The solid target ladder held target foils each 0.75 inches by 1.5 inches in size. This ladder could be lifted and rotated in and out of the beam remotely. In addition it could be manually rotated about its vertical axis; this feature was used to minimize losses due to traversal through the target at large scattering angles. The target angle was known with an accuracy of about 2° . Figure 21 shows the convention used to define the target rotation angle. For the forward electron angle kinematics the target angle was usually set between 10° - 20° with respect to the beam, while at the backward angle kinematics the target angle was set at -20° with respect to the beam.

In the experiment carbon, iron, and gold targets were used. The main properties of the targets are listed in Table. 2. The iron and one of the gold targets had two foils sandwiched together. A microscope was used to measure the dimensions of the foils (accuracy = $8\mu\text{m}$) and a balance was used to measure their masses (accuracy = 5mg). Assuming uniform density and thickness the areal density of the targets were calculated (Table. 2). The isotopic abundances of the targets were as follows: carbon 89.9 % ^{12}C with 1.1 % ^{13}C contamination, iron 91.76 % ^{56}Fe with 5.9 % ^{54}Fe and 2.1 % ^{57}Fe contamination and gold 100 % ^{197}Au . The largest contaminant, ^{54}Fe , had only a 0.3% effect on the target thickness, thus the target impurities are neglected in the analysis.

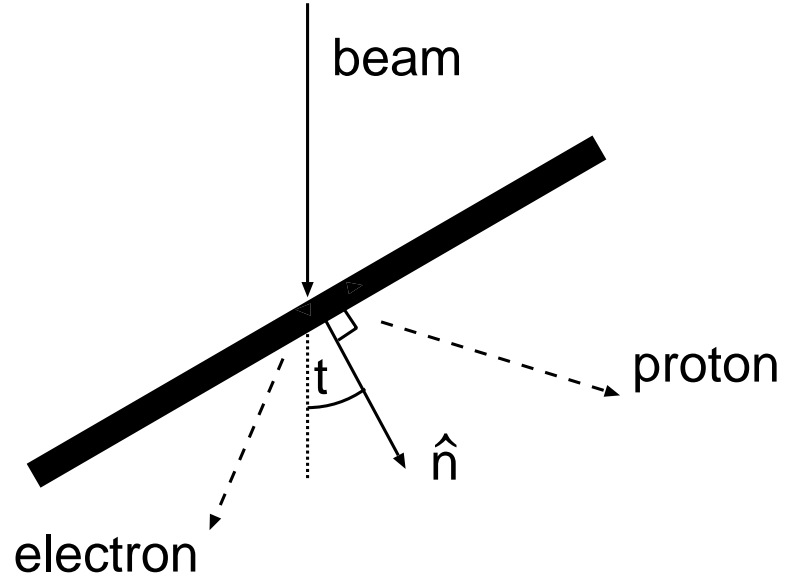


Figure 21: The angle of the solid target with respect to the beam. The target angle, t , is defined to be positive when the normal to the target, \hat{n} is directed towards the SOS.

Table 2: List of solid targets and their properties

Target	% of radiation length %	density (g/cm ³)	Thickness (mg/cm ²)	Thickness uncertainty %
C	0.5	2.27	230.3	0.23
Fe	2.2	8.11	309.1	0.07
Au	3.1	19.28	195.9	0.10

3.3.2 Cryotarget

The cryotarget system had six target cells and 2 dummy cells. There were three 4 cm cells and three 15 cm cells. Each cell is a thin aluminum cylinder made from beer can stock. The can bottoms which are 0.31 mm thick formed the exit windows. The entrance window was made of 0.18 mm thick aluminum. The four cells of each type were designed to hold liquid hydrogen, deuterium and helium and one set of dummy cells to measure background from the Al end caps. In the experiment only the 4 cm hydrogen cell (exact length 4.20 ± 0.01 cm, the spherical shape of the end cap caused a variation in target length of about 0.05% for a 1.0 mm change in beam position), and the 4 cm dummy cells were used. The dummy cells consisted of two Al plates to simulate the end caps of the normal cells. The plates were about 10 times thicker than the end caps. A schematic of the cells is shown in Figure 22.

The cryotarget system has three separate cryogenic loops, each loop linked to a short and long target cell. Each target loop consists of a circulation fan, a target cell, heat exchangers and high and low powered heaters, which formed the cooling and regulating units of the target system. During the experiment hydrogen in its liquid phase was kept in the 4 cm cell. The hydrogen was maintained in the liquid phase by flowing it continuously through a heat exchanger. The heat exchanger was cooled to 15 K by a constant flow of cryogen maintained by the end station refrigerator (ESR). The hydrogen in the target cell had a temperature of 19 K and a pressure of 29 PSIA. Under these conditions the hydrogen is 3 degrees below its boiling point. The target had to be regulated very carefully to keep the temperature and pressure steady, since the density of hydrogen changes very steeply with temperature and pressure ($-1.25\%/K$ and $0.01\%/PSIA$ respectively). This was achieved by monitoring the temperature very precisely with Cernox resistor

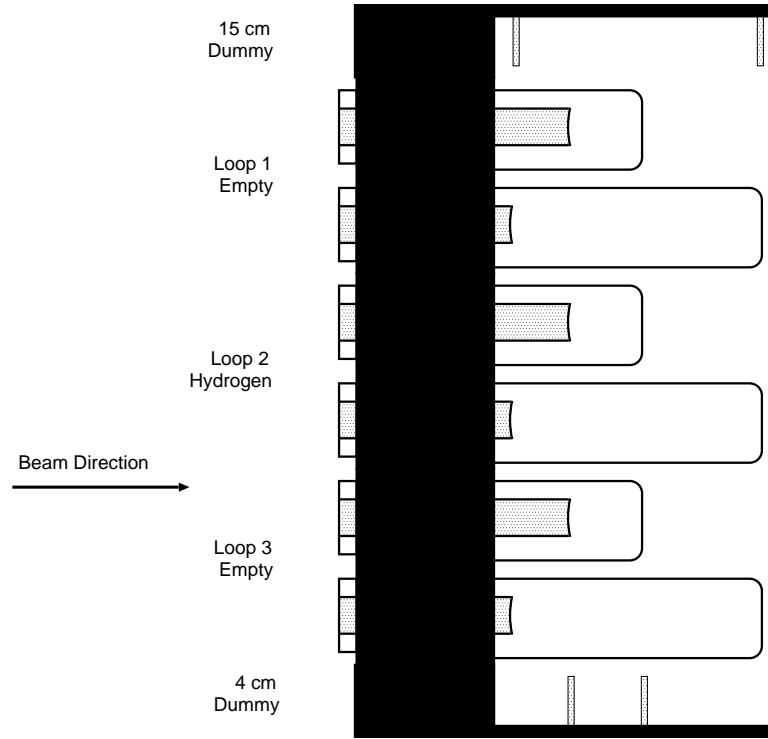


Figure 22: Schematic of the Cryotarget Cells

thermometers (with an accuracy of 50 mK corresponding to 0.1% uncertainty in the density). The effects of local boiling were studied with elastic scattering from liquid hydrogen and liquid deuterium targets and the yields were found to follow the change in beam current to better than 1 % up to $70 \mu\text{A}$. The main contamination in the hydrogen target comes from deuterium which was found to be less than 0.3% from analysis of the gas after the experiment. A more complete description of the Hall C cryogenic target system can be found in reference [51].

3.4 Spectrometers

The major experimental equipment in Hall C at CEBAF consists of two magnetic spectrometers, a medium resolution, large acceptance super-conducting spectrometer for central momentum up to 7.4 GeV/c called the High Momentum Spectrometer (HMS) and a medium resolution, large acceptance spectrometer with a shorter flight path called the Short Orbit Spectrometer (SOS). The SOS has a maximum central momentum of 1.5 GeV/c. In this experiment the HMS was used to detect electrons while the SOS was used to detect protons, except at the highest Q^2 point where the roles of the spectrometer were reversed. The co-ordinate system used in the two spectrometers is shown in the Figure 23. In this system (also called the transport system) the Z axis is along the central ray of the spectrometer with positive in the direction of the particle trajectory. X is the bend direction with X and Z forming the bend plane. The positive X is defined as the direction towards which higher momentum particles bend; this is vertically down for both of these upward bending spectrometers. Thus the Y axis is along the horizontal with positive directed to the left as seen by the particle. The Y and Z at the target form the scattering plane.

3.4.1 High Momentum Spectrometer

The HMS is a 25° vertical bend spectrometer, with three super-conducting quadrupole magnets and one super-conducting dipole magnet in a QQQD configuration. The four magnets and the detector stack are supported on a single carriage that rotates around a central bearing. The detector shielding hut, built around the detector stack, is supported on an independent carriage. The whole spectrometer rotates on a pair of rails between 12.5° and 90° with respect to the beam line. The HMS

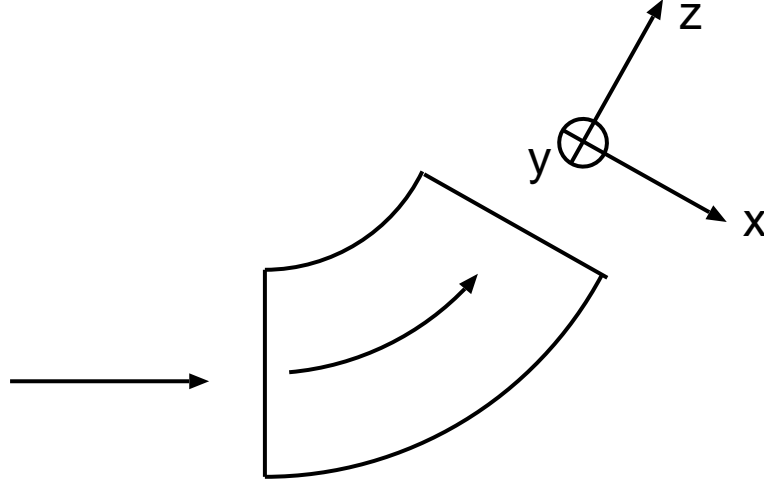


Figure 23: Side view of the spectrometer co-ordinate system

can analyze particles with central momentum up to $p_{max} = 7.4 \text{ GeV}/c$ and has a momentum acceptance of $\pm 10\%$ about the central momentum. The momentum resolution of the HMS is 2.0×10^{-3} and the angular resolutions are 0.8 mrad and 1.2 mrad, for scattering in and out of the scattering plane, respectively. The procedure for optimizing these performance parameters is described in the next chapter in Section 4.5. Figure 24 shows a side view of the HMS spectrometer and detector hut.

The quadrupoles determine the transverse focusing properties of the spectrometer and to a large extent its acceptance. The HMS quadrupoles are all cold iron super-conducting magnets, with soft iron around the super-conducting coils to enhance the field at the center and also reduce stray field. The quadrupoles are powered by three Danfysik System 8000 power supplies which can provide up to 1250 amps at 5 volts. The quadrupoles are maintained on a stable hysteresis curve by running the currents up to 20% higher than their 4 GeV/c values and then

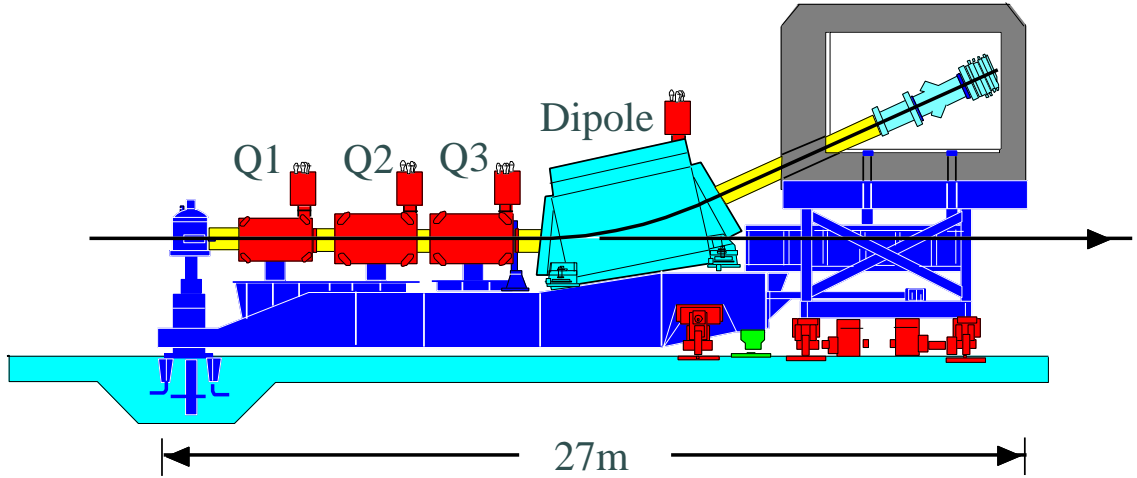


Figure 24: Side view of the HMS

bringing the current down to the desired set point. In addition to the quadrupole coils, each magnet has multipole windings. These correction coils can be powered by three Oxford power supplies, capable of providing up to 100 amps at 5 volts, but were not used during this experiment.

The dipole is the dispersive element in the system and determines the central momentum of the spectrometer. To date the dipole magnet has been operated and tested at currents up to 1300 Amps. This corresponds to a central momentum of just over 4 GeV/c. The HMS dipole has an effective length of 5.26 meters, a bend radius of 12.06 meters, and a gap width of 42 cm. Its actual dimensions are 5.99 meter long, 2.75 meters wide, and 4.46 meters high. It is configured to achieve a 25 degree bending angle for 4 GeV/c momentum particles at a central field excitation of 1.11 T. It was determined that the hysteresis for the dipole was sufficiently small that no special setting procedure was required to reproducibly set the magnet.

An NMR probe is used to monitor and regulate the dipole field. The set point

currents are used to monitor the field settings for the quadrupoles. The fields were stable at the 10^{-4} level. The magnets are precooled with liquid nitrogen and cooled to the operating temperature with 4.3 K liquid helium, provided by the CEBAF Central Helium Liquefier (CHL). Under standard operating conditions, the HMS magnets require a flow of approximately 100 liters per minute, running in parallel to the four magnets. The power supplies are all cooled with water from the Hall C low conductivity water (LCW) system.

A collimation mechanism is attached to the entrance of the spectrometer. This mechanism consists of a slit box which allowed remote insertion of three different collimating slits. All three slits were made from HEAVYMET (machinable Tungsten with 10% Cu Ni; density=17 g/cm³). The first slit is a 1.25 inch thick array of small holes (0.2 inch in diameter), called the sieve slit. The sieve slit was used to tag the trajectories of the electrons in order to study the optics of the spectrometer. The other two slits are octagonal apertures designed to define the solid angle acceptance of the HMS. Each of these slits is 2.5 inch thick and has flared apertures. The larger of the two slits subtends a solid angle of ~ 6.8 msr and was designed to accept trajectories which pass cleanly through the rest of the spectrometer for a point target (for a momentum bite of $\pm 8\%$). The small slit was designed to only accept trajectories with large spectrometer acceptance for an extended target. In this experiment all data was taken with the large octagonal collimator. The spectrometer was operated under vacuum of the order of 10^{-4} PSI. The entrance and exit vacuum windows were made of aluminized mylar.

The HMS was operated in a point-to-point tune in both the dispersive and non-dispersive direction. This tune provides a large momentum, solid angle, and extended target acceptance. In this tune, Q1 and Q3 focus in the dispersive direction and Q2 focuses in the transverse direction. Figure 25 shows the extreme

Table 3: Measured HMS Performance

Maximum central momentum (for normal use)	4.4 GeV/c*
Momentum bite $[(p_{max} - p_{min})/p_0]$	20%
Momentum resolution $[\delta p/p]$	0.2%
Solid angle (no collimator)	7 msr
Angular acceptance - scattering angle	$\pm 42mr$
Angular acceptance - out of plane	$\pm 82mr$
Reconstructed non bend plane angle resolution	0.8 mr
Reconstructed bend plane angle resolution	1.2 mr
Extended target acceptance	± 8 cm
Vertex reconstruction accuracy	± 1 mm
*Not the maximum limit of the spectrometer	

beam envelopes of the HMS for a point-to-point tune.

The optical axis of each magnet was determined using a magnetic colloidal solution [52]. The optical axes were found to be different from the mechanical axes by up to 2 mm, and all magnets were aligned with respect to the optical axis. When installed, the magnets were aligned to 0.2 mm, but they can move out of alignment when the spectrometer is rotated. The magnets can move out of alignment by up to 1.0 mm, but the positions are reproducible up to 0.5 mm. The nominal focal plane is defined to be the plane perpendicular to the central trajectory, positioned halfway between the two drift chambers. The true focal plane of the spectrometer is tilted $\sim 85^\circ$ to the ‘nominal’ focal plane.

The quadrupoles fields were mapped, and these field maps were used to determine the current required for a given field integral. The final field values were fine tuned in order to give the best focus at the focal plane and these fields were then checked against those calculated using a optics model of the HMS generated by the COSY INFINITY program [53]. The fine tuning procedure involved varying

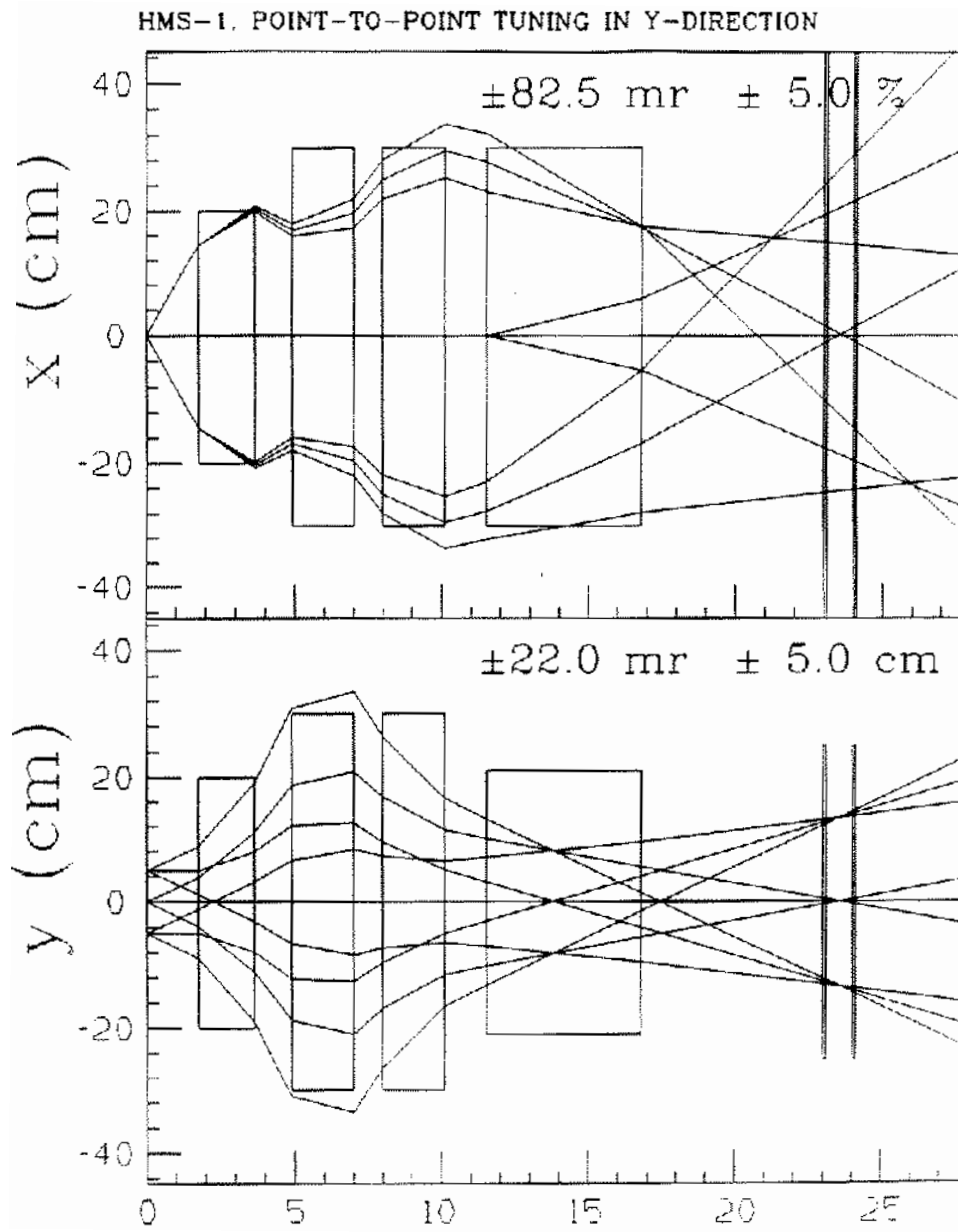


Figure 25: Extreme beam envelope of the HMS for a point-to-point tune

the quadrupole fields in order to determine the derivatives of the x and y positions of the focal point(x_{fp} , y_{fp}) with respect to the quadrupole fields. Once these derivatives were measured, Q2 and Q1 were adjusted in order to center the x (vertical) and y (horizontal) position of the focal point. This procedure was iterated to get the best focus at the focal point. The focus is relatively insensitive to the Q3 setting, so Q3 was fixed during the Q1 and Q2 adjustments. The ratio of Q1 to Q2 after making these adjustments was consistent with the COSY model and consequently Q3 was set to the field determined from the COSY model. From analyzing elastic ($e, e'p$) data at several energies, it was found that the dipole field was 0.9% below the desired value, and the dipole field was readjusted. The final tune gives momentum and field ratios that are consistent with the COSY model. Table. 3 summarizes the final performance of the HMS and is described in more details in Section 4.5.

3.4.2 The HMS Detector Package

The detector packages in the HMS contains a pair of drift chambers, two sets of x-y hodoscopes, a gas Čerenkov detector, and a lead-glass calorimeter. The drift chambers were used for tracking, the hodoscopes were used to form the trigger and for time of flight information, and the calorimeter and Čerenkov were used for particle ID (pion rejection). All of the detector systems were powered by CAEN high voltage power supplies. A schematic of the HMS hut is shown in Figure 26.

Drift Chambers

The HMS drift chambers consists of six planes, two provided x (the dispersive direction) information another two gave y (the non-dispersive direction) information, and the remaining two were rotated $\pm 15^\circ$ from the x planes (called the u

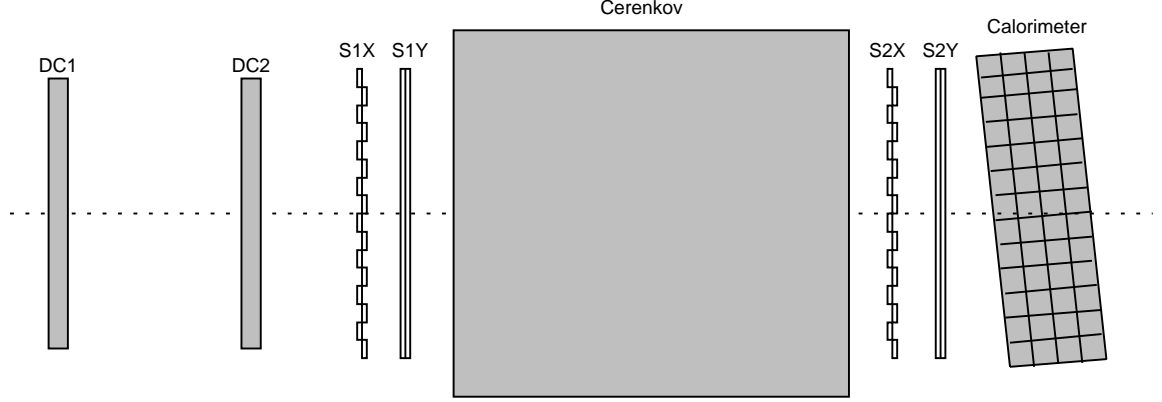


Figure 26: Schematic diagram of the HMS detector hut

and v planes). As seen by incoming particles the planes are encountered in the order x, y, u, v, y', x' . The chambers had an active area of approximately 107 cm (x) by 52 cm (y) with a sense wire spacing of 1 cm. The planes were spaced 1.8 cm apart and the two drift chambers were separated by 81.2 cm. There are planes of field/guard wires in between each plane that maintain the high voltage. The sense wires and the field wires are in a staggered arrangement with respect to each other. The sense wires detect the particles, and the field/guard wires are maintained at negative high voltage in order to isolate the sense wires. The voltage for the guard wires varied from -1800 V to -2500 V, depending on the distance of wire from the nearest sense wire. A schematic of the arrangement of wire is shown in Figure 27.

The signals from the sense wires were amplified and discriminated by LeCroy 2735DC or Nanometric N-277-L amplifier/discriminator cards. They were read out in groups of 16. The discriminator thresholds were provided by an Acopian low voltage supply, which was set at 4.5 Volts. The discriminated signals were then fed into LeCroy multi-hit TDCs (LC1877). On receiving a trigger the TDCs read out all hits (up to 16 per wire) in the last 32 μ s. The particle position is determined by

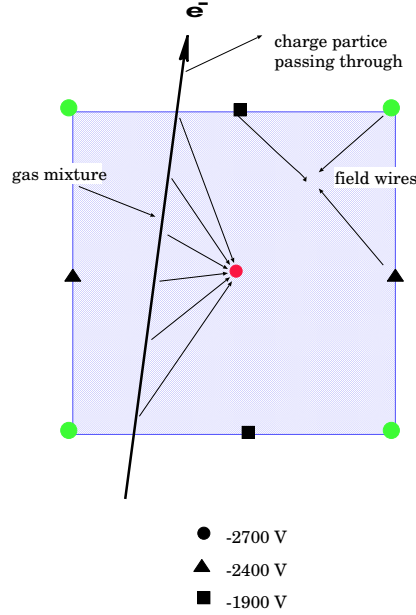


Figure 27: Schematic of the wire arrangement in the HMS Drift Chambers

using the TDC to determine the drift time, which is the time between the particle passing through the chambers and the wire detecting the electrons created by the ionization of the chamber gas. This drift time is converted into a drift distance using drift time to distance maps (during analysis). The time to distance maps were generated from high statistics calibration runs where the drift chambers were uniformly illuminated. The drift distance along with the position of the wires gives the position of the event. The hits in all the six planes are used to determine the trajectory of the particle passing through the chamber. The position resolution per plane is $250 \mu\text{m}$. The HMS chambers are filled with an argon/ethane mixture (equal amounts by weight) with 1% isopropyl alcohol (as a dehydrating agent). The gas mixing system provides two parallel gas lines from a single source. The gas flow is controlled with proportional mass flow control valves. There are temperature controlled alcohol bubblers on the flow to and from the chambers, which monitor

the gas flow.

Hodoscopes

The HMS has two pairs of hodoscope planes, each pair has one plane stacked in the x direction and the other stacked in the y direction. The x planes are made of sixteen elements/paddles, while the y planes are made of ten elements. The hodoscope elements are long narrow strips of BC404 scintillator with light guides and photo multiplier tubes (PMT) on each end (Figure 28). The scintillators are wrapped with one layer of Aluminized Mylar and two layers of Tedlar (PVF) to make them light tight with a minimum amount of external material. The scintillators have approximately 0.5 cm of overlap between the elements in order to avoid missing particles. In the HMS, all of the scintillators are 2.12 cm thick and 8 cm wide. The x elements are 75.5 cm long, and the y elements are 120.5 cm long. The front and back pair of planes are separated by approximately 230 cm. The scintillators are read out from each end by Phillips 2282 PMTs. The output from the PMT is sent to a patch panel in the counting house through ~ 30 feet of RG58 cable, and then ~ 450 feet of RG8 cable. The signals are then split, giving two signals with $1/3$ and $2/3$ of the input signal. The smaller signal goes to a bank of ADCs through ~ 400 ns of RG58 cable delay. The other output is discriminated with Phillips PS7105 discriminators; one set of outputs from the discriminators goes to TDCs and VME scalars through some delays. The other set of outputs is sent to a LeCroy 4654 logic module. This module generates the OR of all tubes on one side (labeled as + while the other side is labeled -) of a given plane (e.g. S1X+). Next the AND of all tubes on each side of a plane, is generated (e.g. (S1X = S1X+ & S1X-)). These outputs are used for the trigger logic. A more detailed description and figure is shown in the trigger subsection.

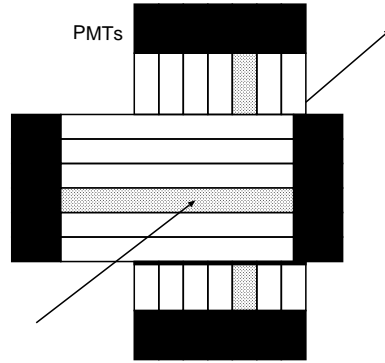


Figure 28: A perspective view of the hodoscope planes is shown

The hodoscopes were calibrated by gain matching the tubes with a ^{60}Co gamma ray source. The tube voltages are set such that the Compton edge from the gamma rays gives a pulse height of 500 mV at the output of the base. Timing calibrations of the scintillators is done using data taken during running. Various corrections and fine tuning were done by an off-line fitting procedure.

Gas Čerenkov Detector

The HMS Čerenkov detector consists of a cylindrical tank ~ 160 cm long and with an inner radius of ~ 75 cm. The tank is designed to run at gas pressures ranging from below atmospheric pressure to pressures up to 3 atmospheres. For this experiment, the tank was filled with just under 1 atmosphere of nitrogen, giving a pion threshold of 6.3 GeV/c (and electron threshold of 22 MeV/c). The average signal from an electron was ~ 7 photo-electrons. There are two mirrors at the back of the tank which reflect the Čerenkov light into the two PMTs on the side of the tank. The light was detected with two 5-inch Burle 8854 PMTs. In addition, the PMT front surfaces were coated with a wavelength shifting coating in order to better match the wavelength of the Čerenkov light with the PMT collection efficiency. The tank has circular entrance and exit windows of 0.04 inch Al. In the

HMS the electron detection efficiency for a 2 photo-electron cut is $\sim 98\%$.

Lead Glass Calorimeter

A lead glass calorimeter is used to measure the energy of the electrons in the spectrometer. The electron is accelerated in the field of a Pb nucleus, emitting Bremsstrahlung radiation. The Bremsstrahlung photons in turn create electron-positron pairs which produce more γ ray photons thus resulting in an avalanche of electron-positron pairs. These electrons (positrons) radiate Cerenkov light in the glass which is collected in phototubes. The total amount of light collected is proportional to the energy of the incident electrons.

The HMS lead glass calorimeters is constructed from 10 cm x 10 cm x 70 cm blocks of TF1 lead glass. The blocks are stacked transverse to the incoming particles, four layers deep. The stack is 13 blocks high, for a total of 52 modules and an active area of 130 cm x 70 cm. The calorimeter is rotated $\sim 5^\circ$ from the optical axis in order to avoid loss through the cracks between the modules (see Figure 26). Each block is wrapped with one layer of aluminized mylar (25 μm) and 2 layers of TEDLAR PVF film (38 μm each) to increase reflection and make the modules light tight. Each module was read out from one end by an 8-stage Phillips XP3462B 5 inch photo-tubes. The operating voltages were set to match the gain of the individual modules. A detailed description of the calorimeter design and performance can be found in ref [54].

The signals from the photo-tubes are taken upstairs to the counting house through ~ 30 feet of RG58 and ~ 450 feet of RG8 coaxial cable. The signal is then split, one set of outputs is sent to an ADC through delay cables and the other set is sent to LC740 linear fan-in modules to be summed. The sum in the first layer (PRSUM) and the sum in the entire calorimeter (SHSUM) are discriminated to give

three logic signals (PRHI, PRLO and SHLO) for the trigger. PRHI and PRLO are high and low thresholds on the energy in the first layer, and SHLO is a threshold set on the total energy in the calorimeter. Also, each group of four modules is summed and sent to scalers for trouble shooting purposes. The electronics diagram of the calorimeter is shown in Figure 32 in the trigger subsection.

The ADC values are corrected in two ways. First, the signal is corrected for attenuation thru the blocks to remove any dependence on the distance from the PMT. Each channel has a gain correction factor, determined by fitting a value for each block in order to match the sum of the blocks to the energy as determined from the momentum reconstruction.

3.4.3 Short Orbit Spectrometer

The SOS is composed of one quadrupole(Q) and two dipole magnets (BM01 and BM02) in a $QD\overline{D}$ arrangement. The quadrupole focuses in the horizontal (non-dispersive) direction and is followed by the two dipoles. The first dipole deflects particles by 33 degrees, while the second dipole deflects by 15 degrees in the opposite direction, such that the total bend of the SOS dipoles is 18 degrees. The two dipole magnets are enclosed in a common yoke. All three magnets (as well as the concrete detector hut) rest on a common carriage assembly. The carriage can be elevated out of plane by hydraulic jacks, allowing the SOS to go out of plane by up to 20° . The spectrometer rests 0.15° below the horizontal without the jacks. The jacks were not used during this experiment. The quadrupole and dipoles are water cooled conventional resistive magnets. They are powered by three separate InverPower power supplies. The quadrupole and BM02 supplies provide 1000 Amps at 160 Volts and the BM01 supply provides 1000 Amps at 250 Volts. The magnets and power supplies are cooled by the Hall C LCW system which provides

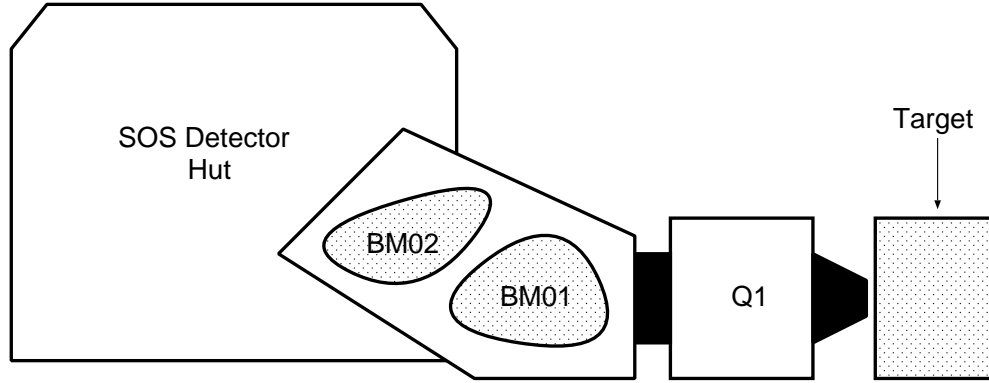


Figure 29: Side view of the SOS

water at 250 PSI. The SOS magnet system combines a large acceptance (both solid angle and momentum bite) with a relatively short path length to the focal plane. The primary object of this spectrometer is to detect short-lived particles like pions and kaons. It has a somewhat limited extended target acceptance (± 2 -3 cm). The maximum central momentum attainable with the SOS magnet system is 1.5 GeV/c. Figure 29 shows a side view of the SOS magnets. A slit box, nearly identical to that in the HMS, was installed in front of the SOS quadrupole allowing remote insertion of different collimators. There are three HEAVYMET collimators and one blank space in the slit box. The first slit is a sieve slit; a 1.25" thick array of small holes (0.2" in diameter). The sieve slit is used to tag the trajectories of the electrons in order to study the optics of the spectrometer. The other two slits are octagonal apertures designed to define the solid angle acceptance of the SOS. Each of these slits is 2.5" thick and has flared apertures. The large slit has a solid angle of ~ 7.55 msr and was designed to keep losses within the spectrometer low for a point target ($\lesssim 2\%$ for a momentum bite of $\pm 15\%$). The small slit was designed to give small losses in the spectrometer for an extended target (almost no loss for $\pm 20\%$ for a 2 cm target). All of our production data were taken using the large

octagonal collimator.

The SOS optical axis of each magnet is the same as its mechanical axis, and so the magnets were positioned using the mechanical axes. When installed, the magnets were aligned to 0.2 mm, but the magnets can move out of alignment when the spectrometer is rotated. The magnets move up to 2 mm, but the positions are reproducible down to 0.5 mm. The dipoles and quadrupole all have Hall probes which measure the fields and are used to regulate the magnet settings.

The SOS was operated in the point-to-point tune, with point to point focusing in both the dispersive and non-dispersive directions. This tune has a large solid angle and very large momentum bite, but a small extended target acceptance (see table 4). The ratio of the dipole fields (D/\overline{D}) was determined by integrating the field for the central trajectory using field maps of the dipoles. Because the quadrupole magnet was never mapped, the field settings were determined using optics models generated with the COSY INFINITY program [53], assuming that quadrupole to be a perfect quadrupole. These settings were examined by comparing the model to elastic scattering data taken with a sieve-slit, and the quadrupole field was found to be higher than expected for the current. The quadrupole current was lowered by 7% in order to match the field used in the model. The nominal focal plane is defined to be perpendicular to the central ray, and located 6 cm in front of the first drift chamber. The true focal plane of the spectrometer is tilted forward with respect to the nominal focal plane by $\sim 70^\circ$. Table 4 summarizes the performance of the SOS, which is also described in greater detail in Section 4.5.

3.4.4 The SOS Detector Package

The detector packages in the SOS is almost identical to the one in the HMS. Just as in the HMS it consists of a pair of drift chambers, two sets of x-y hodoscopes,

Table 4: SOS Performance

	Measured
Maximum central momentum	1.5 GeV/c
Momentum bite $[(p_{max} - p_{min})/p_0]$	40%
Momentum resolution $[\delta p/p]$	0.15%
Solid angle (no collimator)	9 msr
Angular acceptance - scattering angle	$\pm 60mr$
Angular acceptance - out of plane	$\pm 40mr$
Reconstructed non-bend plane angle resolution	7 mr
reconstructed bend plane angle resolution	0.5 mr
Extended target acceptance	± 2 cm
Vertex reconstruction accuracy	± 1.0 mm

a gas Čerenkov detector, and a lead-glass shower counter. In addition, the SOS has an aerogel Cerenkov detector between the back hodoscope pair. The aerogel Cerenkov was not used for this experiment. The layout of the SOS detector package is similar to the HMS apart from it being more compact.

Drift Chambers

The SOS drift chambers were built at Brookhaven National Laboratory (Figure 30). Each chamber consists of sixteen layers of 1/8 inch G10 plates, sandwiched between two 1/2 inch Al plates. The G10 plates consist of alternating planes of wires and cathode foils. The wire planes have alternating sense and field wires. The sense wires are separated by 1 cm and are $30 \mu\text{m}$ in diameter, they detect the electrons and ions created by the incoming particle ionizing the gas in the chamber. The field wires are $60 \mu\text{m}$ in diameter. The field wires and cathode foils are maintained at a large negative high voltage (-1975 V) in order to isolate the sense wires. The wire planes come in pairs that measure position in the same direction and have their wires offset by 0.5 cm. There were 6 wire planes ordered as, u and u' planes

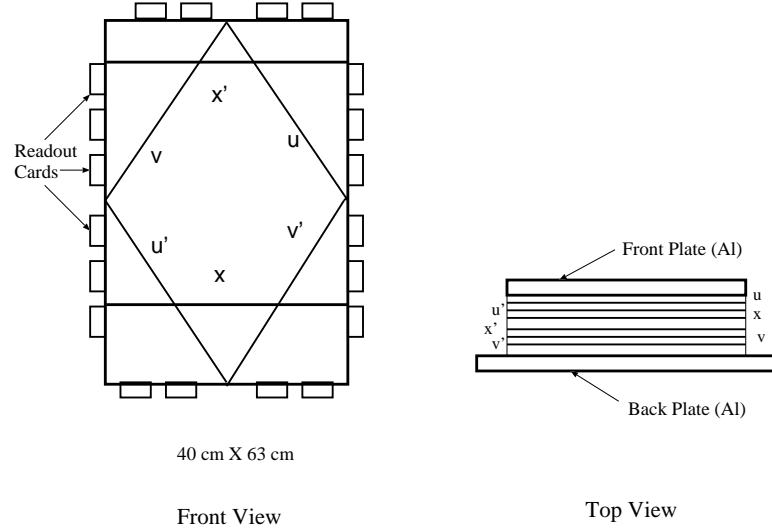


Figure 30: Front and Top Views of the SOS Drift Chambers. The position of the readout cards is shown on the outside of the chamber.

rotated 60° clockwise to the horizontal, x and x' planes measuring the position in the dispersive direction and v and v' planes rotated 60° counterclockwise to the x . There are 64 wires in the x and x' planes, 48 wires in the u , u' , v , and v' planes. The active area of the chambers is 63 cm by 40 cm with cutoffs in the corners.

The SOS used the same gas mixture and gas handling system as the HMS and identical readout electronics. The threshold voltage was set at 1.5 V for the SOS chambers. The final position resolution(σ) per plane for the SOS drift chambers is $200 \mu\text{m}$.

Hodoscopes

The SOS also has two pairs of hodoscope planes, one stacked in the x direction and the other stacked in the y direction. They are identical to the HMS hodoscope planes except for the size and number of elements and the distance between the

pair of planes. In the SOS, the front hodoscope pair is smaller than the back. The front x plane (S1X) has 9 elements, with dimensions 36.5 cm x 7.5 cm x 1.0 cm and the front y plane (S1Y) has 9 elements that are 63.5 cm x 4.5 cm x 1.0 cm. The total active area of the front hodoscope is 63.5 cm x 365 cm. The rear hodoscope planes are larger versions of the front planes. The S2X plane is made of 16 elements, each 36.5 cm x 7.5 cm x 1.0 cm and S2Y has 9 elements, 112.5 cm x 4.5 cm x 1.0 cm. Once again, the widths and lengths of the planes are matched so that the full area (112.5 cm x 36.5 cm) is active. The front and back planes in the SOS are separated by roughly 180 cm.

The scintillators are read out from each end by Phillips 2282 PMTs, and the rest of the readout and the electronics is identical to that of the HMS. The calibration and data acquisition of the SOS hodoscopes are also identical to those of the HMS.

Gas Čerenkov Detector

The SOS gas Čerenkov was designed and built at the University of Colorado. A complete description of the detector can be found in the CEBAF SOS Čerenkov Detector Handbook [55]. The SOS Čerenkov detector is a nearly rectangular aluminum box, 99 cm high, 73.7 cm wide, and 111 cm long. The detector was filled with 1 atmosphere of Freon 12 (CCl_2F_2). The index of refraction for Freon 12 is 1.00108, giving an electron threshold of 11 MeV and a pion threshold of 3 GeV (well above the SOS maximum momentum). The light is reflected onto four photo-tubes by four spherical mirrors. The expected signal is 11 photoelectrons for a relativistic electron. Each photo-tube has a Winston cone (a reflective cone around the photo-tube front face) designed to increase the effective solid angle of the tube. The entrance window is a rectangle, 11" high and 24" wide, with 12"

radius half circles on the top and bottom. The exit window is a 9" by 24" rectangle with 13" radius half circles above and below. Both windows are made of 254 μm Lexan graphics film covered with 50.8 μm Tedlar film. The front window has a total thickness of 39 mg/cm^2 , which is small compared to the thickness of the scintillator material in front of the window and the thickness of the Freon gas (530 mg/cm^2), and therefore does not significantly increase the number of energetic δ -rays that are the dominant contribution to pion misidentification.

The Freon pressure is maintained by the SOS Cerenkov gas handling system. There is a relief valve that opens at 0.5 PSI overpressure, and a solenoid valve that will open to allow freon to flow into the tank at 0.2 PSI underpressure. The solenoid valve is controlled by an Omega pressure meter and a display of the differential pressure is displayed on a monitor in the counting house. Typical pressure variations are at the 0.05 PSID level, corresponding to normal atmospheric pressure changes. The tank is filled by manually opening a release valve at the top of the tank and the freon input valve. The freon valve must be manually adjusted to maintain a pressure of about +0.07 PSID. The tank is filled with approximately 30 lbs of Freon, giving better than 95% purity (for perfect mixing, the final gas purity would be 95%, but since Freon is denser than air and we fill from the bottom, the final purity is higher). The electron detection efficiency for a 2 photo-electron cut is $\sim 98\%$.

Lead Glass Calorimeter

The SOS lead glass calorimeter is identical in design and construction to the HMS calorimeter, except for its size. It was also constructed from 10 cm x 10 cm x 70 cm blocks of TF1 lead glass. The blocks are stacked transverse to the incoming particles, four layers deep. The stack is 11 blocks high in the SOS, for a total of

44 modules and an active area of 110×70 . Just as in the HMS the calorimeter is rotated $\sim 5^\circ$ from the optical axis in order to avoid loss through the cracks between the modules. The electronics and the data acquisition of the SOS calorimeter is identical to that of the HMS calorimeter.

3.5 Detector Electronics

3.5.1 Introduction

The design of the electronics for Hall C was such that the signals from particles traveling at the speed of light in both the spectrometers arrive in the counting house at approximately the same time. This meant that the SOS signals from particles which had a shorter flight path, had to be delayed with cable delays in order to achieve this goal. Once the signals were in the counting house, signals from each of the detectors had dedicated electronic logic units to process them and prepare the inputs for the trigger logic units to generate the pretrigger and trigger signals. These were then passed on to the trigger supervisor which generated the final gates and starts/stops for the ADCs and TDCs of each detector element. The electronic logic for each detector element is described below.

3.5.2 Hodoscope

Each hodoscope plane consisted of 9-16 individual elements; each of which was read out on both sides (the ‘positive’ and ‘negative’ ends). The signals from the tubes were discriminated and the tubes from the positive (and negative) ends were ORed together (e.g. S1X+, S1X-, ...). A hit in a given plane was defined as a coincidence of a hit in one of the positive tubes and a hit in one of the negative tubes, (e.g. S1X = S1X+ OR S1X-). This definition does not require both tubes to be on the same

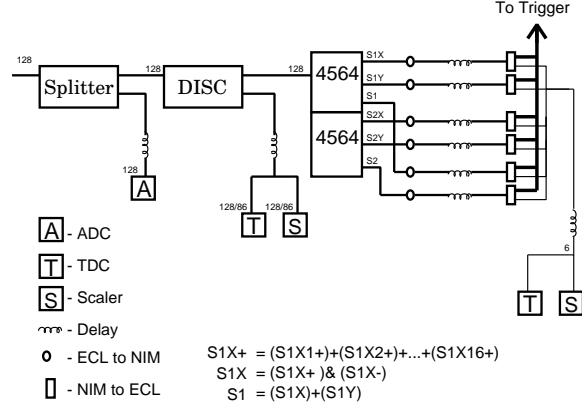


Figure 31: Hodoscope electronics with the number of channels in HMS/SOS

scintillator, but requires much less electronics and did not cause any significant number of random signals. Two scintillator triggers are then formed. ‘STOF’ was defined as the coincidence of one of the front planes and one of the back planes, to give the minimum signals that provides a time of flight measurement in the hodoscopes. ‘SCIN’ required that 3 out of 4 planes fired, and provided a tighter scintillator trigger. The logic diagram is shown in Figure 31.

3.5.3 Shower Counter

The signals from each block of the shower counter were summed to get the total energy deposited in each layer. The sum in the first layer formed the signal PRSUM and the sum of the entire calorimeter gave SHSUM. They were discriminated to give three logic signals PRHI, PRLO and SHLO for the trigger. PRHI and PRLO are high and low thresholds on the energy in the first layer, and SHLO is a cut on the total energy in the calorimeter. Also, the sum of each group of four blocks was sent to scalers for trouble shooting purposes. The electronics diagram of the calorimeter is shown in Figure 32.

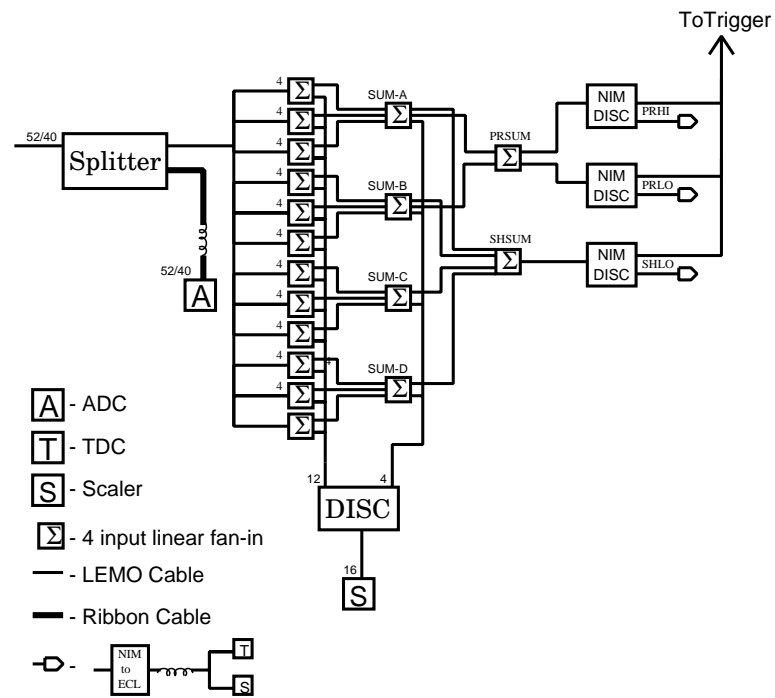


Figure 32: Calorimeter electronics, with the number of channels used in the HMS/SOS.

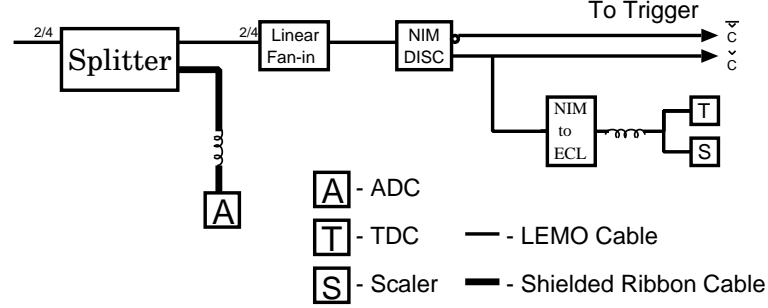


Figure 33: Gas Čerenkov Electronics, with number of channels used in the HMS/SOS.

3.5.4 Čerenkov Counter

The signals from the Čerenkov were summed and used to generate a veto for the trigger. The electronic diagram is shown in Figure 33.

3.5.5 Trigger

The HMS and SOS had separate but identical trigger components. The SCIN signal described earlier formed the basic pretrigger signal. There was an option to clean up the pretrigger with PID signals from the calorimeter and Čerenkov. In case of electrons, the calorimeter and Čerenkov were used to generate ELHI and ELLO, and the final clean electron trigger was an OR of these two called ELREAL. ELHI required a high calorimeter signal (SHLO and PRHI described above), with no cerenkov requirement, while ELLO required a Čerenkov signal, but not a calorimeter signal. In this experiment the PID signals were not used in the trigger since coincidence requirements cleaned up the signals sufficiently. Thus both the HMS and SOS pretriggers were just the SCIN signal which is 3 out of 4 hodoscope planes in coincidence.

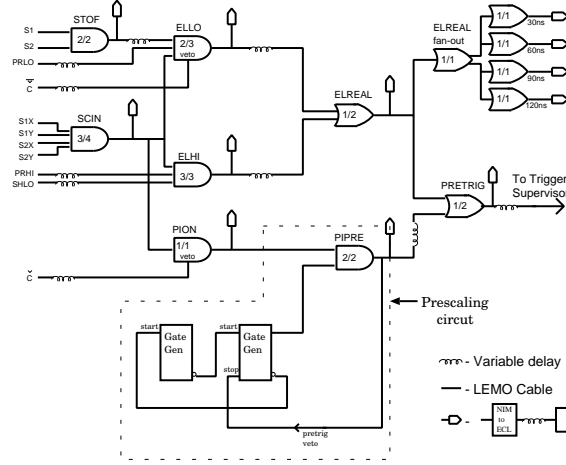


Figure 34: HMS/SOS single arm trigger electronics

There was also a pion trigger to provide the possibility of obtaining a sample of pions in case it was needed to study the pion background. The raw PION signal was defined as a good hodoscope trigger (SCIN) vetoed by the CER signal. This PION trigger was prescaled using a dynamic prescaling circuit. The pion trigger was not used in this experiment. The full trigger logic for the single spectrometer trigger is shown in Figure 34.

The pretriggers are next sent to the 8LM programmable logic(8-Fold logic unit). If the HMS and SOS pretriggers are in coincidence then the 8LM generates a coincidence trigger. After the 8LM the triggers are split, and one copy of the signal is sent to the trigger supervisor (with appropriate delays to ensure that the coincidence triggers reaches the TS before the HMS or SOS trigger), and the other copy is used as the re-timing signals. The re-timing is necessary to ensure that the ADC gates arrive at a fixed time with respect to the time the particle passed thru the detector. The trigger for any given spectrometer comes at a nearly fixed time with respect to the detected particle, but a coincidence trigger has its timing set by

the later of the two spectrometers. For example if the HMS came first, the timing of its ADC gates would be set by the SOS trigger for coincidence events, and the ADC might fail to integrate the signal properly. This is avoided by re-timing the signals with delayed copies of the triggers. These re-timed triggers form the gates and start/stops sent to the various ADCs and TDCs.

3.5.6 Trigger Supervisor

The trigger supervisor (TS) is a piece of electronic hardware build at CEBAF, and was the interface between the trigger hardware and the computer data acquisition. The TS makes all of the decisions about which triggers to respond to as well as determining to what trigger type it belongs. The trigger supervisor determines what hardware needs to be read out based on the trigger type. When a trigger arrives at the TS, it waits $\approx 10\text{ns}$ and then latches all of the enabled trigger types into a data word. It then uses a lookup table to determine what event type the trigger corresponds to and what gates need to be generated. There are four defined event types: HMS, SOS, COIN, and PED events, they correspond to a HMS, a SOS, a coincidence and a pedestal event. The pedestal events were triggers generated by a random signal generator which was used to determine the pedestals of all the ADCs. If multiple triggers come in the 10 ns window, the TS has to decide what kind of trigger it is. For example, if both the HMS and SOS triggers come within 10 ns, the TS treats the event as a coincidence. Normally, this should be very rare because the coincidence window in the 8LM is larger than the 10 ns, so any HMS and SOS overlap in the TS should also form a COIN trigger in the 8LM, and the singles triggers are delayed so that the COIN trigger will always reach the TS first. For PED and COIN triggers, gates go out to all of the fastbus modules, while for the singles triggers, only the appropriate spectrometer

Table 5: 8LM Trigger Logic

output signal	definition
HMS PRETRG	$= (HMS) \& (EN1)$
SOS PRETRG	$= (SOS) \& (EN1)$
COIN PRETRG	$= (COIN) \& (EN1)$
PED PRETRG	$= (PED) \& (GO) \& (\overline{EN1})$
HMS TRIG	$= (HMS) \& (EN1) \& (\overline{BUSY})$
SOS TRIG	$= (SOS) \& (EN1) \& (\overline{BUSY})$
COIN TRIG	$= (COIN) \& (EN1) \& (\overline{BUSY})$
PED TRIG	$= (PED) \& (GO) \& (\overline{EN1}) \& (\overline{BUSY})$

and beamline Fastbus modules receive gates and starts. In order to reduce the event size, the TDCs normally operated in sparsified mode, not giving an output for a channel if there was no stop signal after the common start, and the ADCs were programmed to ignore all channels that have a signal smaller than a threshold value for that channel. To determine this threshold values, the run was divided into two different data acquisition modes. First, a fixed number of events (usually 1000) generated by a random trigger were recorded with the data sparsification disabled. This allowed measurement of the pedestal values for the ADCs. The rest of the run was recorded with sparsification enabled and with real triggers. The data acquisition mode is controlled using the TS status outputs. There are two outputs from the TS that determine the modes. The TS GO signal is active at all times when a run is in progress. The TS EN1 signal indicates that a run is in progress and normal data taking is enabled. Finally, the TS BUSY signal is active whenever the TS is busy processing an event. These control signals were sent to the 8LM logic module along with the trigger signals, HMS, SOS and Pedestal (PED, from a pulser). The programmed logic the 8LM is shown in table 5.

Figure 35 shows the trigger supervisor related electronics.

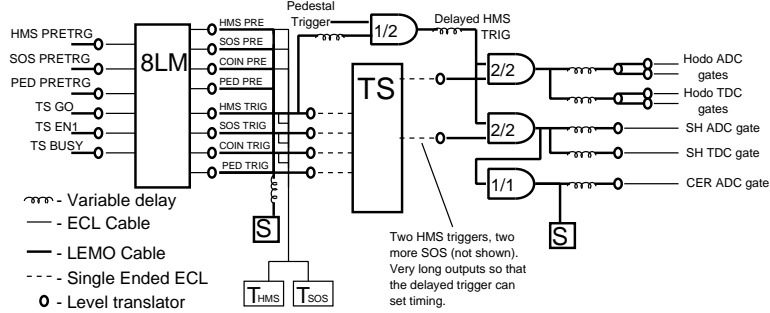


Figure 35: Trigger Supervisor Electronics

The 8LM has eight outputs. Four are used for the HMS, SOS, COIN, and PED pretriggers. A pretrigger is generated for each incoming pretrigger during the appropriate part of the run, even if the TS was busy (i.e. PED pretriggers are passed during the beginning of the run, the physics pretriggers are passed, and coincidence triggers generated, during the normal running). The other four outputs are the HMS, SOS, COIN, and PED triggers. These are identical to the pretriggers except that they also require that the BUSY signal is not on. These triggers are fed directly to the TS. After the TS sends out the gates, each spectrometer retimes the gates it receives with respect to the single arm trigger for that spectrometer, as described in the last subsection. The gates from the TS are then delayed and have their widths fixed so that they are timed properly for use as ADC gates and TDC starts.

3.5.7 Other Diagnostic Signals

All intermediate signals are sent to scalers and TDCs. The TDCs are used mainly as latches, and tell which signals were present when the trigger was taken. The scalers allow diagnosis of certain types of electronics problems in the intermediate

steps of trigger formation. We also use the scalers to measure computer and electronics dead time.

3.6 Data Acquisition

The CEBAF Online Data Acquisition (CODA) system was used for this experiment. This system is the standard data acquisition component of the experimental equipment of Hall C and is described in Reference [56]. The schematic of the system is shown in Figure 36.

CODA provides the user interface and manages the DAQ sub-systems. During data taking CODA handle the triggers from the trigger supervisor (TS) module. Depending on trigger type the event builder (EB) reads data fragments from the fastbus and VME crates also called Readout Controllers (ROCs). The EB reads data from these crates, or ROCs, and adds on the header information into the event word. These event words are then written into the event file. Depending on event type, each event had information from HMS, SOS or both crates. In addition to the spectrometer information, some beam related quantities like beam position, beam loss and beam raster readback values were recorded for each event. Typical event sizes were ~ 500 B/event, which gave a data rate of ~ 1 Megabyte per second for an event rate up to 2 kHz.

3.7 Kinematics

Table 6 lists the kinematic settings of experiment E91-013.

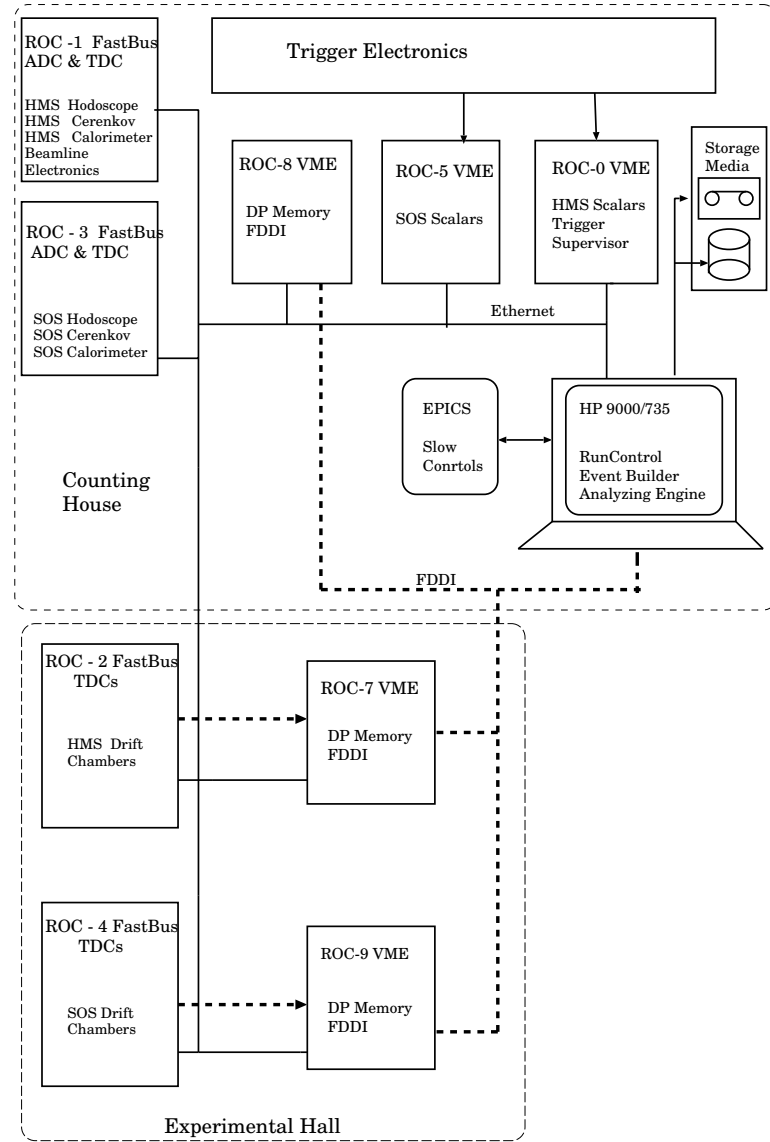


Figure 36: Schematic of the Data Acquisition System in Hall C

Table 6: Table of Kinematics for Experiment E91-013, the central proton angles in bold represent the conjugate angle.

Label	Beam Energy (GeV)	Central electron Energy (GeV/c)	Central electron Angle	Central proton Energy (MeV)	Central proton Angle	Q^2 (GeV/c) ²	ϵ
kine A	2.445	2.075	20.5	350	36.4,39.4 43.4,47.4,51.4 55.4 , 59.4,63.4 67.4,71.4, 75.4	0.64	0.93
kine D	0.845	0.475	78.5	350	27.8 31.8 35.8,39.8, 43.8,47.8	0.64	0.38
kine C	3.245	2.255	28.6	970	32.6,36.6, 40.6 , 44.6,48.6, 52.6	1.82	0.83
kine E	1.645	0.675	80.0	970	22.8 , 26.8,30.8 34.8	1.82	0.31
kine B	2.445	1.725	32.0	700	31.5,35.5 39.5, 43.5 47.5,51.4,55.4	1.28	0.81
kine F	3.245	2.550	50.0	1800	25.5 28.0,30.5	3.31	0.67

Chapter 4

Data Analysis

4.1 Introduction

The offline analysis of the raw data were done using the Hall C analysis software called the Hall C Engine. In this chapter the analysis code is discussed and its major components such as tracking and event reconstruction are elaborated along with calibration and optimization procedures. The analysis also relies on calibration of the detectors, beam and the spectrometers themselves so these topics are also elaborated in this chapter. The physics simulation and the other analysis tools are also discussed.

4.2 Analysis Engine

The flowchart of the analysis code is shown in Figure 37. The engine reads and decodes the detector information, generates tracks and particle identification information for each event and then reconstructs the basic physics quantities for that event. The various detector parameters and calibration parameters are then submitted to the engine as separate input files. The output from the engine are arranged in three forms:

- Report files which contained the hardware and software scalars and the various detector efficiencies.
- A set of histograms, which were used to monitor the detectors and other hardware during the run and also for trouble shooting and testing.
- The event by event information on the tracking, particle identification and the basic physics quantities such as missing energy and momentum. These were written in the Ntuple format of Physics Analysis Workstation (PAW) [57] available from the CERN program library.

Input parameters, software scalars, histograms and tests are handled using the Cebaf Test Package (CTP) [58].

The initialization section defines the various run parameters such as the input and output filenames and the histogram definition files. Some of these files are then read to set various detector parameters that define the locations, calibrations coefficients and other decoding information relevant to the detector elements. After all of the run parameters are defined, the first few events are analyzed. These are initialization type events. These events contain the runtime options and kinematics of the run. Once these initialization events have been analyzed, the engine passes onto the main event loop.

In the main event loop each event is processed according to the event type. For scalar events the relevant scalars are incremented. For physics events, they are analyzed according to trigger type, if the particular trigger type is requested to be analyzed. As described in Section 3.5.5 there are four types of physics triggers. The physics events are passed to the main reconstruction routine for each trigger type, where the event is reconstructed, particle identification information is recorded and the physics quantities are calculated. The event reconstruction is described in

Hall C analysis engine routine flow

CSA 7/95

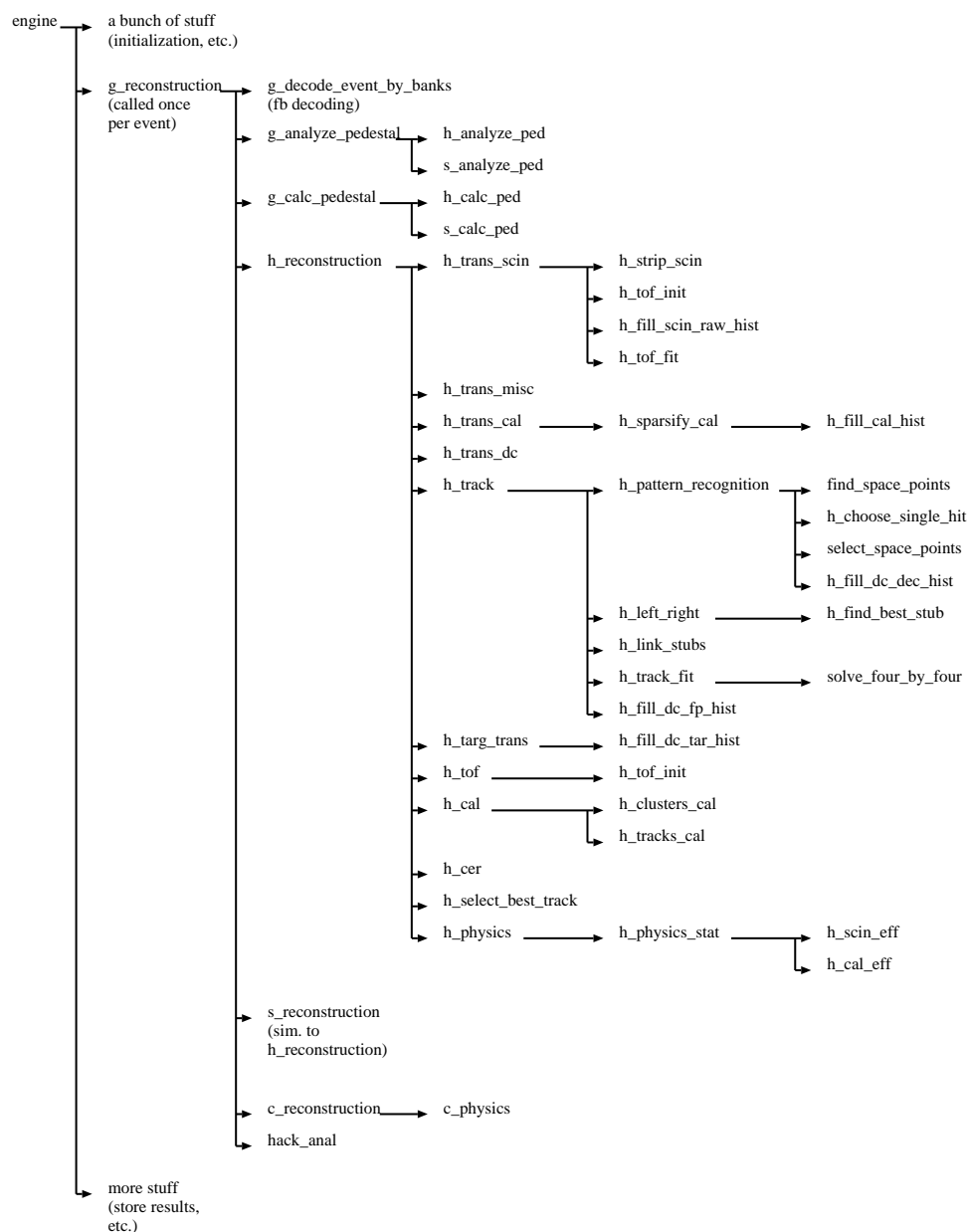


Figure 37: Software Flow Chart for the Hall C Analysis Engine.

the next subsection.

After running through the data file the engine writes the output files. As mentioned earlier these output files consist of scalar report files with the final values for the hardware and software scalers, the histogram files containing detector summary histograms and Ntuple files containing event by event information. An elaborate description of the Hall C engine can be found in Reference [59].

4.2.1 Event Reconstruction

The reconstruction code is split into two sections, one for each spectrometer. The data structures and analysis code are the same for the two spectrometers. Figure 38 shows the flow chart for the HMS reconstruction. The SOS reconstruction is identical.

The hodoscope hits are the first to be decoded. This decoded information is used to determine a preliminary velocity and start time of the particle. The start time is the time when the particle passed through the drift chamber. The start time is used to calculate the distance of the particle trajectory from the wires which recorded the hits. After the hodoscopes have been processed the drift chamber, calorimeter and Cerenkov counter hits are decoded.

After all detector information is decoded, the tracking routine is called. The tracking algorithm and the tracking efficiency is discussed in Section 4.3. Once a track has been determined the position and angles of the track at the spectrometer focal plane (Figure 39) is recorded. Next the time of flight between the front and back planes of the hodoscopes and the energy deposited in the calorimeter for each track is calculated. Finally, each track is reconstructed back to the target to give the momentum, the angle in the dispersive direction and the position and angle in the non-dispersive direction. The reconstruction is done by a Taylor expansion

h_reconstruction (called once per event)

```

h_trans_scin [gets corr scin times, hit pos, start time; calc initial beta, fit beta if enough times]
  h_strip_scin [finds scin w/ real hits (good tdc), converts raw hits to arrays over hits]
    h_tof_init [initializes track-indep qties for tof fit]
    h_fill_scin_raw_hist
    h_tof_fit [fits beta from t and z]
h_trans_misc [fills hms_decoded_misc common block]
h_trans_cal
  h_sparsify_cal [computes energy dep using only cal info]
  h_fill_cal_hist [translates raw drift and start times to decoded info]
h_trans_dc
h_track [finds and fits tracks in fp]
  h_pattern_recognition [gets space points]
    find_space_points [finds points within DC by looking at non-parallel planes]
    h_choose_single_hit [handles case where one sp has multiple hits in one plane]
    select_space_points [keeps sp only if it has good # hits, good # combinations]
    h_fill_dc_dec_hist
  h_left_right [fits stubs to all poss L-R combinations of drift distances]
  h_find_best_stub [fits line to sp's in single chamber (assumes yp = 0?)]
  h_link_stubs [looks at sp stubs and links them into tracks]
  h_track_fit [finds track residuals]
  solve_four_by_four
  h_fill_dc_fp_hist
h_targ_trans [transforms tracks from focal plane to target using polynomial map]
  h_fill_dc_tar_hist
h_tof [finds t, tof, beta w/ ph, vel, and time offset corrections (uses track info)]
  h_tof_fit [fits beta from t and z]
h_cal [computes cal PID qties; corrects energy dep for impact point dependence]
  h_clusters_cal [finds clusters and computes size, pos, and uncorrected energy dep]
h_tracks_cal [matches clusters to dc tracks]
h_select_best_track [selects best track based on chi-sq, dE/dx, Etot, and beta]
h_physics [performs final physics analysis of HMS qties]
  h_physics_stat [calculates statistics and efficiencies]
    h_dc_trk_eff
    h_scin_eff
    h_cal_eff
    h_cer_eff

```

Figure 38: Software Flow Chart for the HMS Event Reconstruction.

in terms of the focal plane position and angles. The coefficients of the Taylor expansion are the reconstruction matrix elements discussed in Section 4.4. All the basic physics quantities are calculated for this final track and also the scalars and histograms are incremented. If there was a final track in both spectrometers and if the event was a coincidence type event the coincidence physics quantities are calculated, and coincidence tests and histograms are incremented.

4.2.2 Cebaf Test Package

The Cebaf Test Package (CTP) software was written at CEBAF to provide a flexible way to store and modify histogram, test, and scalar definitions and other analysis parameters. CTP is modeled loosely on the LAMPF Q system [60]. The CTP shares variables with the Fortran code by registering all shared variables using calls to CTP C subroutines. CTP uses remote procedure calls (RPC) to access these shared variables. In addition, variables that are not part of the engine's Fortran code can be defined and used to create tests and to define histograms. The main use of CTP is to input parameters to the engine, to control the analysis via run time flags and to define the histograms, tests, and scalar reports to be output. The parameters and histogram and test definitions are stored in ASCII files and read in at the beginning of the analysis code. At the end of each event, the CTP tests are evaluated. The histograms and software scalars are incremented using the results of the tests. In addition CTP also allows the user to examine and modify variables when running the event display code. This makes the event display a valuable debugging tool. A detailed description of CTP can be found in Reference [58].

4.3 Tracking

The tracking algorithm [61] is made up of four major steps as listed below:

- Identify space points (collections of hits in a chamber package) in each chamber.
- Resolve left-right ambiguities of hits in drift chambers associated with each space point.
- Link space points from each chamber to a trial track.
- Determine the track position and angles by fitting all hits on a track. Evaluate error matrix and goodness of fit.

The space point is identified for each group of hits in a chamber, by finding the intersection of each pair of hits (omitting pairs of parallel wires). Events with too few or too many hits, (as defined by two user defined parameters) are rejected. Then all combinations of pairs are tested to see if the distances between the intersections are less than a constant called the space point criterion. The minimum number of combinations is a user defined parameter. Next the left-right ambiguity is resolved for each wire in the space point. If all the planes fire, one could resolve the left-right ambiguity using the fact that the pair of planes in each direction are offset with respect to each other. However a more robust method is used which can handle events where some planes are missing. A track is fit to each left-right combination (also called a stub, there are 2^6 stubs per space points) and the fit with the lowest χ^2 is picked. This step in the algorithm is optimized by using the small angle approximation. This approximations uses the fact that wires of each plane are closely spaced (1.0 cm) and there is an offset of half the

Table 7: Parameters used in the tracking algorithm

Parameters	HMS	SOS
Maximum hits per event per chamber	30	30
Minimum hits per event per chamber	5	5
Minimum combinations	6	6
Space point criterion (cm)	1.2	1.2
x Stub criterion (cm)	30	50
y Stub criterion (cm)	10	10
x' Stub criterion (rad)	0.5	0.5
y' Stub criterion (rad)	0.5	0.5

this spacing (0.5 cm) between parallel planes. Hence if there are hits in any two parallel planes the algorithm chooses the left-right combination that makes the particle go between the wires. The small angle approximation is used for all of the SOS planes and the y, y' planes in the HMS. This is done for both the front and the back chambers. The next step consists of fitting a track through each pair of stubs in the front and back chambers. This track gives the trajectory of the particle through the drift chambers in terms of a pair of positions x, y (in the spectrometer coordinate system (Figure 23) and a pair of angles x' and y' in the x and y direction respectively. Here four parameters, one each of the positions and angles, called the stub criteria are used to determine which stubs can be considered to be part of the same track. Finally all the tracks which meet these criteria are recorded. Table 7 lists all the parameters which form an integral part of the tracking algorithm. The values listed in the table were optimized to get the best tracking efficiency for this experiment.

4.3.1 Multiple Tracks

Multiple tracks can occur because there were multiple particles passing through the detectors at the same time or because the tracking algorithm could fit two or more tracks through the same space point. The latter usually occurs if there are “noisy” wires or multiple hits in some planes. In case of multiple tracks for an event, the best track is selected by applying restrictive conditions on the particle velocity and the calorimeter signal. For multiple tracks beyond this point the track with the best χ^2 is selected as the final track. Most of the multiple track events were found to be of the second type (caused by extra hits / noisy wires); however, the fraction of multiple track events is always less than 0.1%.

4.3.2 Tracking Efficiency

Tracking efficiency is a very important correction factor, which is needed for accurate measurement of cross-sections (experimental yields). There are two important components which contribute to the tracking inefficiency: the inefficiency of the detectors (wire-chambers) and the inefficiency of the algorithm used to determine the tracks. In this experiment these inefficiencies were not measured separately. The determination of tracking efficiency involved defining a method to measure the efficiency and also conducting tests to check if this method is a true measure of the tracking efficiency.

The tracking efficiency is measured by using a small region of the triggering hodoscope planes to tag events which should have passed through the wire chambers. Thus the fraction of these events which are tracked by the wire chambers give the tracking efficiency. The variation of the tracking efficiency within a plane was checked by examining the efficiency when different regions of the wire chamber were

illuminated. Two tests were performed to ensure that the method described above is a measure of the tracking efficiency. Using the tracking efficiency as measured above the corrected yields from various runs covering a wide range of kinematics were compared and found to agree within 1%. Secondly the measured tracking efficiency was compared with the expected efficiency using wire chamber plane efficiency. The wire chamber plane efficiencies were determined by using the same small region of the hodoscopes to tag events which must have passed through the wire chambers and then the fraction of these events which fired at least one wire per planes of the chambers gives the plane efficiency. Since the tracking algorithm required at least five planes firing per chamber, the expected probability of finding a track is given by,

$$P = (6P^5 - 5P^6)^2 \quad (77)$$

where P is the plane efficiency. This probability was found to match the measured tracking efficiency to 1%. These two tests tell us that the error involved in tracking is 1%. The typical tracking efficiency for both spectrometers was $> 97\%$.

4.4 Event Reconstruction

As we have already seen, the two wire chambers in each spectrometer are used to determine the trajectory of the particle at the detector plane defined as the plane half way between the two wire chambers perpendicular to the central trajectory (z axis in the spectrometer coordinate system Figure 39). This plane was also defined as the focal plane for this experiment. Usually the focal plane is a surface along which the momentum of the particle determines its position in the dispersive direction. For this experiment the detector plane was called the focal plane. The trajectory of the particle in the focal plane is given in terms of two positions

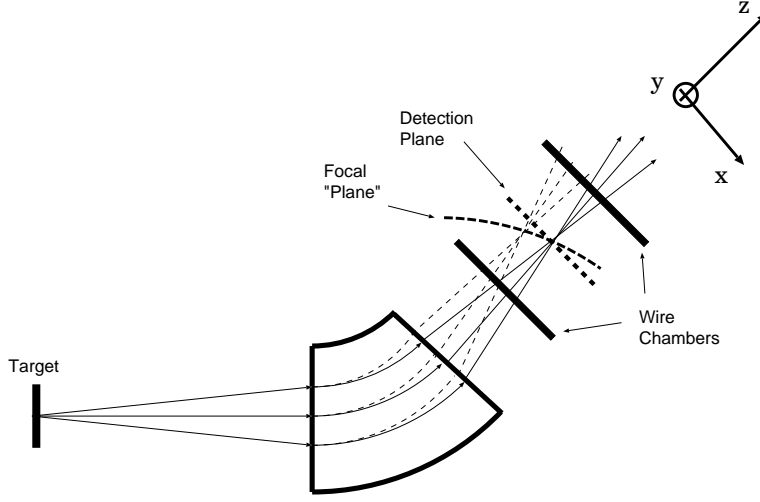


Figure 39: The Focal Plane

$(x_{fp}$ and y_{fp}) and two angles (x'_{fp} and y'_{fp}) as shown in Figure 39. The position angle combination (x_{fp}, x'_{fp}) describes the event track in the dispersive plane of the spectrometer, while the other combination (y_{fp}, y'_{fp}) describes the track in the plane perpendicular to it (scattering plane). Using these focal plane track information one can reconstruct the relative particle momentum $\Delta p/p$ (also called delta), the position and angle in the scattering plane (y_{tar}, y'_{tar}) and the angle in the dispersive plane (x'_{tar} , also called out of plane angle) of the event at the target, relative to the central ray through the spectrometer. The position in the dispersive direction (x_{tar}) cannot be reconstructed since it was used as an assumption in the momentum reconstruction.

The reconstruction of the position, angle and the relative momentum is carried out by a Taylor expansion (in the focal-plane coordinates) of the solutions of the equation of motion of charged particles in the magnetic fields of the spectrometer. The particle transport from the focal-plane to the target can be expressed in the matrix formalism of Penner [62]. The target quantities labeled *tar* can be expressed

in terms of the focal-plane coordinates labeled fp and the transfer coefficients or matrix-elements M_{jklm} .

$$q_{tar}^i = \sum_{jklm} M_{jklm}^i (x_{fp})^j (x'_{fp})^k (y_{fp})^l (y'_{fp})^m, \quad (78)$$

where $q_{tar}^{1,2,3,4}$ corresponds to x'_{tar} , y_{tar} , y'_{tar} and $\Delta p/p$ respectively.

$$M_{jklm}^i = \langle q_{tar}^i | x_{fp}^j x_{fp}'^k y_{fp}^l y_{fp}'^m \rangle. \quad (79)$$

The symmetry about the center of the focal plane (mid-plane symmetry) imposes certain restrictions on these transfer coefficients M_{jklm} . The target coordinates in the dispersive plane ($\Delta p/p$ and x'_{tar}) can have combinations of the focal plane coordinates $(y_{fp})^l$ and $(y'_{fp})^m$ only for even powers of $l + m$, while the target quantities calculated in the scattering plane can have combinations of the focal plane quantities $(x_{fp})^j (x'_{fp})^k$ only for even powers of $j + k$. The coefficients for the rest of the combinations are usually zero and are called forbidden coefficients. The reconstruction coefficients for each spectrometer was determined using the COSY INFINITY [53] program which was used to model magnetic components of the spectrometer. However, since these models did not have the exact field value at each point in these massive spectrometers and due to inhomogeneities in the magnetic fields of the spectrometers, the calculated transfer coefficients were not optimal, and hence do not describe the optical properties of the spectrometer precisely. It has been shown by Loffler *et al.* [63] that the optical properties of a spectrometer can be best determined by experiments where rays of particles are traced over the full solid angle acceptance. Hence solid angle defining slits, the so called sieve slits introduced in Section 3.4, were used in both spectrometers to study the optical properties of the spectrometer. The sieve slits (shown in Figure 40) allow us to populate the large acceptance of the spectrometer simultaneously with

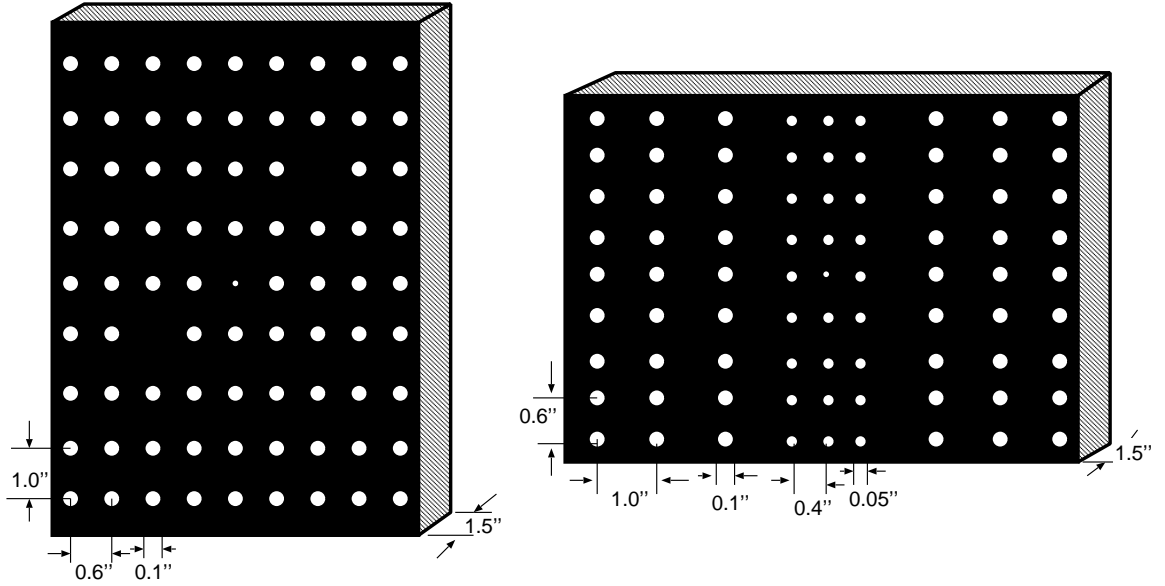


Figure 40: The Hms and the SOS sieve slits

many pencil beams thus enabling us to study variation in the optical properties of the spectrometer over the full acceptance. The experimental procedure and the procedure to optimize the transfer coefficients are described next.

4.4.1 Experimental Procedure

A beam of 845 MeV electrons was incident on a ^{12}C target with the spectrometers parked at $\approx 29^\circ$. The scattered electrons were detected in both spectrometers. A series of runs were taken, each with the central momentum of the spectrometer aligned to position the elastic peak at different location in the $\pm 10\%$ ($\pm 20\%$) of the HMS (SOS) momentum acceptance in steps of 2% (2.5%). This is called a delta scan. Such a scan was also repeated with sieve slits in place in the spectrometer. These data were used to optimize the $\Delta p/p$ transfer coefficients. The delta scan was also repeated with an incident beam of 1645 MeV, to check the reproducibility of the matrix elements.

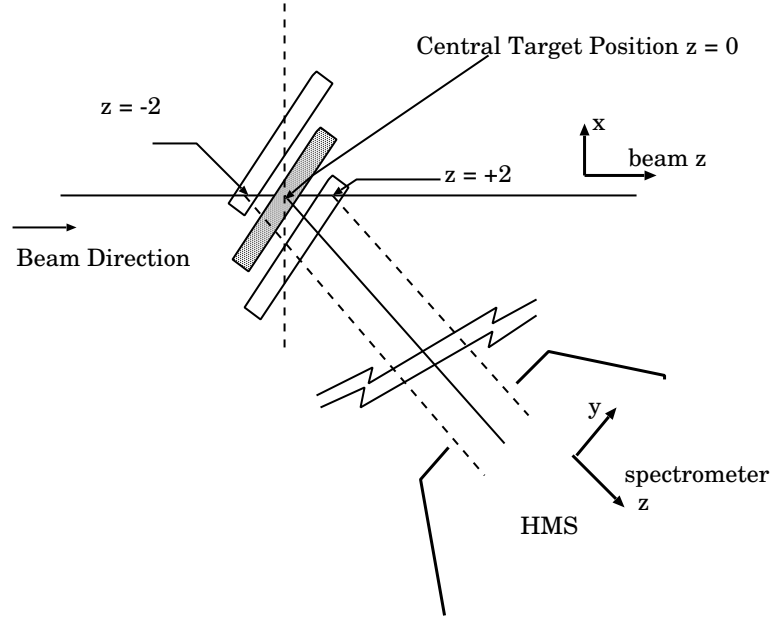


Figure 41: A schematic of the slanted target arrangement. The break in the picture indicates that the upper half is a side view while the lower half is a top view.

In another experiment a beam of 845 MeV electrons was incident on a ^{12}C slanted target. The slanted target helps us scan the y_{tar} acceptance of the spectrometers by raising and lowering the slanted target in the vertical direction, in steps of 1.0 (0.5) cm for the HMS (SOS), as shown in Figure 41. This ensures that the beam intercepts the target at different position along the beam direction (z axis). The central momentum of the spectrometer was set for the electron excitation of the Delta resonance so that the entire momentum acceptance of the spectrometer was approximately uniformly illuminated. All data were collected with the sieve slits in place. These data were used to optimize the y_{tar} , x'_{tar} and y'_{tar} matrix elements. Once again data were also taken at 1645 MeV to check the reproducibility of the matrix elements.

4.4.2 Optimization Procedure

The code (Hall) C Matrix-element Optimization Package, CMOP [64] was developed to process the experimental data described above and obtain an optimal set of matrix elements which would give the best resolution in all the reconstructed quantities. The optimization philosophy is to start with a set of matrix elements generated by modeling the magnetic fields in the spectrometer using COSY [53]. For each event from the experiments described above in Section 4.4.1, the focal plane quantities are mapped to target using the COSY generated matrix elements. This process gives us the first approximation to the target quantities $\Delta p/p$, x'_{tar} , y_{tar} and y'_{tar} . From the target, each event is then mapped to the sieve slits by drifting them through the space between the target and the spectrometer entrance. Now one can determine the sieve slit hole closest to the path of the particle and since the absolute position of each sieve slit hole is known this leads to a geometrical determination of the angles and y position of the particle trajectory at the target. These geometrically determined angles and positions are compared to the reconstructed angles and positions. The square of the difference between the reconstructed and the geometrical quantities are calculated and a subset of the data for which this difference squared passes certain tests (eg. radii of the holes) are retained, which is then fit via the singular value decomposition method (SDV) [65].

The SDV method involves decomposing the design matrix to expose any possible singularities. Once the singularities have been edited out of the fit, new matrix elements are obtained by Gaussian backward substitutions [65]. The equations that are solved or minimized to generate the new matrix elements can be written compactly as follow [66]:

$$\Sigma a_{i,j,k,l}(x - x_0)_{fp}^i (y - y_0)_{fp}^j (x' - x'_0)_{fp}^k (y' - y'_0)_{fp}^l - qtar = 0. \quad (80)$$

where $a_{i,j,k,l}$ are the elements of design matrix, $x_{fp}, y_{fp}, x'_{fp}, y'_{fp}$ are the focal plane quantities, $x_{0fp}, y_{0fp}, x'_{0fp}, y'_{0fp}$ are the offsets at the focal plane, and $qtar$ is one of the target variables ($y_{tar}, x'_{tar}, y'_{tar}, \delta$). Equation 80 is written down for each event. For N events if the number of parameters being varied is M , such that $N - M > 0$, the problem is over-determined. Once the new parameters are obtained, the data is mapped again from the focal plane to the target and this procedure is iterated till the desired resolutions are achieved. The standard convergence condition used is,

$$\left(\frac{|{}^r\chi_i^2 - {}^r\chi_{(i-1)}^2|}{{}^r\chi_{(i-1)}^2} < 0.0075 \right) \text{ and } (N_i - N_{(i-1)} < 0). \quad (81)$$

Where

$${}^r\chi_i^2 = \frac{\chi^2}{D.F.}, \quad (82)$$

i is the number of iterations and N_i is the number of events that are accepted for the fit in the i th iteration. The typical uncertainty in the focal plane quantities is used as weight. Usually one starts with the tests set to larger than the actual radii of the holes and in subsequent iterations the tests are reduced to values corresponding to the radii of the holes. While fitting the y_{tar} and δ matrix elements the reconstructed y_{tar} and δ are compared with the spectrometer set values for the corresponding slanted target run and the delta scan run, respectively. The set value of y_{tar} is given by,

$$Z = d \times \tan(\theta_i), \quad y_{tar} = Z \times \sin(\theta_s). \quad (83)$$

Where d is the vertical translation of the slanted target (refer to Figure 41) while Z is the position along the beam direction, θ_i is the inclination of the slanted target and θ_s is the spectrometer central scattering angle. Similarly the set value of δ is

given by $\delta = \frac{(p-p_0)}{p_0}$, where p_0 is the central momentum setting of the spectrometer and p is the momentum of the scattered particle given by,

$$p = \frac{1}{\eta} \left[E_0 - \frac{E_l}{2} - E_e \left(1 + \frac{E_e}{M} \right) \right] - \frac{E_l}{2}, \quad (84)$$

where the recoil factor η is given by

$$\eta = 1 + \frac{(2E_0 - E_l) \sin^2(\theta_0/2)}{M}. \quad (85)$$

Here M is the target mass, E_0 the beam energy, E_e is the excitation energy ($E_e = 0$ for elastic scattering), E_l is the mean energy loss due to Landau straggling in the target and θ_0 scattering angle.

Along with the four reconstructed target quantities the offsets at the focal planes are also fitted (these are the zeroth order matrix elements). In the HMS the matrix elements up to 5th order were optimized while for the SOS they were optimized up to 6th order. Figures 42 and 43 show the results of optimization procedure for the SOS.

During the optimization it was found that the best results were obtained when some of the forbidden matrix elements were allowed to be non-zero. This was later attributed to the HMS quadrapole coils being rotated with respect to each other by ≈ 1 -2 mrad.

4.5 Spectrometer and Beam Energy Calibrations

4.5.1 Beam Energy

A precise measurement of the beam energy is an essential requirement for many experiments at CEBAF. The standard practice has been to measure the fields required to bend the beam, as it traverses the set of bending magnets in the HALL

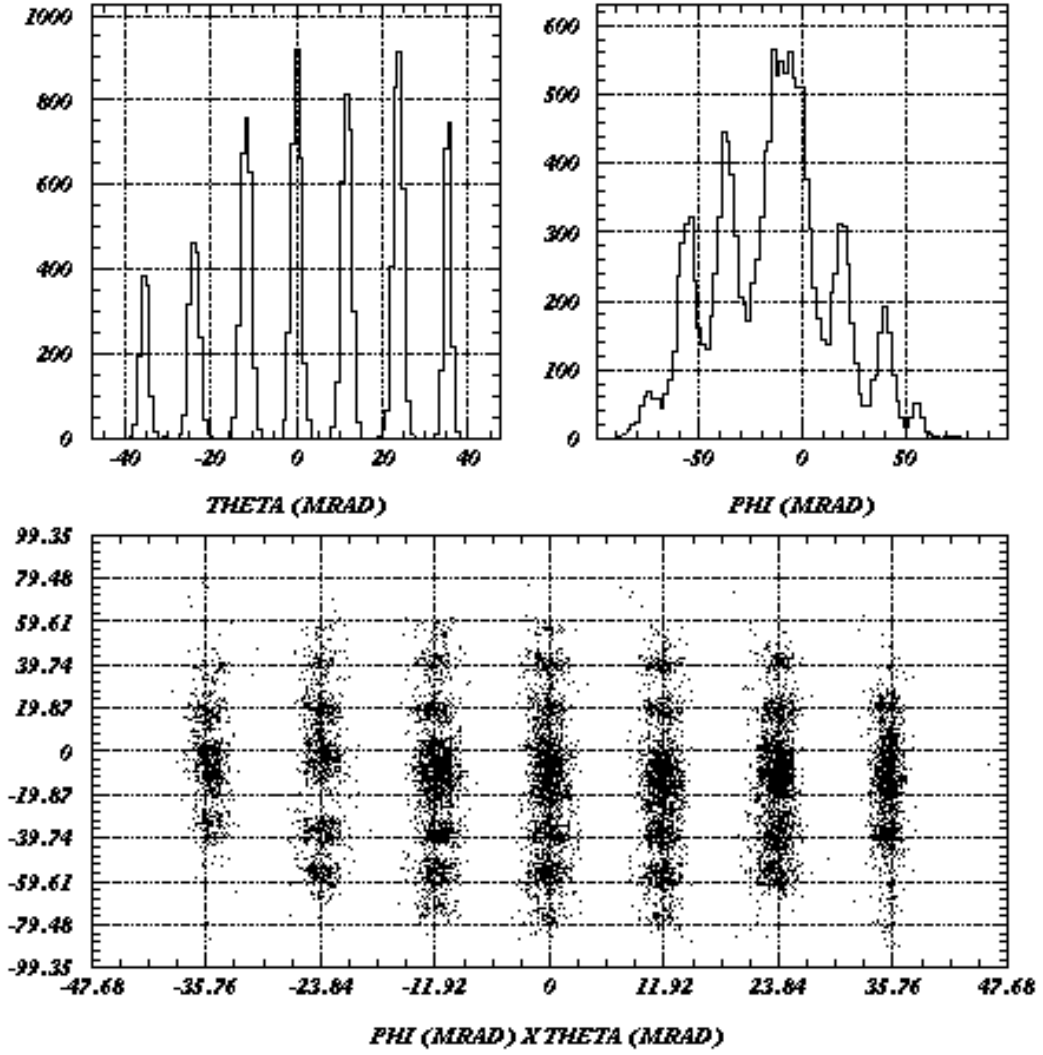


Figure 42: Optimized reconstruction of the angles x'_{tar} and y'_{tar} for the SOS

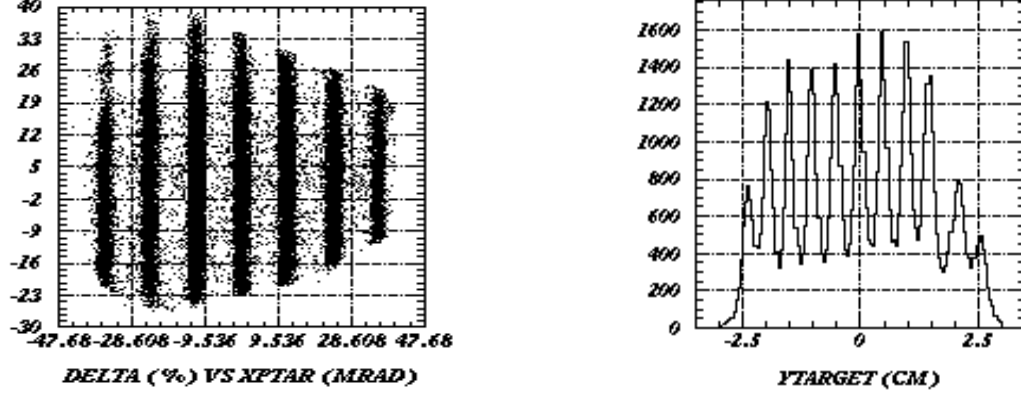


Figure 43: Optimized y_{tar} reconstruction for the SOS.

C Arc. From such a measurement one can then calculate the beam energy. This method is dependent on the absolute knowledge of $\int Bdl$, which is difficult to measure and maintain to high precision. Hence one must have additional checks to ensure a higher degree of reliability. In this section three such schemes for determining the beam energy using just kinematic information from the data are described.

Differential Recoil Method

Energy determination using the method of differential recoil relies on the fact that the difference in recoil energies, for (in)elastic scattering between "heavy" and "light" masses is a function of the beam energy. By measuring this differential recoil energy in a composite target we can calculate the incident beam energy. The recoil energy is,

$$E_{recoil} = \frac{q^2}{2M} \approx \frac{2E^2}{M} \sin^2\left(\frac{\theta}{2}\right). \quad (86)$$

Hence for a composite target the differential recoil energy is,

$$\Delta E_{recoil} = 2E^2 \sin^2\left(\frac{\theta}{2}\right) \left(\frac{1}{M_1} - \frac{1}{M_2}\right). \quad (87)$$

In addition the position, x_{fp} along the focal plane is a function of the energy of the detected electron and it can be written in terms of a polynomial known as the dispersion polynomial,

$$E_f = \Gamma B(1 + d_o + d_1(x - x_c) + d_2(x - x_c)^2 + \dots). \quad (88)$$

Where Γ is the conversion factor (in MeV/Tesla) between the magnetic field B of the spectrometer and the energy of the particles along the central trajectory, d_j is the spectrometer dispersion coefficients and x_c is the position of the central ray. For each peak in the spectrum of a certain target, the energy E_f is expressed in terms of the excitation energy of that state and the incident beam energy E_o . It is written as,

$$E_f = \frac{1}{\eta} \left[E_o - \frac{E_{loss}}{2} - E_x \left(1 + \frac{E_x}{2M} \right) \right] - \frac{E_{loss}}{2}. \quad (89)$$

Where M is the mass of the target, η is the recoil factor as defined by Eq. 85. E_{loss} is the mean energy loss due to ionization in the target given by,

$$E_{loss} = c_1 \frac{Z}{A} t \left[\ln\left(\frac{c_2 t}{\rho}\right) \right]. \quad (90)$$

Where 't' is the effective thickness of the target and ρ is the target density. The parameters E_o , Γ and the coefficients d_j are determined simultaneously by using the two equations in a least squares fit to the energy calibration data. One pass beam was used to perform delta scans on a carbon and a BeO target. The carbon data were used for calibrating the focal plane. The position of the 4.4 MeV excited

state of C was measured at the focal plane. The measurements were repeated for runs ranging from $\delta = -5\%$ to $\delta = +5\%$. These focal plane positions were then used to obtain the dispersion parameters, d_o, d_1 and d_2 , which are related to δ as follows,

$$\delta = d_o + d_1 * (X_{fp} - X_{offset}) + d_2 * (X_{fp} - X_{offset})^2. \quad (91)$$

These parameters were determined by fitting the data to the equation: $E_f = \Gamma * B * (1 + \delta)$, where Γ is a constant and B is the magnetic field, and E_f is the energy of the scattered electron. These parameters were used to obtain the focal plane positions of the oxygen ground state and the first excited state of Be (2.49 MeV) from the delta scan on the BeO target. The focal plane positions gave the recoil energies which were used to obtain the beam energy. The different sources of uncertainty and their contribution to the total uncertainty is listed in Table 8

Diffraction Minima Method

This method involves a measurement of the cross sections of the carbon ground state and the first excited state at the dispersive minima. A plot of the ratios of these two cross sections (ground state to first excited state of carbon) is shown in Figure 44. This reaction is calculated to have a diffractive minimum at $q^2 = 0.129 \text{ GeV}^2$ [67]. For a beam energy of about 845 MeV this would lie at a scattering angle of about $\theta_{scatt} = 24.8$. By determining the angle where the minima occurs we can calculate the energy using,

$$q^2 = -4EE' \sin^2 \theta, \quad \text{where} \quad (92)$$

$$E' = E / (1 + 2E \sin^2 \theta / M) \quad (93)$$

Table 8: Beam energy uncertainties for the differential recoil method. The nominal beam energy is 845 MeV

Sources	Error	ΔE
Uncertainty in the determination of peak centroid	0.05 cm	1.30 MeV
Focal plane calibration error	10^{-3}	0.70 MeV
Uncertainty in scattering angle measurement	1 mrad	0.25 MeV

The uncertainties in this method arise from the errors in the measurement of the scattering angle. Additional sources of error are due to inaccuracies in the determination of the ratio of σ_{0+} to σ_{2+} .

Data were taken at angles close to the diffractive minima at 24.85° , using one pass beam (845 MeV) on a carbon target. The counts in the elastic as well as the first excited state of carbon were plotted as a function of the scattering angle. The ratio of the counts in these two states was also determined as a function of the scattering angle. The cross section of these two states were calculated theoretically for scattering angles ranging from 23.0 to 26.0° for a beam energy of 845 MeV, using MEFCAL [68] for the ground state and FOUBES [69] for the excited state. The ratio of the theoretical cross sections were then fitted to the measured ratio to determine the minima. Figure 44 shows the counts in the elastic and the first

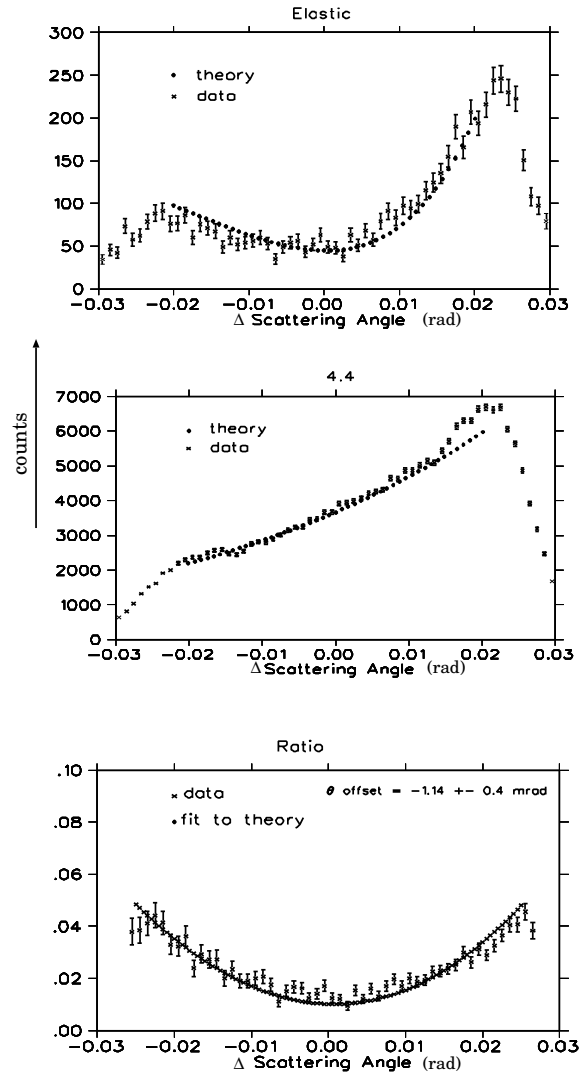


Figure 44: The counts in the elastic (top panel) and first excited state (middle panel) and their ratio (bottom panel) as a function of difference in the scattering angle. The solid lines are fits to the data.

Table 9: Uncertainties in the beam energy determination using the diffractive minima method. The nominal beam energy is 845 MeV.

Sources	Error	ΔE
Minima fitting error	0.40 mrad	0.76 MeV
Systematic error in scattering angle reconstruction	0.60 mrad	0.38 MeV
Systematic error in survey measurement of collimator position	0.40 mrad	0.30 MeV

excited state and their ratio. The various sources of error and their contribution are listed in Table 9.

Beam Energy from $H(e,e'p)$

Beam energy can also be determined from elastic scattering of electrons from protons. If we know the momentum and the angle of either the scattered electron or the scattered proton, we can reconstruct the energy of the incident beam of electrons from this information. This method has the advantage that it can be used at all beam energies unlike the first two methods which can be used only at one and two pass energies. But it has the disadvantage of being the most inaccurate of the three methods discussed. This is because the resolution and systematic errors of both the spectrometers have to be folded into this type of measurement. The uncertainties of this method are listed in Table 10. The uncertainties were determined by varying the the listed parameters and calculating its effect on the

Table 10: Uncertainties in beam energy determination using $H(e, e'p)$

Sources	Error	ΔE
HMS momentum error	10^{-3}	1.5 MeV
SOS momentum error	1.5×10^{-3}	2.0 MeV
HMS scattering angle error	1 mrad	2.5 MeV
SOS scattering angle error	3 mrad	+3.0 -3.5 MeV

beam energy.

The results from the various methods have been listed in Table 11.

4.5.2 Spectrometer Momentum

Measurements of cross-sections require a very accurate determination of the central momentum of the spectrometer. The momentum calibration depends on a accurate knowledge of the beam energy and scattering angle. The momentum calibration of the two spectrometers has an accuracy of $\approx \pm 0.15\%$.

The central momentum of the spectrometers were calibrated using elastic $H(e, e')$ data at the same energy but different angles and elastic $H(e, e'p)$ data at several energies. Here we use the fact that elastic (e, e') and $(e, e'p)$ kinematics are over determined so the measured momentum of the spectrometer can be checked against momentum determined from the elastic scattering angle. Using the $(e, e'p)$ data it

Table 11: Beam energy measurements

Nominal	Method	Energy	Error
845.0	Differential Recoil method	844.7 MeV	1.5 MeV
845.0	Diffractive Minima method (first run)	844.7 MeV	0.9 MeV
845.0	Diffractive Minima method (second run)	845.1 MeV	0.9 MeV
2445.0	Elastic H(e,e'p)	2444.9 MeV	5.0 MeV

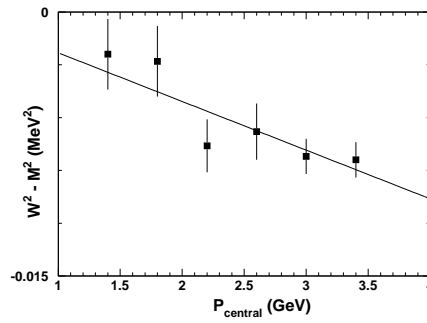


Figure 45: Difference in the reconstructed and expected invariant mass as a function of central momentum, for the HMS

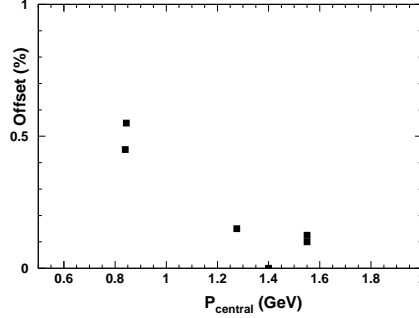


Figure 46: Difference between expected and the measured central momentum of the SOS.

was found that the HMS central momentum was 0.9% lower than that predicted by the model of the spectrometer. This was corrected before the elastic $H(e, e')$ data were collected. The (e, e') data found an offset in the central momentum of the order of $\approx 0.15\%$, which is consistent with the offsets in the reconstructed $\delta \left(\frac{p_0 - p}{p_0} \right)$ found from the $(e, e'p)$ data. Figure 45 shows the difference between the reconstructed and expected invariant mass as a function of central momentum, obtained from the (e, e') data at a beam energy of 4.045 GeV. The fit to this data, assuming fixed offsets in beam energy and reconstructed δ , gives an offset of 0.15% in δ and no offset in the beam energy.

For the SOS the central momentum differed from the model by up to 0.55% as determined using $H(e, e'p)$ data, although, this difference varied with momentum and was about 0.1-0.15 % at most kinematics. The difference between the expected and the measured central momentum for the SOS is shown in Figure 46.

It was also noticed that in the HMS the vertical position of the focal point (defined as the waist of the hour-glass like x_{fp} vs y_{fp} plot) varied with momentum. This variation is shown in Figure 47, however careful studies showed that this

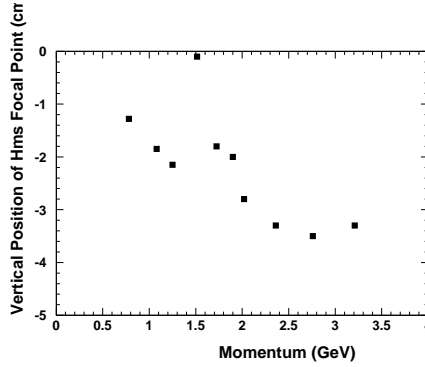


Figure 47: HMS focal point variation with momentum

variation had negligible effect on the reconstruction of the angles and momenta of the spectrometer.

4.5.3 Spectrometer Angles

Measurements of cross-section require a very accurate determination of the scattering angle. The calibration of the angles of the spectrometers rely on accurate optical surveys of the spectrometer, beamline and target positions. The scattering angle of the spectrometer is determined from surveyed markings on the floor of the hall. These markings are accurate to better than 2 mm and thus gives rise to uncertainties of the order of 0.1 mrad in the HMS and 0.3 mrad in the SOS. However, most of the uncertainties come from magnet motion as the scattering angle is varied. The motion of the magnets was studied by optical surveys of the magnet positions at several angles. The scattering angle of the spectrometer can also be determined using sieve slit data, which also relies on careful pointing survey (described below) of the spectrometer.

The positions of the target, scattering chamber, collimators and sieve slits, magnets and the detectors were surveyed before and after the experiment.

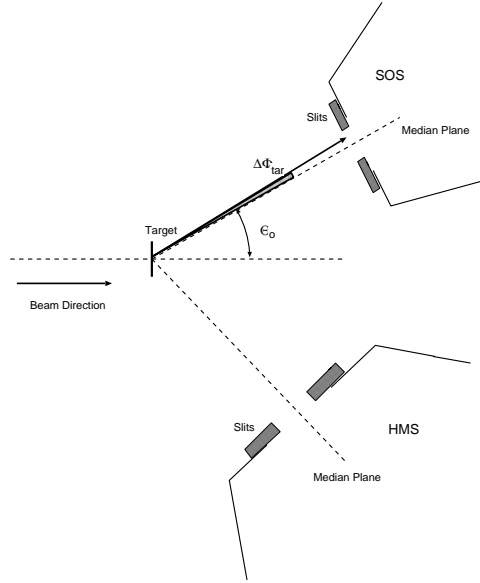


Figure 48: HMS and SOS Scattering Plane, the symbols defined here are used in Table. 12

The position of the central axis (Figure 48) of the two spectrometers is surveyed with the spectrometers parked at several angles. These surveys are then used to check if straight lines drawn from the spectrometers cross at the center of the target. These kind of surveys are called pointing surveys. The pointing survey was done at several angles to determine the relative motion between the magnets when the spectrometers are rotated and also the level of the rails on which the spectrometers move. In addition the height of the rails at these angles are also surveyed. Optical survey measurements had an accuracy of about $150\text{-}200\ \mu\text{ m}$. The pointing survey determined that the HMS mispointed to the right of the target by up to 1.9 mm horizontally at certain angles and up to 1.5 mm vertically. The mispointing as function of spectrometer angle is shown in Figure 49. The SOS pointing survey found that the SOS mispoints to the left by up to 4.0 mm at certain angles but it mispoints by 2.0 mm on the average. The SOS also mispoints

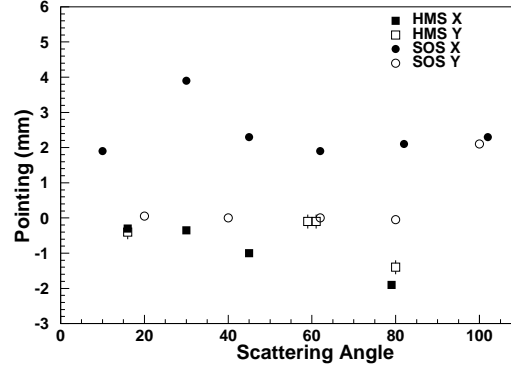


Figure 49: HMS and SOS mispointing, deviation from the ideal triple intersection point (two spectrometers central axis and the target center) as determined during a pointing survey.

by 2.0 mm vertically at certain angles but on the average there was no vertical mispointing. The results of the pointing survey along with the surveyed position of the sieve slit relative to the median plane of the spectrometer was used during optimization of the spectrometer transfer coefficients (matrix elements) described in Section 4.4. This ensures that the reconstructed scattering angle includes most of the magnet motion and other variations in the spectrometer position.

It was also found that the magnets in the spectrometer themselves had certain displacement from their nominal positions which varied with the angle of the spectrometer. The displacement of the magnets as a function of the angle is shown in Figure 50.

Survey of the rails on which the spectrometers rotate found that the SOS rails were displaced from the level up to 1.5 mm at certain angles this changes the out-of-plane angle by about 0.15 mrad. The HMS rail surveys and the magnet motion information was combined to generate a model for the offsets as a function of the

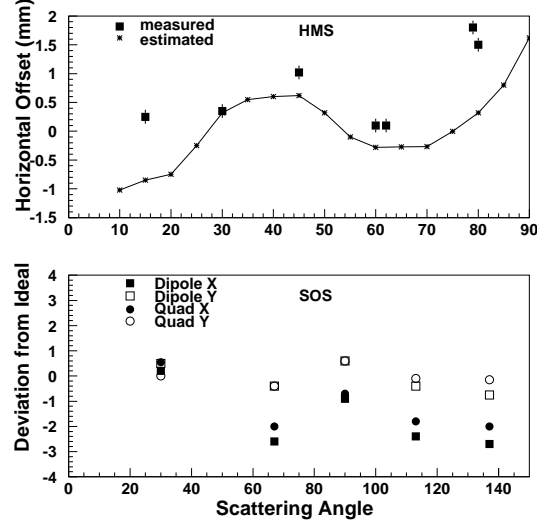


Figure 50: HMS and SOS magnet motion, offsets in the magnet positions as a function of scattering angle

spectrometer angle and the model along with the measured offsets are shown in Figure 50.

It is also known from these surveys that the SOS is -0.15 degrees out of plane with respect to plane made by the HMS and the target center.

From all the survey results it is estimated that the magnet positions for the HMS were stable to about 1.0 mm (2.0 mm for the SOS). Using all the survey information along with the data taken with a sieve slit and a slanted target (which allows the position in z where the beam hits the target to be varied, described in Section 4.4) one can determine the central scattering angle with an uncertainty of 1.0 mrad (1.5 mrad for the SOS). The experimental procedure with the sieve slit and slanted target is described in 4.4. Table 12, shows the various sources of uncertainty in the determination of the the scattering angle in the two spectrometers.

Table 12: Uncertainty in the Scattering Angle of HMS and SOS

Error in	Optical Survey [mrad]	Sieve-Slit Determined [mrad]
spectrometer median plane	0.2	-
sieve-slit position	0.4	-
central scattering angle Θ_o (<i>Figure 48</i>)	0.1 (0.3 for SOS)	1.0 (1.5 for SOS)
scattering angle $\Delta\Phi_{tg}$ relative to Θ_o	-	< 1.0 (3.0 for SOS)

4.5.4 Spectrometer Resolutions

The resolution of the two spectrometers was checked over the full momentum bite of the spectrometer by scanning the elastic peak of a ^{12}C target over the full momentum bite of the spectrometer (δ scan with the ^{12}C peak). The elastic peak in the reconstructed momentum spectrum was fitted to a Gaussian. Figure 51 shows the standard deviation of these fits as a function of the reconstructed δ ($\frac{p-p_0}{p_0}$) for each spectrometer. This shows that the resolution of the spectrometers were stable over the momentum bite used in this experiment. The average HMS resolution is about 0.2 % and the average SOS resolution is about 0.15 %.

4.6 Detector Calibrations

A sequence of calibrations had to be performed in order to match the timing of the individual scintillator elements and to match the gains of the calorimeter and Cerenkov signals. The Cerenkov counters were calibrated by calculating the gains for each PMT by determining the single photo-electron peaks from the pedestal subtracted ADC signals from each channel (4 in SOS/ 2 in HMS). The hodoscope and the calorimeter calibration involved fitting to event information from high

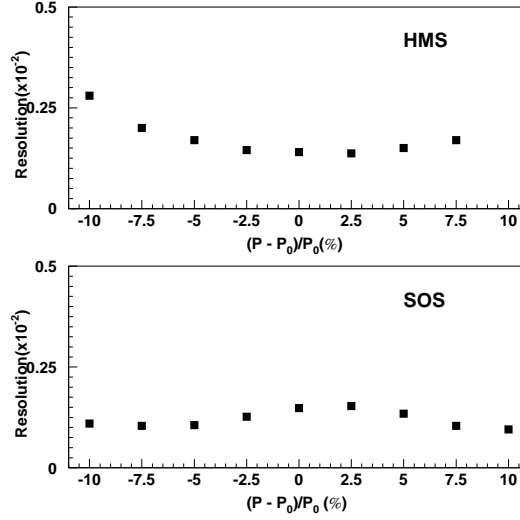


Figure 51: HMS and SOS resolution as determined for 840 MeV electrons.

statistics runs, taken for this purpose, where large regions of the detector were illuminated.

4.6.1 Hodoscope Timing Corrections

There are several corrections in going from the TDC value of an event to the time of the event. The scintillators used in the hodoscope had a mean time resolution of ~ 70 -100 ps (in bench tests), and so all timing corrections had to be carefully fit to achieve a final resolution close to this limit. The TDC scale (ps/channel) was determined using a Time Interval Generator and also checked using the RF signal (499 MHz) from the accelerator. The time variation due to changes in the TDC scale over the range of TDC values, was of the order of ± 25 ps which is better than the intrinsic resolution of the scintillators.

The second major correction is the pulse height correction. The timing signal

comes from a fixed threshold discriminator; the exact time at which the threshold is exceeded relative to the peak time depends on the height of the signal. Thus, large signals will fire the discriminator earlier than small signals and corrections for this effect are called pulse height corrections. These corrections are typically hundreds of picoseconds and have a significant effect on the resolution of the detector. The pulse height corrections are fitted by taking crossed pairs of scintillators (to limit the region of the scintillator that is hit) and then comparing their mean times (each element is read out by a PMT on each end). Using the mean time eliminates the dependence on position along the scintillator and leaves only the pulse height walk correction and an overall offset. By applying a trial correction to the pulse height walk in three of the four PMTs, the remaining dependence on the ADC value gives the form of the pulse height variations in the uncorrected tubes. We use a correction of the form,

$$\Delta t = PHC * \sqrt{\max(0, (ADC/PHOFF - 1))} + t_0 \quad (94)$$

where ADC is the raw ADC value, and PHC, PHOFF are the timing correction parameters, and t_0 is an arbitrary offset between the two scintillators.

Other corrections include the variation in the propagation time for the signal to travel from the point where the scintillator was hit to the PMTs, and overall timing offsets between the individual signals. Once the pulse height correction is known, the velocity of light propagation along the scintillator element can be measured by taking the difference in times of PMTs on the opposite ends of an element. This velocity is the average velocity for the signal to reach the PMT which accounts for the fact that most of the light does not go directly towards the PMT but reflects off the sides of the scintillator. The velocity correction therefore depends on both the index of refraction and the geometry of the scintillator. A

velocity was measured for each plane, and all elements in that plane used this average correction. Finally, each tube has its own offset due to variations in cable length or different response times of the PMTs. These are fit in the same way as the pulse height corrections. The mean time is generated for a pair of scintillators, with velocity and pulse height walk corrections included. The offsets are adjusted in order to make the time between the scintillator hits agree with the velocity of the particle determined using the measured momentum and known masses of the particles.

4.6.2 Lead Glass Calorimeter Calibrations

Attenuation in the lead glass gives a variation of signal with distance from the PMTs, because each block was only read out on one end. To correct for the attenuation, the signal from each block was multiplied by a correction factor based on the event position. This correction was checked by looking at the distributions of measured energy as a function of distance from the PMTs. In addition to correcting for attenuation, it is necessary to correct the gains of the individual modules. The operating high voltages for the calorimeter PMTs were adjusted to match the size of the output signal. This corresponds to a gain variation between the blocks, since the large momentum acceptance of the spectrometers gives rise to large variation in the input signals. The absolute gains were found to vary up to 50% between the different modules. The different lead glass modules were gain matched by varying the gain correction factor so as to minimize the difference between the energy sum from all blocks and the true energy of the electron, for true electron events. The true energy is determined from the reconstructed electron momentum and good electron events were defined using the Cerenkov counter.

4.7 Coincidence Timing

As described earlier (Section 3.4 and Section 4.6) the hodoscope planes were used to determine the time of events at the target. The scintillator times for each track at the focal plane (called Focal Plane Time), along with information on the path of the particle (determined with parameters from a COSY model, optimized to give the best coincidence time resolution) was used to determine the times of the event at the target. These times included the corrections described in Section 4.6 and were measured in each spectrometer. These single arm times along with the coincidence TDCs give the relative event times. This is called the raw cointime and this time is then corrected for the actual path taken by the particle and projected back to the target. The raw coincidence time is given by,

$$\text{cointime}_{raw} = \tau_{\text{proton arm}} - \tau_{\text{electron arm}} - TDC_{sos}, \quad (95)$$

here $\tau_{\text{proton arm}}$ and $\tau_{\text{electron arm}}$ are the single arm times and TDC_{sos} is the coincidence TDC started by the proton trigger and stopped by the electron trigger. There were coincidence TDCs in each of the spectrometers and hence we had two measurements of coincidence time. A typical coincidence time spectrum is shown in Figure 52. The 2 ns micro-structure of the beam was resolved. The typical coincidence time resolution was about 0.5 ns. A window of about ± 1.5 ns about the mean of the central peak was used as the cut to select the coincidence events. The number of background events per channel was determined by using two shaded regions on either side of the main peak in Figure 52). The contributions from background events in the good cointime region was then subtracted to give the background corrected coincident events.

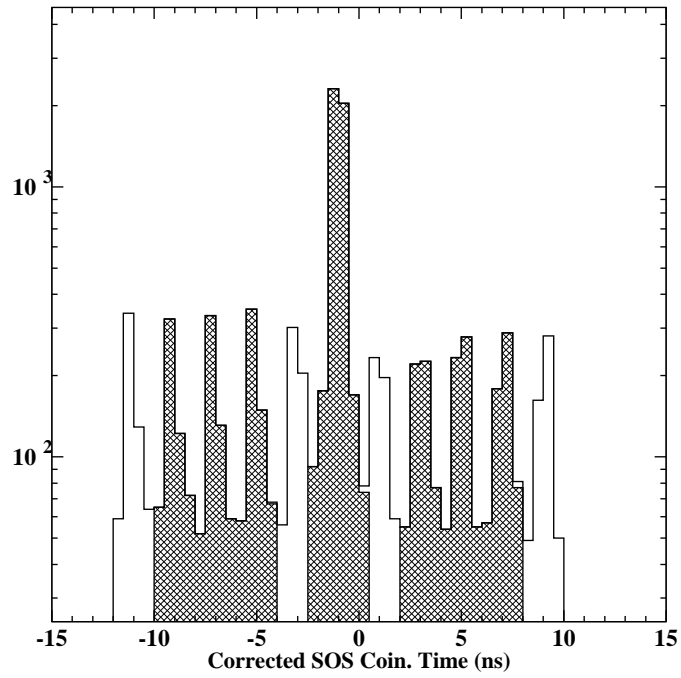


Figure 52: A typical corrected coincidence time spectrum is shown in log scale. The shaded peak in the center is taken as the good cointime peak while the shaded region on either side of the peak is used to calculated the random coincidences

4.7.1 Coincidence Blocking and Synchronization Corrections

We have seen that a cut on coincidence time was used to define the good coincident events. It was found that in order to use this information reliably some corrections need to be applied to the coincident events. These corrections are essentially due to four effects: blocked coincidences, self-timing events, loss of synchronization between detectors in a spectrometer and the loss of synchronization between the two spectrometers.

Some coincidence events get blocked when a random prescaled singles event (which would not ordinarily be recorded) occurs just before a true coincidence event. This leads to early stops in the coincidence time TDCs and makes the gates to the ADCs narrower than usual and thus tight cuts on the cointime would miss these blocked coincident events. In this experiment the SOS rates were always higher than the HMS rates and thus the majority of the coincident blocked events were random SOS events arriving just before a true coincidence event. This effect is corrected for by determining the fraction of the total coincidence events that were blocked and then correcting the good coincidence events by this fraction. The blocked events can be identified in the HMS coincidence time spectrum, since the blocked events lie outside the coincidence trigger window and arrive earlier than real coincidence events. The fraction of blocked events was almost always $< 1.0\%$ and in the worst case it was about 1.8% of the events.

The self-timing problem arises when some late trigger from one of the spectrometers can cause the trigger supervisor gate to arrive at the retiming AND gate (see Figure 35) after the delayed trigger from the the other spectrometer, thus the coincidence time TDC on this spectrometer is started and stopped by the late spectrometer (hence the name self timed event). The retiming incorporated into

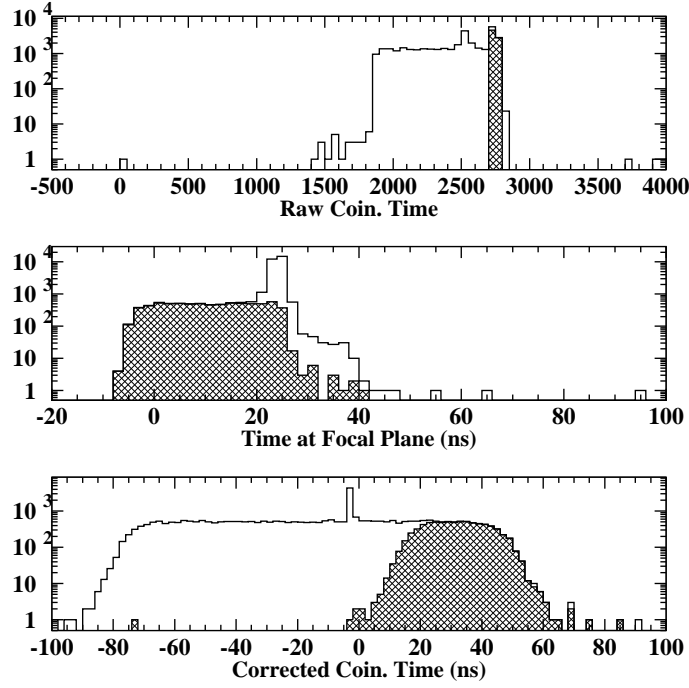


Figure 53: The self timed events are shaded, panel 1 shows the raw coincidence time, panel 2 shows the coincidence time at the focal plane and panel 3 shows the path length corrected coincidence time

the trigger logic was designed to avoid these events. However, it turned out that although the SOS had enough range in delay to avoid self timed events the HMS did not have enough delay and self timed events occurred. The HMS self timed events are shown in Figure 53. It turns out that in calculating the corrected coincidence time when one subtracts the focal plane time from the raw coincidence time both these quantities are smaller by the same amount and the effect is canceled. The self timed events are thus a part of the background in the corrected cointime distribution (see Figure 53). Since the self timed events occur when one spectrometer is very late, the tight cointime cut we apply automatically removes

the self timed events.

The synchronization problem arose from bugs in the data acquisition system when it was used in a 'buffered' mode. In this mode information for up to 8 events were stored in internal buffers of the ADCs and TDCs, while the data acquisition computers were busy. Thus this problem occurred only during high rate running. This problem can occur in two ways, the detectors within a single spectrometer can be out of sync with each other or the two spectrometers can be out of sync with each other. The synchronization problem of both types effected less than 1% of events in most cases except for forward proton angle runs in kinematics A where in the worst case it was a 10% effect. The first kind can be easily detected as the tracks from a given event do not correspond to the hits in other detectors and thus the diagnostic histograms looking at the difference between the tracks and the hits in each detector can easily pick out these runs. These problems were usually caught online and these runs were thrown out and data was retaken. The second kind is more subtle and cannot be detected easily. An algorithm was designed to identify events with this problem and the coincident counts were corrected for this effect. The algorithm consisted of summing the HMS and the SOS cointimes to form a checksum. Since the HMS cointime = - SOS cointime + constant, the checksum defined as HMS cointime + SOS cointime must lie within a well defined small range. Events outside this range were the out of sync events. Figure 54 shows the range of checksum for good events. A cut on checksum was used to determine the fraction of events which were out of sync and the coincidence yields were corrected with this fraction. This cut on checksum was used as a standard cut along with the tight cut on cointime.

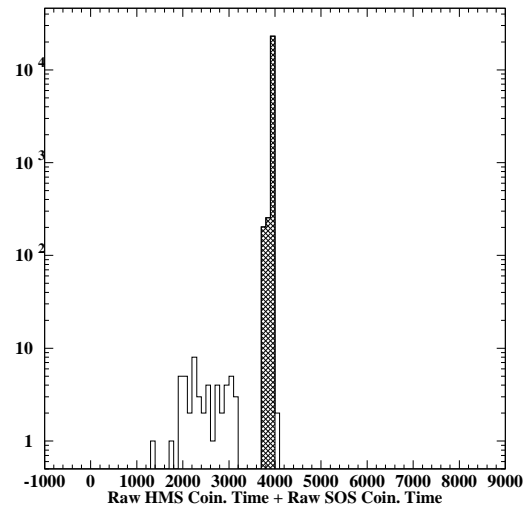


Figure 54: The sum of the raw HMS and SOS coincidence time is shown. This was called the checksum, with the shaded region corresponding to the events which are in sync or good events.

4.8 Electronic Dead Time and Computer Dead time Corrections

One of the corrections to the experimental yield is from data acquisition deadtimes. These are of two kinds, electronic deadtime and computer deadtime. The electronic deadtime occurs when triggers are not counted because the electronic hardware is busy processing the previous triggers. The scalers used in the experiment record the counts at a smaller rate R_{eff} than the true rate R_{true} . Since this is governed by Poisson statistics, the probability distribution of time between events is given by,

$$P(t) = R \exp^{-Rt} . \quad (96)$$

If τ is the width of the logic signal, the logic modules miss events which come within a time τ of each other. If the probability for this to occur is small (ie. for small dead times) the fraction of measured events is given by the probability for events to be separated by times greater than τ ,

$$\frac{N_{expt}}{N_{true}} = \int_{\tau}^{\infty} R \exp^{-Rt} dt = \exp^{-R\tau}, \quad (97)$$

for the small deadtimes encountered in this experiment this can be approximated as $\frac{N_{expt}}{N_{true}} \approx 1 - R\tau$.

In the trigger nearly all gates were 30 ns wide thus the τ for this experiment was 30 ns. The electronic dead time was measured by generating copies of the trigger with widths of 60, 90, 120 ns (A trigger arriving, for example 75 ns, after another would be counted for widths < 75 ns but would not be counted for widths > 75 ns). Counting these signals and making a linear extrapolation to zero deadtime

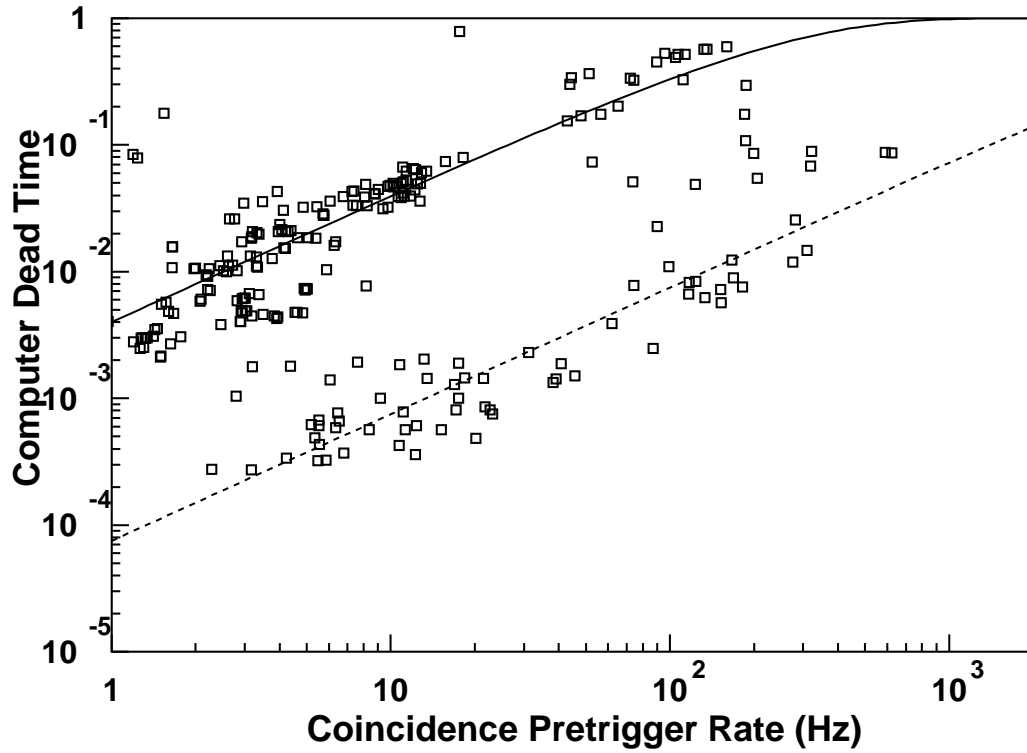


Figure 55: The solid line corresponds to the expected dead time for a processing time of $400\mu\text{s}$ while the dashed line corresponds to the expected dead time for a processing time of $75\mu\text{s}$. The pretrigger rate is the average rate over the entire run, it will be different from the instantaneous rate for runs where the beam was off for part of the run or if the current changed during the run.

the electronic dead time is given by,

$$K_{elec} = \frac{N^\tau}{N^{2\tau}} \quad (98)$$

where N^τ is the counts recorded by the scaler for the gate of length τ and $N^{2\tau}$ is the counts recorded for the gate which is twice as long. The electronic deadtimes were very low in this experiment. The HMS electronic dead time was always $<0.1\%$ while for the SOS it was always $<0.03\%$.

The other kind of dead time, computer dead time, arises as a result of the data acquisition computers being busy processing an event and not being available to process events generated while the computers are busy. In this case the hardware triggers are generated but they are blocked by the busy signal. The computer deadtime correction is defined to be the ratio of the actual number of events of interest to the number processed by the trigger supervisor. This is usually given by the ratio of pretriggers to triggers.

The typical non-buffered processing time was about $400\mu s$ for most of the runs in Dec 1995 the data was taken in non-buffered mode. For those runs which were run in buffered mode the processing time was about $75\mu s$. and there were just a few runs which used this mode. In this mode event are stored in a buffer before they are processed so that events arriving when the trigger supervisor is busy are not lost. However the processing time here is an effective time and can vary from run to run.

4.9 Detector Efficiencies

The Calorimeter and Čerenkov detector efficiencies were determined by selecting a sample of good electron events from data on elastic scattering off a liquid hydrogen

Table 13: The efficiency of the PID detector are listed

Kinematics	HMS Cal	HMS Č
A	0.992	0.995
B	0.992	0.995
C	0.992	0.995
D	0.976	0.995
E	0.984	0.995
F	0.990 (SOS)	0.992 (SOS)

target. The good electrons were selected by applying a narrow cut on invariant mass and a cut on the Čerenkov detector while determining the calorimeter efficiency and a cut on the calorimeter while determining the Čerenkov efficiency. The calorimeter and Čerenkov efficiencies for the different kinematics are listed in Table. 13.

4.10 Proton Absorption

Protons are strongly interacting particles and some of them will undergo a nuclear interaction as they traverse the detector stack. Such interactions can result in loss of the proton before it can reach the scintillators and cause a trigger. This would artificially reduce the coincidence yield. This absorption was measured directly using the $H(e,e'p)$ data. Each electron in the coincidence acceptance region must have knocked out a proton; thus the fraction of “missing” protons compared to the coincident electrons is the absorbed fraction. The coincident electrons were selected from a small region in the center of the acceptance and then compared to the corresponding protons. The ratio of the proton yield to the electron yield give the fraction of the protons which were not absorbed. It is also possible to estimate the fraction of protons absorbed by using the nuclear interaction lengths

(the mean free path between nuclear interactions) and the thicknesses of all the materials in the proton's path [70].

Table 14 (15) lists the properties of the materials that a proton must traverse on its way from the target through the SOS (HMS). The mean free path between nuclear collisions, $\bar{\lambda}$, is taken as the average of the total interaction length and the inelastic interaction length. These interaction lengths are taken from Reference [70] which lists both the mean free path between nuclear collisions, λ_T , and the mean free path between inelastic interactions, λ_I , as calculated from $\lambda = \frac{A}{N_A \times \sigma}$. The elastic cross section being very peaked in the forward direction, elastic scattering will only remove a small fraction of the protons from the acceptance. Thus the average of the total interaction length and the inelastic contribution is used.

Assuming that a proton traversing one quarter of the third scintillator is sufficient to cause a 3/4 trigger, the predicted transmission in the SOS is

$$PT_{SOS \text{ calculated}} = e^{-\sum_i X_i / \bar{\lambda}_i} = e^{-0.0582} = 0.943, \quad (99)$$

and for the HMS:

$$PT_{HMS \text{ calculated}} = e^{-\sum_i X_i / \bar{\lambda}_i} = e^{-0.0673} = 0.935. \quad (100)$$

Using the elastic scattering data on hydrogen the proton transmission in the SOS was measured to be 0.951 ± 0.005 . Note that it is independent of the proton momentum (at least over this limited range covered in this experiment). Note also, that this is in agreement with the theoretical estimate. Elastic scattering on hydrogen with the protons detected in the HMS was used to measure the proton transmission in the HMS. The measured HMS transmission is 0.945 ± 0.002 , and is consistent with the theoretical estimate. A detailed account of proton absorption results can be found in reference [71]. Proton transmission of 0.95 was used to

Table 14: Materials in SOS.

Absorber	Density (g/cm^3)	Thickness (cm)	λ (g/cm^2)	X (g/cm^2) Areal density	X/λ (10^{-3})
3.37cm LH	0.0708	3.37	47.3	0.239	5.04
5 mil Al target window	2.70	0.0127	88	0.0343	0.39
8 mil Al chamber window	2.70	0.0203	88	0.0548	0.62
Air (no vac. coupling)	0.00121	~ 15	75	0.0182	0.24
Kevlar	0.74	0.0127	~ 70	0.0094	0.13
Mylar	1.39	0.0076	72	0.0106	0.15
Kevlar	0.74	0.0381	~ 70	0.0282	0.40
Mylar	1.39	0.0127	72	0.0177	0.25
Air (DC 1 through S2)	0.00121	~ 149	75	0.180	2.40
Mylar cathode	1.39	7(0.00125)	72	0.0122	0.17
Wire (effective) W $6 \times 30\mu m + 6 \times 60\mu m$	19.3	12(0.0002)	147.7	0.00469	0.03
Ar/Ethane (50/50 weight)	0.00154	6(0.6178)	~ 70	0.00571	0.08
Mylar cathode	1.39	7(0.00125)	72	0.0122	0.17
Wire (effective) W $6 \times 30\mu m + 6 \times 60\mu m$	19.3	12(0.0002)	147.7	0.00469	0.03
Ar/Ethane (50/50 weight)	0.00154	6(0.6178)	~ 70	0.00571	0.08
Poltysty. (1.04 overlap)	1.03	2(1.04)	70	2.142	30.61
Cerenkov windows (2mil tedlar, 10mil lexan)	~ 1.39	2(0.030)	~ 70	2(0.042)	1.21
Freon 12 (1atm)	0.00493	100	87	0.493	5.67
Mirror (rohacell, mylar, carbon)	-	-	~ 70	0.45	6.43
Poltysty. (1.10 overlap)	1.03	0.25(1.10)	70	0.283	4.05
Total	-	-	-	-	58.2

Table 15: Materials in HMS.

Absorber	Density (g/cm^3)	Thickness (cm)	λ (g/cm^2)	X (g/cm^2) Areal density	X/λ (10^{-3})
3.37cm LH (after scatt.)	0.0708	3.37	47.3	0.239	5.04
5 mil Al target window	2.70	0.0127	88	0.0343	0.39
16 mil Al chamber window	2.70	0.0406	88	0.1096	1.24
Air (no vac. coupling)	0.00121	~ 15	75	0.0182	0.24
Kevlar	0.74	0.0381	~ 70	0.0282	0.40
Mylar	1.39	0.0127	72	0.0177	0.25
Kevlar	0.74	0.0381	~ 70	0.0282	0.40
Mylar	1.39	0.0127	72	0.0177	0.25
Air (exit pipe through S2)	0.00121	~ 256	75	0.310	4.13
2mil Mylar (entr/exit)	1.39	0.0051	72	0.0071	0.10
Sense Wires (effective) 25 μ m W, 6 planes	19.3	0.000038	147.7	0.00073	0.005
Field Wires (effective) 150 μ m Al/Au (99/1) 18 planes	2.70	0.0068	89.1	0.0184	0.21
Ar/Ethane (50/50 weight)	0.00154	8.3	~ 70	0.0128	0.18
2mil Mylar (entr/exit)	1.39	0.0051	72	0.0071	0.10
Sense Wires (effective) 25 μ m W, 6 planes	19.3	0.000038	147.7	0.00073	0.005
Field Wires (effective) 150 μ m Cu/Be (50/50) 18 planes	5.40	0.0068	87.9	0.0368	0.42
Ar/Ethane (50/50 weight)	0.00154	8.3	~ 70	0.0128	0.18
Polysty. (1.067 overlap)	1.03	2(1.067)	70	2.198	31.40
Čerenkov windows (40mil Al entrance/exit)	2.70	2(0.102)	88.5	2(0.275)	6.22
Čerenkov gas N ₂	0.00125	150	64.2	.1875	2.92
Rohacell Mirror support	~ 0.05	~ 1.8	~ 70	0.09	1.3
Mirror SiO ₂	2.20	0.3	83.1	0.66	3.13
Polysty. (1.067 overlap)	1.03	0.25(1.067)	70	0.275	7.94
Total	-	-	-	-	67.34

correct the proton yield in both spectrometers.

4.11 The $(e, e'p)$ Monte Carlo Simulation - SIMC

The PWIA Monte Carlo simulation SIMC was adapted from the $(e, e'p)$ simulation written for SLAC experiment NE18 [72]. It was converted to simulate the Jlab Hall C spectrometers in the coordinate system used in Hall C (Figure 23). The main pieces of the simulation are the event generator, which includes the cross-section weighting and radiative corrections, and the spectrometer models. The single arm Monte Carlos written for each of the Hall C spectrometers to study the optical properties of the two spectrometers were used as the spectrometer models of the two arms of the coincidence simulation SIMC. This PWIA simulation was a crucial part of the analysis. It was used in extracting transparency and in extracting the deradiated spectral functions, described in later sections. In this sections the main features of SIMC are described.

4.11.1 The Philosophy

The philosophy behind SIMC is to randomly generate the energy and position of the incident electron within the energy and spatial spread of the beam (the ionization losses in the target were also incorporated) and then randomly generate the momenta and angles of the scattered electron and the proton vectors with a flat distribution over a region larger than than the actual spectrometer acceptance. This defined the basic event at the scattering vertex. Next it was allowed for any or all the particles to emit real or virtual photons and the corresponding particle vectors were adjusted to account for such processes (see Section 4.11.6). The

scattered electron and proton were then transported through the target incorporating the ionization losses involved and finally transported through the appropriate spectrometer model. These spectrometer models contained the detailed optics, apertures and multiple scattering in the interfering material of the spectrometer (described in Section 4.11.2). The surviving events were then reconstructed back to the target and the energy loss corrections used in the data analysis were employed here as well. Finally the missing energy E_m and the missing momentum \mathbf{p}_m for the events were determined. Each successful event was assigned a weight of $K\sigma_{ep}S(E_m, \mathbf{p}_m)W_{radcor}W_{gen}$, where $K\sigma_{ep}$ is the basic e-p cross-section, with $K = E_p'\mathbf{p}_{p'}$, $S(E_m, \mathbf{p}_m)$ is the spectral function weight, W_{radcor} is the radiative correction weight and W_{gen} is the generation weight. Each of these weights are described in the next few sections of this chapter. The events were then stored along with the weights for each event. The normalization factor was also calculated as the experimental luminosity and the phase space volume divided by the total number of events generated.

$$\text{Normfactor} = \frac{\mathcal{L}\Delta E_p\Delta\Omega_p\Delta E_e\Delta\Omega_e}{N_{gen}}, \quad (101)$$

where \mathcal{L} is the experimental luminosity, $\Delta E_p\Delta\Omega_p\Delta E_e\Delta\Omega_e$ is the phase space volume, and N_{gen} is the number of generation attempts.

4.11.2 Spectrometer Models

The single arm spectrometer models consists of a set of forward matrix elements which transport the particles to every major aperture in the spectrometer, checking that the events makes it through each of these apertures. The forward matrix elements were generated by COSY as described in Section 3.4. All the intervening material in the spectrometer was included, the energy loss and multiple scattering

was computed for all the material. The effect of multiple scattering was simulated by a Gaussian distributions of the in-plane and out-of-plane angles, which had a standard deviation of [70],

$$\sigma = \frac{13.6}{p\beta} z \sqrt{l_{rad}} (1 + 0.088 \log_{10}(l_{rad})) \quad (102)$$

The treatment of external Bremsstrahlung is described in Section 4.11.6. The forward matrix elements were checked by comparing the focal plane distributions of the model with those of the data as described earlier in Section 3.4. The spectrometer models also contained sets of reconstruction matrix elements which transported the particles back to the target. The optimized set of matrix elements used in reconstructing the data was not used in the simulation because the optimized set cannot be inverted to get the forward matrix elements set. To get consistent results with the simulation the reconstruction matrix elements should be the inverse of the forward set, hence the COSY package was used to invert the forward set of matrix elements and these were used in the simulation. They were checked by comparing the model reconstructed distributions at the target with those of the data, for elastic $H(e, e'p)$ scattering. The reconstructed momentum, scattering and out of plane angle and the target length in the two spectrometer is shown in Figure 56. The figure shows the model acceptance reconstruction compared to the data.

Other tests include comparing the Monte Carlo yields for elastic $H(e, e'p)$ scattering with those determined from the data and ensuring that these results were independent of the cuts applied (Section 5.1). These results were also used to determine how well the acceptance function of the spectrometers is known and to determine the systematic uncertainty of the acceptance . The performance of the simulation was also compared to the data from the nuclear targets. Figure 57

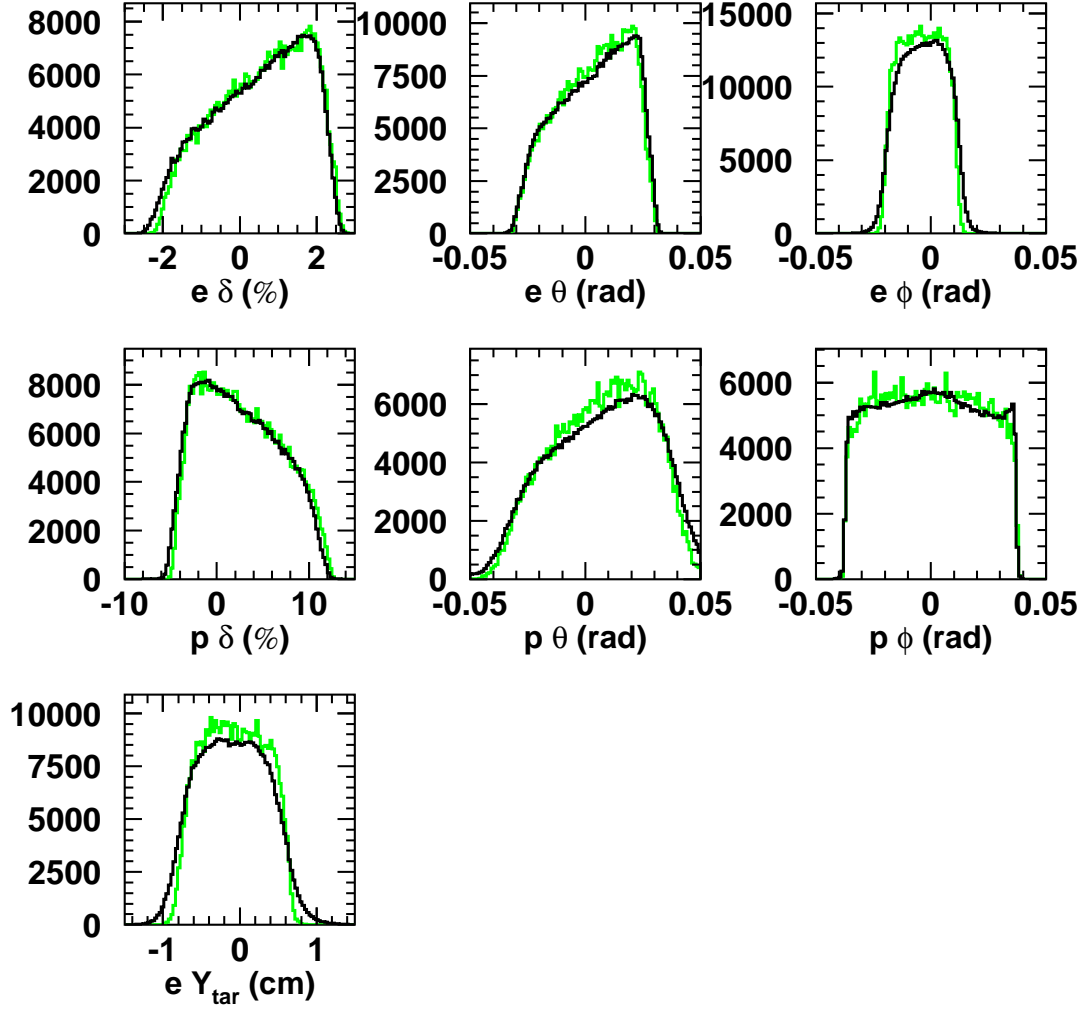


Figure 56: The reconstructed angles and momenta of the two spectrometers for Hydrogen ($e, e'p$) compared to the simulated distributions. The data is corrected for proton absorption, tracking inefficiency and background subtracted.

demonstrates the performance of the simulation with $^{12}C(e, e'p)$ scattering compared to data.

4.11.3 Off-Shell σ_{ep} Cross-section

The deForest prescription [13] σ_{cc1} was used in the simulation to describe the fundamental cross-section for quasi-elastic scattering of electrons from bound nucleons. The uncertainty arising from using this prescription was estimated by performing test-bench calculations with another deForest prescription σ_{cc2} . The PWIA cross-section was found to change by less than 2%. The structure functions used in calculating the fundamental cross-sections were the dipole form factor for the proton electric form factor G_E^p and the Gari and Krumpelmann parameterization for the proton magnetic form factor G_M^p [73]. These parameterization have been found to describe the data up to Q^2 of 8 GeV². [22, 74]

4.11.4 Model Spectral Functions

The model spectral functions were obtained from SLAC experiment NE18 [72, 49]. These spectral functions were based on Independent Particle Shell Model (IPSM), which describes the nucleus as a sum over nucleons occupying distinct shells. The assumption that the spectral function can be factored into a momentum distribution $\rho(\mathbf{p}_m)$ times a energy distribution $L(E_m)$ was also employed. Under this assumption the IPSM spectral function can be written as:

$$S(E_m, \mathbf{p}_m) = (2j + 1) \sum_{n,j,l} \rho_{njl}(\mathbf{p}_m) L_{njl}(E_m) \quad (103)$$

The momentum distributions were computed by using the code DWEOPY [75], which solves the Schrödinger equation in an optical potential (optical potentials have been discussed in Section 2.4). Wood-Saxon potentials were used for this

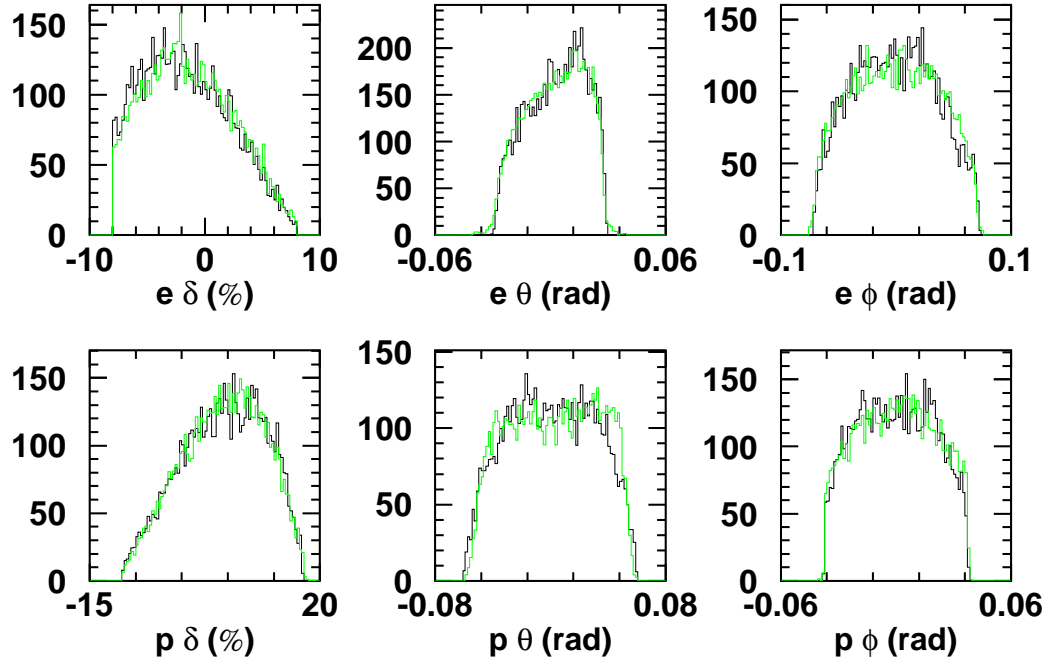


Figure 57: The reconstructed angles and momenta of the two spectrometers for Carbon ($e, e'p$) compared to the simulated distributions. The data is corrected for proton absorption, tracking inefficiency and background subtracted, data is dark and simulation is grey.

Table 16: Fermi energy of ^{12}C , ^{56}Fe and ^{197}Au

Target	E_{Fermi}
^{12}C	15.96
^{56}Fe	10.18
^{197}Au	5.78

purpose. The parameters of these potentials were obtained by fitting to previous data on same or similar targets. A detailed description of these parameters are given in Appendix A. The non-locality of the potential is corrected in terms of the Perey factor as described in Section 2.4. The separation energy distribution $L(E_m)$ were given in terms of the Lorentzian shape associated with an isolated resonance,

$$L(E) = \frac{1}{\pi} \frac{\Gamma/2}{(E - E_B)^2 + (\Gamma/2)^2} \quad (104)$$

where E_B is the central binding energy of the shell. The Lorentzians were cut-off at the minimum proton separation energy E_s^{min} of a nucleus and renormalized to 1. The minimum proton separation energy is given by the mass difference $M_{A-1} + M_p - M_A$. The width parameters Γ were taken from either fits to low- Q^2 data or were determined using the formula of Brown and Rho [76],

$$\Gamma(E) = \frac{(24\text{MeV})(E - E_F)^2}{(500\text{MeV}^2) + (E - E_F)^2} \quad (105)$$

with E taken to the central binding energy E_B and E_F is the Fermi energy.

It is well known that due to short range nucleon-nucleon correlations, the spectral function extends beyond the Fermi momentum and causes some of the single-particle strength to appear at larger E_m and $|\vec{p}_i|$ [82] and thus some of the strength is outside the experimental acceptance. Since the ISPM spectral function does not account for correlations, the simulation overestimates the yield. Hence the Monte

Table 17: Correlation tail correction to the transparency

Nuclei	Correction
^{12}C	1.11 ± 0.03
^{56}Fe	1.26 ± 0.08
^{197}Au	1.32 ± 0.08

Carlo yield must be corrected for these excess protons. Assuming that these correlations produce an uniform suppression of the IPSM spectral function strength for $|\mathbf{p}_m| < 300 \text{ MeV}/c$, the correlation correction factor is estimated as described in Reference [49] by,

$$\text{Correlation correction} = \frac{\int_0^{80} S_{IPSM}(E_m, \mathbf{p}_m) dE_m d^3\mathbf{p}_m}{\int_0^{80} S_{correlated}(E_m, \mathbf{p}_m) dE_m d^3\mathbf{p}_m}. \quad (106)$$

Here the correlated spectral functions are model spectral functions which include effects of correlation. Table 17 gives the value of these correlation correction factors for each target. The model uncertainties of this correction is discussed in Section 5.3.1. The IPSM spectral function corrected for correlations using the factors listed in Table 17, will be referred to as $S_{PWIA}^{CC}(E_m, \mathbf{p}_m)$ in the rest of the thesis. The experimental yield compared to the corrected simulated yield is the transparency at the given momentum transfer squared Q^2 .

4.11.5 Generation Weight

While generating the various event quantities, the generation volume is defined by limits which are usually larger than the actual acceptance of the spectrometer. These limits can be refined once there is partial information about the event, with refinements governed by the apertures of the spectrometer and the cuts imposed on the reconstructed E_m , \mathbf{p}_m and the particle vectors and the range of E_m over

which the spectral function is defined. For example, to account for events which radiate into the acceptance of the spectrometer, generation limits wider than the spectrometer acceptance are required. However, once the electron momentum has been generated the range of photon energies required to produce a successful event can be determined and thus one can refine the generation limits with this information. The generation weight reduces the event weight to compensate for these restricted/refined limits.

4.11.6 Radiative Corrections

Electrons radiate in the presence of an electric field due to changes in their velocity brought about by Coulomb interactions and radiation resulting from such deceleration of the electron is called bremsstrahlung. The incoming and outgoing electrons can interact with the Coulomb field of the nucleus involved in the scattering process, which results in emission and reabsorption of virtual photons and emission of real, soft photons. Such processes are known as internal bremsstrahlung. The electrons can also interact with the Coulomb field of a nucleus other than the one involved in the scattering process and thereby radiate photons. These radiations are known as external bremsstrahlung. In an experiment involving electrons scattering off some target, the radiative processes have a twofold effect on the data. Firstly the cross section of the process is modified and secondly the kinematics (energy, momentum, angle) of the electron are changed. Although these are real physical processes, they are experiment specific, and so most theoretical calculations do not take these effects into account. Thus, in order to get to the underlying physics, and also to directly compare with theoretical calculations, one needs to unfold these radiative processes from the data. The procedure for doing such radiative corrections was first derived by J. Schwinger [77], and was later modified

by Mo and Tsai [78]. Radiative correction formulas for coincidence $(e, e'p)$ reactions were calculated from the Mo and Tsai formulation by Makins et. al. [79]. The derivation of these formulae is very well described in references [72] and [79]. This section is an illustration of how the above mentioned formulae are used in the PWIA Monte Carlo SIMC.

The cross-section for radiating energy E_e along the incoming electron direction \hat{k} , $E_{e'}$ along the scattered electron direction \hat{k}' , $E_{p'}$ along the direction of the scattered proton \hat{p}' and also radiating any number of soft photons with energy less than ΔE , calculated to all orders, (note that this cross-section is different from the cross-sections defined in the rest of the thesis) is given by,

$$\frac{d\sigma}{d\Omega_e dE_e dE_{e'} dE_{p'}} = \frac{d\sigma}{d\Omega_e}|_{ep}(1 - \delta_{hard}) \frac{\lambda_e \lambda_{e'} \lambda_{p'}}{(\sqrt{k k'})^{\lambda_e} (\sqrt{k k'})^{\lambda_{e'}} (\sqrt{M p^{o'}})^{\lambda_{p'}}} \times \frac{1}{E_e^{1-\lambda_e} E_{e'}^{1-\lambda_{e'}} E_{p'}^{1-\lambda_{p'}}}. \quad (107)$$

Here the total energy radiated is $\omega_{total} = E_e + E_{e'} + E_{p'}$ and the $\bar{\lambda}$ s are the angular distribution functions of the photons radiated in the three directions. The angular distribution of the radiation is approximated as,

$$A_{extnd_{peaking}}(\hat{\omega}) = \lambda_e \delta(\hat{\omega} - \hat{k}) + \lambda_{e'} \delta(\hat{\omega} - \hat{k}') + \lambda_{p'} \delta(\hat{\omega} - \hat{p}'). \quad (108)$$

This simple approach to the angular distribution is also known as the 'extended peaking approximation' and the λ s are given by the following expressions,

$$\lambda_e = \frac{\alpha}{\pi} [\ln(\frac{4k^2}{m^2} - 1)] + \frac{\alpha}{\pi} [2\ln(\frac{k}{k'} + \ln(\frac{1 - \cos\theta_e}{2})], \quad (109)$$

$$\lambda_{e'} = \frac{\alpha}{\pi} [\ln(\frac{4k'^2}{m^2} - 1)] + \frac{\alpha}{\pi} [2\ln(\frac{k}{k'} + \ln(\frac{1 - \cos\theta_e}{2})], \quad (110)$$

$$\lambda_{p'} = \frac{\alpha}{\pi} [\ln(\frac{p'^o + |p'|}{p'^o - |p'|}) - 2]. \quad (111)$$

Where k, k' and p' are the magnitude of the incident electron momentum, scattered electron momentum and the scattered proton momentum, respectively, and p'^o is the proton energy. If only the first term in each of Equation 109-111 is used we get the simpler: peaking approximation. δ_{hard} is the contribution from the second order virtual photon radiation to the vertex corrections, and is given by,

$$\delta_{hard} = 2\alpha [-\frac{3}{4\pi} \ln(-q^2/m^2) + \frac{1}{\pi} - \sum_i \delta_i^{vp}(q^2)], \quad (112)$$

where \sum_i sums over the different flavors of leptons with mass m_i and,

$$\delta_i^{vp} = \frac{1}{3\pi} [-\frac{5}{3} + \ln(-q^2/m_i^2)]. \quad (113)$$

All of the above expressions are for internal bremsstrahlung. However, photons are also emitted when the electrons are in the field of nuclei other than those involved in the hard scattering process (external bremsstrahlung). The proton being massive emits negligible amounts of external radiation. Both E_i^{int} and E_i^{ext} are emitted in the same direction, thus if the internal and external bremsstrahlung are added together we can write the cross-section in terms of E_i and E_f radiated along k and k' as,

$$\begin{aligned} \frac{d\sigma}{d\Omega_e dE_i^{int} dE_i^{ext} dE_f^{int} dE_f^{ext} dE_{p'}} &= \frac{d\sigma}{d\Omega_e} |_{ep} (1 - \delta_{hard}) \frac{1}{\Gamma(1 + bt_i)} \frac{1}{\Gamma(1 + bt_f)} \\ &\frac{(bt_i + \lambda_i)}{k^{bt_i} (\sqrt{k k'})^{\lambda_i}} \frac{(bt_f + \lambda_f)}{k'^{bt_f} (\sqrt{k k'})^{\lambda_f}} \frac{dE_i}{E_i^{1-\lambda_i-bt_i}} \frac{dE_f}{E_f^{1-\lambda_f-bt_f}} \Phi_i^{ext}(E_i) \Phi_f^{ext}(E_f). \end{aligned} \quad (114)$$

Here we have neglected the proton radiation and the same is done for the rest of

the discussion. The function Φ^{ext} is a correction for external radiation which has large photon energies and has the form,

$$\Phi_i^{ext}(E_i) = 1 - \frac{bt_i}{bt_i + \lambda_i} \frac{E_i}{k_i}, \quad (115)$$

and

$$b = 1/9(12 + \frac{Z+1}{ZL_1 + L_2}), \quad (116)$$

$$L_1 = \ln(184.15) - \frac{1}{3}\ln(Z), \quad (117)$$

$$L_2 = \ln(1194.) - \frac{2}{3}\ln(Z). \quad (118)$$

In the Monte Carlo SIMC the photon energies $E_e, E_{e'}$ and $E_{p'}$ along the incoming electron, the outgoing electron and the proton directions, respectively, are generated separately and the total energy radiated is the sum of these energies (as mentioned earlier the proton radiation is small and can be neglected). This comes about because in Equation 107 above the energy and angular distribution of radiation in the three directions factorize into three independent functions. The shape of each of these distributions has the form,

$$\frac{1}{\Gamma(1+bt)} \frac{bt+\lambda}{k^{bt}(\sqrt{k k'})^\lambda} \frac{dE}{E^{1-\lambda-bt}}. \quad (119)$$

If we rename $g = bt + \lambda$ and $C = \frac{bt+\lambda}{\Gamma(1+bt)} \frac{1}{k^{bt}(\sqrt{k k'})^\lambda}$, we get the form,

$$C * E^{g-1} dE. \quad (120)$$

Hence we can use this simple form to generate the energy radiated in a given direction between limits E_{max} and E_{min} . The generating function must normalize to 1 between these limits so we have,

$$N * \int_{E_{min}}^{E_{max}} (E^{g-1}) dE = 1, \quad (121)$$

or

$$N = \frac{g}{E_{max}^g - E_{min}^g}. \quad (122)$$

Thus for each of the radiation tails, the energy radiated in that particular direction is randomly generated in the range $E_{max} - E_{min}$ using the generating function or energy shape,

$$G = \frac{gE^{g-1}}{E_{max}^g - E_{min}^g}. \quad (123)$$

The limits E_{max} and E_{min} are determined from the limits of the model spectral function, the limits on the energy and momenta of the incident and scattered particles determined from the spectrometer acceptance and the randomly generated energy and momenta of the incident and scattered particles.

Once the energy radiated in each of the tails is known, the next step is to use these energies to modify the momentum and energy of the incident and scattered particles involved in the reaction. This is done for each event by subtracting off the radiated energy from the randomly generated vertex energies (energy of the particles at the reaction vertex).

Next the radiation weight is calculated for each event which is then assigned to that event. The radiation weight is the probability of radiating soft or hard photons of a given energy. The radiation weight has three components. The first

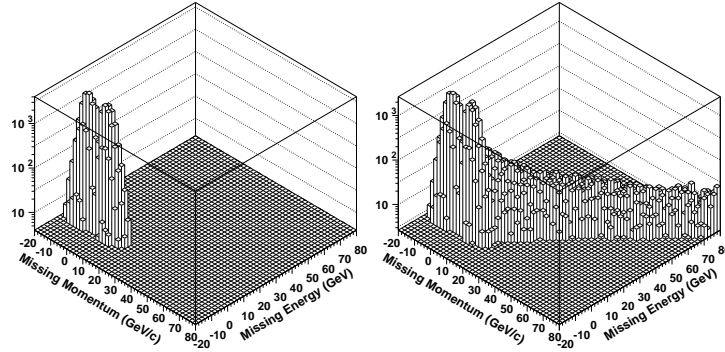


Figure 58: The effect of radiation for hydrogen is shown in the E_m vs p_m distribution, with (right panel) and without (left panel) radiation. The radiation of real photons show up as the tail.

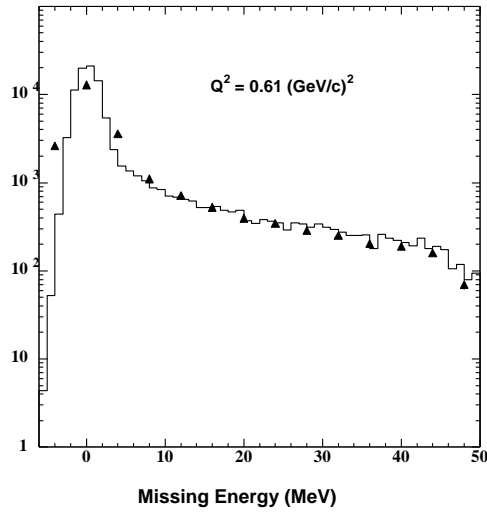


Figure 59: Plot of the missing energy spectrum of hydrogen, solid line is the calculation using Monte Carlo SIMC and triangles are data, with statistical errors only.

component is the probability of emitting a photon and has the correct radiative tail shape. This comes from Equation 119 and the generating function (Equation 123). From these equations we get the weight for each of the three tails as,

$$W_{rad}^i = C/g * ((E_{max}^i)^g - (E_{min}^i)^g); i = e, e', p'. \quad (124)$$

The product of the three weights for the three tails give us W_{rad}^{soft} .

$$W_{rad}^{soft} = W_{rad}^e W_{rad}^{e'}. \quad (125)$$

The second component is the multiplicative correction factor due to external radiation Φ_i^{ext} , as described in equation 115. This too is calculated for each tail and includes the external radiation suffered in the exit windows of the scattering chamber and the entrance windows of the spectrometers and the air in between these windows. The final component is the due to the vertex corrections and is given by $(1 - \delta_{hard})$. So finally the product of all these little pieces gives us the radiation weight for an event,

$$W_{rad}^{event} = W_{rad}^{soft} \Phi_e^{ext} \Phi_{e'}^{ext} (1 - \delta_{hard}). \quad (126)$$

When the data are binned in terms of E_m and P_m , we have accounted for events which radiated into a particular bin by modifying the vertex. The E_m and P_m were changed by the total radiated energy, hence they contribute to bins they radiated into and not the ones they would have if there was no radiation. In addition the radiation weight assigned to each event accounts for events which radiated out of the bin. These two features together constitute the radiative correction procedure of the Monte Carlo SIMC. Thus using the described procedure we can generate radiated spectra with SIMC. This method obtains correct multi-photon angular

distributions and hence is also known as the 'multi-photon' technique. However, one must remember that it does involve the peaking approximation at the single photon level.

As an illustration of how the procedure works, Figure 58 compares an unradiated missing energy vs missing momentum spectrum with a radiated spectrum for Hydrogen target. One can clearly identify the radiative tails in this figure. In Figure 59 the hydrogen missing energy spectrum is compared with the same calculated using the Monte Carlo. While the resolution of the Monte Carlo did not match the data, the integrated strength did compare very well with the data as described in Section 5.1.

The procedure described above is one of the three radiative correction procedures which are available in SIMC. The procedure described is the one currently in use. Various comparisons of the different procedures were done by the NE18 [72] and they found agreement to be better than 1% within the different procedures. Since the above procedure approximates the angular distribution most effectively, it is the procedure of choice.

4.11.7 Coulomb Corrections

The Coulomb distortions arise from the fact that the incoming and outgoing electrons interact with the electromagnetic field of the target nucleus. The effect of the Coulomb potential is to increase the momentum transfer q and also to cause an increase in the electron flux in the vicinity of the target nucleus. These effects can be accounted for by appropriately changing the electron wave used to calculate the coincidence cross-section of the $(e, e'p)$ reaction. This approach is also equivalent to summing the contributions from Feynman diagrams in which the electron and the nucleus exchange one, two or more photons while the nucleus still remains in

its initial state. It can be shown that this kind of distortion of the electron wave can be approximated by attaching a phase factor to the plane wave expansion [80], which scales with the nuclear dimension and the strength of the Coulomb field. In addition the effective momentum of the electron is changed to $\bar{\mathbf{k}} = \mathbf{k} - \Delta\mathbf{k}$, where $\Delta\mathbf{k}$ is the average electrostatic field around the electron, given by

$$\Delta k = \frac{\int V_c(\mathbf{r})\psi^2(\mathbf{r})d\mathbf{r}}{\int \psi^2(\mathbf{r})d\mathbf{r}} = f \frac{Z\alpha}{R_c} = \langle V_C \rangle, \quad (127)$$

here the factor f varies between 1.1 and 1.5 depending on the size of the nucleus, at the center of the nucleus $f = 1.5$. Such calculations have been done by Knoll et al. [27], and they provide an useful formula to estimate the effect of the Coulomb distortion on the cross-section:

$$\frac{\Delta\sigma}{\sigma_{max}}(\%) \approx 0.3 \frac{q}{k_o} Z. \quad (128)$$

Where σ_{max} is the cross-section at the maximum of the distribution and k_o is the momentum of the incident electron. This equation suggests that the Coulomb corrections get smaller as the energy of the incident electron increases and thus at high electron energies this correction may be neglected.

In the physics model used in the code SIMC 4.11, Coulomb corrections can be switched on or off. The correction prescription involves using the average Coulomb field $\langle V_C \rangle$ to apply a shift to the incident and outgoing electron momentum which in turn shifts the momentum transfer and the missing momentum. Changing in the electron momentum also means that the calculated cross-section for the process changes. The reduced cross-section is obtained by,

$$\sigma_{cc}^{reduced} = \left(\frac{k_i^{eff}}{k_i} \right)^2 \sigma_{cc} \quad (129)$$

Table 18: Coulomb radius and the Coulomb factor $V_C = f_C \frac{\alpha Z - 1}{R_C}$ for the three targets.

Target	$R_C = 1.18A^{1/3}(\text{fm})$	$V_C(\text{MeV})$
^{12}C	2.70	3.25
^{56}Fe	4.51	9.4
^{197}Au	6.88	19.8

where $k_i^{eff} = k_i + f_c \frac{\alpha Z}{R_C}$. The effective momentum transfer is given by,

$$\vec{q}^{eff} = \vec{q}(1 + f_c \frac{\alpha(Z-1)}{R_C} \frac{1}{k_f}) + f_c \frac{\alpha(Z-1)}{R_C} \frac{\vec{k}_i}{k_i} (1 - \frac{k_i}{k_f}), \quad (130)$$

and so the missing momentum is shifted by,

$$\Delta \vec{q} = \Delta \vec{P}_m \approx f_c \frac{\alpha(Z-1)}{R_C} \left(\frac{k_f - k_i + q}{k_f} \right). \quad (131)$$

For the averaged Coulomb potential the factor f is taken to be 1.2, but at the center of the potential it is 1.5. In SIMC the value of f is randomly generated for every event and it is constrained to have a value between 1.0 and 1.5 using $0.5 * (3.0 - (\text{rand})^{2/3})$. From this prescription one gets the magnitude of the shifts and the corrections to the cross-section as shown in Tables 18. and 19.

The effect of the Coulomb correction was investigated by comparing the results of the Monte Carlo with and without the corrections. The results of this comparison are tabulated in Table 20. The Coulomb shift in the data and the Monte Carlo should be done consistently since we use missing momentum \mathbf{p}_m cuts in comparing data to Monte Carlo. However, it was realized that the the missing momentum is not Coulomb shifted in the data while the Monte Carlo outputs Coulomb shifted missing momentum. In order to study the effect of this discrepancy the Coulomb shift in the missing momentum of the Monte Carlo ntuples were subtracted, and

Table 19: Change in the missing momentum ΔP_m and the correction to the cross-section.

Kine	q	$\Delta P_m(\text{MeV})$			$\frac{\sigma_{corrected}}{\sigma} = \left(\frac{k_i^{eff}}{k_i}\right)^2$		
		^{12}C	^{56}Fe	^{197}Au	^{12}C	^{56}Fe	^{197}Au
A	0.84	0.75	2.16	4.55	1.0026	1.0077	1.0162
B	1.27	1.06	3.06	6.45	1.0026	1.0077	1.0162
C	1.55	0.79	2.30	4.80	1.0020	1.0058	1.0122
D	0.84	3.20	9.30	19.60	1.0077	1.0220	1.0471
E	1.55	2.70	7.90	16.80	1.0039	1.0113	1.0241
F	2.55	1.60	4.70	9.90	1.0020	1.0058	1.0122

Table 20: Change in counts $\frac{\Delta N}{N}$ between 0-80 MeV in E_m with and without Coulomb corrections. Here conj refers to the conjugate angle for the given kinematic setting (A-F), and the extreme proton angle settings around the conjugate angle for kinematics A is called A5 and A10.

Kine	Θ_{Prot}	$\frac{\Delta N}{N}$		
		^{12}C	^{56}Fe	^{197}Au
A1	conj	0.0065	0.043	0.045
A5	conj +16	0.0105	0.019	0.015
A10	conj -16	0.0489	0.006	0.096
B	conj	0.0148	0.0255	0.044
C	conj	0.001	0.0065	0.039
D	conj	0.017	0.080	0.153
E	conj	0.043	0.083	0.166
F	conj	0.018	0.012	0.019

Table 21: Change in counts $\frac{\Delta N}{N}$ between 0-80 MeV in E_m with cuts on Coulomb shifted and non-shifted missing momentum ($-300 < \mathbf{p}_m < 300$)

Kine	Θ_{Prot}	$\frac{\Delta N}{N}$		
		^{12}C	^{56}Fe	^{197}Au
A1	conj	0.000	0.000	0.000
A5	conj +16	0.007	0.005	0.006
A10	conj -16	0.006	0.002	0.003

the number of counts with cuts on the shifted and the non-shifted missing momentum (and other nominal cuts) were recorded. Table 21 shows the fractional difference between the two approaches.

The effect of the Coulomb corrections at backward angles is much larger than the correction at forward angles. This is because the correction is inversely proportional to the incident electron momentum and the backward angle points are at much lower momentum compared to the forward angle points. For the forward angle kinematics the correction is $< 2\%$ for ^{12}C , $< 4\%$ for ^{56}Fe and $< 5\%$ for ^{197}Au . Also the discrepancy of cutting on the Coulomb shifted \mathbf{p}_m in the Monte Carlo and the non-shifted \mathbf{p}_m in the data was found to be negligible at conjugate angles, and $\leq 0.6\%$ for the extreme angles on either side of the conjugate angle.

4.12 Extracting Transparency

The nuclear transparency T_θ was determined by,

$$T_\theta = \frac{\int_V d^3p_i dE_m N_{exp}(E_m, \vec{p}_i)}{\int_V d^3p_i dE_m N_{PWIA}(E_m, \vec{p}_i)} \quad (132)$$

where V is the finite experimental phase space volume (with $E_m < 80$ MeV and $|\vec{p}_i| < 300$ MeV),

Table 22: Standard Data Constraints for E91-013. The calorimeter requirement depends on the kinematics. Note that there is no Čerenkov constraint for kinematics F, with electrons in the SOS.

Cut	Values
HMS δ (%)	± 8
SOS δ (%) (p in SOS)	-10 - 20
SOS δ (%) (e ⁻ in SOS)	± 15
HMS X'_{tar} (rad)	± 0.075
HMS Y'_{tar} (rad)	± 0.040
SOS X'_{tar} (rad)	± 0.045
SOS Y'_{tar} (rad)	± 0.060
Missing Energy (MeV)	0 - 80
Missing Momentum (MeV/c)	± 300
Kine. A e ⁻ Calorimeter (GeV)	> 1.0
Kine. B e ⁻ Calorimeter (GeV)	> 1.0
Kine. C e ⁻ Calorimeter (GeV)	> 1.0
Kine. D e ⁻ Calorimeter (GeV)	> 0.2
Kine. E e ⁻ Calorimeter (GeV)	> 0.4
Kine. F e ⁻ Calorimeter (GeV)	> 0.8
e ⁻ Čerenkov (npe)	> 1
Coincidence time cut (ns)	± 1.5
Backgrd. Sample Width (ns)	6

$N_{exp}(E_m, \vec{p}_i)$ is the normalized experimental yield and $N_{PWIA}(E_m, \vec{p}_i)$ is the normalized yield of the simulation. The integration of the yields over missing energy and missing momentum E_m and P_m ensures that averaging over the initial energy and momentum of the knocked out proton.

The experimental yield was determined using cuts listed in Table 22, they were corrected for tracking efficiency, detector efficiencies, computer dead time and proton absorption. The PWIA yield was calculated with the Monte Carlo SIMC

using the cuts listed in Table 22 for the same amount of charge as accumulated experimentally. Using the experimental and PWIA yields the transparency was determined for all proton angles. The transparency for a given Q^2 was determined by taking the yield weighted average of the transparency for the different proton angles. This ensures that the experimental yield is averaged over the full Fermi cone over which protons are scattered. The same procedure is repeated for the PWIA yield. This was done for all three targets and at all Q^2 .

4.13 Extraction of Spectral Functions

4.13.1 Derivation

In this section the derivation of the formulae used in extraction of the spectral functions is performed, by starting with the basic relation between the experimental counts and cross-section of the scattering process. One can measure the energy of the scattered electron $E_{e'}$, the scattered proton energy $E_{p'}$ and the two angles for each of the two scattered particles, $\Omega_{e'}(\theta_{e'}, \phi_{e'})$, $\Omega_{p'}(\theta_{p'}, \phi_{p'})$. The yield from $(e, e'p)$ scattering in some volume of phase space $V'(E_{e'}, E_{p'}, \Omega_{e'}, \Omega_{p'})$ is,

$$N(E_{e'}, E_{p'}, \dots) = L * \int_{V'} \frac{d^6\sigma}{dE_{p'} d\Omega_{p'} dE_{e'} d\Omega_{e'}} dE_{p'} d\Omega_{p'} dE_{e'} d\Omega_{e'}, \quad (133)$$

here L is the experimental luminosity and $\frac{d^6\sigma}{dE_{p'} d\Omega_{p'} dE_{e'} d\Omega_{e'}}$ is the basic experimental yield including all physical processes like radiation. This general expression can be factorized as the product of the unradiated one photon exchange (OPE) yield and a redistribution due to Bremsstrahlung radiation as,

$$N(E_{e'}, E_{p'}, \dots) = L * \int_V d^6V \int_{p'e'} R(\mathbf{p}'_r, \mathbf{e}'_r; \mathbf{p}', \mathbf{e}') \frac{d^6\sigma_{OPE}}{dE_{p'} d\Omega_{p'} dE_{e'} d\Omega_{e'}} dE_{p'} d\Omega_{p'} dE_{e'} d\Omega_{e'}, \quad (134)$$

where $R(\mathbf{p}'_r, \mathbf{e}'_r; \mathbf{p}', \mathbf{e}')$ represents the redistribution and the smearing due to radiation. For clarity the label OPE will be dropped from here onwards with the understanding that all cross-sections are for OPE processes.

In an experiment the yield is further smeared by the experimental resolution and limited by the acceptance of the spectrometers used to detect the particles and hence the yield must include the acceptance function $A(\mathbf{p}'_{exp}, \mathbf{e}'_{exp}; \mathbf{p}'_r, \mathbf{e}'_r)$ which transforms the nominal experimental variables p'_r, e'_r to reconstructed variables p'_{exp}, e'_{exp} ,

$$N(E'_{exp}, E'_{p'_{exp}}, \dots) = L * \int_{V_{exp}} d^6V \int_{\mathbf{p}'_r, \mathbf{e}'_r} A(\mathbf{p}'_{exp}, \mathbf{e}'_{exp}; \mathbf{p}'_r, \mathbf{e}'_r) d^3p'_r d^3e'_r \\ \int_{\mathbf{p}'_{e'}} R(\mathbf{p}'_r, \mathbf{e}'_r; \mathbf{p}', \mathbf{e}') \frac{d^6\sigma}{dE_{p'} d\Omega_{p'} dE_{e'} d\Omega_{e'}} dE_{p'} d\Omega_{p'} dE_{e'} d\Omega_{e'}. \quad (135)$$

The experimental yield is measured over some fixed range of the measured quantities, which is used to define the volume V_{exp} . If the data is binned in $(E_m^{exp}, \mathbf{p}_m^{exp})$ space, the yield can be expressed as,

$$N(E_m^{exp}, \Delta E_m^{exp}, \mathbf{p}_m^{exp}, \Delta \mathbf{p}_m^{exp}) = L * \int_{E_m \Delta E_m} dE_m \int_{\mathbf{p}_m, \Delta \mathbf{p}_m} d^3p_m \int_{V_{exp}} d^6V \\ \delta(E_m - (E_e - E'_{exp} - E'_{p_{exp}} + M_p - T_{exp}^{rec})) \delta(\mathbf{p}'_m - (\mathbf{p}_e - \mathbf{p}'_{exp} - \mathbf{p}'_{p_{exp}})) \\ \int_{\mathbf{p}'_r, \mathbf{e}'_r} A(\mathbf{p}'_{exp}, \mathbf{e}'_{exp}; \mathbf{p}'_r, \mathbf{e}'_r) d^3p'_r d^3e'_r \\ \int_{\mathbf{p}'_{e'}} R(\mathbf{p}'_r, \mathbf{e}'_r; \mathbf{p}', \mathbf{e}') \frac{d^6\sigma}{dE_{p'} d\Omega_{p'} dE_{e'} d\Omega_{e'}} dE_{p'} d\Omega_{p'} dE_{e'} d\Omega_{e'}. \quad (136)$$

To make the above expression tractable one has to make some assumptions and approximations. These assumptions are,

- The spectrometers do not bias the measured quantities,

$$\mathbf{p}'_{exp} = \mathbf{p}'_r,$$

$$\mathbf{e}'_{exp} = \mathbf{e}'_r.$$

- The spectrometer acceptances are independent of each other,

$$A(\mathbf{p}'_{exp}, \mathbf{e}'_{exp}; \mathbf{p}'_r, \mathbf{e}'_r) = A(\mathbf{p}'_{exp})A(\mathbf{e}'_{exp})\delta(\mathbf{p}'_{exp} - \mathbf{p}'_r)\delta(\mathbf{e}'_{exp} - \mathbf{e}'_r).$$

- The effects of radiation can be incorporated in terms of smearing and re-distribution of the incident and outgoing electron and the outgoing proton as,

$$\int R(\mathbf{p}'_r, \mathbf{e}'_r; \mathbf{p}', e') \frac{d^6\sigma}{dE_{p'}d\Omega_{p'}dE_{e'}d\Omega_{e'}} dE_{p'}d\Omega_{p'}dE_{e'}d\Omega_{e'} = \frac{d^6\sigma^R}{dE_{p'}^{exp}d\Omega_{p'}^{exp}dE_{e'}^{exp}d\Omega_{e'}^{exp}}.$$

Since the measurements are made in the spectrometer coordinates, one has to use the Jacobian for transforming to the spectrometer coordinates which is given by,

$$|J| = \frac{1}{(1 + (\Delta\theta_{e'})^2(\Delta\phi_{e'})^2)^{3/2}(1 + (\Delta\theta_{p'})^2(\Delta\phi_{p'})^2)^{3/2}},$$

here $\Delta\theta_{e'/p'}$ and $\Delta\phi_{e'/p'}$ are angles measured in the spectrometers relative to the central angles in the e' and p' arms respectively. Under these assumptions the expression for experimental yield can be written as,

$$\begin{aligned} N(E_m^{exp}, \Delta E_m^{exp}, \mathbf{p}_m^{exp}, \Delta \mathbf{p}_m^{exp}) &= L * \int_{E_m, \Delta E_m} dE_m \int_{\mathbf{p}_m, \Delta \mathbf{p}_m} d^3p_m \int_{V_{exp}} d^6V \\ &\delta(E_m - (E_e - E'_{exp} - E'_{p_{exp}} + M_p - T_{exp}^{rec})) \delta(\mathbf{p}'_m - (\mathbf{p}_e - \mathbf{p}'_{exp} - \mathbf{p}'_{p_{exp}})) \\ &|J| A(\mathbf{p}'_{exp}) A(\mathbf{e}'_{exp}) \frac{d^6\sigma^R}{dE_{p'}^{exp}d\Omega_{p'}^{exp}dE_{e'}^{exp}d\Omega_{e'}^{exp}} \end{aligned} \quad (137)$$

Note that the right hand side of Equation 137 can be evaluated by Monte Carlo techniques and is the basis of the Monte Carlo SIMC described in Section 4.11. In evaluating this integral one calculates the radiation smeared cross-section under the PWIA whereby one can factorize the cross-section in terms of the e-p cross-section σ_{ep} and the radiation smeared spectral function $S^R(E_m, p_m)$ [13],

$$\frac{d^6\sigma^R}{dE_{p'}^{exp}d\Omega_{p'}^{exp}dE_{e'}^{exp}d\Omega_{e'}^{exp}} = E_{p'}^{exp} p_{p'}^{exp} \sigma_{ep} S^R(E_m^{exp}, p_m^{exp}). \quad (138)$$

So using this factorization gives,

$$\begin{aligned}
N(E_m^{exp}, \Delta E_m^{exp}, \mathbf{p}_m^{exp}, \Delta \mathbf{p}_m^{exp}) &= L * \int_{E_m, \Delta E_m} dE_m \int_{\mathbf{p}_m, \Delta \mathbf{p}_m} d^3 p_m \int_{V_{exp}'} d^6 V' \\
&|J| A(\mathbf{p}_{exp}') A(\mathbf{e}_{exp}') E_{p'}^{exp} p_{p'}^{exp} \sigma_{ep}^R S^R(E_m^{exp}, p_m^{exp}) \\
&\delta(E_m - (E_e - E_{exp}' - E_{p_{exp}'}' + M_p - T_{exp}^{rec})) \delta(\mathbf{p}_m' - (\mathbf{p}_e - \mathbf{p}_{exp}' - \mathbf{p}_{p_{exp}'}')). \quad (139)
\end{aligned}$$

Here $S^R(E_m, p_m)$ is the radiation smeared spectral function. Here another approximation is made, the cross-section σ_{ep}^R and the spectral function $S^R(E_m, p_m)$ does not change significantly within the bin of size $\Delta E_m, \Delta \mathbf{p}_m$. Under this assumption the cross-section and spectral function can be taken out of the integral. This gives us,

$$\begin{aligned}
N(E_m^{exp}, \Delta E_m^{exp}, \mathbf{p}_m^{exp}, \Delta \mathbf{p}_m^{exp}) &= \\
&L \bar{E}_{p'}^{exp} \bar{p}_{p'}^{exp} \bar{\sigma}_{ep}^R \bar{S}^R(E_m, p_m) |J| \int_{E_m, \Delta E_m} dE_m \int_{\mathbf{p}_m, \Delta \mathbf{p}_m} d^3 p_m \int_{V_{exp}'} d^6 V' \\
&\delta(E_m - (E_e - E_{exp}' - E_{p_{exp}'}' + M_p - T_{exp}^{rec})) \\
&\delta(\mathbf{p}_m' - (\mathbf{p}_e - \mathbf{p}_{exp}' - \mathbf{p}_{p_{exp}'}')) A(\mathbf{p}_{exp}') A(\mathbf{e}_{exp}'). \quad (140)
\end{aligned}$$

Here $\bar{E}_{p'}^{exp}, \bar{p}_{p'}^{exp}, \bar{\sigma}_{ep}^R$ and \bar{S}^R are averages over a bin of size $\Delta E_m, \Delta \mathbf{p}_m$. In the above expression the terms within the second integral can be seen as a Jacobian to go from $(E_{p_{exp}'}', \Omega_{p_{exp}'}')$, $(E_{e_{exp}'}', \Omega_{e_{exp}'}')$ space to E_m^{exp}, p_m^{exp} space, and because of the acceptance functions $A(\mathbf{p}_{exp}')$ and $A(\mathbf{e}_{exp}')$ it cannot be evaluated analytically and one must resort to Monte Carlo techniques in order to evaluate it. If one expresses $\epsilon'(\mathbf{p}', \mathbf{e}'; E_m, \mathbf{p}_m)$ as,

$$\begin{aligned}
&\int_{E_m, \Delta E_m} dE_m \int_{\mathbf{p}_m, \Delta \mathbf{p}_m} d^3 p_m \int_{V_{exp}'} d^6 V' \delta(E_m - (E_e - E_{exp}' - E_{p_{exp}'}' + M_p - T_{exp}^{rec})) \\
&\delta(\mathbf{p}_m' - (\mathbf{p}_e - \mathbf{p}_{exp}' - \mathbf{p}_{p_{exp}'}')) A(\mathbf{p}_{exp}') A(\mathbf{e}_{exp}') \\
&= \int_{E_m, p_m} \epsilon'(\mathbf{p}', \mathbf{e}'; E_m, \mathbf{p}_m) d^3 p_m dE_m, \quad (141)
\end{aligned}$$

where $\epsilon'(\mathbf{p}', \mathbf{e}'; E_m, \mathbf{p}_m)$ is function for converting the phase space in $(\mathbf{p}', \mathbf{e}')$ to phase space in terms of E_m, \mathbf{p}_m , using a Monte Carlo simulation of the spectrometers to evaluate the integral $\int_{E_m, \mathbf{p}_m} \epsilon'(\mathbf{p}', \mathbf{e}'; E_m, \mathbf{p}_m) d^3p_m dE_m$ as described below.

A Monte Carlo model of both the spectrometers with all the apertures and detector efficiencies is made. The experimental phase space is then populated with uniform distributions in $E_{e'}, E_{p'}, \Omega_{e'}$ and $\Omega_{p'}$ (the experimentally observable variables). This ensures that all combinations of these six variables (within the experimental acceptance) are sampled. In other words the probability of finding an event with $(E_{e'}, E_{p'}, \dots)$ can be written as,

$$P(E_{e'}, E_{p'}, \dots) = P(e')P(p'), \quad (142)$$

where

$$\begin{aligned} P(e') &= 1 && \text{for } \text{abs}(E_{e'}) \leq \Delta E_{e'}, \text{ and for } \text{abs}(\Omega_{e'}) \leq \Delta \Omega_{e'}, \\ &= 0 && \text{otherwise,} \\ P(p') &= 1 && \text{for } \text{abs}(E_{p'}) \leq \Delta E_{p'}, \text{ and for } \text{abs}(\Omega_p) \leq \Delta \Omega_p, \\ &= 0 && \text{otherwise.} \end{aligned}$$

Where $\Delta E_{e'}$ is the acceptance in $E_{e'}$ and $\Delta \Omega_{e'}(\theta_{e'}, \phi_{e'})$ is the angular acceptance of e' arm and $\Delta E_{p'}$ is the acceptance in $E_{p'}$ and $\Delta \Omega_p(\theta_p, \phi_p)$ is the angular acceptance of p arm. So the probability of having an event in a bin B of volume

$$\Delta E_{e'} \Delta E_{p'} \Delta \theta_{e'} \Delta \phi_{e'} \Delta \theta_{p'} \Delta \phi_{p'}$$

is 1, if it is within the experimental apertures. The Monte Carlo is used to generate N_{tried} events in a volume V_{gen} , and the Monte Carlo counts are then binned in E_m and p_m space. Now if there are N_{ij} counts in the bin (i, j) , of volume $\Delta E_m \Delta \mathbf{p}_m$

which we will define as unit volume and if $\mathcal{P}_{\mathcal{B}'}$ is the phase space volume defined by the experimental apertures, we can write,

$$\begin{aligned} \frac{N_{tried}}{V_{gen}} * \mathcal{P}_{\mathcal{B}'} &= \sum_{ij} N_{ij} \text{ (} ij \text{ is sum over all } E_m \text{ and } p_m \text{),} \\ &= N_{MonteCarlo} \end{aligned} \quad (143)$$

This implies,

$$\int \epsilon'(E_{e'}, \dots) dE_m d^3p_m = N_{MonteCarlo} * \frac{V_{gen}}{N_{tried}} = \mathcal{P}_{\mathcal{B}'}. \quad (144)$$

N_{tried} is the total number of trials in the Monte Carlo, V_{gen} generation volume in $(E_{e'}, \dots)$ space over which the events are randomly generated and $N_{MonteCarlo}$ is number of counts in all E_m and p_m space.

Now substituting the expression for $\int \epsilon'$ shown above one gets,

$$N(E_m^{exp}, p_m^{exp})_{B'} = L\bar{K}|J|\bar{\sigma}_{ep}\bar{S}^R(E_m^{exp}, p_m^{exp})\mathcal{P}_{\mathcal{B}'}, \quad (145)$$

here $\bar{K} = \bar{E}_{p'}\bar{p}_{p'}$. which brings us to the desired equation

$$\bar{S}^R(E_m^{exp}, p_m^{exp})_{B'} = \frac{N(E_m^{exp}, p_m^{exp})_{B'}}{L\bar{K}|J|\bar{\sigma}_{ep}\mathcal{P}_{\mathcal{B}'}}. \quad (146)$$

From here onwards the label *exp* is dropped with the understanding that all kinematic quantities such as E_m and p_m are calculated from measured experimental quantities. Note that the spectral function so extracted is smeared by radiation. The procedure to remove this radiation smearing is discussed in Section 4.14.

4.13.2 Procedure

For each of the electron kinematics data were collected over a range of proton kinematics. To get a complete picture one has to combine the data from all the

proton kinematics with their correct weights. The procedure used to do this is described below. The phase space acceptance is calculated by uniformly illuminating both spectrometers in the Monte Carlo simulation for each proton kinematics. The same number of successful events are generated for each kinematics. So for the $(i, j)^{th}$ bin in E_m, p_m space one gets,

$$P(i, j) = \frac{N_{ij} * V_{gen} * (\text{computer efficiency})}{N_{tried}}. \quad (147)$$

The computer efficiency used here arises from the refining of the limits in which events are generated, once partial information about the event is known. These refinements are based on the acceptance of the spectrometers and are done to increase the speed of generation.

The data is then binned in E_m and p_m bins and for each event, σ_{ep} the off shell cross-section multiplied by kinematic factors, is determined. Each event is then weighted by $L * \frac{1}{\sigma_{ep} E_{p'} p_{p'}}$. Thus for any given proton kinematics the spectral function for a $(i, j)^{th}$ bin is,

$$S^R(i, j) = \frac{1}{L * P(i, j)} \sum_{counts} \frac{1}{\sigma_{ep} E_{p'} p_{p'} |J|}, \quad (148)$$

and

$$[\Delta S^R(i, j)]^2 = \left(\left(\frac{\partial S^R(i, j)}{\partial P(i, j)} \right)^2 (\Delta P(i, j))^2 + \left(\frac{\partial S^R(i, j)}{\partial N(i, j)} \right)^2 (\sqrt{counts})^2 \right). \quad (149)$$

Here *counts* is the number of counts $N(i, j)$ in that bin.

Since there are multiple proton kinematics a weighted average for each bin over all kinematics is done. This is given by,

$$S_{av}^R(i, j) = \frac{\sum_{k=1}^n S_k^R(i, j) / (\Delta S_k^R)^2}{\sum_{k=1}^n 1 / (\Delta S_k^R)^2}, \quad (150)$$

and

$$[(\Delta S_{av}^R)^2(i, j)]^{-1} = \sum_{k=1}^n 1/(\Delta S_k^R)^2. \quad (151)$$

This gives us the average spectral function for each bin in E_m, p_m space. One must note that the spectral function extracted from the data using the procedure described above is not the spectral function as defined under PWIA. The spectral function thus obtained is a product of the average distorted spectral function and the transparency. Unlike the PWIA it includes the effects of final state interactions and other distortions of the scattered electron (like coulomb distortion) and the scattered proton. In addition these spectral functions are radiation smeared. However, the effects of radiation averaged over a bin in E_m and p_m can be removed from the distorted spectral function. The procedure for doing such a deradiation is described in Section 4.14.

Next one integrates over E_m to get the momentum distribution and integrate over p_m to get the energy distribution. This is done as follows,

$$\int S^R(i, j)dE = \rho(p_m) = \sum_{E_{min}}^{E_{max}} E_{bin} * S^R(i, j), \quad (152)$$

and

$$[\Delta \rho(p_m)]^{-1} = \sqrt{\sum_{E_{min}}^{E_{max}} \left(\frac{S^R(i, j)}{\Delta S^R(i, j)} \right)^2} * \rho(p_m), \quad (153)$$

similarly

$$\int S^R(i, j)d^3 p_m = 4\pi * \sum_{p_{min}}^{p_{max}} p_{bin} * p^2 * S^R(i, j), \quad (154)$$

and

$$[\Delta S^R]^{-1} = \sqrt{\sum_{p_{min}}^{p_{max}} \left(\frac{S^R(i, j)}{\Delta S^R(i, j)} \right)^2} * 4\pi * S^R. \quad (155)$$

4.14 Deradiating the Spectral Functions

In the procedure described above we have not accounted for the fact that the experimental spectra get modified due to internal and external bremsstrahlung radiation. These radiative processes have twofold effect on the data. Firstly the cross section of the process is modified and secondly the kinematics (energy, momentum, angle) of the electron are also changed. Although, these are real physical processes, they are experiment specific, and so most theoretical calculations do not take these effects into account. Thus, in order to get to the underlying physics, and also to directly compare with theoretical calculations, one needs to unfold these radiative processes from the spectral function extracted from the data.

As mentioned earlier the data is binned in missing energy E_m and missing momentum P_m , which means that for any given bin, the radiative processes would add some events from neighboring bins into this bin and also displace some events into the neighboring bins. So any unfolding procedure must recover events which were lost from a bin and also remove the events which radiated into the given bin.

The unfolding procedure described below uses the Monte Carlo simulation SIMC, this simulation uses model spectral functions and includes a mechanism to radiate the simulated events [72], which is based on the radiative correction formalism developed by Mo and Tsai [78]. For details about how radiative corrections are done in the Monte Carlo was discussed in Section 4.11.6.

Our unfolding procedure involved calculating a correction factor for each E_m , P_m bin. To get these correction factors, one runs the Monte Carlo simulation SIMC for a fixed number of successes and a fixed amount of charge, once with the radiation turned on and once with the radiation process turned off. Next both the radiated and the non-radiated events are binned in E_m and P_m , and each event

is weighted by the model spectral function. For events in the radiated spectra each event has an additional radiation weight which accounts for the events which radiated out of a given bin. The radiated events also have their kinematics slightly modified due to radiation, this accounts for events which radiate into a given bin. The events are also normalized with their correct luminosity. Thus the contents of bin (i, j) in the two cases mentioned above can be written as,

$$N_{i,j}^{rad}(Em, p_m) = \sum_{k=1}^n W_k * W_k^{rad} * L,$$

$$\text{where } n \text{ is the number of events in the bin}(i, j) \quad (156)$$

and

$$N_{i,j}^{norad}(Em, p_m) = \sum_{k'=1}^{n'} W_{k'} * L,$$

$$\text{where } n' \text{ is the number of events in the bin}(i, j). \quad (157)$$

Here L is the luminosity and W_k is the weight due to the model spectral function.

Now from these two quantities we can calculate the correction factor as,

$$C_{i,j}^{rad}(Em, p_m) = \frac{N_{i,j}^{rad}(Em, p_m) - N_{i,j}^{norad}(Em, p_m)}{N_{i,j}^{rad}(Em, p_m)}. \quad (158)$$

This correction factor accounts both for events radiating out of a given bin and those radiating into a given bin. To get deradiated spectral function one must apply this correction factor $C_{i,j}^{rad}(Em, p_m)$, to equation 4.13.2, which was derived in the previous section as the correct procedure for extracting spectral functions from data. That equation now becomes,

$$S^{derad}(i, j) = \frac{1}{L * P(i, j)} \left[\sum_{counts} \frac{1}{\sigma_{ep} E_{e'} p_{p'}} - C_{i,j}^{rad} * \sum_{counts} \frac{1}{\sigma_{ep} E_{e'} p_{p'}} \right], \quad (159)$$

and

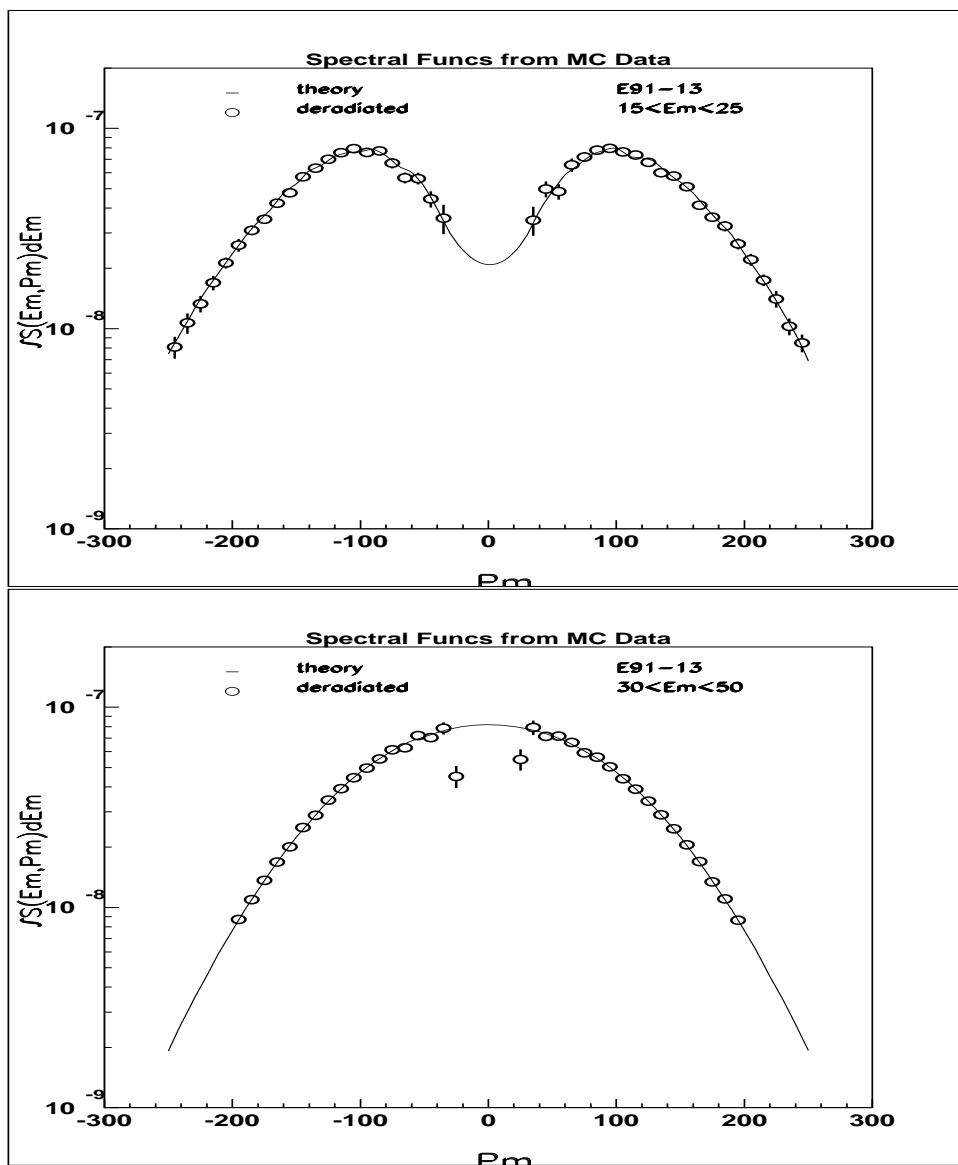


Figure 60: Spectral Function Extracted from Monte Carlo Data

$$\begin{aligned}
[\Delta(S^{derad}(i, j))]^2 &= ((\frac{\partial S^{derad}(i, j)}{\partial P(i, j)})^2 (\Delta P(i, j))^2 + (\frac{\partial S^{derad}(i, j)}{\partial C_{ij}^{rad}})^2 (\Delta C_{ij}^{rad})^2 \\
&+ (\frac{\partial S^{derad}(i, j)}{\partial N(i, j)})^2 (\sqrt{[Counts - Counts * C_{i,j}^{rad}]})^2).
\end{aligned} \tag{160}$$

Here *Counts* is the number of events $N(i, j)$ in the bin(i,j), and multiple proton kinematics are combined as described earlier,

$$S_{av}^{derad}(i, j) = \frac{\sum_{k=1}^n S_k^{derad}(i, j) / (\Delta S_k^{derad})^2}{\sum_{k=1}^n 1 / (\Delta S_k^{derad})^2}, \tag{161}$$

and

$$[(\Delta S_{av}^{derad})^2(i, j)]^{-1} = \sum_{k=1}^n 1 / (\Delta S_k^{derad})^2, \tag{162}$$

and as described in the previous section one can extract the momentum and energy distributions from the above quantities. We first try this out on Monte Carlo data where we should be able to get back the model spectral function from the radiated Monte Carlo data. The results of such an exercise is shown in Figure 60. At the highest and lowest p_m the phase space varies very rapidly and thus the averaging over these edge bins have larger systematic uncertainties.

This deradiation procedure is dependent on the model spectral function which is an essential input in this method. This model dependence is unavoidable, so one must use an iterative procedure in order to get the final spectral function from the data. The schematic of the iterative procedure is shown in Figure 61. The test involves comparing the new spectral function with that obtained from the last iteration, where the new spectral function is given by,

$$S_{new}(Em, p_m) = \frac{N_{model}(Em, p_m)}{N_{data}(Em, p_m)} S_{data}(Em, p_m). \tag{163}$$

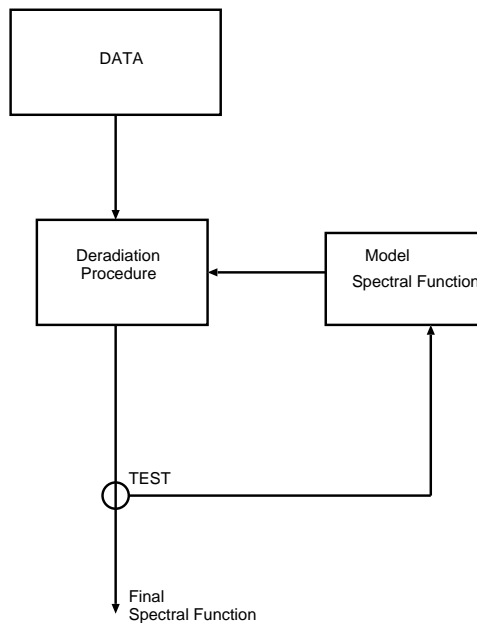


Figure 61: Schematic of the iterative procedure used to handle the model dependence

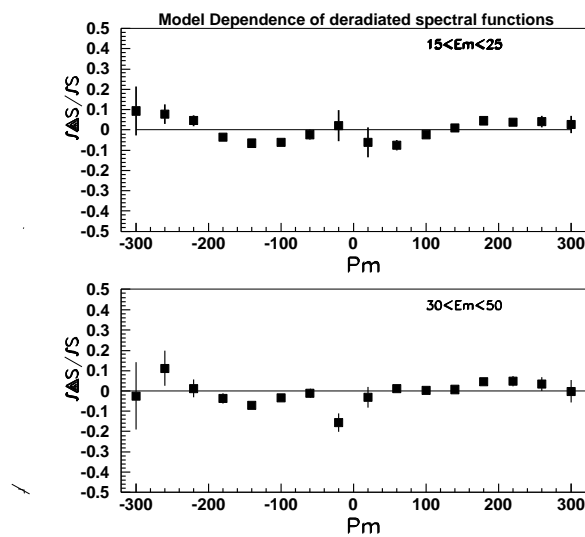


Figure 62: The model dependence of the deradiation process

The iteration is continued till the integral over all E_m and p_m of the new spectral function defined by Equation 163 differs by less than 1% from the integral of the spectral function from the previous iteration. This iterative procedure was tested by applying the procedure on simulated data created by using some model spectral functions which were deliberately distorted.

The model dependence of this procedure was estimated by using a starting model which had incorrect radii and shape. The radius of the erroneous model was 40% bigger. The final spectral function obtained was compared with the spectral function obtained by starting with a good model. The results are shown in Figure 62. Similar tests were also done with models where the p and s shells missing energy ranges were swapped. The procedure was successful in extracting the correct spectral function after several iterations.

The deradiated spectral functions extracted from the data by this procedure are spectral functions that include distortions due to FSI and also include nuclear transparency. As described in Section 4.13 they are the average of the distorted spectral function over the bin size ΔE_m and Δp_m . We will denote it as $S^D(E_m, p_m)$ from here onwards.

4.15 Longitudinal and Transverse Separation of the Spectral Function

The $(e, e'p)$ coincidence cross-section can be expressed in terms of four structure functions as shown,

$$\frac{d^6\sigma}{dE_{e'}d\Omega_{e'}dE_{p'}d\Omega_{p'}} = p'E_{p'}\sigma_{Mott}\frac{Q^2}{(\mathbf{q}^2\epsilon)} \times [\epsilon W_L(\omega, q, p') + W_T(\omega, q, p') + v_{LT}W_{LT}\cos\phi + v_{TT}W_{TT}\cos 2\phi]. \quad (164)$$

The interference terms W_{LT} and W_{TT} are a function of $\sin \theta_{pq}$ where θ_{pq} is the angle between the \vec{q} vector and the outgoing proton direction. In parallel kinematics θ_{pq} is zero, thus the interference terms drop out, giving,

$$\frac{d^6\sigma}{dE_{e'}d\Omega_{e'}dE_{p'}d\Omega_{p'}} = p'E_{p'}\sigma_{Mott}\frac{Q^2}{(\mathbf{q}^2\epsilon)}[\epsilon W_L(\omega, q, p') + W_T(\omega, q, p')]. \quad (165)$$

In the plane wave impulse approximation the cross-section can also be factorized as,

$$\frac{d^6\sigma}{dE_{e'}d\Omega_{e'}dE_{p'}d\Omega_{p'}} = p'E_{p'}\sigma_{ep}S(E_m, \mathbf{p}_m) \quad (166)$$

Where $\sigma_{ep} = \sigma_{Mott}\frac{Q^2}{\mathbf{q}^2\epsilon}[\epsilon|F_L(Q^2)|^2 + |F_T(Q^2)|^2]$. Here F_L and F_T are electric and magnetic proton form factors. This shows that the longitudinal-transverse character of the cross-section is governed by the nucleon current in this approximation. We also make the approximation that the difference in the proton distortion for W_L and W_T can be neglected. The accuracy of this approximation must be checked with a theoretical calculation.

Thus from the two Equations 165 and 166 we get the relation:

$$S(E_m, \mathbf{p}_m) = \frac{[\epsilon(E_m, \mathbf{p}_m)W_L(\omega, q, p') + W_T(\omega, q, p')]}{[\epsilon(E_m, \mathbf{p}_m)|F_L(Q^2)|^2 + |F_T(Q^2)|^2]} \quad (167)$$

Now one would like to separate the longitudinal and transverse spectral function using the above equation and the spectral functions extracted from the forward and backward angle data (which have different values of ϵ the photon polarization). However, there are variations in the Q (momentum transfer) and the ω (electron energy loss) acceptances between the forward and the back angle kinematics, (see Figure 63). In addition at the backward angle the \mathbf{p}_m acceptance is restricted to $\approx \pm 80$ MeV. This means we must restrict the forward angle spectral function to a

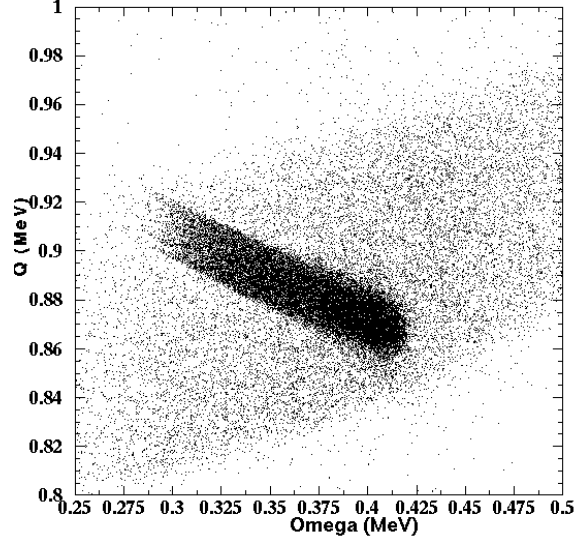


Figure 63: ω (electron energy loss) vs q for the forward and back angle data

similar range in \mathbf{p}_m in order to match the acceptances. Thus the spectral functions at the forward and backward angle for $\mathbf{p}_m < \pm 80$ MeV only is used to get the separated spectral functions.

Extraction of the spectral function from the data involves binning the data in small bins of missing energy (E_m) and missing momentum (\mathbf{p}_m). The q (momentum transfer) and the ω (electron energy loss) are averaged over these small bins, this removes the large variation in q . For $\mathbf{p}_m < \pm 80$ MeV the average value of q for each bin at the forward and backward angle is shown in Figure 64. It is clear that they match very well in this scheme.

Now since the forward and back angle measured (distorted) spectral functions correspond to same average q , ω and p' per bin, we can use Equation 167 to separate

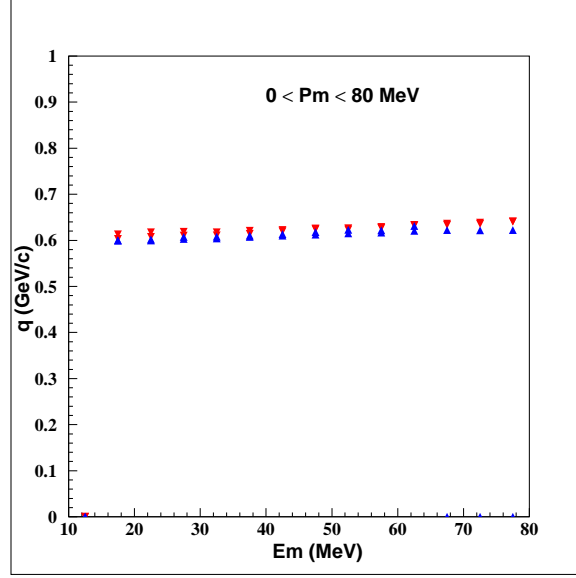


Figure 64: q for the forward (triangles) and back angle (inverted triangles) averaged over small bins in E_m and \mathbf{p}_m . The \mathbf{p}_m is restricted to ± 80 MeV. data

the longitudinal and transverse spectral functions. They are given by,

$$S^D(E_m) = \int S^D(E_m, \mathbf{p}_m) p_m^2 d\mathbf{p}_m = \int \frac{\epsilon W_L + W_T}{F(\epsilon)} p_m^2 d\mathbf{p}_m \quad (168)$$

where $F(\epsilon) = \epsilon |F_L(Q^2)|^2 + |F_T(Q^2)|^2$ and the integration over either E_m or \mathbf{p}_m is necessary to reduce the statistical errors. Representing all forward angle quantities with a superscript 'f' and all back angle quantities with the superscript 'b' we get,

$$W_L(E_m) = \frac{S_b^D(E_m)F^b - S_f^D(E_m)F^f}{\epsilon^b - \epsilon^f}, \quad (169)$$

and

$$W_T(E_m) = \frac{\epsilon^f S_b^D(E_m)F^b - \epsilon^b S_f^D(E_m)F^f}{\epsilon^f - \epsilon^b}. \quad (170)$$

From these we get the separated spectral functions as ,

$$S_L(E_m) = \frac{W_L(E_m)}{G_E^2}, \quad (171)$$

and

$$S_T(E_m) = \frac{W_T}{\frac{Q^2}{4M_p^2} G_M^2}. \quad (172)$$

Under the approximation that the virtual photon couples to a single nucleon the longitudinal and the transverse spectral functions are equal,

$$S_L = S_T. \quad (173)$$

Deviation from this PWIA result is usually measured in terms of the difference $S_T - S_L$ and the ratio of the response functions R_G . The the ratio R_G of the response functions is given by,

$$R_G = \sqrt{\frac{4M_p^2 W_T}{Q^2 W_L}} = \sqrt{\frac{S_T}{S_L} \frac{G_M}{G_E}}. \quad (174)$$

If $S_L = S_T$ then $R_G = \mu_p$.

4.16 Error Analysis

The separation of the longitudinal and the transverse spectral function uses the cross-section at the forward and the backward angles, so the uncertainty in the operated spectral functions is governed by the uncertainties at the forward and the backward angles. The uncertainty is given by,

$$\begin{aligned} \sigma_{L/T}^2 = & \left(\frac{\partial S_{L/T}}{\partial S_{fwd}} \right)^2 \sigma^2(S_{fwd}) + \left(\frac{\partial S_{L/T}}{\partial S_{bwd}} \right)^2 \sigma^2(S_{bwd}) + \\ & 2 \left(\frac{\partial S_{L/T}}{\partial S_{fwd}} \frac{\partial S_{L/T}}{\partial S_{bwd}} \right) \sigma(S_{fwd}) \sigma(S_{bwd}) Cov(S_{fwd}, S_{bwd}) \end{aligned} \quad (175)$$

Here S_{fwd}, S_{bwd} are the spectral functions at the forward and backward angles while $\sigma(S_{fwd}), \sigma(S_{bwd})$ are the uncertainties corresponding to these spectral functions and $Cov(S_{fwd}, S_{bwd})$ is the covariance between them.

For the statistical uncertainties of the separated spectral functions the covariance is zero and so just the first two terms in Equation 175 contribute. For example the statistical uncertainty in the separated response functions is given by,

$$\sigma_{W_L(\mathbf{p}_m)}^2 = \frac{(\sigma(S^b)^2 + \sigma(S^f)^2)}{(\epsilon_b - \epsilon_f)^2} \quad (176)$$

and

$$\sigma_{W_T(\mathbf{p}_m)}^2 = \frac{(\epsilon^f \sigma(S^b)^2 + \epsilon_b \sigma(S^f)^2)}{(\epsilon_f - \epsilon_b)^2} \quad (177)$$

The covariance between the two is given by,

$$Cov(W_L, W_T) = -\frac{\epsilon^f (\sigma(S^b))^2 + \epsilon_b (\sigma(S^f))^2}{(\epsilon_b - \epsilon_f)^2}. \quad (178)$$

The various terms in the above equations are as described in the previous section.

However, for certain systematic errors the covariance is non-zero and thus the forward angle and backward angle uncertainties are correlated. The systematic uncertainties in the spectral functions at the forward and backward angles can be divided into two types,

- Correlated systematic uncertainties - These are uncertainties in quantities (example, the central scattering angle) which are correlated between the forward and the backward angle data.
- Normalization type or scale type - These are uncertainties in the quantities which do not vary between the forward and backward angle points. (example,

the uncertainty in the absolute normalization and the uncertainty in the charge measurement,)

The correlated uncertainties propagate to the separated spectral functions in terms of Equation 175, while the normalization type uncertainties propagate directly into the separated spectral functions. In addition the normalization type uncertainties do not effect the ratio of the separated spectral functions R_G . Thus the ratio of the separated spectral functions has lower uncertainties than the separated spectral functions themselves. The systematic uncertainties of the ratio R_G is given by,

$$\left(\frac{\sigma_{R_G}}{R_G}\right)^2 = \left(\frac{\sigma_{W_L}}{W_L}\right)^2 + \left(\frac{\sigma_{W_T}}{W_T}\right)^2 - \left(\frac{2\text{Cov}(W_L, W_T)}{W_L W_T}\right). \quad (179)$$

Chapter 5

Results

5.1 Absolute Normalization

The elastic scattering of electrons from a liquid hydrogen target was used to determine the absolute normalization. Data were collected at each conjugate angle kinematic setting listed in Table. 6, where data were taken on nuclear targets. Because hydrogen has a single proton there is no final state interaction and thus the experimental yield should match the yield calculated using the PWIA simulation SIMC (Section 4.11). This is subject to conditions that all the detectors worked with 100% efficiency and that the spectrometer acceptance and the radiative effects and the e-p cross-section were modeled correctly by the simulation SIMC. Hence this method of comparing the experimental yield corrected for detector efficiencies and proton absorption with calculated yield is a very effective test of the spectrometer models and the radiative effects included in the simulation. Data were collected for both inclusive $H(e, e')$ scattering (singles) and exclusive $H(e, e'p)$ scattering (coincidence). The experimental yield, corrected for tracking efficiency and proton absorption was compared with the simulated yield. Both data and the simulated yields were normalized to the same luminosity. The set of constraints

Table 23: Nominal Data Constraints applied to the Hydrogen data

Cut	Values
HMS δ (%)	± 8
SOS δ (%) (p in SOS)	-10 - +20
SOS δ (%) (e ⁻ in SOS)	± 15
HMS X'_{tar} (rad)	± 0.075
HMS Y'_{tar} (rad)	± 0.040
SOS X'_{tar} (rad)	± 0.045
SOS Y'_{tar} (rad)	± 0.060
Missing Energy (MeV)	± 25
Missing Momentum (MeV/c)	± 50

applied to both the data and the simulation are listed in Table. 23. In addition to these nominal constraints it was also required that the invariant mass of each event correspond to the proton mass in order to ensure a true elastic scattering event. The coincidence yield for the $Q = 1.8$ GeV point is low because the gas mixture in the HMS wire chambers was bad following a power outage (at this setting the protons were detected in the HMS), which led to large inefficient regions in the chamber. In addition to this the wire chambers were not optimized for protons (they were optimized for electrons which have a different $\frac{dE}{dx}$ than protons). Under these circumstances we were unable to make a reliable measurement of the tracking and wire chamber efficiency of the protons. This behavior was observed only for hydrogen; the data on the other targets were taken several days later and were not effected.

The results of these comparisons are shown in Table 24 and in Figure 65, where the ratio of the experimental to the simulated yields are listed. In addition to comparing the total yields the reconstructed momentum and angular distributions

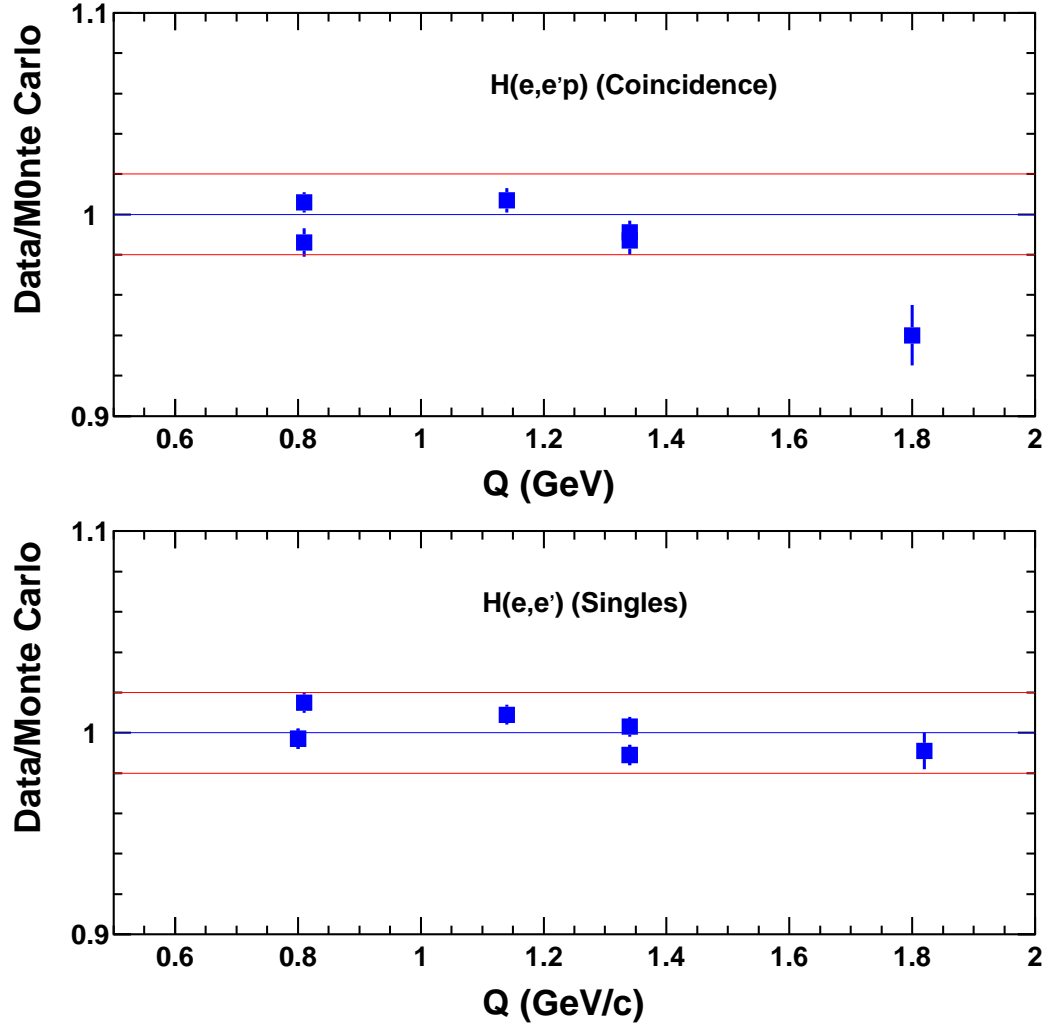


Figure 65: The ratio of the data yield to the Monte Carlo yield with the cuts shown in Table. 23. Top panel is for the $H(e, e'p)$ data while the bottom panel is for the $H(e, e')$ data. The coincidence yield at $Q = 1.8$ GeV is low because of a malfunctioning wire chamber, as described in the text.

Table 24: The ratio of the data yield to the Monte Carlo yield

Q (GeV)	Data/Simulation $H(e, e'p)$	Data/Simulation $H(e, e')$
0.80	1.006 ± 0.005	1.015 ± 0.005
1.13	1.007 ± 0.005	1.009 ± 0.005
1.34	0.991 ± 0.005	1.003 ± 0.005
0.80	0.986 ± 0.005	0.997 ± 0.005
1.35	0.987 ± 0.005	0.989 ± 0.005
1.82	$0.94 \pm 0.012 \pm 0.06$	0.991 ± 0.007

for both spectrometers were also compared with the simulated distributions, as discussed in Section 4.11, where a typical comparison was shown in Figure 56. The simulation reproduces the detailed shapes of all the reconstructed momentum and angles, however, the simulation underestimates the effects of multiple scattering and detector resolutions (as seen in the E_m spectra in Figure 66). This may be caused by the reconstruction and the optics of the spectrometer not being perfectly optimized and thus there might be some residual non-physical dependences of the missing energy and other reconstructed quantities. However, the good agreement in shapes of the reconstructed quantities tell us that our representation of the acceptance function is accurate but the representation of the resolution function is somewhat less accurate.

The constraint dependence of the spectrometer model and acceptance was studied by varying the constraints (Table. 23) on the reconstructed quantities (momentum, angles missing energy and missing momentum) by about ± 10 -15%. Each of the constraints on both spectrometer was individually varied.

The radiative effects included in the simulation were tested by comparing the missing energy spectra from the data and the simulation at high missing energies where all of the contributions to $H(e, e'p)$ scattering are due to radiative effects.

The results of these comparison are shown in Figure 66. The radiative tails are well reproduced up to missing energies of 80 MeV.

It was concluded from the studies and results listed above that the acceptance and the absolute normalization is known to 1.5% in this experiment.

5.2 Systematics of The Experiment

Some of the systematic uncertainties in the experimental data due to the experimental equipment and effects like proton absorption and random coincidences are discussed here. The remaining uncertainties are due to model dependencies of the physics simulation and these will be discussed in the Section 5.3.

5.2.1 Systematic Variations in The Data

Data were collected at six different kinematic settings (A-F, as listed in Table 6), at each kinematic setting the electron scattering angle was kept fixed while the proton angle was changed in steps of 4° . Under these conditions for the same experimental luminosity, the electron singles yield must remain constant over all proton angles in a given kinematic setting. However, the singles yield can be different due to variations in the detector efficiencies, variations in the detector calibration, variations in the beam and other time dependent systematic variations. Hence the changes in the singles yield greater than the expected statistical uncertainties was used as a measure of systematic variation in the data. The percent variation of the singles yield, defined as the standard deviation of the mean yield divided by the square root of the number of runs is listed in Table 25 for each of the kinematic settings. An alternative method for quantifying the systematic variations of the data involves, comparing the coincidence yield from duplicated data sets (runs).

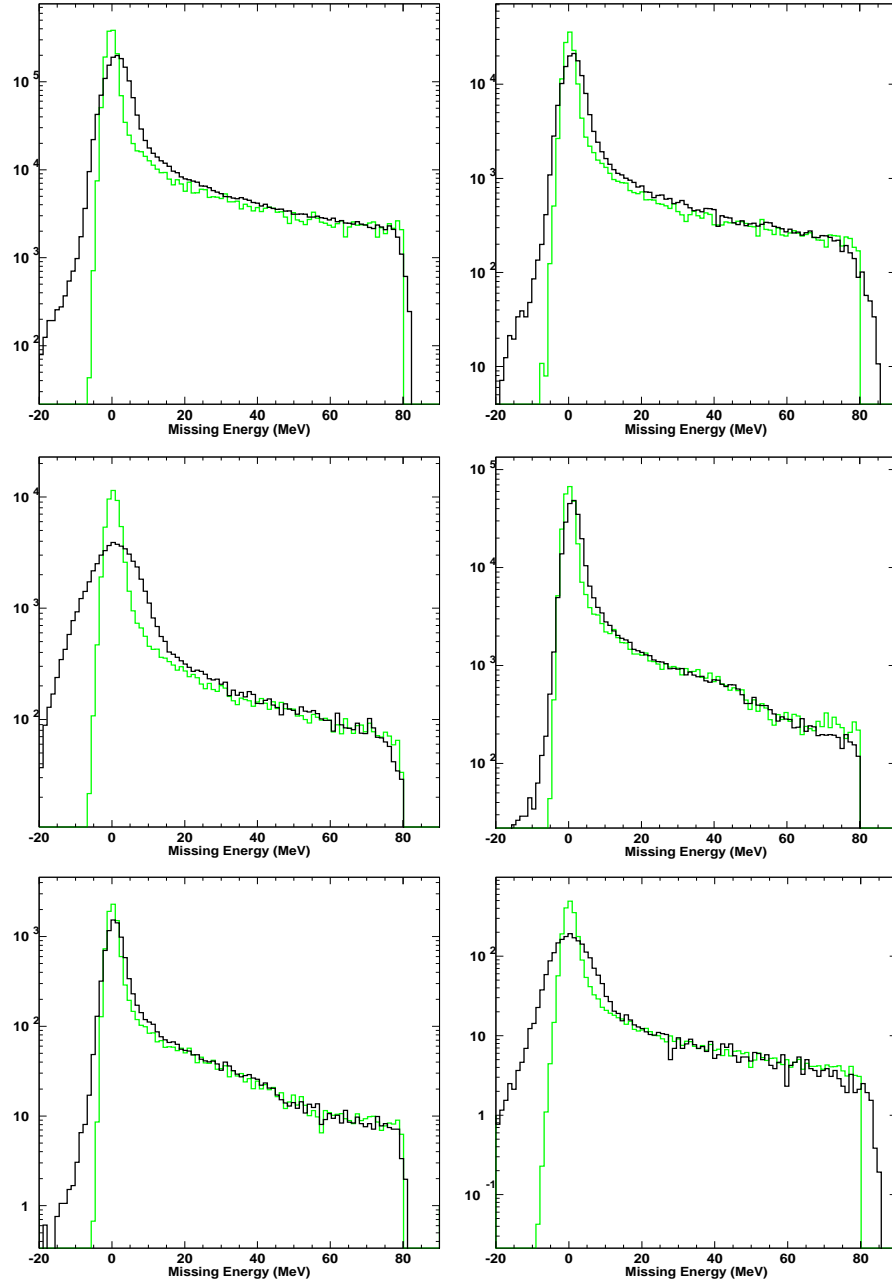


Figure 66: The reconstruction of $H(e, e'p)$ scattering

Table 25: Singles Yield Stability. The % variation in the average (weighted by charge) of the singles yields. The variation is calculated from the standard deviation of the mean over the square root of the number of runs. For Kinematics A-D, both Dec. 1995 and May 1996 data are used in the averages.

Kinematics	Target	% Variation in Singles Yield	Total # of Runs
A	C	0.22	16
B	C	0.33	13
C	C	0.19	17
D	C	0.37	16
E	C	0.69	13
F	C	1.02	9
A	Fe	0.26	14
B	Fe	0.31	11
C	Fe	0.29	18
D	Fe	0.57	14
E	Fe	0.63	14
F	Fe	0.35	11
A	Au	0.19	18
B	Au	0.49	12
C	Au	0.42	19
D	Au	0.82	10
F	Au	1.74	16

For each kinematic setting the central proton angle (conjugate angle) was duplicated for this purpose. The percent variation in the coincidence yield is listed in Table 26. The relatively large variation in yields for Kinematics F is due to the fact that half of the data were taken with the scintillator phototubes of one side of one plane (S2Y-) of the HMS hodoscope turned off. Excluding that data set the variation from data set to data set is much less than 2%. The statistical uncertainty is less than 1%. Again, with the exception of Kinematics F, the stability of the coincidence yields over all the kinematic settings are on the order of 1%. The statistical error is less than 1%.

Table 26: Coincidence Yield Stability. The % variation in the average (weighted by charge) of the coincidence yields for the conjugate angle setting at each kinematics. The variation is calculated from the standard deviation of the mean over the square root of the number of runs. For Kinematics A-D, both Dec. 1995 and May 1996 data are used in the averages.

Kinematics	Target	% Variation in Coin. Yield	Total # of Runs
A	C	0.59	4
B	C	0.66	5
C	C	1.02	5
D	C	0.80	4
E	C	1.05	6
F	C	2.13	2
A	Fe	0.49	4
B	Fe	0.15	3
C	Fe	0.15	2
D	Fe	1.24	2
E	Fe	0.85	2
F	Fe	0.48	4
A	Au	0.65	4
B	Au	0.50	5
C	Au	1.03	4
D	Au	1.02	5
F	Au	1.87	8

Table 27: The average over all runs (weighted by luminosity) of the discrepancy due to variation in constraints, for the three targets are shown.

Target	Average Discrepancy
C	0.997 ± 0.008
Fe	0.995 ± 0.010
Au	0.994 ± 0.011

5.2.2 Constraint Dependency

The nominal constraints (also called cuts) are listed in Table 22. The cut dependence of the data was tested by varying each constraint (cut) by 20%-30% and estimating the discrepancy between the yields with the nominal cuts and with the modified cuts. The discrepancy was measured for each kinematics and for each target and is averaged over data sets from each proton angle. The discrepancy was found to be less than 1% in most cases and, the average discrepancy for the three targets is shown in Table. 27. This study was used to assign a 1.0% systematic uncertainty to the data, due to constraint dependence. A detailed account of this study can be found in Ref. [71]

The experimental spectra for missing energy and the reconstructed angular distributions were aligned with the simulated missing energy spectra and angular distributions. The mean offsets needed to achieve alignment for each kinematic setting are listed in Table 28. In all cases the offsets were small (except for the energy offsets in Kinematics E). These offsets were due to small variations of the reconstruction of the events at the target with the kinematics. It was found that the SOS momentum reconstruction had a small dependence on the central momentum setting of the spectrometer and this along with the small variations in the beam position, the small misalignments in the magnets and the target caused these

Table 28: The mean offsets needed in order to align the experimental missing energy spectra and the reconstructed angular distributions with the simulated spectra

Kinematics	Target	Offsets				
			HMS		SOS	
		E_m	x'_{tar}	y'_{tar}	x'_{tar}	y'_{tar}
		(MeV)	(mrad)	(mrad)	(mrad)	(mrad)
Kine A	Carbon	2.95	0.71	1.34	-0.2	-1.46
	Iron	2.57	0.44	1.22	-0.09	-0.99
	Gold	1.02	0.71	0.91	0.11	-0.07
Kine B	Carbon	2.36	0.17	0.56	-0.46	-1.32
	Iron	2.08	0.14	0.35	-0.52	-0.36
	Gold	0.77	0.17	0.08	-0.52	-0.35
Kine C	Carbon	2.48	1.14	0.48	-0.56	-0.14
	Iron	2.34	1.05	0.31	-0.54	-0.15
	Gold	0.55	0.32	-0.09	-0.37	-0.57
Kine D	Carbon	0.52	0.94	-0.16	-0.04	-1.64
	Iron	1.05	0.23	-0.33	0.1	-1.81
	Gold	0.16	0.25	-0.64	0.08	-0.72
Kine E	Carbon	5.76	-1.41	-2.81	0.02	-1.48
	Iron	4.06	-1.73	-3.45	-0.4	-0.93
	Gold	-	-	-	-	-
Kine F	Carbon	1.97	1.40	0.43	-0.22	-1.70
	Iron	1.83	1.47	0.10	-0.28	-0.81
	Gold	0.62	1.35	-0.08	0.07	0.40

Table 29: Systematic Uncertainties in the Data.

Item	% Uncertainty in Data Yield
Current Measurement	1
Solid Target Thickness or Cryo. Target Thickness	0.1 0.5
HMS Tracking Eff.	1
SOS Tracking Eff.	1
Proton Absorption	
Kine A - E	0.5
Kine F	1.0
Background Subtraction	0.1
Constraint Stability	1.0
Run Stability	1
Sum in Quadrature	
Kine A-E	2.3
kine F	2.5

offsets.

5.2.3 Summary

The systematic uncertainties of the data are listed in Table 29. The sum in quadrature of all the sources of uncertainty is 2.3 % for kine A-E and 2.5 % for kine F. As mentioned earlier these do not include the systematic uncertainties due to the model dependence which is summarized in Section 5.3.

The results of this experiment are discussed in the next three sections. First we extract nuclear transparency using the IPSM spectral functions in a PWIA simulation employing the procedure described in Section 4.12. The experimental yield and the PWIA simulation yield is determined over a fixed phase space volume

defined by the constraints in Table 22 and they are averaged over the initial motion of the proton in the nucleus by averaging the transparency over all the proton angles covered, for each kinematics. The extracted transparency is compared with the transparency measured in previous experiments and a few theoretical models.

Next the distorted deradiated spectral functions are extracted from the data using the procedure outlined in Section 4.13 and Section 4.14. These spectral functions include the nuclear transparency, ie. they are the product of the distorted spectral function and the transparency (labeled $S_D(E_m, p_m)$). These spectral functions are then projected into E_m or p_m space, compared to a few theoretical calculations and used to extract transparency.

In the last section the measured distorted spectral functions are used to separate the longitudinal and the transverse spectral functions over a limited range in p_m . The ratio of the transverse to the longitudinal response is also calculated. By extending the longitudinal spectral function to all p_m under the assumption that the ratio of transverse to longitudinal is independent of p_m we calculate the transparency yet again using just the extended longitudinal spectral function. This can be thought of as a rough estimate of the transparency of protons knocked out in single nucleon processes.

5.3 Transparency

Figures 67-69 compare the missing energy spectra from the three nuclear targets (C, Fe, Au) with the corresponding simulated spectra. The measured and simulated spectra have been normalized to have the same number of counts, to assist in comparing the detailed shapes. The carbon spectra show that the data has less strength than the simulation in the dip region between the $1p_{3/2}$ and the $1s_{1/2}$

shells. This effect was studied by moving the s shell peak to higher missing energies. The data suggests that the s shell peak is a few MeV higher than what is used in the model, which is based on previous experiments.

The iron spectra show the largest discrepancy between simulation and experiment. The iron spectra have their strength shifted and the simulated shell widths of the deeply bound states do not match the data. However, since we integrate over missing energies between 0 and 80 MeV, the transparency calculation are insensitive to the details of the shape of the missing energy spectra. This has been tested and is discussed in Section 5.2.2. Spectral functions were also extracted (Section 5.4) from the data and used to calculate the transparency.

The nuclear transparency as a function of proton angle for the three targets is shown in Figures 70-72. The upper panels compare the data and simulation yields as a function of proton angles, illustrating the coverage of the Fermi cone. The lower panels show the transparency as a function of proton angles with the solid lines corresponding to the transparency averaged over all proton angles, this illustrates the left-right (about the conjugate angle) asymmetry of the transparency seen in the data. This asymmetry is caused by the LT interference term in the offshell cross-section which is in excess of the LT interference strength already present in the deForest prescription σ_{cc1} . This asymmetry decreases with Q^2 and it is a small asymmetry at $Q^2 = 3.2 \text{ GeV}^2$ where we have data only on one side of \vec{q} .

As mentioned earlier the weighted average of the transparency at all proton angles is taken as the transparency at a given Q^2 . Table 73 lists the transparency as a function of Q^2 for the three targets. The uncertainty in the transparency quoted in this table is the 1% statistical uncertainty and 2.3% (2.5% for kinematics F) systematic uncertainty and the model-dependent uncertainty added in quadrature.

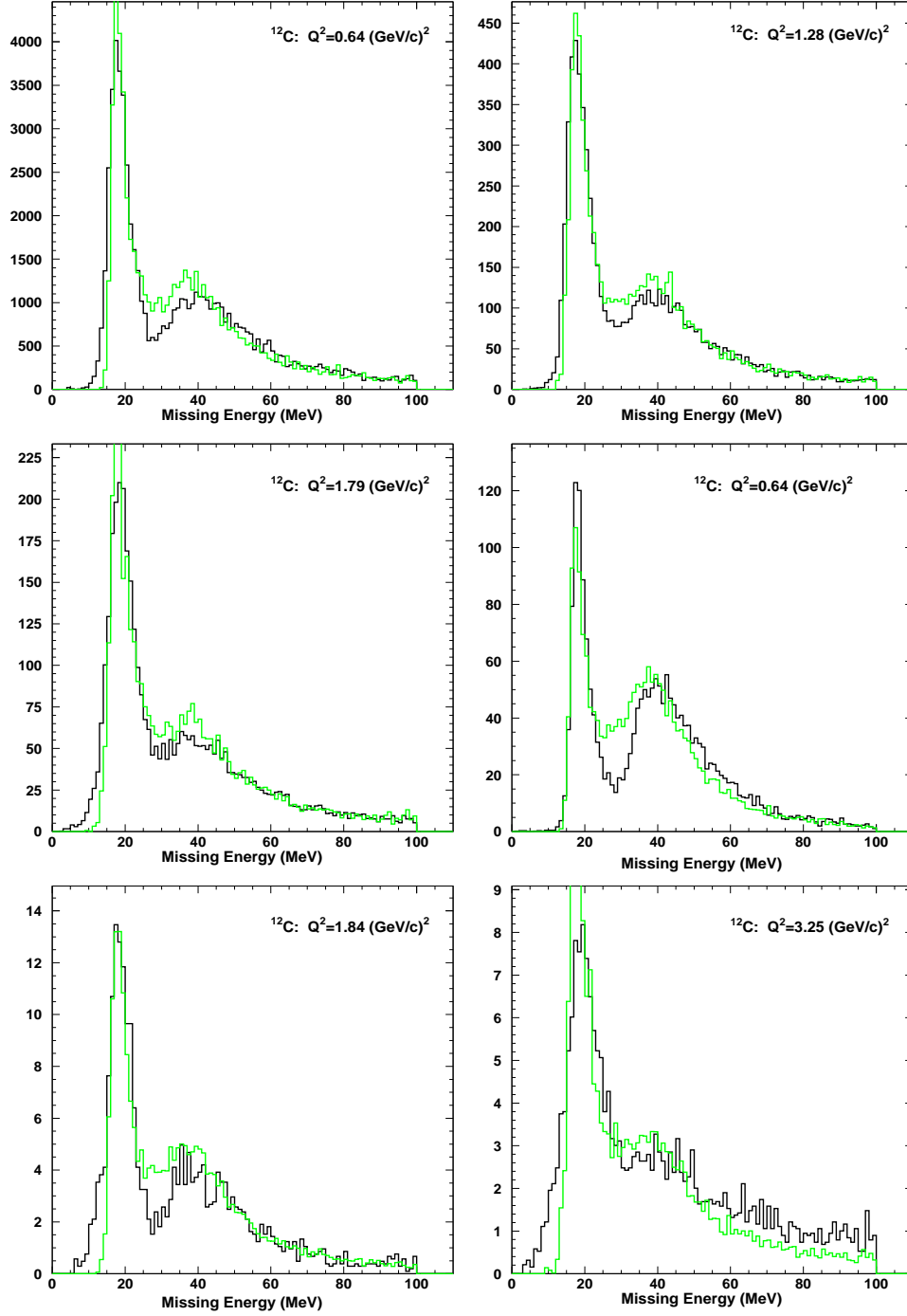


Figure 67: Carbon Missing Energy Spectra Compared to Simulated Spectra. Data are black and simulation is grey. Kinematics are A-F, left to right, then down.

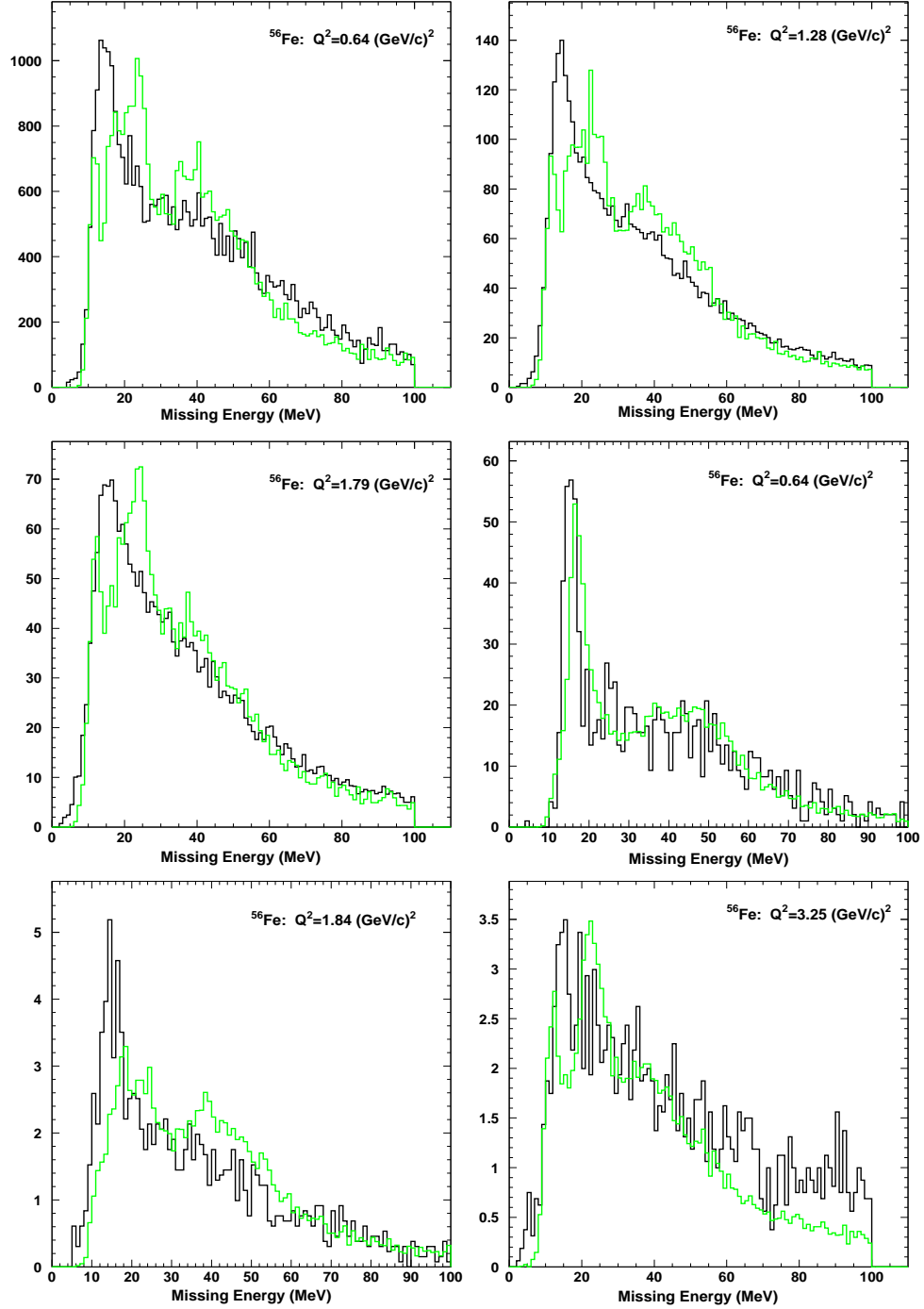


Figure 68: Iron Missing Energy Spectra Compared to Simulated Spectra. Data are black and simulation is grey. Kinematics are A-F, left to right, then down.

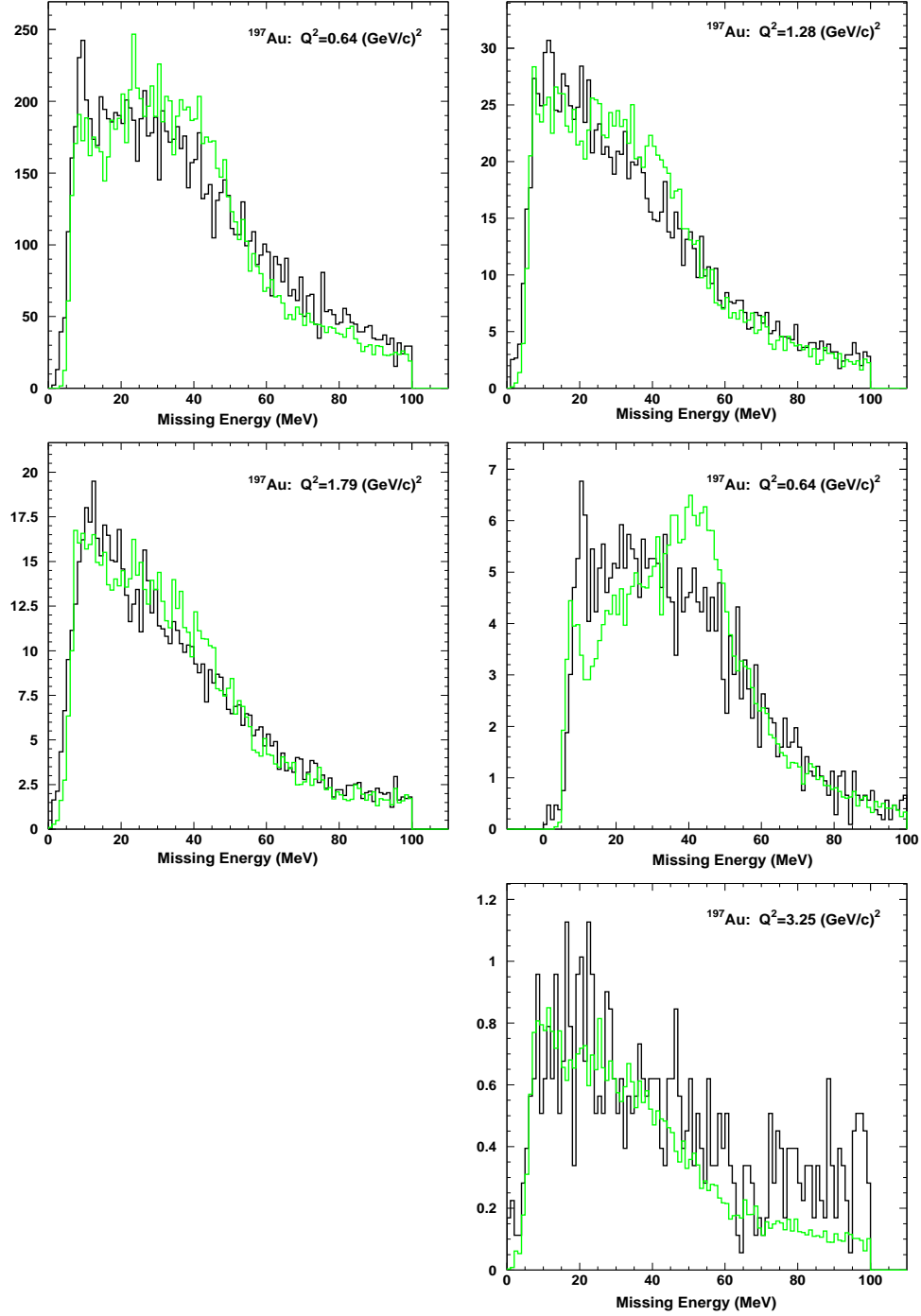


Figure 69: Gold Missing Energy Spectra Compared to Simulated Spectra. Data are black and simulation is grey. Kinematics are A-F, left to right, then down. Note gold data were not taken for Kinematics E.

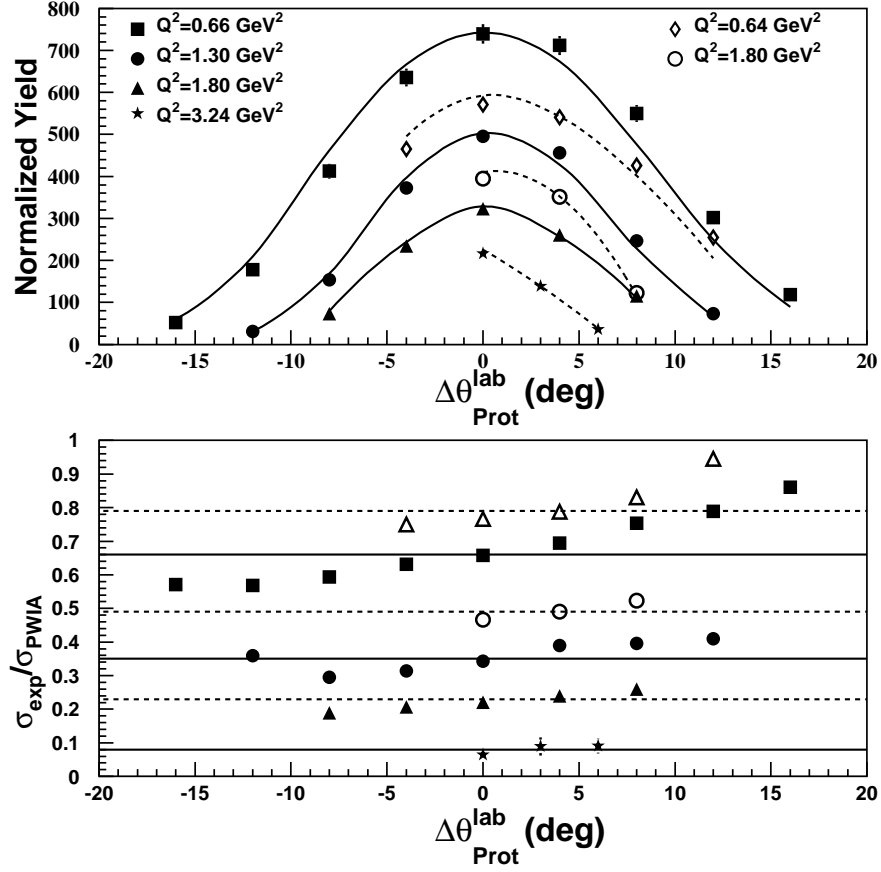


Figure 70: The upper panel displays the coincidence yield for ^{12}C . For clarity the yields at the forward angle points kine A-F (solid symbols) have been scaled by 0.13, 0.8, 1.0, 14.0 and the back angle points kine D and E (open symbols) have been scaled by 2.6 and 18 respectively. The lower panel shows the transparency which have been offset by 0.05, -0.25, -0.35, -0.5 respectively for kine A-F and by 0.15 and -0.10 respectively for kine D and E. The solid lines are the simulated yield normalized to the measured transparency. Statistical uncertainties only are shown.

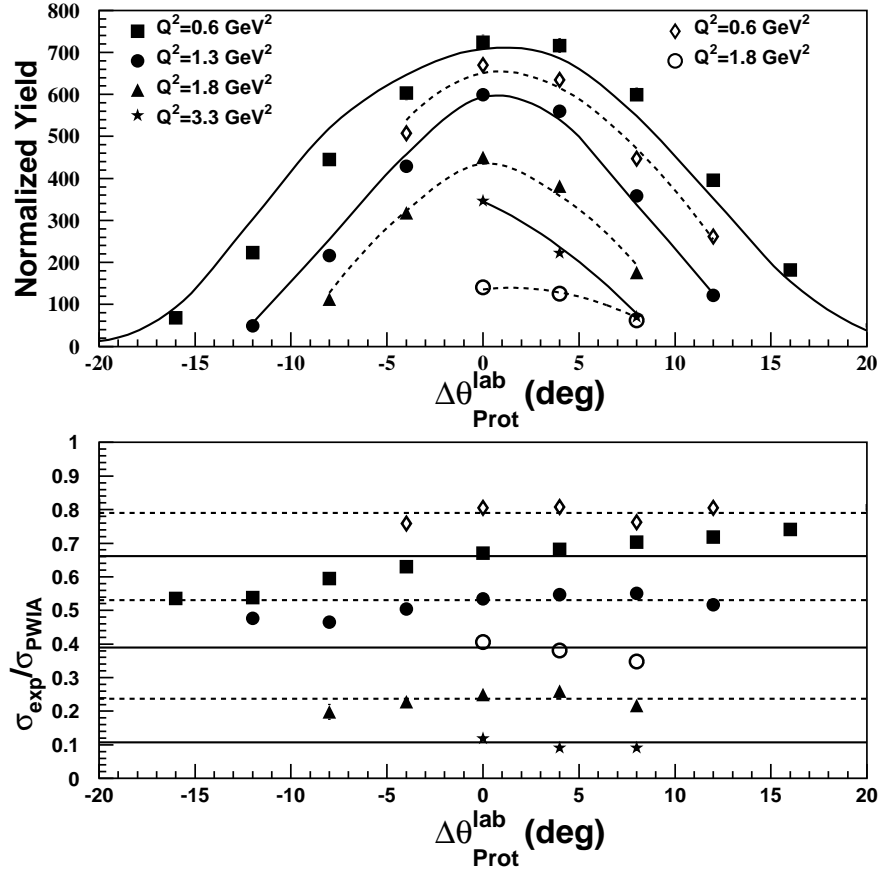


Figure 71: The upper panel displays the coincidence yield for ^{56}Fe . For clarity the yields at the forward angle points kine A-F (solid symbols) have been scaled by 0.21, 1.6, 2.25, 35.0 and the back angle points kine D and E (open symbols) have been scaled by 5 and 12 respectively. The lower panel shows the transparency which have been offset by 0.20, 0.10, -0.15, -0.3 respectively for kine A-F and by 0.25 and -0.05 respectively for kine D and E. The solid lines are the simulated yield normalized to the measured transparency. Statistical uncertainties only are shown.

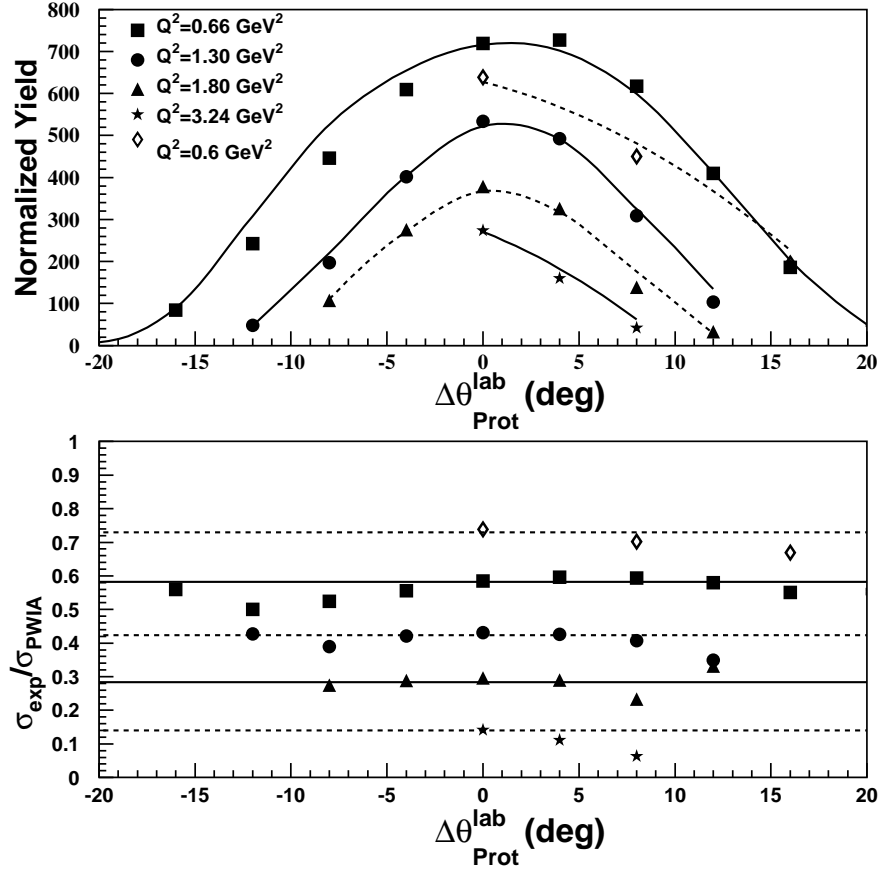


Figure 72: The upper panel displays the coincidence yield for ^{197}Au which have been scaled by 0.55, 0.4, 5.5, 80.0 and 15.0 for clarity and correspond to the forward angle points kine A-F and the backward angle point kine F respectively. The open points correspond to the backward angle point at Q^2 0.6 GeV^2 (kine D). The lower panel shows the transparency which have been offset by 0.2, 0.1, 0.0, -0.15 and 0.3 respectively for kine A-F and kine D. The solid lines are the simulated yield normalized to the measured transparency. Statistical uncertainties only are shown.

Table 30: Nuclear Transparency. The error bars include the systematic uncertainties and the model dependent uncertainties in the experimental data yields with the statistical uncertainties in parenthesis.

Kinematics	Q^2	Transparency		
	$(\text{GeV}/c)^2$	^{12}C	^{56}Fe	^{197}Au
A	0.64	$0.61 \pm 0.03(0.02)$	$0.47 \pm 0.05(0.01)$	$0.38 \pm 0.04(0.01)$
B	1.28	$0.60 \pm 0.03(0.02)$	$0.44 \pm 0.05(0.01)$	$0.32 \pm 0.04(0.01)$
C	1.79	$0.57 \pm 0.03(0.01)$	$0.40 \pm 0.04(0.01)$	$0.29 \pm 0.03(0.01)$
D	0.64	$0.64 \pm 0.03(0.02)$	$0.54 \pm 0.06(0.01)$	$0.43 \pm 0.05(0.01)$
E	1.84	$0.59 \pm 0.03(0.01)$	$0.44 \pm 0.05(0.01)$	-
F	3.25	$0.58 \pm 0.03(0.02)$	$0.42 \pm 0.04(0.01)$	$0.28 \pm 0.03(0.01)$

Figure 73 shows the transparency as a function of Q^2 along with results from previous experiments at MIT-Bates (^{12}C , ^{58}Ni , ^{181}Ta targets) and SLAC NE18 (^{12}C , ^{56}Fe , ^{197}Au targets) and Figure 74 shows the transparency as a function of Atomic Number A. The results of this experiment are in agreement with the results of NE-18, but the statistical uncertainties are much lower. The backward angle points (kinematics D and E) are higher than the forward angle points for all targets. This indicates that there might be an excess of transverse strength (since the backward angle points are more transverse in nature), compared to what is included in the PWIA model. This also highlights the need for performing a L and T separation using this data to investigate how much of the transverse strength is single particle in nature. Such a separation was performed and the results (Section 5.5) show an enhancement in the transverse spectral function suggesting contributions from multi-nucleon processes such as meson exchange currents.

The relative independence of T with Q^2 at the larger Q^2 puts constraints on the media modification of the proton form factor, since the Q^2 dependence of T is not effected by the uncertainties in the model spectral function or the correlation

corrections. There is $2.5 \pm 2.4\%$ rise in transparency at the two highest Q^2 points, averaged over the three targets. Since the free p-N cross-section decreases by $\approx 2\%$ over this range in Q^2 the media modification of the e-N cross-section must be $< 2\%$.

5.3.1 Model Dependence

All the components of the simulation (the off-shell e-p cross-section, the radiative effects and the model IPSM spectral functions) contribute to the model dependence of the transparency results. In addition the correlation corrections mentioned earlier in this section also contribute to the model dependence.

The model dependence of the off-shell e-p cross-section was checked by using an alternative prescription σ_{cc2} instead of the nominal σ_{cc1} . The simulation yields were found to be $\approx 1.5\%$ lower, and varied by $\pm 0.5\%$ with target and kinematics. Thus the systematic uncertainty due to the model dependence of the e-p cross-section is quoted as $\pm 1.5\%$. A recent review of this problem is given by Pollock *et al.* [83], where six different prescriptions are compared. In the kinematic range where most of the world data exists the variation between the different prescriptions was about 3.0% . However since σ_{cc1} is the most popular prescription, it was used in this experiment to facilitate comparison with previous experiments.

The model dependence of the radiative effects were determined by studying the large missing energy and large missing momentum region of the simulated $H(e, e'p)$ scattering. The large missing energy and large missing momentum region is dominated by internal bremsstrahlung. The variation in the ratio of experimental to simulated yield when the upper limit of the missing energy range is varied, was used to determine the uncertainty in the internal correction procedure. A 1.5% variation in this ratio was observed when the missing energy limit was varied

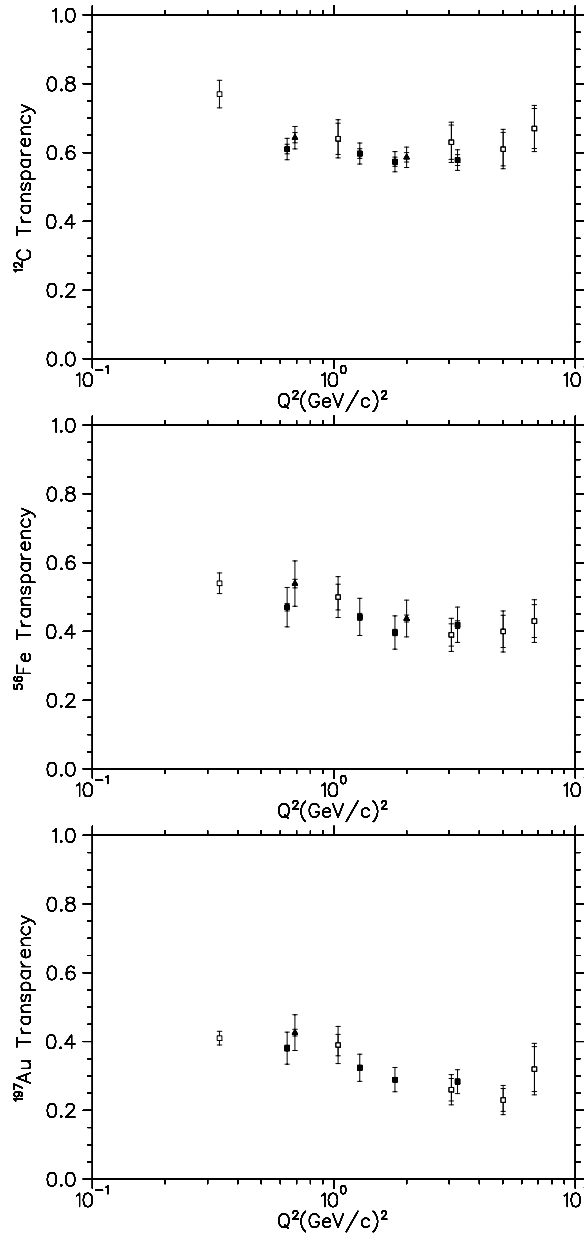


Figure 73: Transparency vs. Q^2 . ^{12}C , ^{56}Fe , and ^{197}Au are shown top to bottom. The filled symbols are E91-013 data, and the open symbols are data of Makins *et al.* (with the exception of the Bates data for ^{12}C , ^{58}Ni , and ^{181}Ta at $Q^2=0.34$ (GeV/c) 2). The outer error bars are the total uncertainty (systematic, statistical and model dependent) the inner error bars are statistical and systematic added in quadrature. The Q^2 of both back angle points (D and E) are offset slightly for clarity. In all cases these back angle points have the slightly larger transparency for a given Q^2 . (Horizontal log scale.)

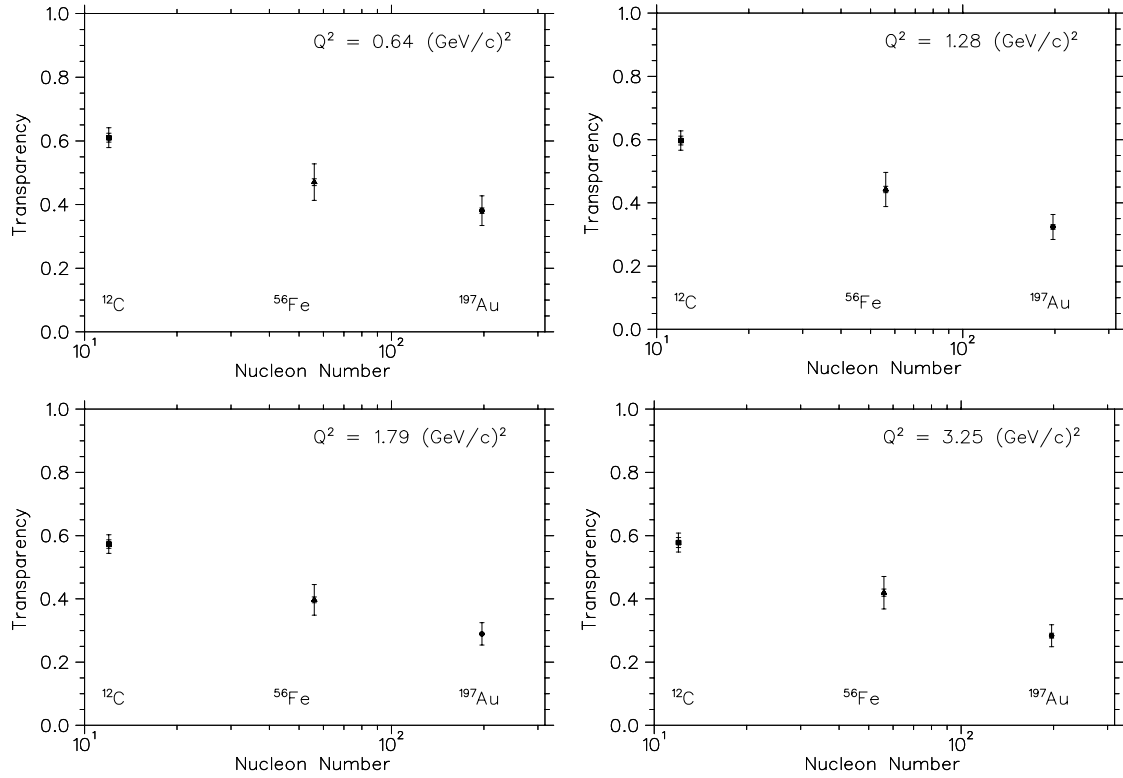


Figure 74: Transparency vs Nucleon Number. The squares are ^{12}C , the triangles are ^{56}Fe , and the circles are ^{197}Au . The kinematics are A,B,C,F left to right and then down. The error outer bars are total uncertainties and the inner error bars are systematic and statistical uncertainties added in quadrature. The back angle points (C and E) have been omitted for clarity. (Horizontal log scale.)

from 50 MeV to 130 MeV. In addition to this the $H(e, e'p)$ yields for alternative schemes of simulating the internal bremsstrahlung differed by $\approx 2\%$, [79]. These results were used to assign an systematic uncertainty of 2% to the simulation of internal bremsstrahlung. The uncertainty in simulating the radiative effects due to external bremsstrahlung was estimated to be 2% [79] from the changes in the simulated yields when the radiation lengths of the C and Fe were varied.

The systematic uncertainty due to the model spectral function was calculated by estimating the uncertainty in the momentum distribution and uncertainty in the energy distribution. The uncertainty in the momentum distribution is directly related to the uncertainty in the widths of the distributions. The linearity of the transparency as a function of the proton angle, constrains the uncertainty in the momentum distribution to $\sim 4.0\%$. [71]. The uncertainty in the energy distribution was estimated from the sensitivity of the transparency to E_m constraints. In addition the position of the centroids of the $1s_{1/2}$ and $1p_{3/2}$ peaks were varied by about 5 MeV in the nominal IPSM model for carbon. In this test the yields changed by $<0.7\%$. From these tests the uncertainty in the energy distribution was estimated to be 2%. Thus the net model dependent uncertainty for the three targets is the sum in quadrature of the momentum and energy uncertainties, i.e. 4.5 %. As a test, the change in the simulated yields when an alternative model spectral functions is used were calculated. For carbon a model spectral function based on DWIA calculations done by Zhalov [84] was used and the yields were found to differ by 2% for the conjugate proton angle in Kinematics A,B and C. However the DWIA model used in this test was not significantly different from the PWIA model especially for $|p_m| < 150$ MeV which is covered by the conjugate angle. Hence this is not a strong test of the model dependence. But still the

results were well within the quoted 4.5 % uncertainty. For the iron target an alternative model spectral function was obtained from Hartree-Fock calculations done by Horowitz [85]. Using the same shell energy widths as the nominal IPSM model the yields were found to change by about 8%. However we will see in the next section that the transparency extracted using the the measured spectral function are consistent with the results of this section indicating that the models used here are accurate to better than the 4.5% uncertainty.

The systematic uncertainty in the correlation correction factor was estimated from the changes in simulated yields when two different correlated spectral functions were used as described in Reference [49]. They were found to be 3% for carbon and 6% for iron and gold. In addition to this the correlation corrections were calculated for ^4He , ^{16}O and nuclear matter by Benhar [86]. He found that the corrections were A independent when he integrated over all E_m but were A dependent when the E_m was cut off at 80 MeV. This is consistent with the model of the correlation correction, which distributes a constant fraction of the nucleons at lower missing energies to higher missing energies. These studies and other studies show that the correlation correction is the largest theoretical/model uncertainty in this experiment.

A list of systematic uncertainties due to various components of the simulations is shown in Table 31. This table also has the sum in quadrature of all the different sources for all three targets.

Since the model uncertainties are different for each target they will effect the study of A dependence of the transparency and the comparison to experimental results extracted using different models. However, because the model dependence is almost independent of Q^2 , one can study the Q^2 dependence of the transparency without including the model dependence.

Table 31: Model-Dependent Uncertainties.

Item	% Uncertainty in Simulated Yield
Internal Radiation	2
External Radiation	2
σ_{ep}	1.5
Model Spectral Function:	
^{12}C	4.5
^{56}Fe	4.5
^{197}Au	4.5
Correlation Correction:	
^{12}C	3
^{56}Fe	6
^{197}Au	6
Sum in Quadrature:	
^1H	3.2
^{12}C	5.7
^{56}Fe	8.0
^{197}Au	8.0

5.3.2 Comparison to Theoretical Models

The theoretical calculations discussed in this section are based on -

- DWIA which was discussed in Section 2.4,
- Correlated Glauber calculations introduced in Section 2.6.3
- Inter Nuclear Cascade (INC) models.

DWIA Calculations

Most DWIA calculations found in the literature have been done for low Q^2 , some authors put the limit of their validity at $Q^2 \leq 2 \text{ GeV}^2$ [87]. Some of the popular calculations include DWEOPY developed by Guisti et al. [23]. However, these calculations are not valid at the higher Q^2 values of E91-013. The DWIA calculation presented here is based on the effective empirical interaction (EEI) developed by J. Kelly [88]. The parameters of the optical potential in this calculation, used to describe the final state interactions of the outgoing proton, were determined from fits to inelastic proton scattering data over a range of proton kinetic energies, $100 < T_p < 650 \text{ MeV}$. In these calculations nuclear matter density was folded with the density dependent p-N interaction. Some authors [89] have shown that the medium modifications of the p-N interaction is an intrinsic part of these DWIA calculations. Figure 75 compares the extracted transparency with the EEI calculations.

From the figure we can see that the calculation predicts the transparency of carbon at low Q^2 very well but under estimates the iron and the gold transparency. The kinks in the calculation are due to the variations in the independent data sets used in obtaining the EEI. The discrepancy gets bigger with increasing target mass.

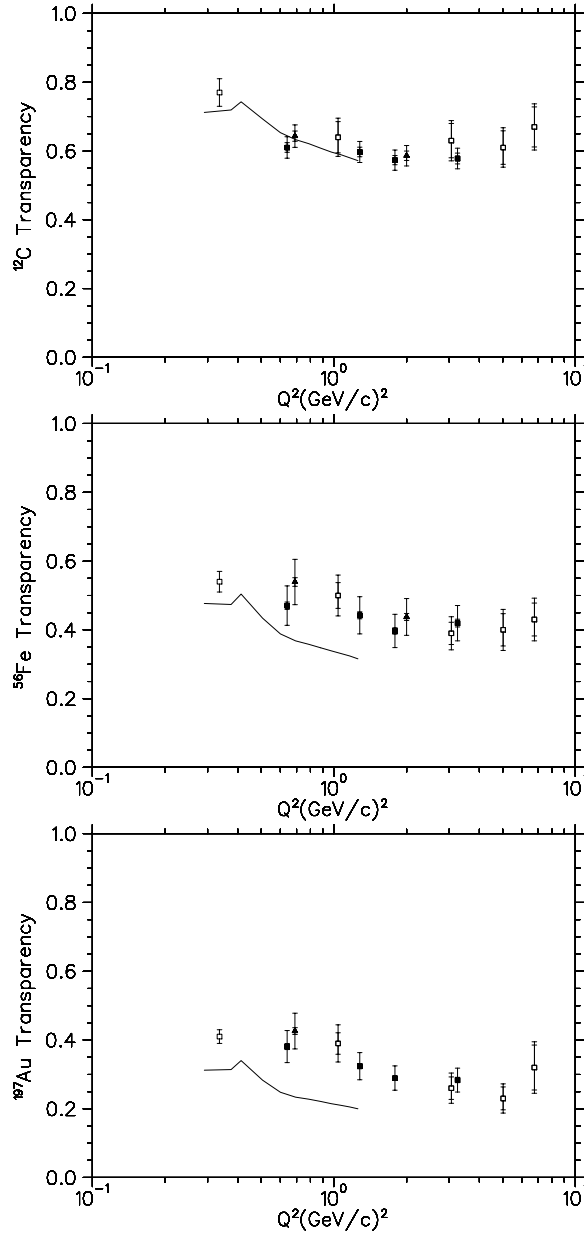


Figure 75: The EEl calculation of transparency for ^{12}C (top), ^{56}Fe (middle) and ^{197}Au (bottom) compared to the data (data is same as described in Figure 73, horizontal log scale).

The authors explain this discrepancy in terms of the multi-nucleon absorption of the virtual photon. Since the calculation does not include this reaction channel the it underestimates the experimental transparency. However, the L-T separation described in Section 5.5 do not support such a claim.

Correlated Glauber Calculations

Glauber calculations are done under the assumption that the struck nucleon moves undeflected along a straight trajectory parallel to its original direction. The nuclear transparency is calculated in terms of the probability of the struck nucleon to not encounter other nucleons on its way out, integrated over all paths. Glauber calculations are valid for high Q^2 only and some authors put the limit of applicability at 2.0 GeV^2 [88, 92] while others assert they should apply down to 500 MeV^2 . The correlations between the proton and other nucleons are included in terms of the pair correlation function as defined in Section 2.6.3. However, the correlation between the spectator nucleons is neglected in some calculations (eg. Gao et al. [90]). As mentioned in Section 2.6.3 the “correlation hole” $(\rho_p(\mathbf{r}')\rho_a(\mathbf{r}'') - \rho_{pa}(\mathbf{r}', \mathbf{r}''))$ is positive and so the pair correlation function enhances the transparency. Figure 76 shows the experimentally measured transparency compared to the Glauber calculations of Gao et al. [90].

These calculations used nuclear wave functions generated by Pieper [91] using the Argonne V18 potential. The transparency was calculated by averaging the probability of the proton to exit without encountering other nucleons (the total p-N cross-section was used to calculate the probability) over multiple configurations of the nucleons in the nucleus, using a Monte Carlo technique. From Figure 76 it is clear that the calculations agree with the measured transparency of carbon but under estimates the transparency with increasing target mass. The calculation

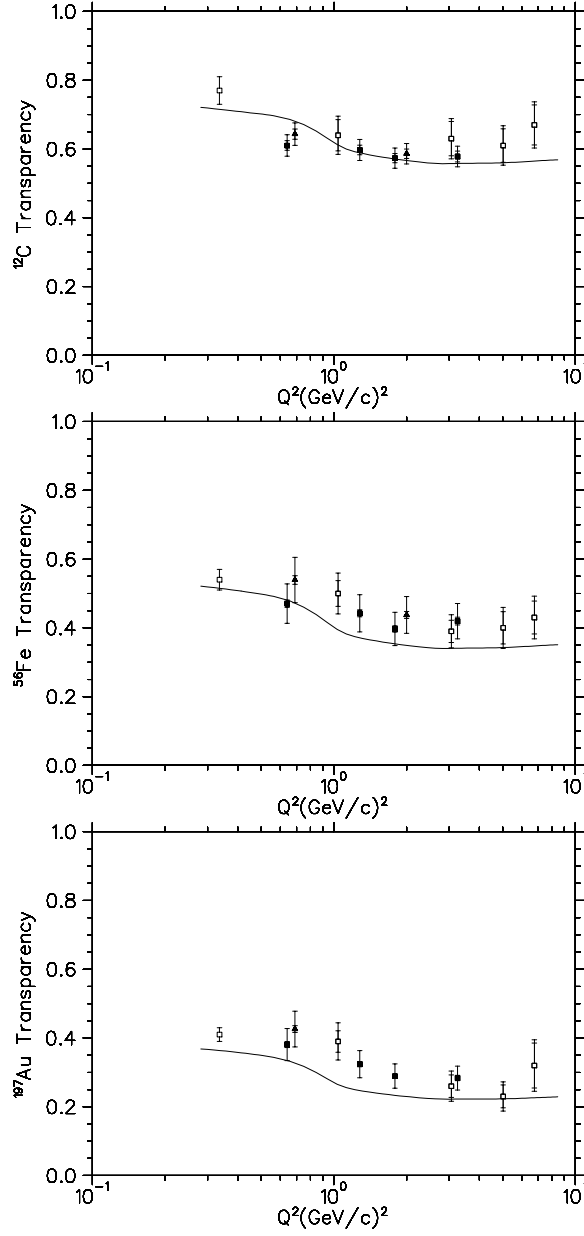


Figure 76: Correlated Glauber calculation of transparency for ^{12}C (top), ^{56}Fe (middle) and ^{197}Au (bottom) compared to the data (data is same as described in Figure 73, horizontal log scale).

also predicts a stronger Q^2 dependence in carbon than is measured.

In Figure 77 the measured transparency is compared to yet another Glauber type calculation, this one is from Nikolaev et al. [92]. In these calculations the Glauber approximations were applied but a simple Fermi parameterization was used for the nuclear density and only inelastic p-N cross-section was used to calculate the transparency. These calculations do not include any correlations between the nucleons. The author claims that the reduced density around the proton due the repulsive p-N interaction at short distances (hole effect) cancels with the increased interaction between the proton and the spectator nucleons due to the correlations between the spectator nucleons(spectator effect). The calculated transparency seems to overestimate the carbon measurement but agrees with the measurements on other targets within the systematic uncertainties.

Inter Nuclear Cascade Calculations

This calculation was done by Golubeva et al. [93] and involves a scheme in which the nucleons in the nucleus are treated as a mixture of degenerate Fermi gases. The calculation uses a Monte Carlo technique where for each event an electron strikes a proton and the proton propagates through the nucleus undergoing a series of elastic or inelastic reactions. The probability of such interactions is governed by the total cross-section of free nucleons. Each struck nucleon undergoes its own series of interaction resulting in a cascade of scattered particles. Pauli blocking is included by ensuring that only reactions which have recoil momenta greater than the Fermi momentum get accepted. The transparency is calculated as the fraction of the protons surviving within a given experimental acceptance compared to PWIA calculations of the same. The NE-18 acceptance was used by the authors in their calculations. The nucleon-nucleon correlations are neglected in these calculations.

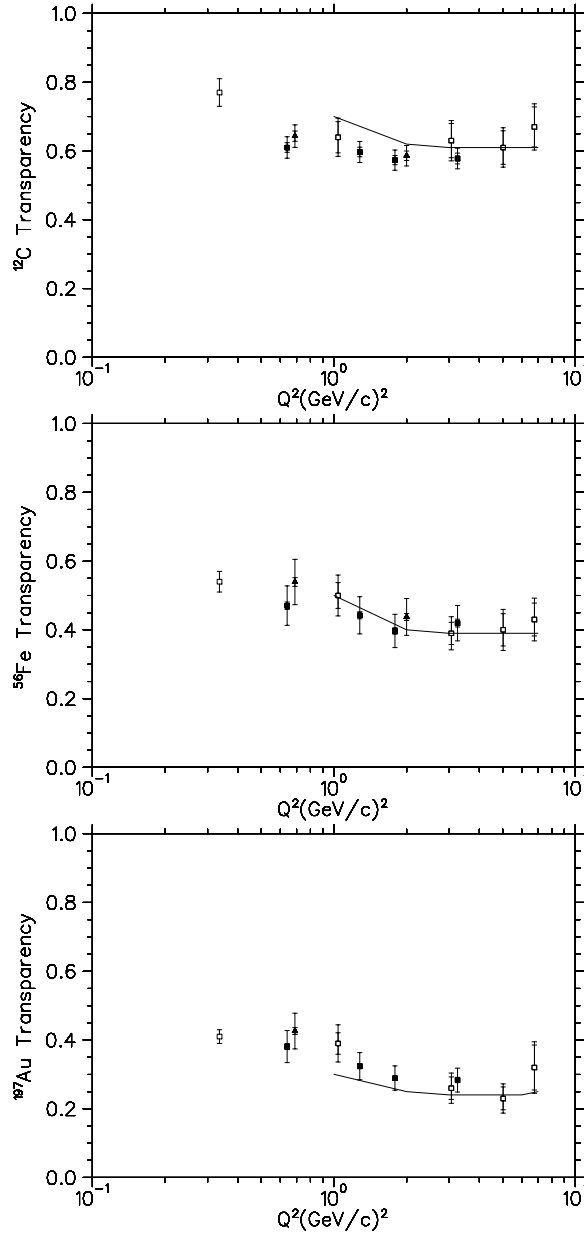


Figure 77: Glauber calculation of Nikolaev et al. for ^{12}C (top), ^{56}Fe (middle) and ^{197}Au (bottom) compared to the data (data is same as described in Figure 73, horizontal log scale).

Thus effects of coherent scattering of the outgoing nucleon is neglected, which the authors claim are negligible because they are suppressed by Pauli blocking as the deflections due to coherent scattering is small. In Figure 78 the calculations of transparency under the INC model is compared with the measured transparency. The INC transparency is over estimated for all targets, but they seem do a better job with the Q^2 dependence. The calculation shows an bigger increase in T at large Q^2 than expected from p-N cross-section.

5.3.3 Summary

The transparency is remarkably flat as a function of Q^2 for carbon even though the p-N cross-section changes by over 50% in the energy range covered in this experiment. Both DWIA and Glauber calculations underestimate the transparency as the target nucleus get heavier and the discrepancies are larger than the uncertainties of the measurement.

5.4 Spectral Functions

The deradiated spectral function was extracted from the data on the three targets at all the kinematic settings using the procedure described in Section 4.13. These spectral functions are distorted spectral functions since they include the effects of FSI and they are a product of transparency and the spectral function as mentioned earlier, they are labeled as $S^D(E_m, p_m)$. In the plots shown in this section the experimental spectral function was integrated over p_m or E_m (in other words projected into E_m or p_m space respectively) and compared to the IPSM model spectral functions used in the transparency analysis. The uncertainties shown are the sum in quadrature of the statistical and the systematic uncertainties. The

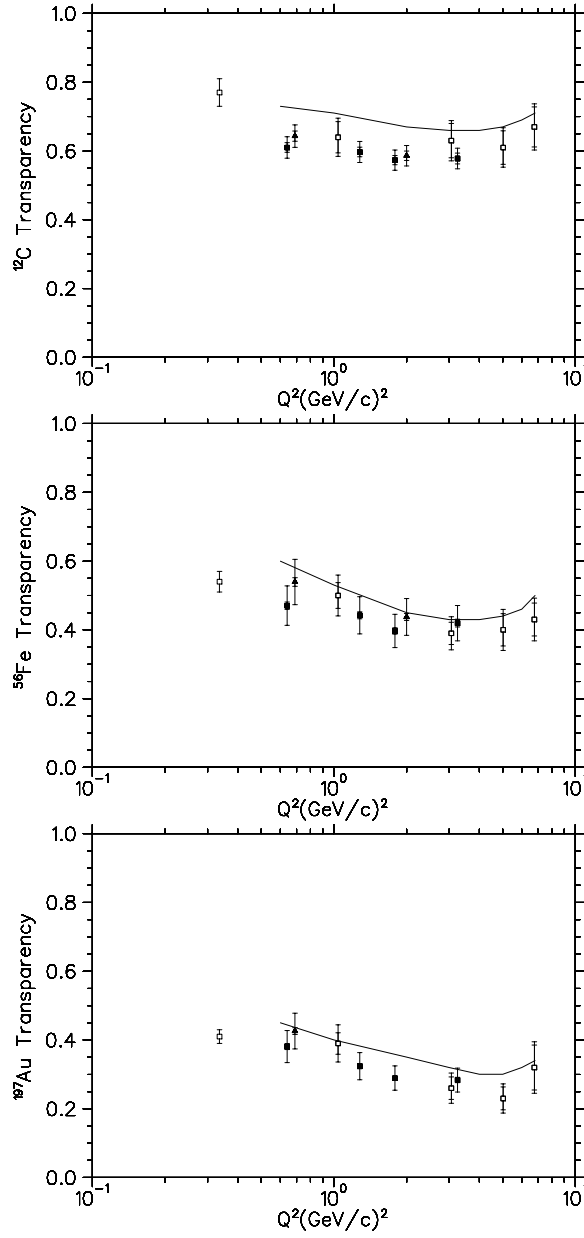


Figure 78: Inter Nuclear Cascade calculation of Golubeva et al. for ^{12}C (top), ^{56}Fe (middle) and ^{197}Au (bottom) compared to the data (data is same as described in Figure 73, horizontal log scale).

systematic uncertainties are discussed in the next section and the experimental spectral function are compared to a few calculations.

5.4.1 Systematic Variations

The nominal cuts used to constrain the data are shown in Table. 22. In order to estimate the sensitivity of the procedure to variations in these cuts, they were varied one at a time and the percent change in the integrated spectral function recorded. Table 32 shows the variation for the different cuts averaged over all targets. From Table 32 it is clear that there is very little variation with the angular cuts but about ≈ 1.5 % variation with the cuts on the HMS and SOS reconstructed delta. The sum in quadrature of the variation is 2.64 %.

As described earlier in Section 4.14, the model dependence of this procedure was tested by starting the iterative deradiation process with a ^{16}O model instead of ^{12}C and after several iterations the extracted spectral function was compared with a spectral function extracted using a correct ^{12}C model. The results is shown is Figure 62. This figure shows that the model dependence of the procedure is $< 5.0\%$. The systematic variation in the extraction procedure is determined by comparing the extracted spectral functions from Monte Carlo data with the input spectral functions. This uncertainty is determined for each bin in E_m and p_m and the figure quoted in the table is average over all bins.

The summary of the systematic uncertainties in extracting spectral functions is shown in Table 33.

Table 32: The mean variation of the integrated spectral function when the nominal cuts are changed one at a time. The standard deviation is shown in parentheses

Cuts	kineA	kineC	kineD	kineE	Average
hdelta(± 10)	0.6% (0.08)	1.4% (0.4)	1.8% (0.5)	1.7% (0.6)	1.3 %
hdelta(± 6)	1.2% (0.4)	1.2% (0.5)	1.5% (0.4)	1.5% (0.7)	1.6 %
sdelta(-12+20)	1.2% (0.4)	0.3% (0.1)	0.5% (0.2)	0.3% (0.1)	0.6 %
sdelta(-8+18)	1.4% (0.4)	2.2% (0.2)	0.7% (0.2)	0.4% (0.1)	1.2%
hms $y'_{tar}(\pm 0.06)$	0.03% (0.02)	0.08% (0.05)	0.11% (0.07)	0.15% (0.1)	0.12%
hms $y'_{tar}(\pm 0.04)$	0.22% (0.02)	0.15% (0.07)	0.13% (0.05)	0.17% (0.08)	0.16%
hms $x'_{tar}(\pm 0.095)$	0.042% (0.01)	0.08% (0.02)	0.11% (0.03)	0.15% (0.03)	0.1%
hms $x'_{tar}(\pm 0.075)$	0.6% (0.15)	0.4% (0.05)	0.55% (0.23)	0.16% (0.06)	0.45%
sos $y'_{tar}(\pm 0.08)$	0.17% (0.1)	-	0.02% (0.01)	0.08% (0.02)	0.7%
sos $y'_{tar}(\pm 0.06)$	0.6% (0.3)	0.2% -	0.5% (0.1)	0.03% (0.007)	0.4%
sos $x'_{tar}(\pm 0.065)$	0.02% (0.0)	-	-	-	0.02%
sos $x'_{tar}(\pm 0.045)$	-	-	-	-	-
Total sum in quadrature					2.64 %

Table 33: Systematic Uncertainties in extracting the spectral functions

Item	% Uncertainty in Data Yield
Current Measurement	1
Solid Target Thickness	0.1
HMS Tracking Eff.	1
SOS Tracking Eff.	1
Proton Absorption	1
Constraint Stability	2.6
Run Stability	1
Sum in Quadrature	3.4
Extraction procedure	3.5(average)
Total systematic uncertainty	4.9
Model Dependence	5.0

5.4.2 p_m and E_m Distributions

The deradiated spectral functions integrated over E_m are shown in the Figures 79 - 85 below. For carbon the spectral function are shown integrated over the p shell ($15 < E_m < 25$ MeV) and the s shell ($30 < E_m < 50$ MeV) respectively, these are followed by spectral functions for all three targets integrated over $0 < E_m < 80$ MeV. In the figures below each of the p_m distributions are compared to the IPSM spectral function described in Section 4.11.4. The model is normalized to have the same number of protons as in the data, ie. the integral over $|p_m| < 300$ MeV of the model spectral function is normalized to be same as that of the measured spectral function. In cases where the data is available only over a limited range in p_m and does not extend up to $|p_m| < 300$ MeV, the measured and the model spectral function were integrated over that limited range. The nominal cuts listed in Table 22 were applied in all cases.

Figure 86 shows the typical missing energy distribution for the three targets.

They are compared to IPSM spectral functions, which have Lorentzian energy distributions for each shell as described in Section 4.11.4. The integral over $0 < E_m < 80$ MeV of the model spectral function is normalized to be same as that of the data.

These figures indicate that the IPSM spectral functions can describe the shape and the radii of the distributions. However because no left-right asymmetry is incorporated in the model they cannot reproduce the asymmetry observed in the data. In addition there are some differences in the shapes at low missing momentum. The left-right asymmetry decreases as a function of Q^2 , just as seen in the transparency results (Figures 70-72). For carbon it was determined that the experimental strength in the spectral functions at the lowest p_m bins can be accounted for by small admixture of the s shell strength. It was found that about 8% admixture could account for the anomalous strength. Previous high resolution experiments at NIKHEF [94] have found spectroscopic strengths in the region $E_m < 27$ MeV of 4.1% of the 1p strength (8.2% of the 1s strength). Our results are consistent with these previous measurements.

The variation with Q^2 in the iron and gold spectral functions (see also Figures 88-91) at low \mathbf{p}_m is not understood. It is possible that the anomalous Q^2 dependence is caused by the variation in the resolution at the different kinematics. These variations in the resolution are an artifact of the reconstruction of the spectrometer quantities having some small unphysical dependences (the optimization of the reconstruction had some small kinematic dependence).

The left-right asymmetry can be attributed to the presence of a stronger interference response W_{LT} . The off-shell cross-section σ_{ep} includes an interference response which gives rise to a left-right asymmetry, but the asymmetry seen in the spectral functions is in addition to this asymmetry in the off-shell cross-section. At

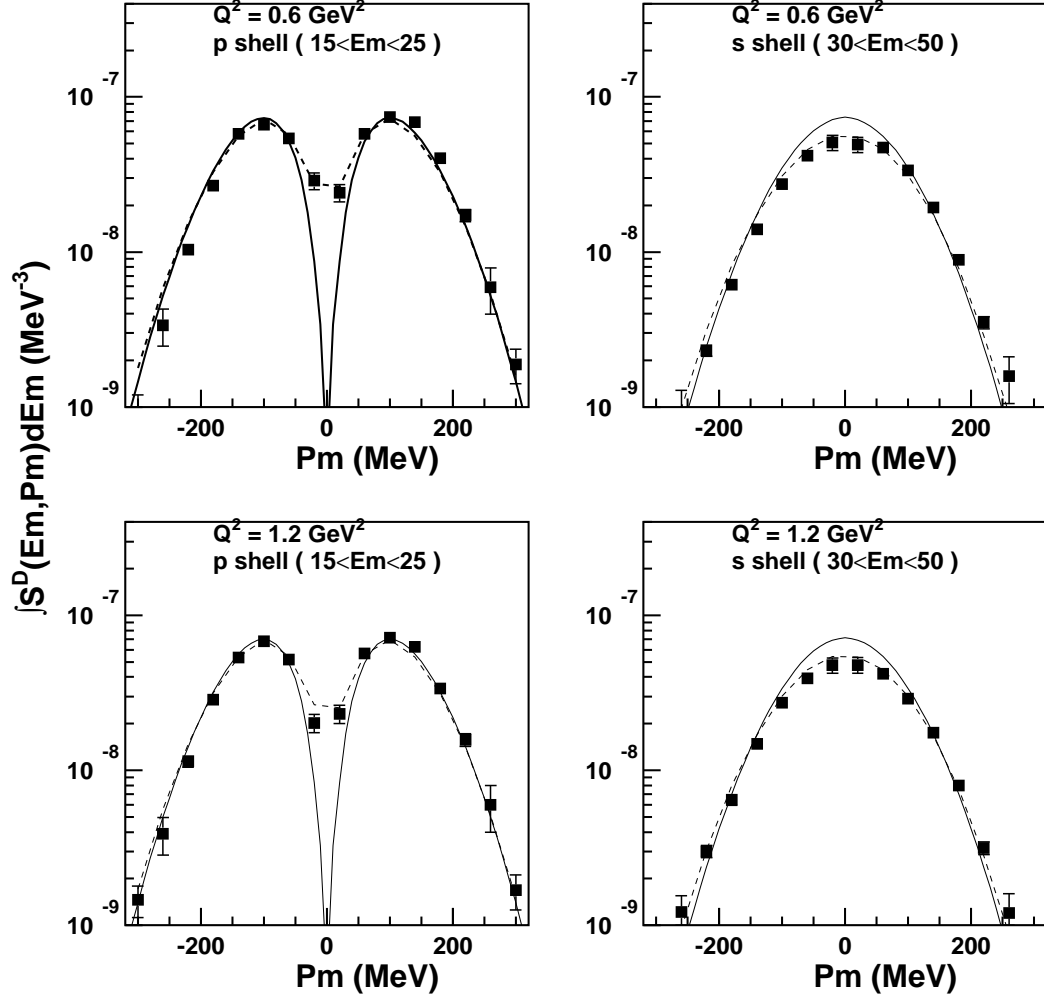


Figure 79: The momentum distribution of the p shell (left panels) and the s shell (right panels) protons in carbon at Q^2 of 0.6 GeV^2 (upper panels) and 1.2 GeV^2 (lower panels) are shown along with the IPSM spectral function (solid line) described in Section 4.11.4. The dashed line shows the 8% admixture of the p and s shell models. The integral over $|p_m| < 300 \text{ MeV}$ of the model is normalized to be equal to the measured spectral function integrated over the same range. The sum in quadrature of the statistical and systematic uncertainties are shown.

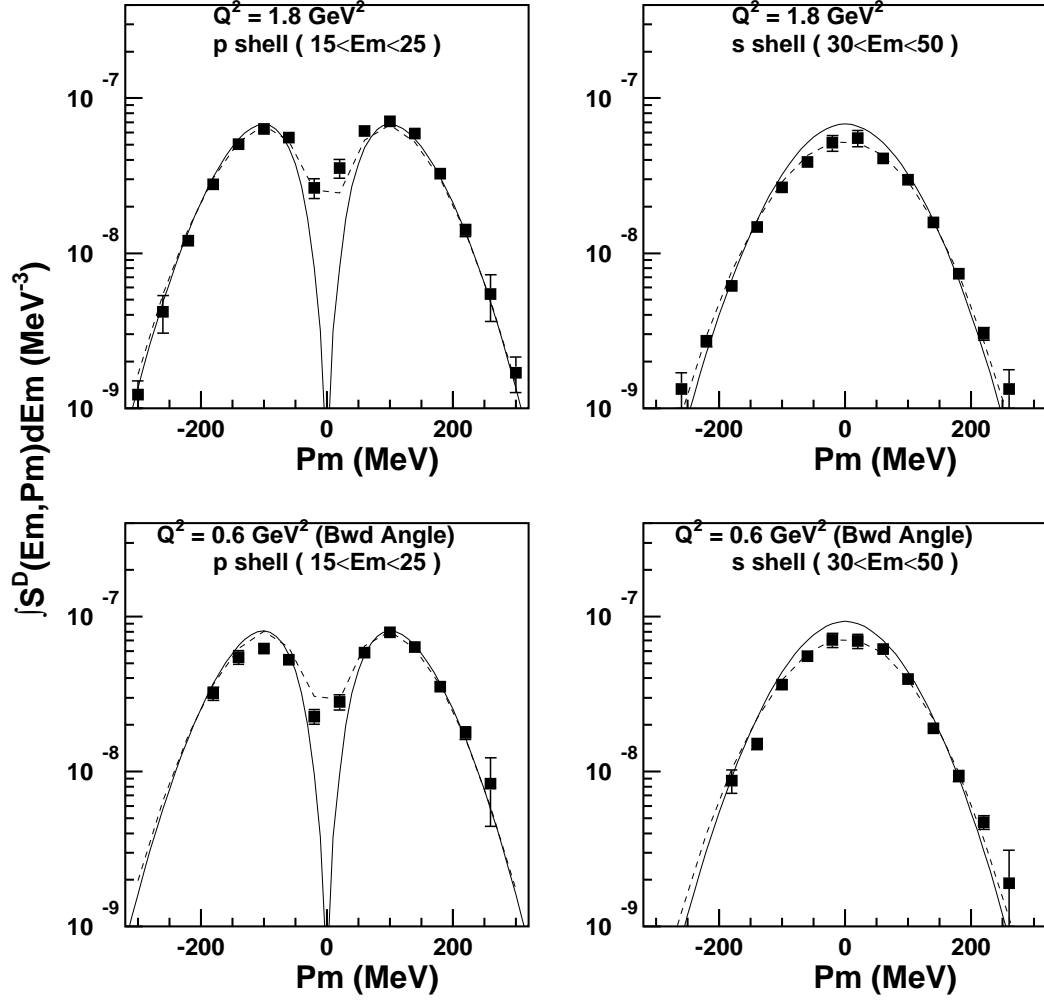


Figure 80: The momentum distribution of the p shell (left panels) and the s shell (right panels) protons in carbon at Q^2 of 1.8 GeV^2 (upper panels) and 0.6 GeV^2 (lower panels) are shown along with the IPSM spectral function (solid line) described in Section 4.11.4. The dashed line shows the 8% admixture of the p and s shell models. The integral over $|p_m| < 300 \text{ MeV}$ of the model is normalized to be same as the data integrated over the same range. The $Q^2 = 0.6 \text{ GeV}^2$ point corresponds to the backward angle data. For the lower panels the integral between $0 < p_m < 220 \text{ MeV}$ was used to normalize the model. The sum in quadrature of the statistical and systematic uncertainties are shown.

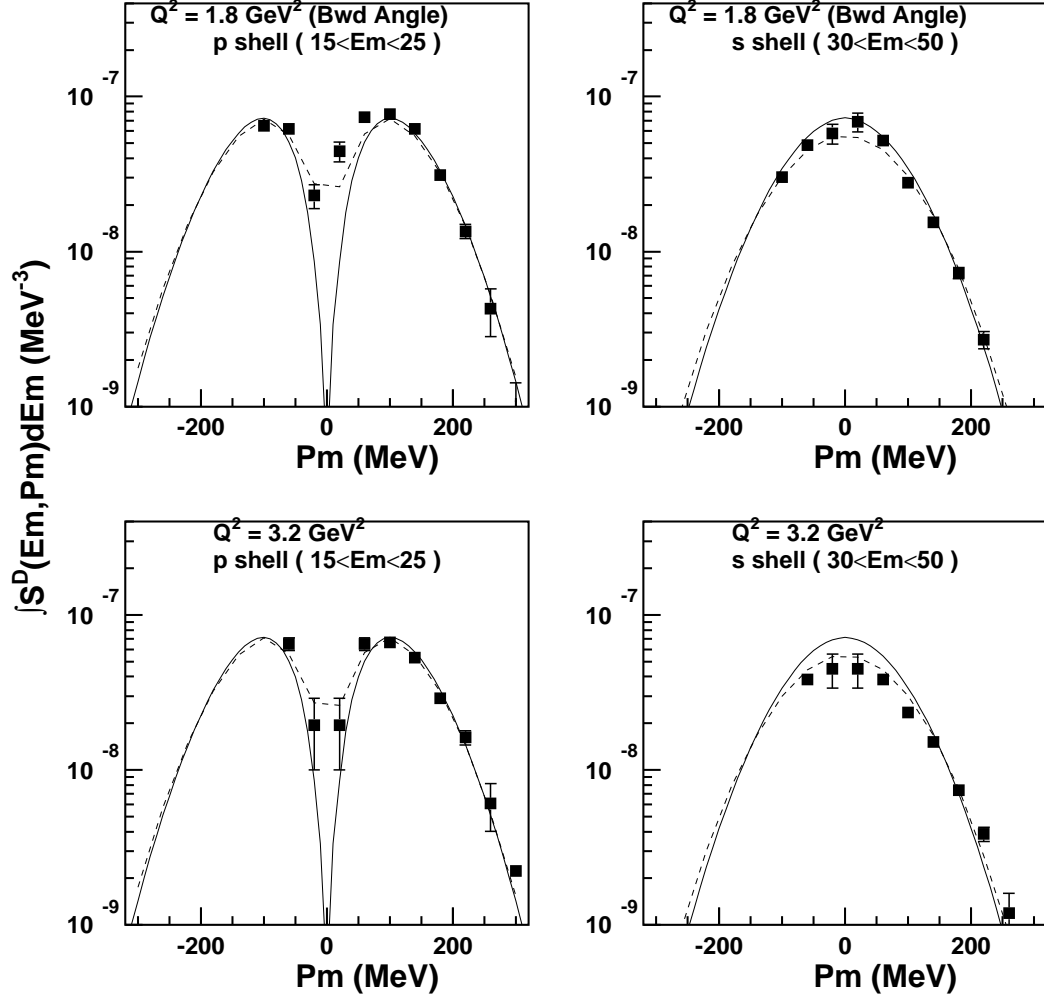


Figure 81: The momentum distribution of the p shell (left panels) and the s shell (right panels) protons in carbon at Q^2 of 1.8 GeV^2 (upper panels) and 3.2 GeV^2 (lower panels) are shown along with the IPSM spectral function (solid line) described in Section 4.11.4. The dashed line shows the 8% admixture of the p and s shell models. The integral over $0 < p_m < 300 \text{ MeV}$ of the model is normalized to be equal to the measured spectral function integrated over the same range. The $Q^2 = 1.8 \text{ GeV}^2$ point corresponds to the backward angle data. The sum in quadrature of the statistical and systematic uncertainties are shown.

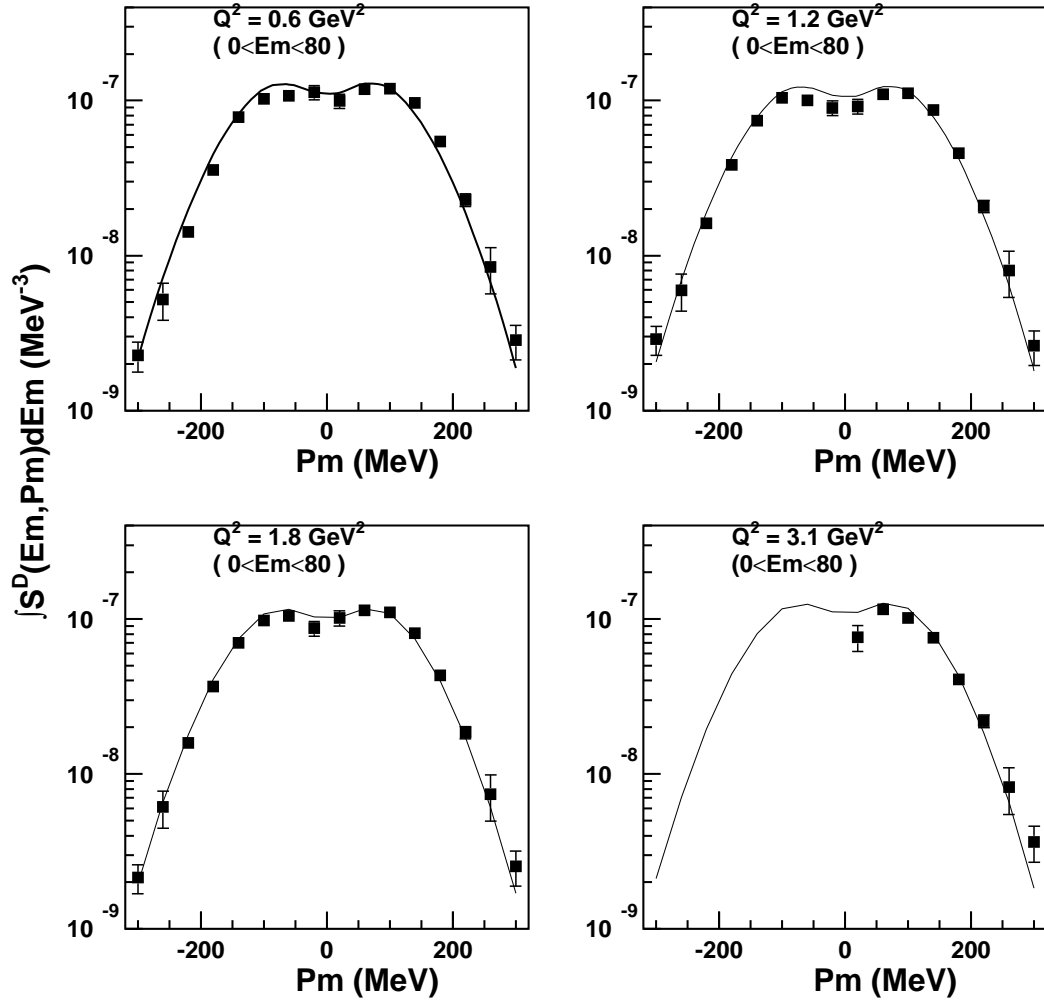


Figure 82: The momentum distribution of the protons in carbon at Q^2 of 0.6 GeV^2 (upper left panel), 1.2 GeV^2 (upper right panel), 1.8 GeV^2 (lower left panel) and 3.2 GeV^2 (lower right panel) are shown along with the IPSM spectral function (solid line) described in Section 4.11.4. The integral over $|p_m| < 300 \text{ MeV}$ of the model is normalized to be equal to the measured spectral function integrated over the same range. At Q^2 of 3.2 GeV^2 (lower right) the integral over $0 < p_m < 300 \text{ MeV}$ was used for normalization. The sum in quadrature of the statistical and systematic uncertainties are shown.

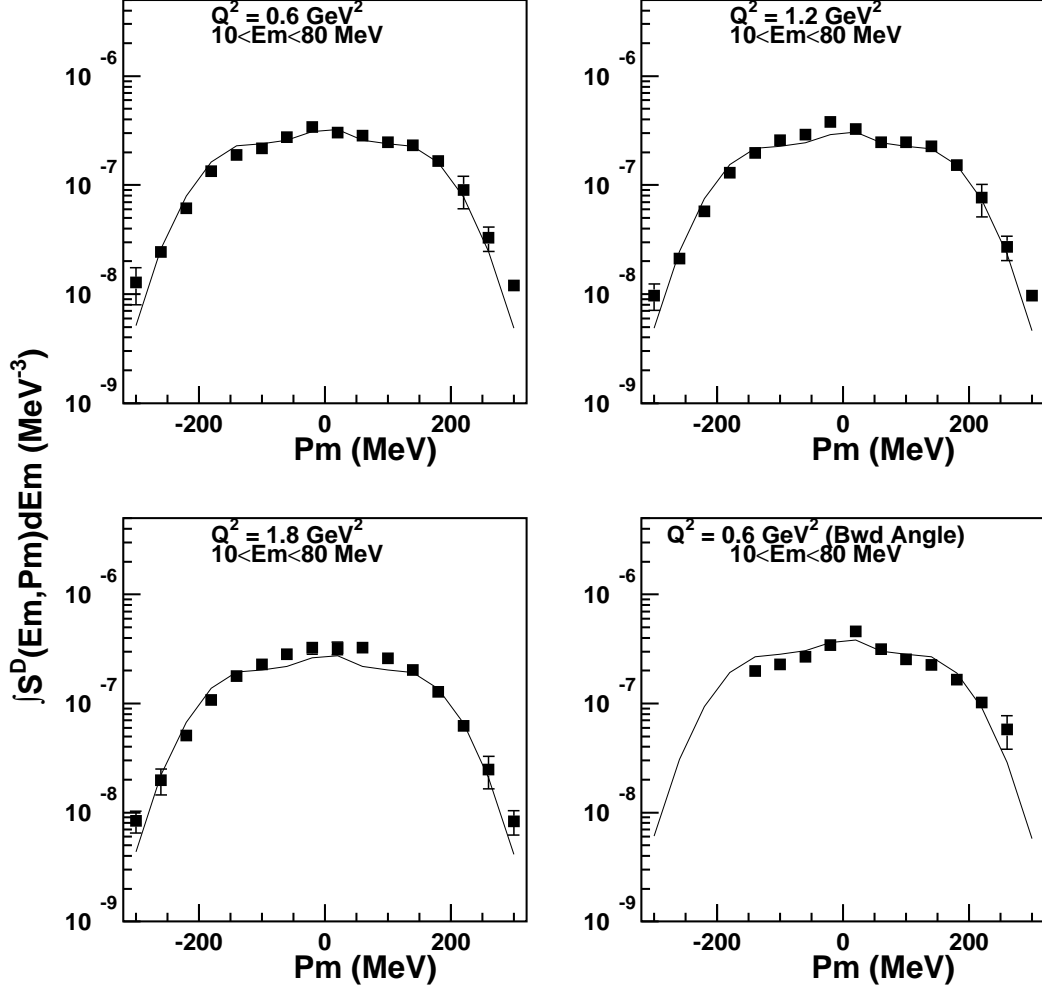


Figure 83: The momentum distribution of the protons in iron at Q^2 of 0.6 GeV^2 (upper left), 1.2 GeV^2 (upper right), 1.8 GeV^2 (lower left) and 0.6 GeV^2 (lower right) are shown along with the IPISM spectral function (solid line) described in Section 4.11.4. The integral over $|p_m| < 300 \text{ MeV}$ of the model is normalized to be equal to the measured spectral function integrated over the same range. The $Q^2 = 0.6 \text{ GeV}^2$ point (lower right) corresponds to the backward angle data. For cases where the measured spectral function covers a small range in p_m , the normalization was done over the limited range. The sum in quadrature of the statistical and systematic uncertainties are shown.

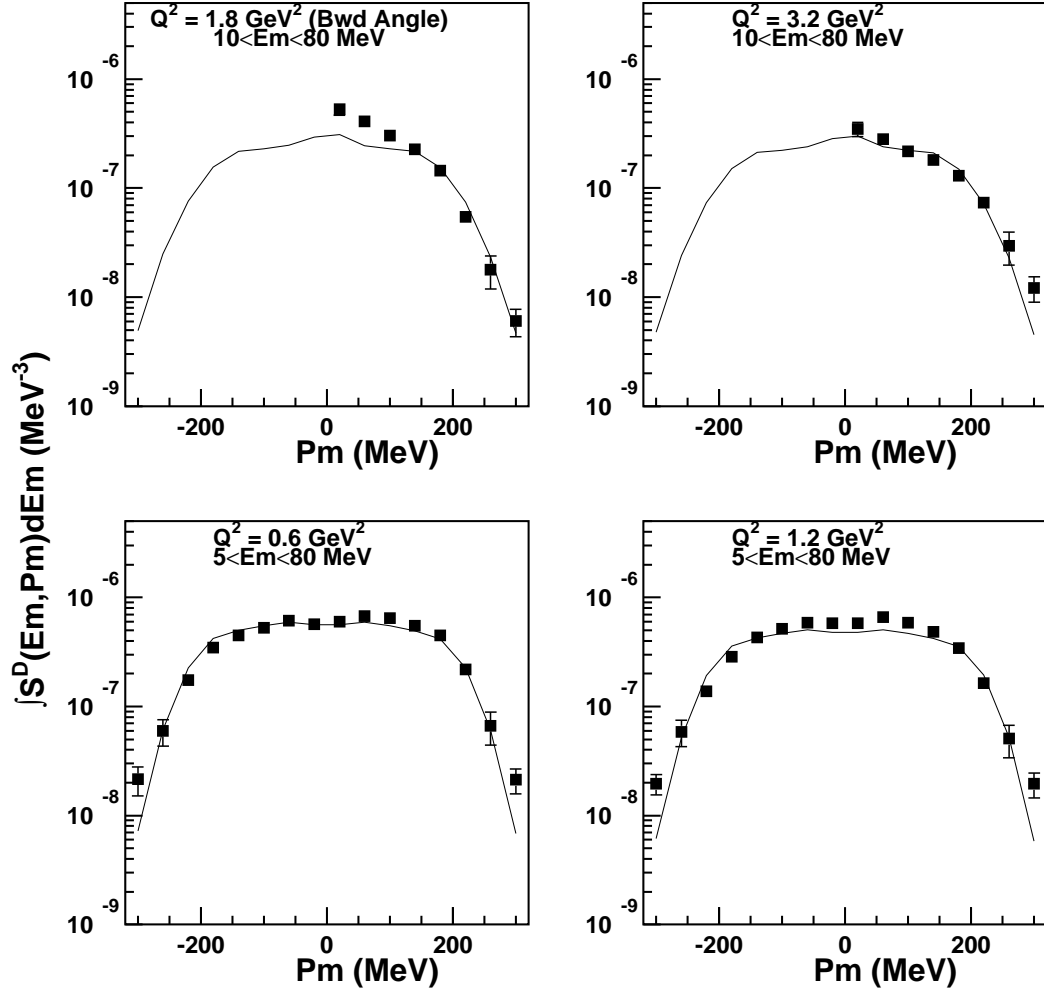


Figure 84: The momentum distribution of the protons in iron at Q^2 of 1.8 GeV^2 (upper left) and 3.2 GeV^2 (upper right) and in gold at Q^2 of 0.6 GeV^2 (lower left) and 1.2 GeV^2 (lower right) are shown along with the IPSM model (solid line) described in Section 4.11.4. The integral over $|p_m| < 300$ MeV of the model is normalized to be equal to the measured spectral function integrated over the same range. The $Q^2 = 1.8 \text{ GeV}^2$ point (upper left) corresponds to the backward angle data. For cases where the measured spectral function covers a small range in p_m , the normalization was done over the limited range. The sum in quadrature of the statistical and systematic uncertainties are shown.

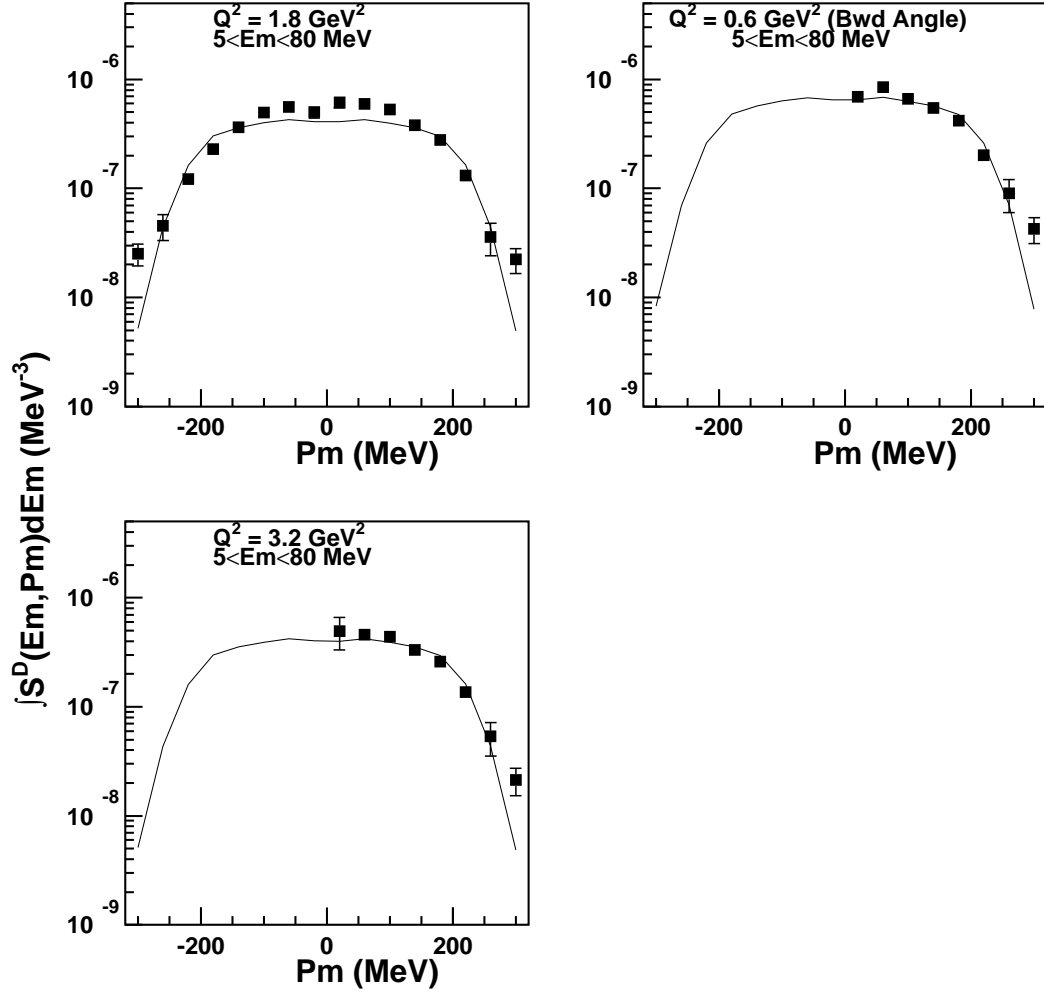


Figure 85: The momentum distribution of the protons in gold at Q^2 of 1.8 GeV^2 (upper left), 0.6 GeV^2 (upper right) and 3.2 GeV^2 (lower left) are shown along with the IPSM model (solid line) described in Section 4.11.4. The integral over $|p_m| < 300 \text{ MeV}$ of the model is normalized to be equal to the measured spectral function integrated over the same range. The $Q^2 = 0.6 \text{ GeV}^2$ point (upper right) corresponds to the backward angle data. For cases where the measured spectral function covers a small range in p_m , the normalization was done over the limited range. The sum in quadrature of the statistical and systematic uncertainties are shown.

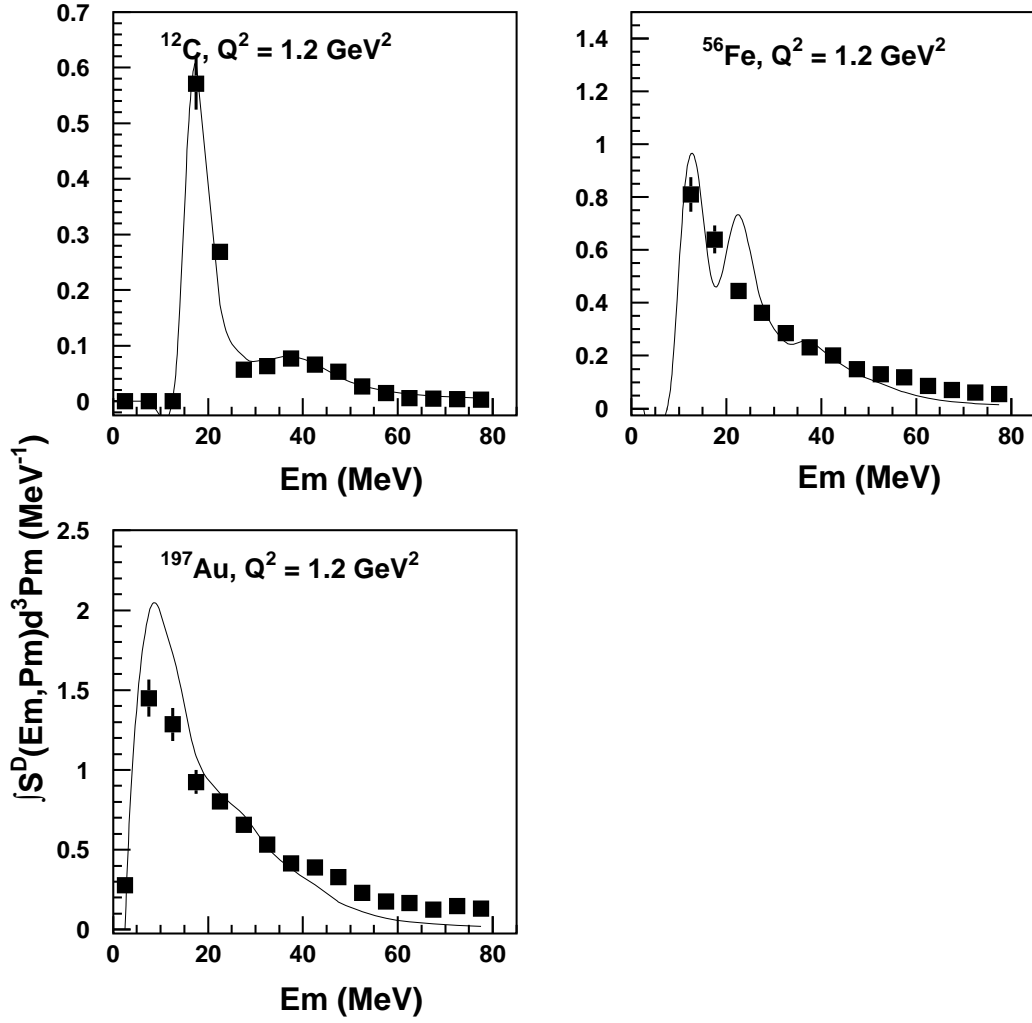


Figure 86: The typical missing energy distribution of carbon, iron and gold at Q^2 of 1.2 GeV^2 are shown along with the IPISM model (solid line) described in Section 4.11.4. The model has been normalized to have same integrated strength as the data over $0 < E_m < 80 \text{ MeV}$. The sum in quadrature of the statistical and systematic uncertainties are shown.

lower momentum transfer the left-right asymmetry has been used to extract the interference response W_{LT} [95] from $D(e, e'p)$ data taken at NIKHEF. For these lower momentum transfers, it has been seen that the asymmetry in the data is not reproduced by DWIA calculations. These calculations tend to show more asymmetry than observed [18, 24]. The authors claim that this discrepancy cannot be attributed to FSI since the different optical potentials do not affect the asymmetry. Some authors [24] have accounted for this by introducing an enhancement in the transverse and the interference response (although these cancel in the parallel kinematics).

The data from this experiment will be used to extract the asymmetry which is in excess of the asymmetry already present in the deForest prescription σ_{cc1} as a function of the transverse momentum and from these asymmetries one can get a measure of the interference response function W_{LT} . More detailed theoretical calculations which can reproduce the observed asymmetries would be very useful in determining the contributions from various reaction mechanisms.

From the E_m distributions in Figure 86 we see that the carbon $p_{3/2}$ and $s_{1/2}$ shell is well described by the IPSM model. However, for the heavier targets the measured spectral functions shows much less structure than the IPSM model, indicating that the shell widths may be larger than the IPSM values. This data indicates that the Brown and Rho formulation (Section 4.11.4, Equation 105) which saturates at about 24 MeV is incorrect for heavier nuclei like iron and gold. Since this formulation is based on data taken in the early $(e, e'p)$ experiments at very low Q^2 , there is a definite need for updating the formula by incorporating the new data.

In Section 5.4.3 where the momentum distributions are plotted together on top of each other, one can see that the spectral functions are approximately independent of Q^2 for the forward angle data. However there are some differences

Table 34: The integral of the measured spectral function for $|p_m| < 300$ MeV and E_m corresponding to the carbon $p_{3/2}$ shell ($15 < E_m < 25$ MeV), $s_{1/2}$ shell ($30 < E_m < 50$ MeV), all carbon ($0 < E_m < 80$ MeV) all iron and all gold ($0 < E_m < 80$ MeV). The statistical uncertainties are < 0.5 % in all cases and the systematic uncertainty is 4.9 %

	Q^2	$n_p^{expt} = \int S_{expt} dE_m d^3p_m$				
	GeV ²	¹² C			⁵⁶ Fe	¹⁹⁷ Au
		$p_{3/2}$ shell	$s_{1/2}$ shell	all	all	all
A	0.64	2.19 (0.11)	0.67 (0.03)	3.18 (0.15)	9.63 (0.47)	23.53 (1.15)
B	1.28	2.10 (0.11)	0.65 (0.03)	3.04 (0.15)	9.10 (0.45)	20.07 (0.98)
C	1.79	2.03 (0.10)	0.62 (0.03)	2.89 (0.14)	8.15 (0.40)	17.07 (0.84)
D	0.64	2.42 (0.12)	0.78 (0.04)	3.38 (0.17)	11.33 (0.56)	27.08 (1.33)
E	1.84	2.17 (0.12)	0.66 (0.03)	3.10 (0.15)	9.18 (0.39)	-
F	3.25	2.15 (0.10)	0.65 (0.03)	3.12 (0.15)	8.91 (0.37)	16.76 (0.82)

between the forward and backward angle spectral functions (Figure 94, 96 and 99) as discussed in the next section. This indicates that the Q^2 dependence of the electron-proton coupling is well described by the off-shell cross-section σ_{ep} . This is important because the off-shell cross-section varies widely over the kinematic range covered. However, the longitudinal- transverse character of the coupling is not well described.

The integral over all E_m and p_m of these spectral functions give us the total number of protons observed and can be thought of as the product of the transparency and the spectroscopic factor. The number of protons detected experimentally in the carbon p and s shells and in all the shells within 80 MeV in carbon, iron and gold are listed in Table. 34.

In Table 34 the number of ¹²C p shell protons observed is higher than those observed in previous experiments, for instance those at NIKHEF [24]. We can calculate the spectroscopic factors by using the observed number of p shell protons

Table 35: Spectroscopic factors (S_α) calculated using the p shell transparency from the EEI model and the spectroscopic factors corrected for any excess transverse strength (S_α^{corr}) in the p shell region using results from Section 5.5 . The uncertainties are the sum in quadrature of systematic and statistical uncertainties.

Kinematics	Q^2	S_α	S_α^{corr}
	GeV ²		
A	0.64	2.98 ± 0.15	2.83 ± 0.30
B	1.28	3.13 ± 0.16	-
C	1.8	3.03 ± 0.15	2.76 ± 0.46

and dividing by the transparency for the p shell protons calculated with a DWIA model. We use the EEI calculations of J. Kelly [88] since this calculations is in agreement with our measurement (Figure 75). The p shell transparency at $Q^2 = 0.64$ and 1.28 GeV² were calculated by J. Kelly [96] to be 0.72 and 0.67 respectively. Although his calculations do not extend to $Q^2 = 1.8$ GeV² we will use a transparency of 0.67 for calculating the spectroscopic factor. In Section 5.5 we will discuss the transverse and longitudinal strength in the p shell region. Using that information one can correct the number of protons in the p shell region for any excess transverse strength in the p shell region (using the procedure to extrapolate the longitudinal spectral function, outline in Section 5.5). This gives a corrected spectroscopic factor. However, it should be pointed out that the corrected transparency calculated in Section 5.5 (see Figure 107) using the same procedure is lower and thus does not agree with the EEI calculations. The nominal and corrected spectroscopic factors are listed in Table 35.

The spectroscopic factors in this experiment are $\sim 2\sigma$ higher than the observed spectroscopic factors from NIKHEF (2.18 ± 0.15). A possible explanation is that at the lower momentum transfers the transverse strength was found to be about

Table 36: Nuclear Transparency calculated from the experimental spectral function. The uncertainties are the systematic uncertainties and the model dependent uncertainties added in quadrature

Kinematics	Q^2	Transparency		
	$(\text{GeV}/c)^2$	^{12}C	^{56}Fe	^{197}Au
A	0.64	0.62 ± 0.04	0.48 ± 0.04	0.40 ± 0.04
B	1.28	0.59 ± 0.04	0.45 ± 0.04	0.34 ± 0.03
C	1.79	0.56 ± 0.04	0.41 ± 0.04	0.29 ± 0.03
D	0.64	0.655 ± 0.05	0.56 ± 0.05	0.47 ± 0.04
E	1.84	0.60 ± 0.04	0.46 ± 0.04	-
F	3.25	0.605 ± 0.04	0.44 ± 0.04	0.29 ± 0.03

40% higher than the longitudinal strength, in the NIKHEF experiment [24]. In this experiment however, we observe that the longitudinal and transverse strength for the p shells differ by $\approx 10\%$.

It is instructive to stress the ambiguity between extracting spectroscopic factors and extracting transparency. The spectroscopic factors are extracted by comparing the experimental spectral functions with DWIA calculations which are tuned to fit the experimental data. Once the DWIA calculations match the data it can be claimed that the FSI interactions have been accounted for in terms of the optical potential used in the calculation, hence the integral of the spectral function gives the spectroscopic strength for a given target. In extracting the transparency one does not account for the FSI and hence the transparency so extracted is a product of the spectroscopic factor and the attenuation of the knocked out nucleon. Thus there is a continuous ambiguity as to what fraction of the transparency is attenuation and what fraction is the spectroscopic factor (FSI).

One can extract transparencies from the integral of the experimental spectral

function n_p^{expt} (listed in Table. 34 using,

$$T(Q^2) = \frac{n_p}{n_p^{IPSM}}. \quad (180)$$

Where n_p^{IPSM} is given by,

$$n_p^{IPSM} = \int S_{PWI}^{CC} dE_m d^3p_m, \quad (181)$$

here $\int S_{IPSM}^{CC}$ is the integral of the IPSM spectral function over $0 < E_m < 80$ MeV and $|p_m| < 300$ MeV and corrected for correlations with the correlation correction listed in Table 17. The transparency extracted from n_p^{expt} is shown in Table 36. The uncertainties are higher than those quoted in Section 5.3 because the new transparencies include the uncertainties of the extraction procedure. The transparencies extracted from the measured spectral functions is consistent with the transparencies in Section 5.3 indicating the consistency of the two analysis.

As discussed in Section 2.7.3 the Koltun sum rule for protons only, corrected for recoil energy of the residual system is,

$$\frac{E_Z}{Z} = \frac{1}{2} \left(\frac{A-2}{A-1} \langle T \rangle - \langle E \rangle \right). \quad (182)$$

Here $\frac{E_Z}{Z}$ is the total energy per proton, obtained from nuclear masses and appropriate Coulomb corrections, $\langle T \rangle$ is the mean kinetic energy and $\langle E \rangle$ is the mean removal energy. They are calculated using the extracted spectral functions and the number of protons observed between $0 < E_m < 80$ MeV. The results are listed in Table 37.

The results show that there is deviation of about 1-2 MeV from the Koltun sum rule for all the targets (the deviations are lower than those observed at Saclay [8] which were ~ -2.5 MeV for carbon) and the deviation is negative in all cases

Table 37: The total energy per proton, mean kinetic energy, mean removal energy and the deviation from the Koltun sum rule (Δ) is listed for the three targets.

Target	Q^2	$\frac{E_z}{Z}$	$\langle T \rangle$	$\langle E \rangle$	Δ
	GeV ²	MeV	MeV	MeV	MeV
¹² C	0.6		15.93	25.95	-1.20±0.12
	1.2	-6.93	16.28	25.79	-1.44±0.14
	1.8		16.04	25.62	-1.41±0.14
	3.2		17.34	26.21	-1.71 ±0.17
⁵⁶ Fe	0.6		20.42	30.71	-0.96±0.10
	1.2	-6.93	18.05	29.42	-0.92±0.09
	1.8		17.78	27.77	-1.62±0.16
	3.2		19.13	28.82	-1.74±0.17
¹⁹⁷ Au	0.6		20.18	25.45	-1.99±0.20
	1.2	-4.73	18.37	25.72	-0.96±0.10
	1.8		18.28	24.06	-1.75±0.17
	3.2		19.42	26.05	-1.31±0.13

implying that the nucleons are less bound than expected which is consistent with having strength at higher missing energies. This suggests that the deviation from the sum rule could be due to the short range correlations which push some of the strength to high missing energies. However, one cannot determine the effect of correlations just from the sum rule. It can be estimated using correlated spectral functions, for example using the correlated spectral functions of Benhar *et al.* it was estimated that the contribution to the Koltun sum rule from regions at $E_m > 80$ MeV is -1.756 MeV for iron and -1.974 MeV for gold. These are similar to the deviation from the sum rule shown in Table 37, indicating that some of the deviation is indeed due to short range correlations. The Koltun sum rule is derived under the assumption that there are no three body or many body interactions thus the deviation from the the sum rule could partly be due to contributions from many body interactions.

5.4.3 Comparison to Theoretical Models

The deradiated spectral functions for carbon and iron are compared with DWIA calculations which use the Hartree-Fock model with Skyrme's interaction to describe the single particle aspects of the nuclear structure [97]. The distorted momentum distributions for the nuclear protons is then calculated in terms of these Hartree-Fock single particle bound state wave functions and distorted outgoing proton functions are calculated in the eikonal approximation. The potential used is a Glauber model potential in the optical limit. The potential in terms of the pN scattering amplitude f_{pN} and nuclear density $\rho_N(\mathbf{r})$ is given by,

$$\begin{aligned} ReV(r) &= -\frac{\hbar p_N}{E_N} \frac{\alpha \sigma_{pN} \rho_N(r)}{2}, \quad ImV(r) = -\frac{\hbar p_N}{E_N} \frac{\sigma_{pN} \rho_N(r)}{2}, \\ \alpha &= Re f_{pN} / Im f_{pN}. \end{aligned} \tag{183}$$

These calculations were done by Zhalov et al. [84]. for the NE18 experiment and are valid for the present experiment, since the range of Q^2 covered overlap. Two models were obtained, one of them included the authors' estimates of the effects of color transparency.

Since all the calculations shown here were done just for $p_m > 0$, ie they are symmetric about $p_m = 0$, we have symmetrized the measured spectral functions as $S(p_m) = \frac{(S(p_m > 0) + S(p_m < 0))}{2}$. This removes the left-right asymmetry observed in the measured spectral functions and makes them suitable to be compared with the calculations.

In Figure 87 we see that the DWIA calculations with and without color transparency have almost no difference in the momentum distribution. The momentum distribution matches the data except at very low p_m . In addition the calculations

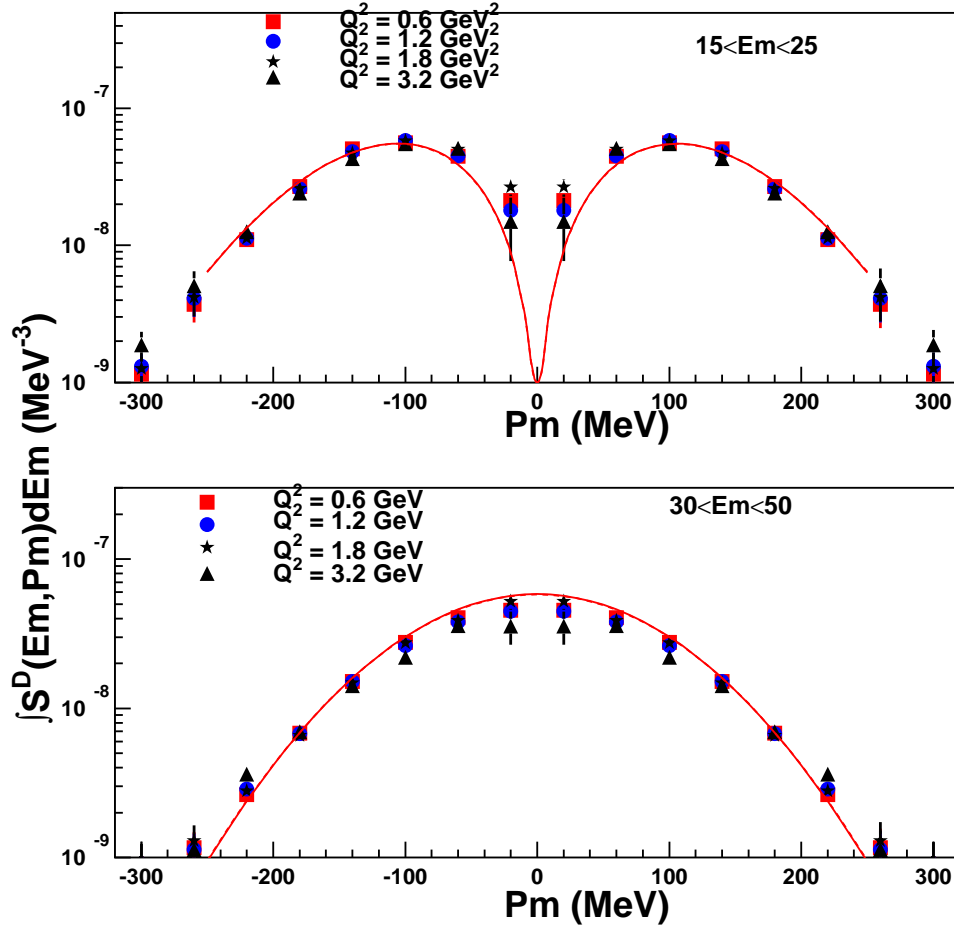


Figure 87: The momentum distribution of the p shell (top panel) and the s shell (bottom panel) protons in carbon at Q^2 of 0.6 - 3.2 GeV^2 are shown along with the DWIA calculations of Zhalov et al. with (dashed) and without (solid) color transparency (here there is almost no difference between the two). They have been normalized so that the integral of the model and measured spectral functions over $|p_m| < 300 \text{ MeV}$ is equal to the integral of the spectral function at Q^2 of 1.8 GeV^2 (kine C). The statistical and the systematic uncertainties added in quadrature are shown.

do not extend to $p_m > 200$ MeV where the differences due to short range correlations are likely to show up. These calculations need to be redone for larger p_m and on both sides of $p_m = 0$ in order to be useful.

In Figure 88 we see that the DWIA calculations with and without color transparency, both, do not describe the momentum distribution correctly at $|p_m| > 100$ MeV. Some of the Q^2 dependence at the low p_m are caused by the symmetrization since the left-right asymmetry varies with Q^2 .

Next the deradiated spectral functions for iron and gold are compared to calculations of Benhar et al. [98] These calculations start with single particle finite nuclei spectral functions to which a nuclear density dependent part is added (also called the nuclear matter correlated part). The density dependent part (or correlated part) is calculated under the local density approximation. The single particle spectral function were the same ones used in this experiment for the physics simulation (described in Section 4.11.4). The recoil-nucleon final state interactions were treated in the local density approximation and used the high energy approximations discussed in Section 2.6.2.

It is interesting that for both iron (Figure 89) and gold (Figure 91) the measured spectral functions show some additional strength at the $p_m > 250$ MeV compared to the model. Since the model incorporates a density dependent correlation tails, the effects of which would show only at $p_m > 250$ MeV, it seems that the model underestimating the strength of these tails. Another possibility is that the long-range correlations neglected in these models are becoming important.

The last comparison is for iron where the spectral function is compared to the calculation based on the code TIMORA of Horowitz [85]. This code is based on the the σ - ω relativistic mean field theory of Walecka [99], where the nucleons in the nucleus interact via exchange of scalar and vector mesons (σ and ω respectively).

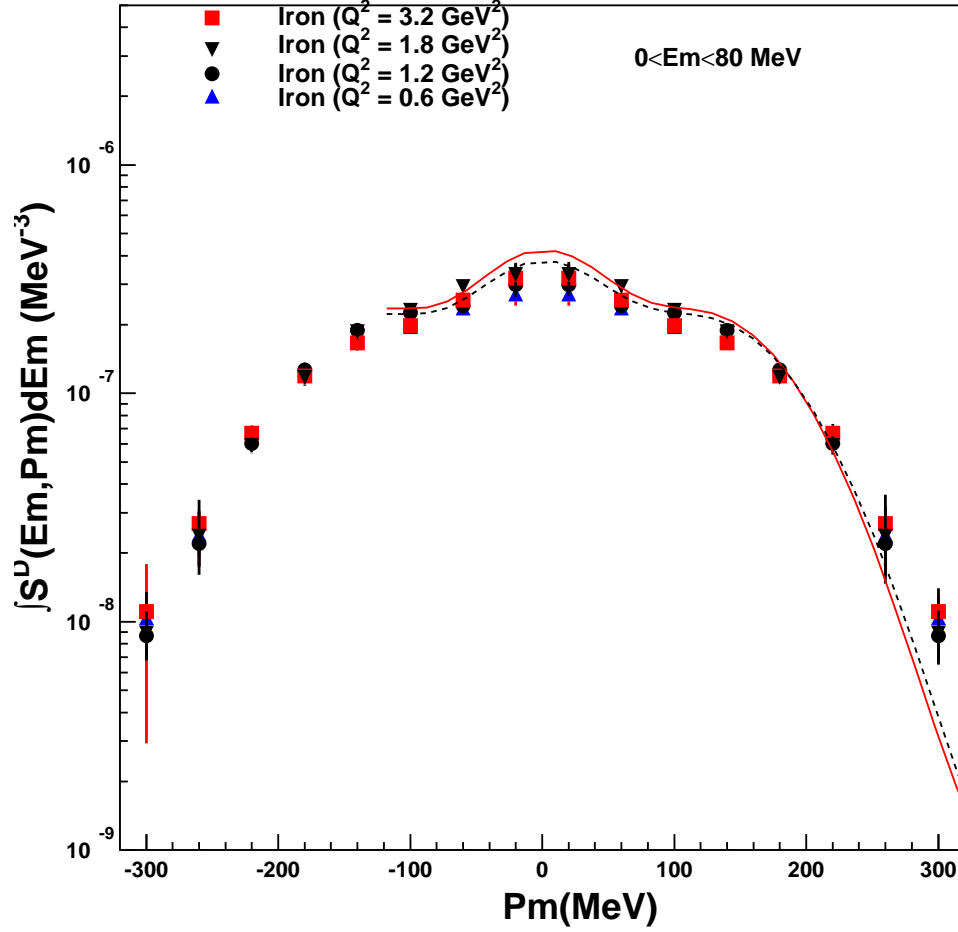


Figure 88: The momentum distribution of the protons in iron at Q^2 of 0.6 - 3.2 GeV^2 are shown along with the DWIA calculations of Zhalov et al. with (dashed) and without (solid) color transparency. They have been normalized so that the integral of the model and measured spectral functions over $|p_m| < 300$ MeV is equal to the integral of the spectral function at Q^2 of 1.8 GeV^2 (kine C). The statistical and the systematic uncertainties added in quadrature are shown.

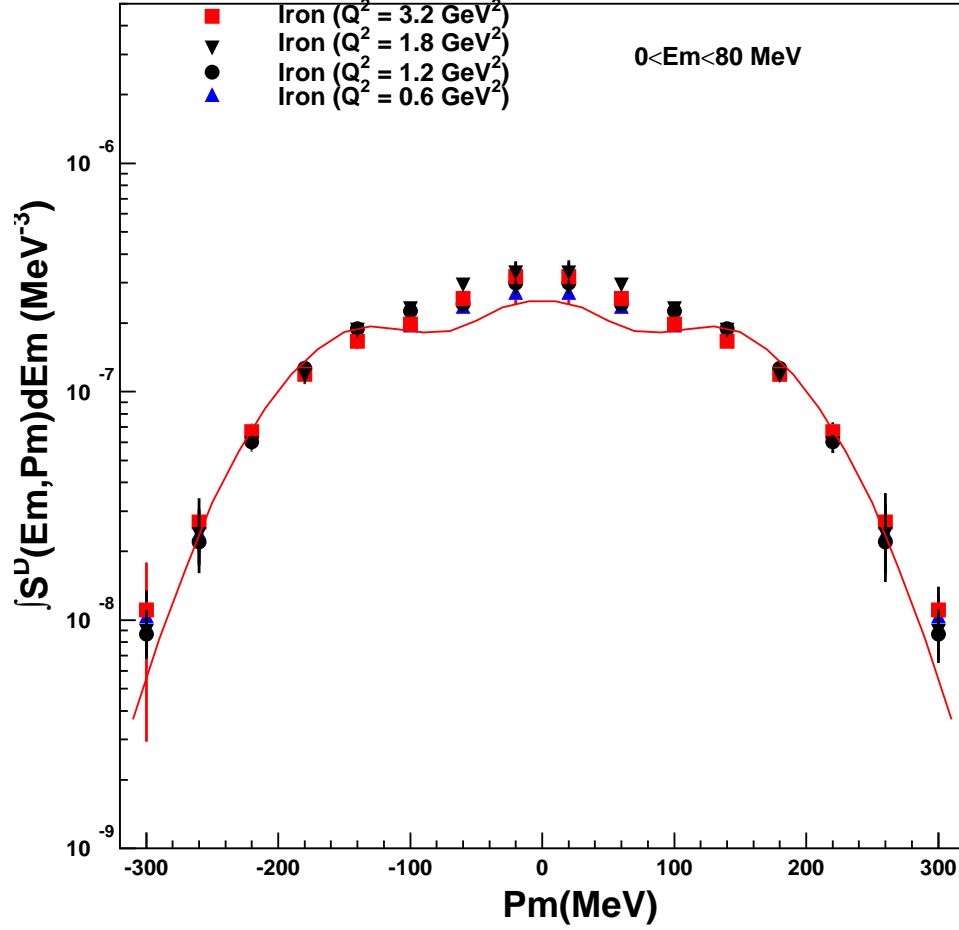


Figure 89: The momentum distribution of the protons in iron at Q^2 of 0.6 - 3.2 GeV^2 are shown along with the calculations of Benhar. They have been normalized so that the integral of the model and measured spectral functions over $|p_m| < 300 \text{ MeV}$ is equal to the integral of the spectral function at Q^2 of 1.8 GeV^2 (kine C). The statistical and the systematic uncertainties added in quadrature are shown.

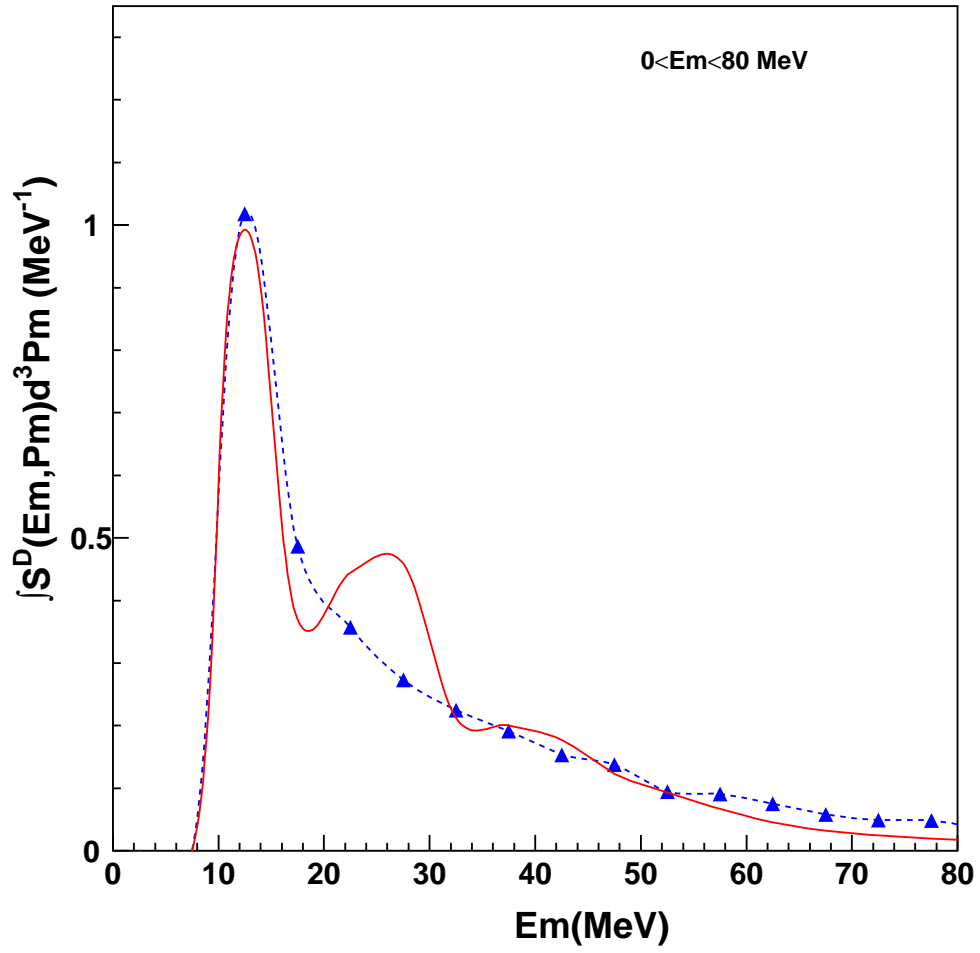


Figure 90: The missing energy distribution of the protons in iron at Q^2 of 1.8 GeV^2 are shown along with the calculations of Benhar et al. (solid). They have been normalized so that the integral of the model and measured spectral functions over $0 < E_m < 80 \text{ MeV}$ are equal. Only the statistical uncertainties shown.

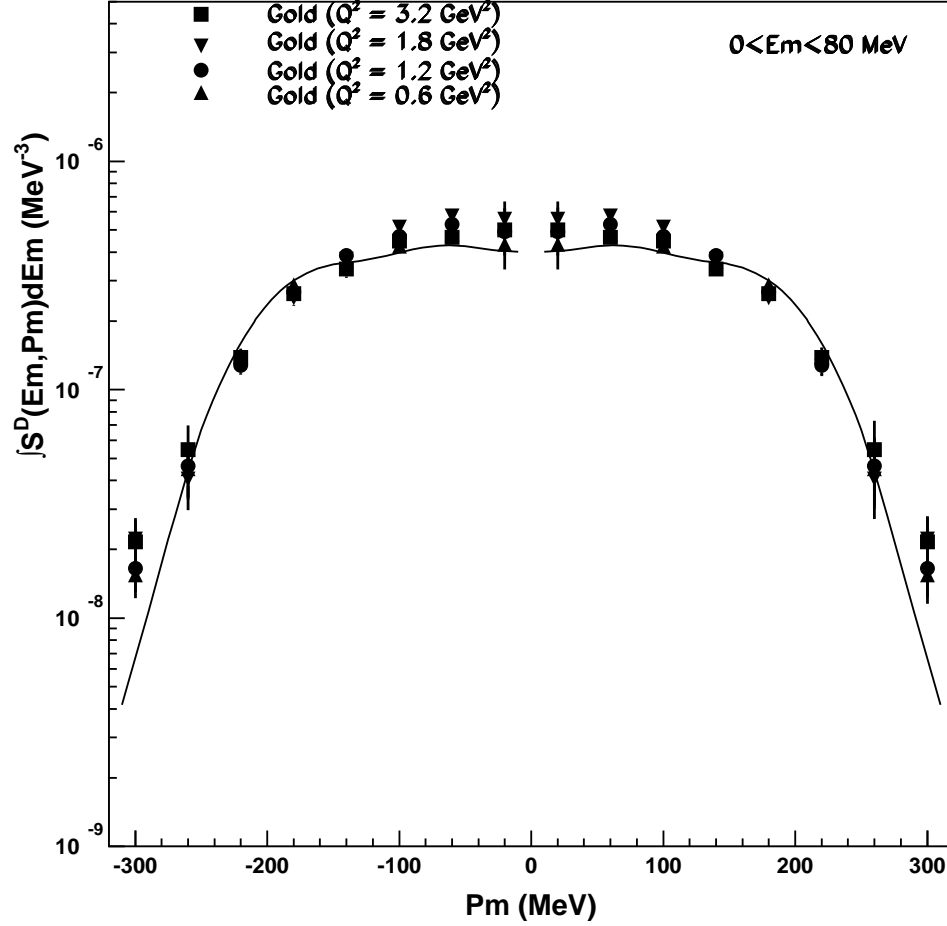


Figure 91: The momentum distribution of the protons in gold at Q^2 of 0.6 - 3.2 GeV^2 are shown along with the calculations of Benhar. They have been normalized so that the integral of the model and measured spectral functions over $|p_m| < 300 \text{ MeV}$ is equal to the integral of the spectral function at Q^2 of 1.8 GeV^2 (kine C). The uncertainties are statistical and systematic added in quadrature.

To this framework Horowitz has also added the exchange of isovector ρ and π mesons. The coupling constants for these fields are calculated from the nuclear matter properties and the rms charge radius of ^{40}Ca .

Starting with initial estimates of the binding energy and the occupation number for each nuclear shell and a mean field potential with Wood-Saxon shape, the Dirac equation is solved for each nuclear shell to calculate the wave function and energy eigen value for the shell. These wave functions then in turn give the shell densities which when integrated over a Greens function gives the new potential. This process is repeated till the energy eigenvalues converge (differ by < 0.05 MeV).

The Timora calculation seems to match the momentum distribution of the data quite well. The missing energy distribution reproduces the shape of the data, which may be an artifact of the fact that the widths of the different shells were tweaked to match the data. However, it is clear that the shells widths used are higher than those observed in the data. This may be the cause of some of the large differences in transparency observed by D. van Westrum [71].

5.5 Separated Response Functions

The deradiated spectral function $S^D(E_m, p_m)$ from the forward and back angle kinematics at Q^2 of 0.6 and 1.8 GeV^2 , shown in the last section, were used to separate out the longitudinal and transverse spectral functions S_L and S_T , following the procedure of Section 4.15. In addition to the longitudinal and transverse spectral functions the ratio of the response functions R_G was also calculated.

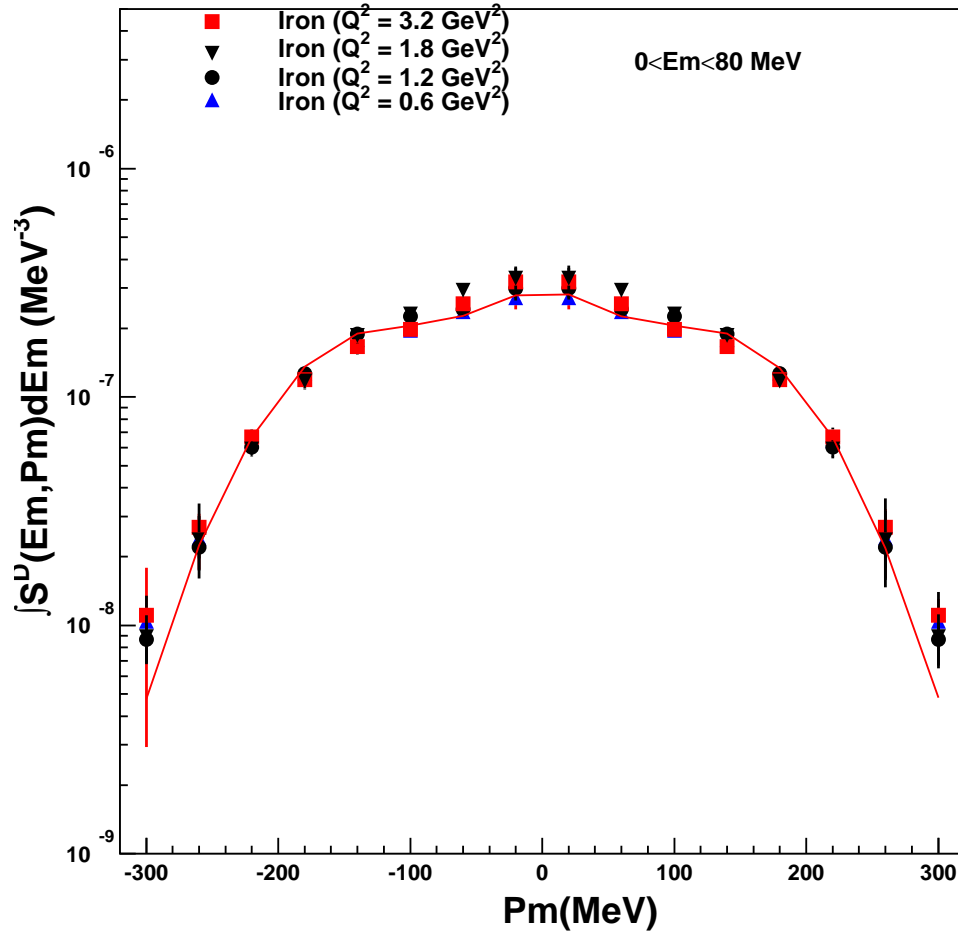


Figure 92: The momentum distribution of the protons in iron at Q^2 of 0.6 - 3.2 GeV^2 are shown along with the Timora calculations in solid. They have been normalized to have integrals equal to that at Q^2 of 1.8 GeV^2 .

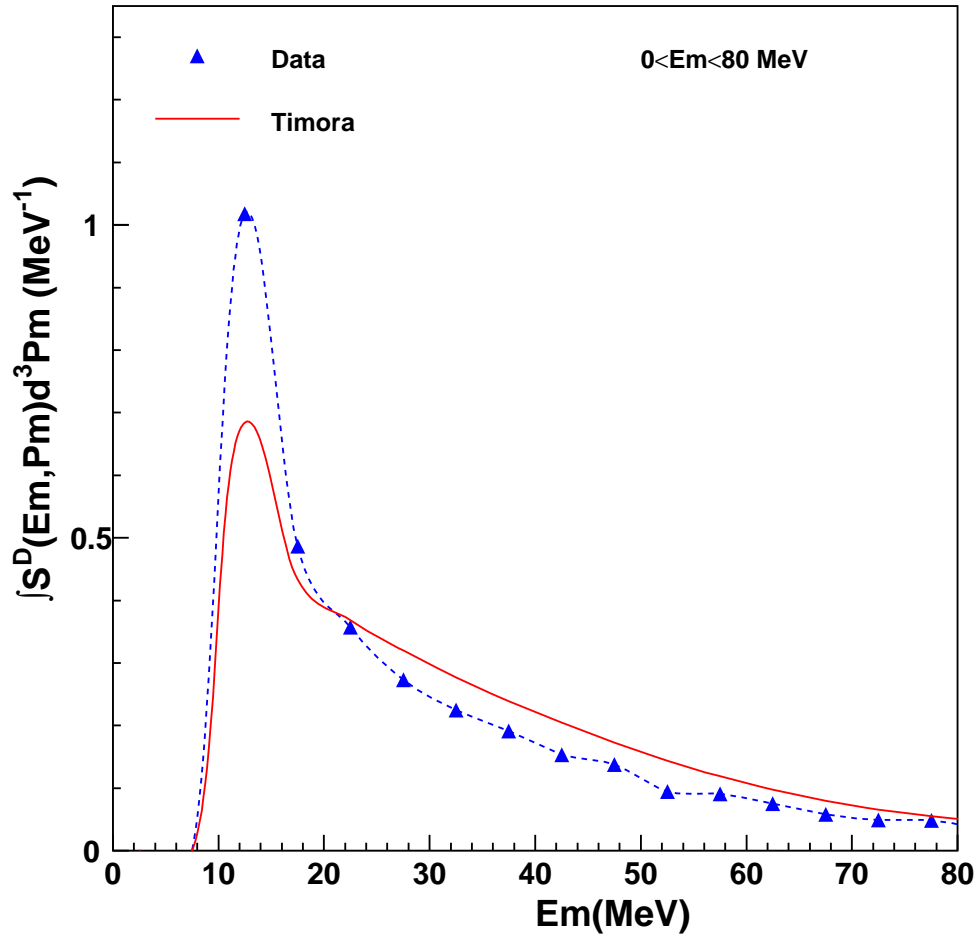


Figure 93: The missing energy distribution of the protons in iron at Q^2 of 1.8 GeV^2 are shown along with the Timora calculations in solid. They have been normalized to have equal number of protons.

5.5.1 Systematic Uncertainties

The systematic uncertainties are divided into two kinds, the correlated point-to-point uncertainties for each of the forward and backward angle measurements and the normalization type uncertainties which are same for all the points and therefore do not effect the ratio R_G .

Table 38 shows the variation of the model cross-section with primary parameters such as beam energy, spectrometer momenta and angles. These are used to determine the point-to-point correlated systematic uncertainties in the measured spectral functions.

Table 39 shows the correlated point-to-point uncertainties and the normalization type uncertainties for all the forward and backward angle points. Using the uncertainties listed in Table 39 one can calculate the systematic uncertainties for the separated spectral functions S_L and S_T . The correlated uncertainties are calculated using Equation 175. The systematic uncertainties in the separated spectral functions are listed in Table 40, the uncertainties in the separation procedure is estimated by applying the separation procedure to simulated data. These uncertainties are determined for each bin in E_m . The numbers quoted in the table are the averages over all bins.

5.5.2 The $Q^2 = 0.6$ (GeV²) Results

The spectral functions at the forward and backward angles for $Q^2 = 0.6$ GeV² are compared in Figs. 94 and 96, for carbon, iron and gold targets. The carbon spectral functions have been split into the p and s shell distributions. In Figure 94 we see that there is very little difference between the forward and the back angle p shell distributions while there are significant difference in the s shell distributions.

Table 38: The variation in the cross-section due to uncertainties in the beam energy the electron momentum and the electron scattering angle for all targets. The last row shows the uncertainties averaged over all targets and summed in quadrature.

Target	Variable	Variation	Kine A	Kine D	Kine C	Kine E
			$\Delta\sigma_{ee'p}\%$			
Carbon	E_{beam}	$\pm 0.25\%$	1.6%	0.3%	0.8%	0.4%
	$E_{e'}$	$\pm 0.2\%$	0.4%	0.4%	0.7%	1.2%
	$\theta_{e'}$	± 1.0 mrad	1.7%	0.60%	2.0%	0.5%
	$P_{p'}$	$\pm 0.2\%$	0.17%	0.7%	0.27%	0.65%
	$\theta_{p'}$	± 1.5 mrad	0.15%	0.33%	0.3%	0.7%
Iron	E_{beam}	$\pm 0.25\%$	0.6%	0.1%	1.0%	0.7%
	$E_{e'}$	$\pm 0.2\%$	0.3%	0.7%	0.7%	0.7%
	$\theta_{e'}$	± 1.0 mrad	1.82%	0.40%	2.18%	0.7%
	$P_{p'}$	$\pm 0.2\%$	0.4%	0.35%	0.3%	0.35%
	$\theta_{p'}$	± 2.0 mrad	0.15%	0.25%	0.5%	0.6%
Gold	E_{beam}	$\pm 0.25\%$	1.0%	0.15%	-	-
	$E_{e'}$	$\pm 0.25\%$	0.4%	0.7%	-	-
	$\theta_{e'}$	± 1.0 mrad	1.82%	0.5%	-	-
	$P_{p'}$	$\pm 0.2\%$	0.5%	0.05%	-	-
	$\theta_{p'}$	± 2.0 mrad	0.01%	0.1%	-	-
	Sum in quadrature		1.86%	0.90%	2.43%	1.49%
	Av. over targets					

Table 39: The correlated point-to-point and the normalization type uncertainties are shown for the forward and backward angle measurements at Q^2 of 0.6 and 1.8 GeV^2

Item	Point-to-point %				Norm type %
	$Q^2 = 0.6 \text{ (GeV}^2\text{)}$		$Q^2 = 1.8 \text{ (GeV}^2\text{)}$		
	Fwd	Bwd	Fwd	Bwd	
Kinematic variables (from Table 38)	1.86	0.90	2.43	1.49	-
HMS Tracking Eff	1.0	1.0	1.0	1.0	-
SOS Tracking Eff	1.0	1.0	1.0	1.0	-
Proton Absorption	-	-	-	-	1.0
Run Stability	1.0	1.0	1.0	1.0	-
Acceptance	0.5	0.5	0.5	0.5	1.5
Current Measurement	-	-	-	-	1.0
Solid Target Thickness	-	-	-	-	0.5
Radiative Corrections	0.5	0.5	0.5	0.5	2.0
Sum in Quadrature	2.64	1.82	3.07	2.39	2.92
Model dependence	-	-	-	-	5.0

Table 40: The correlated point-to-point and the normalization type uncertainties propagated to the separated spectral functions at Q^2 of 0.6 and 1.8 GeV^2

Item	$Q^2 = 0.6 \text{ (GeV}^2\text{)}$		$Q^2 = 1.8 \text{ (GeV}^2\text{)}$	
	S_L	S_T	S_L	S_T
Correlated	13.07	4.82	33.60	4.84
Normalization type	2.92	2.92	2.92	2.92
Separation procedure(average)	1.54	1.20	1.54	1.20
Sum in quadrature	13.48	5.84	33.75	5.78

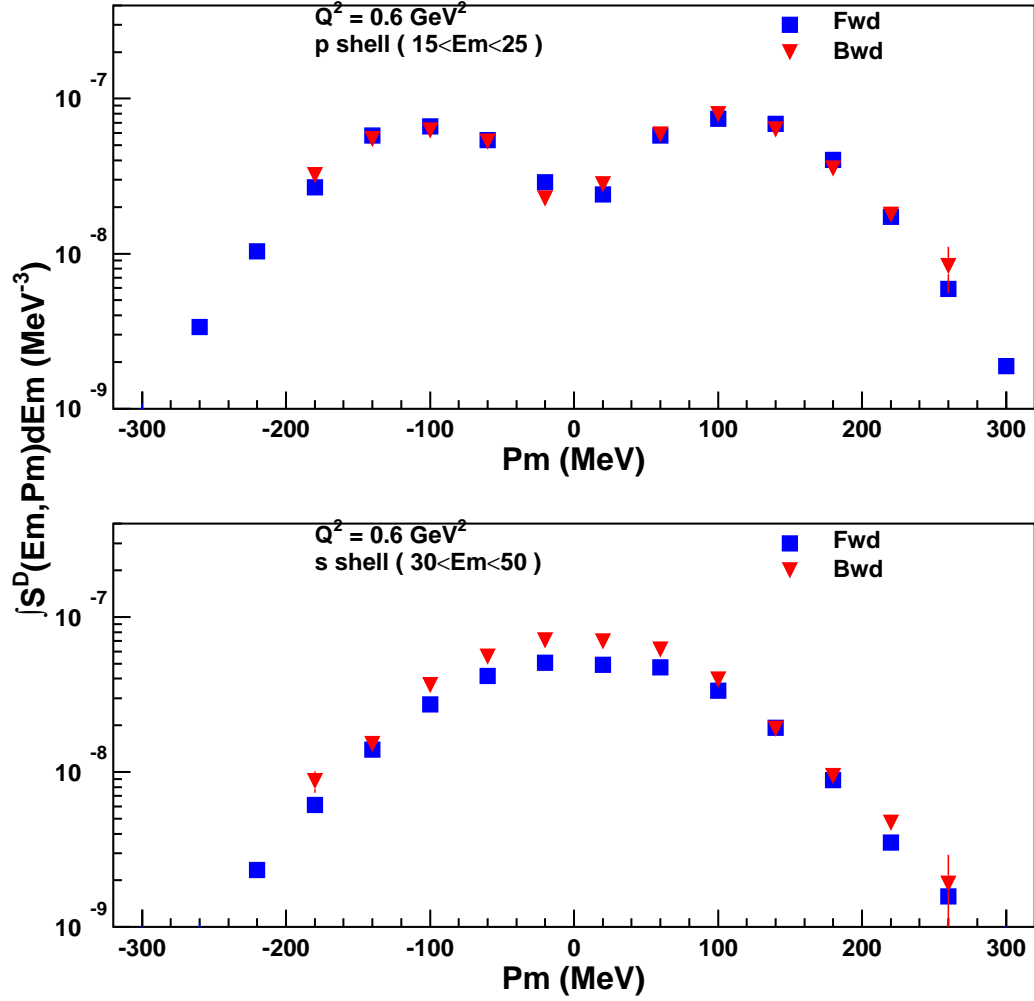


Figure 94: The momentum distribution of the protons in Carbon at Q^2 of 0.6 GeV^2 for the p shell (upper panel) and the s shell (bottom panel). The forward angle distribution (squares) and the backward angle distribution (triangles) are compared. Just statistical errors are shown.

These forward and backward angle spectral functions were used to separate the longitudinal and transverse spectral functions. The separated spectral functions were averaged over the $p_{3/2}$ shell region in carbon and the $f_{7/2}$ shell region in iron, because the resolution of the spectrometer models are not optimized to match those of the data.

The separated spectral functions for $0 < p_m < 80$ MeV for ^{12}C is shown in Figure 95. We see that for the p shell the transverse and the longitudinal strength are almost equal, (transverse is $10\% \pm 10\%$ more than longitudinal). However, there is considerable excess transverse strength in the s shell region. Also there is little excess strength at higher missing energies. It is also seen that the s shell strength in the longitudinal response is peaked at about 38 MeV, while the difference between the transverse and the longitudinal response peaks about 5 MeV higher. This suggests that the shift in the unseparated spectrum is due to the excess transverse strength. We also observe that the longitudinal spectral function extends to high missing energies. This tells us that the single nucleon strength extends to missing energies up to 80 MeV. This is in contrast to previous experiments [10] which observed the longitudinal strength go to zero by 60 MeV in E_m (see Figure 103).

The separated spectral functions for ^{56}Fe are shown in Figure 97. We see that for the f shell the transverse and the longitudinal strength are almost equal (transverse is $15\% \pm 10\%$ more than the longitudinal), but there is considerable excess transverse strength beyond the f shell up to about 60 MeV, at higher missing energies the strengths are almost equal again. The separated spectral functions for ^{197}Au is shown in Figure 98. Here we see that there is excess transverse strength up to about 60 MeV and at even higher missing energies the excess strengths falls off slowly. All the observed results in this section and their consequence are summarized in Section 5.5.5.

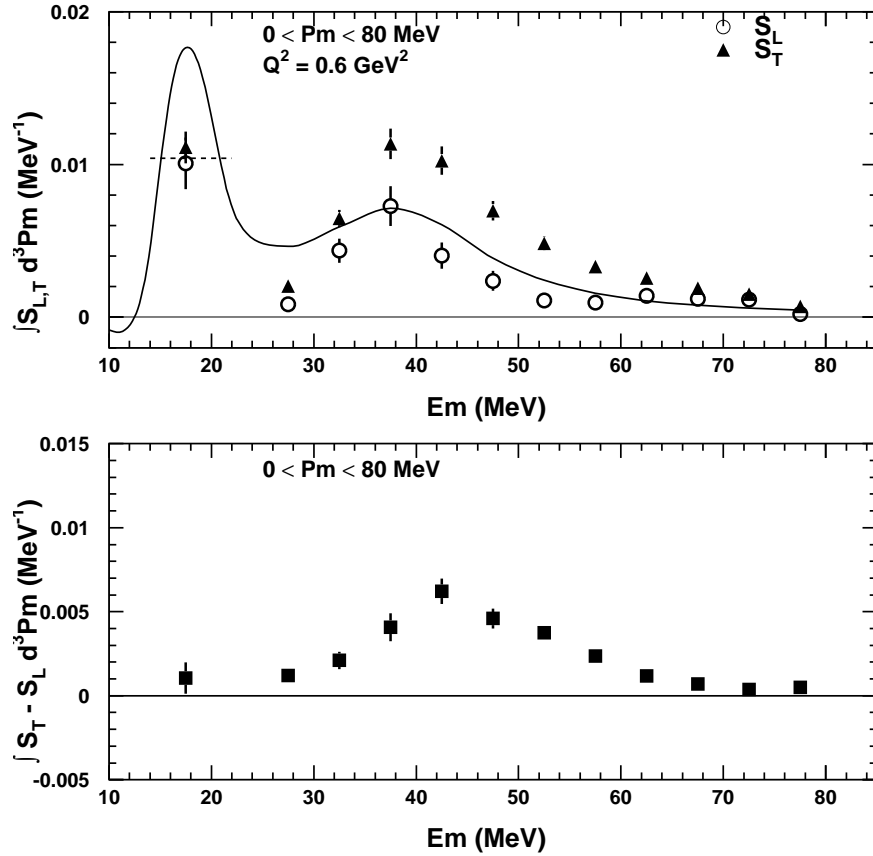


Figure 95: The separated longitudinal spectral functions S_L (open circles) and transverse spectral function S_T (triangles) for carbon at Q^2 of 0.6 GeV^2 are shown on the upper panel, the statistical and systematic uncertainties added in quadrature are shown. The p shell distribution has been averaged over. The solid line in the upper panel is the model longitudinal spectral function extracted from the IPSM spectral function and the dashed line shows the average over the p shell distribution of the model normalized to the measured p shell distribution. The lower panel shows the difference between the transverse and the longitudinal spectral functions. The lower panel shows statistical errors only.

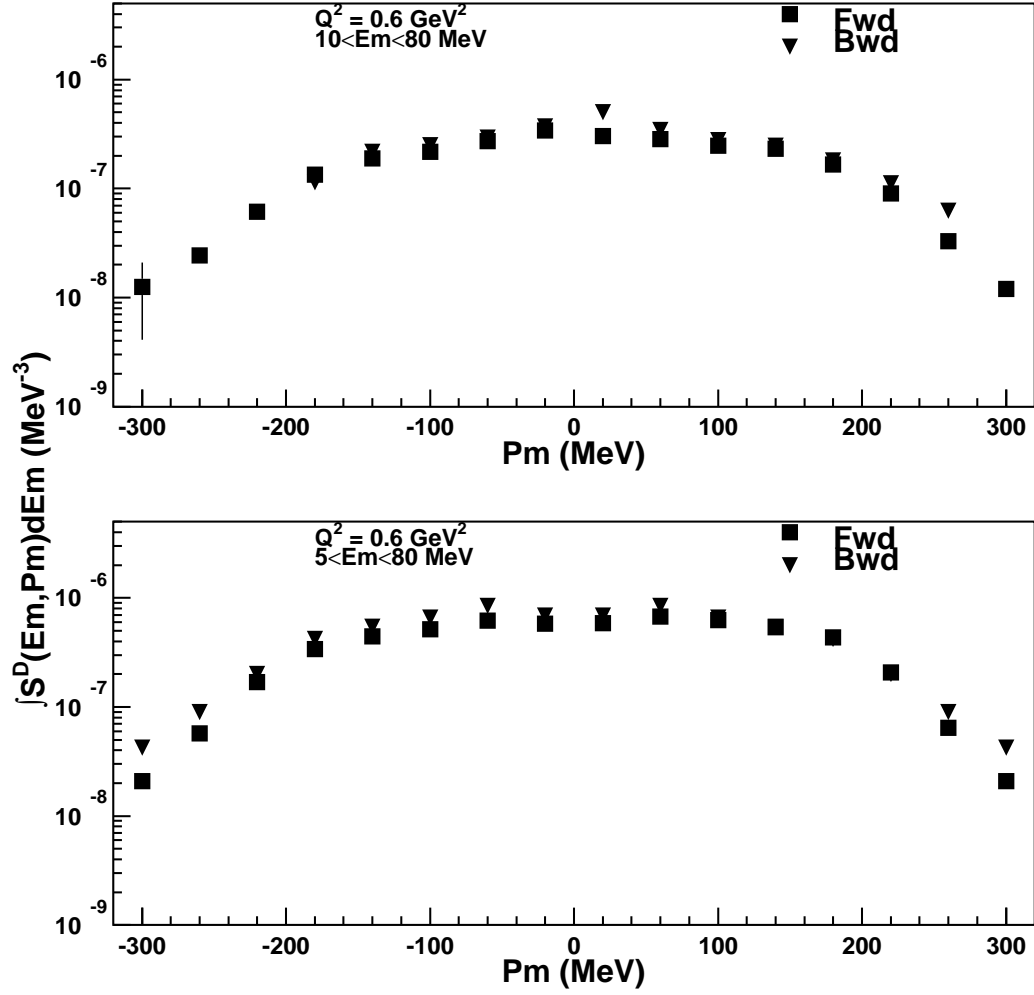


Figure 96: The momentum distribution of the protons in iron (upper panel) and gold (bottom panel) at Q^2 of 0.6 GeV^2 . The forward angle distribution (squares) and the backward angle distribution (triangles) are compared. Errors are statistical only.

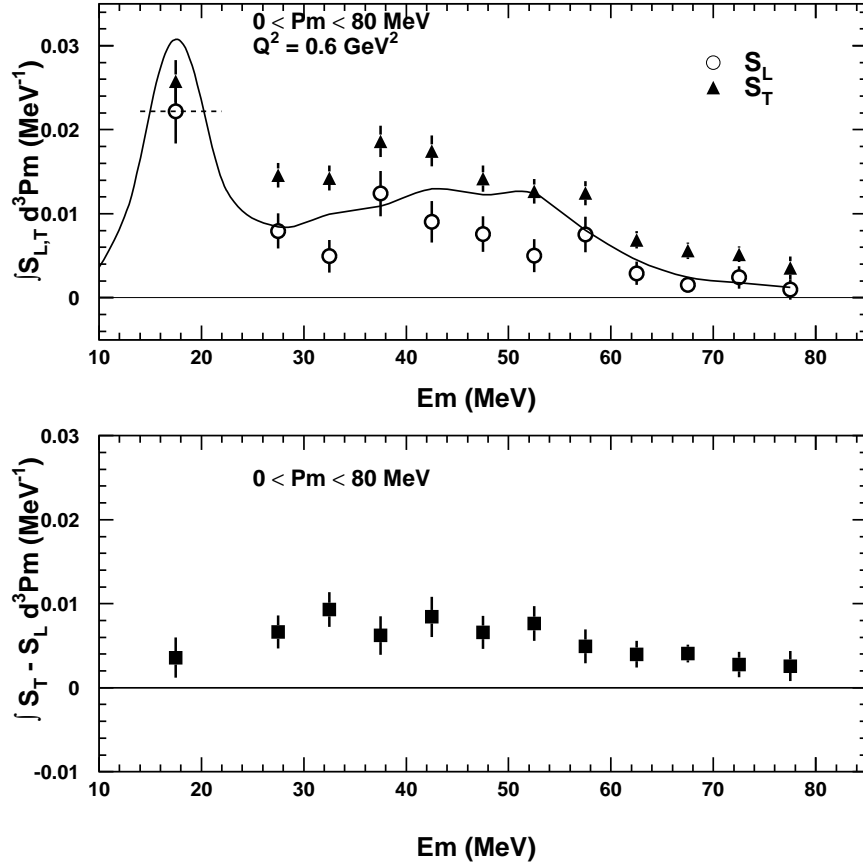


Figure 97: The separated longitudinal spectral functions S_L (open circles) and transverse spectral function S_T (triangles) for iron at Q^2 of 0.6 GeV^2 are shown on the upper panel, the statistical and systematic uncertainties added in quadrature are shown. The peak from 10-25 MeV has been averaged over. The solid line in the upper panel is the model longitudinal spectral function extracted from the IPSM spectral function and the dashed line shows the average over the peak for the model normalized to the measured distribution. The lower panel shows the difference between the transverse and the longitudinal spectral functions. The lower panel shows statistical errors only.

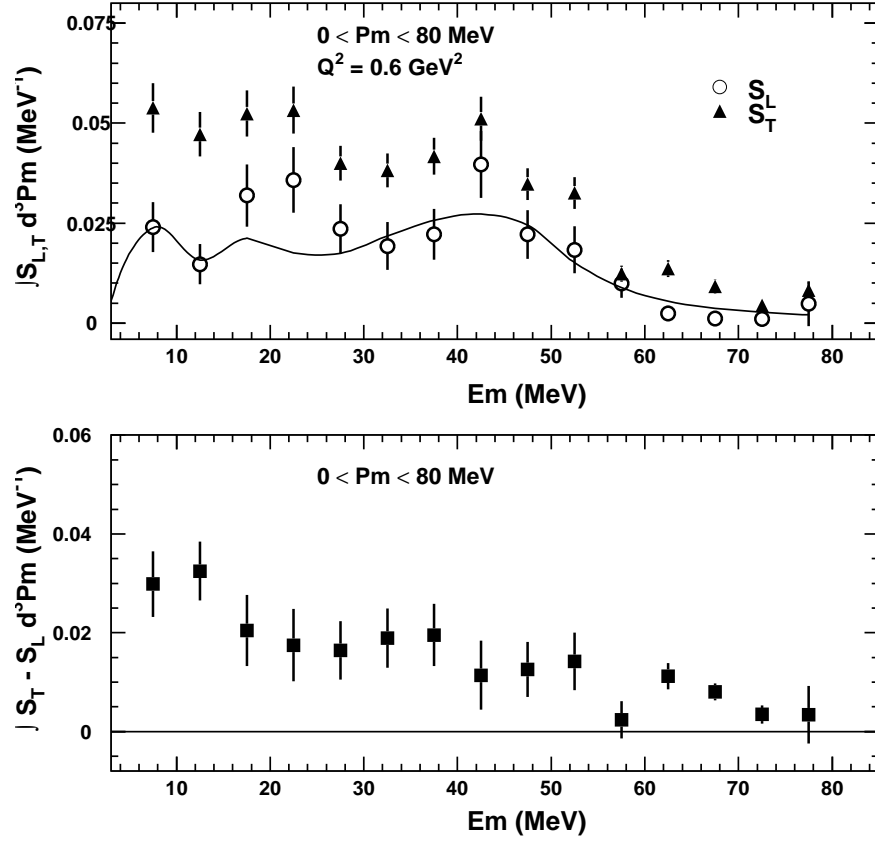


Figure 98: The separated longitudinal spectral functions S_L (open circles) and transverse spectral function S_T (triangles) for gold at Q^2 of 0.6 GeV^2 are shown on the upper panel, the statistical and systematic uncertainties added in quadrature are shown. The solid line in the upper panel is the model longitudinal spectral function extracted from the IPSM spectral function normalized to the forward angle data (kine A). The lower panel shows the difference between the transverse and the longitudinal spectral functions. The lower panel shows statistical errors only.

5.5.3 The $Q^2 = 1.8 \text{ (GeV}^2\text{)}$ Results

The spectral functions at the forward and backward angles for $Q^2 = 1.8 \text{ GeV}^2$ are compared in Figure 99 for the carbon target. The carbon spectral functions have been split into the p and s shell distributions.

Figure 100 shows the separated spectral function for ^{12}C at $Q^2 = 1.8 \text{ GeV}^2$. We see that the transverse strengths is much reduced compared to the transverse strength at $Q^2 = 0.6 \text{ GeV}^2$. The longitudinal spectral function has very large systematic uncertainties and hence is not very informative. Assuming that the longitudinal spectral function is dominantly single particle and Q^2 independent we can compare the S_L ($Q^2 = 0.6$) with S_T ($Q^2 = 1.8$)(Figure 102, bottom panel). Here we see that there still remains some excess transverse strength at $40 < E_m < 65 \text{ MeV}$ but the reduced transverse strength does indicate that the PWIA holds much better at these higher Q^2 .

Once again Figure 101 shows that for the transverse strength is reduced and the large uncertainties in the longitudinal spectral function make it of limited use, however the reduced transverse strength would again indicate that the PWIA holds much better at these higher Q^2 region. The observed results in this section and their consequence are summarized in Section 5.5.5.

Figure 102 shows the ^{12}C longitudinal and transverse spectral functions at the two different Q^2 . The longitudinal spectral functions are consistent with each other at low missing energies but at high E_m the spectral function at the higher Q^2 has more yield. The transverse spectral function at the lower Q^2 has a significant excess compared to the transverse spectral function at the higher Q^2 .

The separated spectral functions were compared with previous data from MIT Bates [10] at $Q^2 = 0.14 \text{ GeV}^2$. The separated response functions from the previous

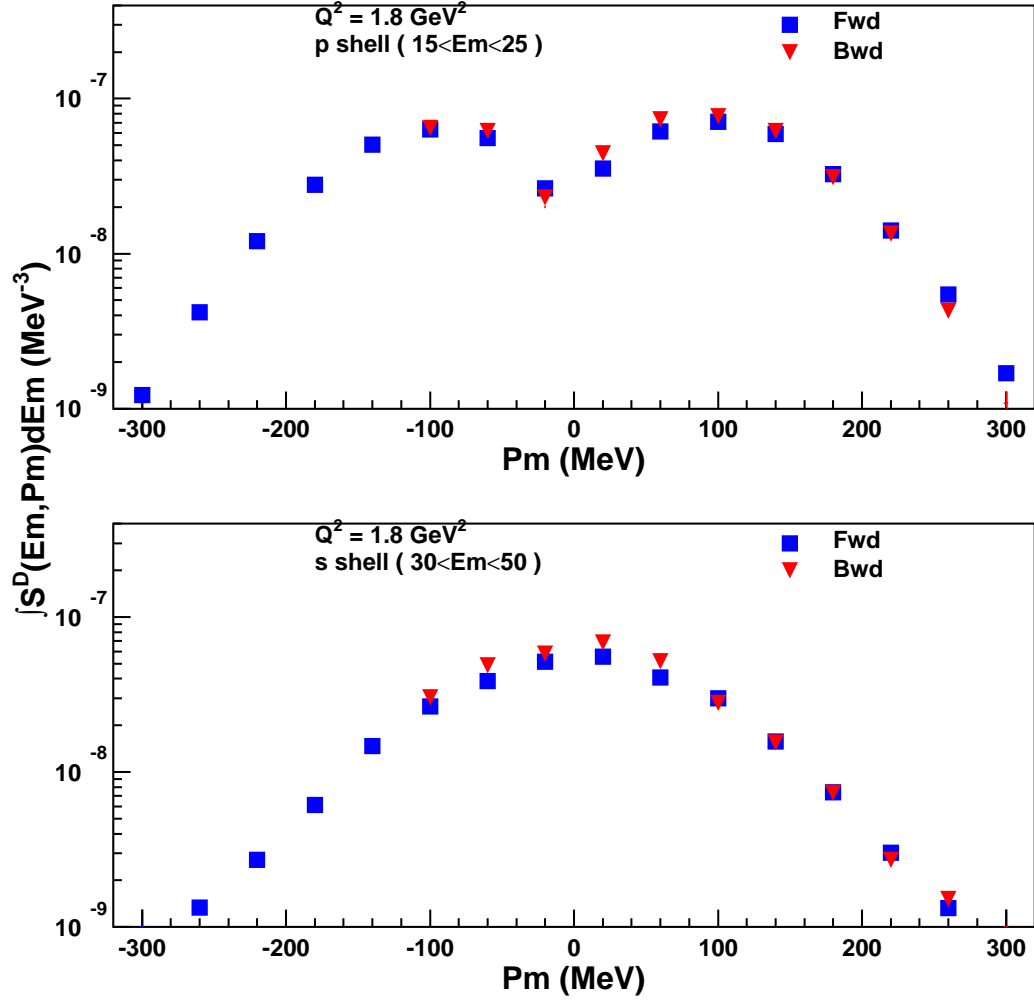


Figure 99: The momentum distribution of the protons in carbon at Q^2 of 1.8 GeV^2 for the p shell (upper panel) and the s shell (bottom panel). The forward angle distribution (squares) and the backward angle distribution (triangles) are compared. statistical errors are shown.

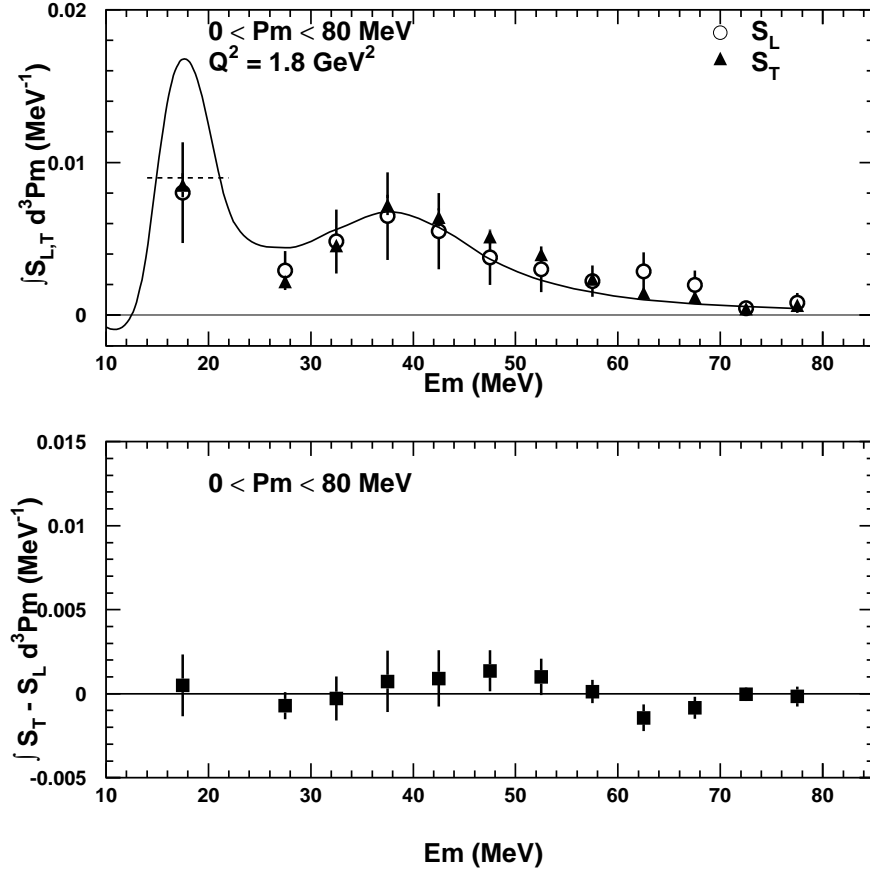


Figure 100: The separated longitudinal spectral functions S_L (open circles) and transverse spectral function S_T (triangles) for carbon at Q^2 of 1.8 GeV^2 are shown on the upper panel, the statistical and systematic uncertainties added in quadrature are shown. The p shell distribution has been averaged over. The solid line in the upper panel is the model longitudinal spectral function extracted from the IPSM spectral function and the dashed line shows the average over the p shell distribution of the model normalized to the measured p shell distribution. The lower panel shows the difference between the transverse and the longitudinal spectral functions. The lower panel shows statistical errors only.

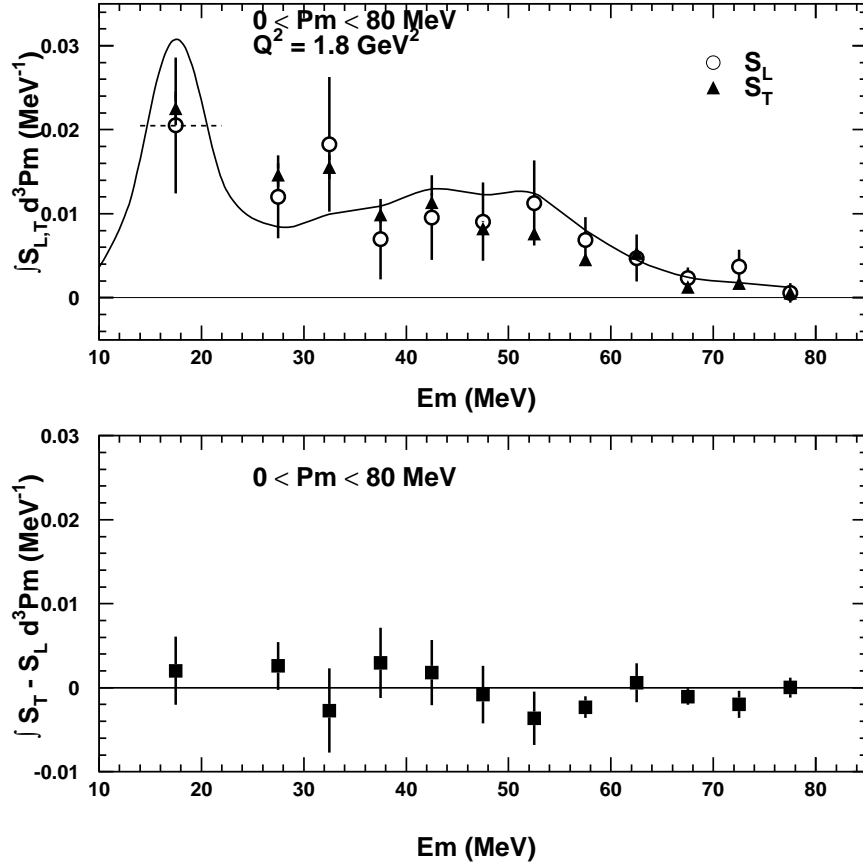


Figure 101: The separated longitudinal spectral functions S_L (circles) and transverse spectral function S_T (triangles) for iron at Q^2 of 1.8 GeV^2 are shown on the upper panel, the statistical and systematic uncertainties added in quadrature are shown. The peak from 10-25 MeV has been averaged over. The solid line in the upper panel is the model longitudinal spectral function extracted from the IPSM spectral and the dashed line shows the average over the peak for the model normalized to the measured distribution. The lower panel shows the difference between the transverse and the longitudinal spectral functions. The lower panel shows statistical errors only.

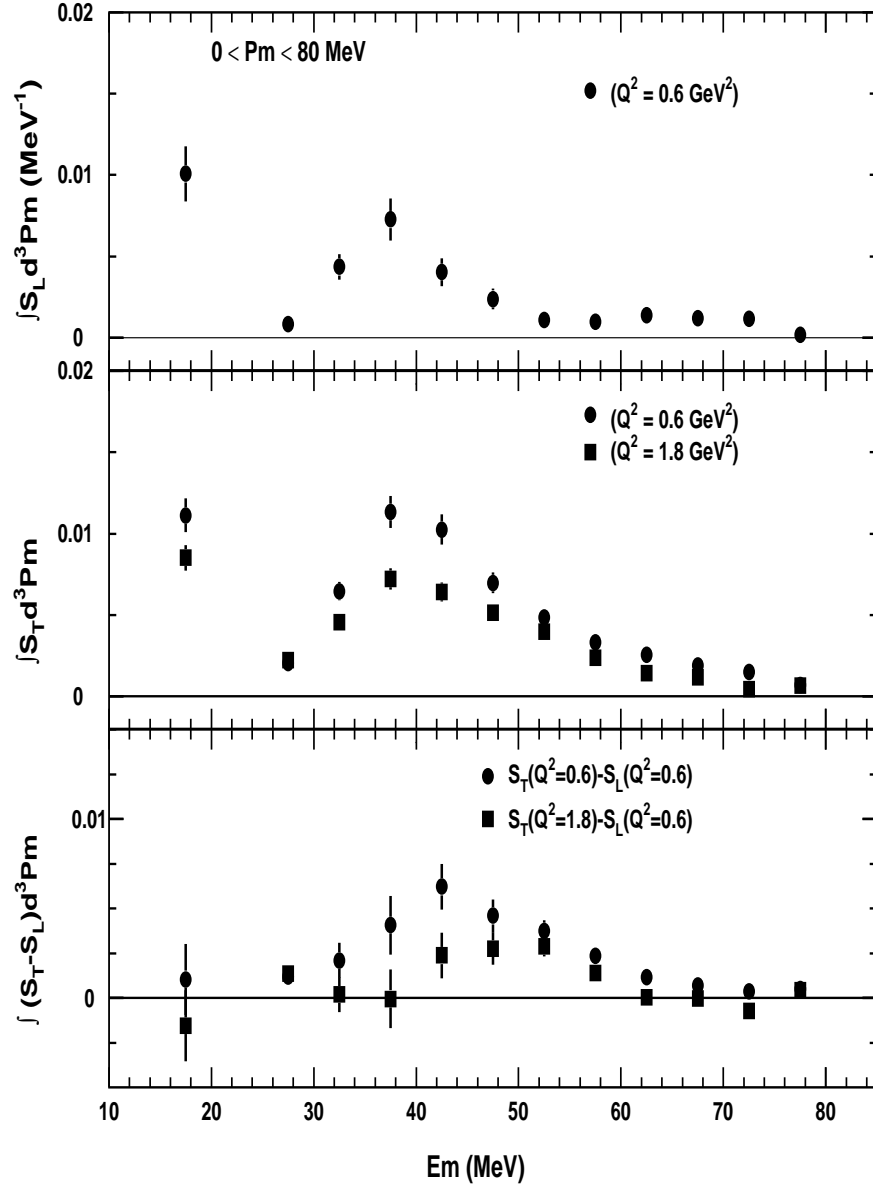


Figure 102: The upper panel shows the carbon longitudinal spectral function S_L at $Q^2 = 0.6$ GeV 2 (open circle) compared with the longitudinal spectral function at $Q^2 = 1.8$ GeV 2 (triangles). The lower panel is the same for the transverse spectral function S_T . The statistical and systematic uncertainties added in quadrature are shown.